Commensurability effect and lock-in transition in Mo/Si superconducting superlattices

O. I. Yuzephovich,* Yu. V. Bomze, M. Yu. Mikhailov, I. M. Dmitrenko, and N. Ya. Fogel

B. Verkin Institute for Low Temperature Physics and Engineering, 47 Lenin Ave., 310164, Kharkov, Ukraine

We report the first observation of the lock-in transition in artificial superconducting superlattices, which takes place in tilted magnetic fields. The measurements were carried out on the Mo/Si layered system. The temperature dependence of the critical angle for the trapping of the vortices in the orientation parallel to the layer planes is determined by the previously known resistive method and by a new method based on the effect of commensurability between the intervortex distance and the superlattice wavelength. The temperature dependences of the critical angle obtained by the two methods practically coincide. The experimental results are consistent with the theoretical predictions of Feinberg and Villard. © *2000 American Institute of Physics.* [S1063-777X(00)00402-3]

INTRODUCTION

Many layered superconductors (high-T_c oxides, artificial superlattices consisting of high-temperature compounds or conventional superconductors, intercalated dichalcogenides, etc.) have an inherently large anisotropy of the physical parameters. It is known that such an anisotropy plays a very important role, giving rise to many new phenomena, such as the dimensional crossover, fluctuation-induced decoupling and melting of the vortex lattice (VL), intrinsic pinning, lock-in transition, and so on. The static and dynamic properties of the vortex matter in the solid phase differ essentially from those in the homogeneous type II superconductors. According to the results of Ref. 1, the unit cell of the VL should be strongly distorted compared to the equilateral triangle that is characteristic for the Abrikosov VL. The VL parameters should depend intrinsically on the anisotropy coefficient $\gamma = (M/m)^{1/2}$ and on the angle between the applied magnetic field **H** and the anisotropy axis. Here M is an effective mass along the normal to the layer planes, and m is the in-plane mass. The influence of the anisotropy on the properties of the layered superconductor is revealed most dramatically in a parallel field and in a range of angles which are close to $\theta = 0°$ ($\theta = 0°$ for **H** parallel to the layers). In particular, for parallel magnetic fields the effect of the commensurability between the intervortex distance in the VL and the layered structure period s leads to oscillations of the critical current, resistivity, and magnetization.[2–6] The theory of the matching effects for this situation was developed in Refs. 7–11. Of special interest is the situation of strong layering considered in Ref. 10. It was shown that when the intrinsic pinning energy E_p exceeds the elastic energy of VL shear deformation E_{el}, the vortices cannot cross the layers, and the period Z_0 of the VL in the direction orthogonal to the layers is fixed and is determined by the initial conditions under which the vortex lattice was formed. This means that the VL should always be commensurable with the periods s of the underlying pinning potential connected with the layered structure. In

this case only the values $Z_0 = N_s$ (N is an integer) are allowed; Z_0 remains constant over a wide range of applied field intensities, while the unit cell area of the vortex lattice varies with the field only on account of flux line displacements along the layers. In the framework of the Lawrence–Doniach approach, for relatively high magnetic fields a sequence of first-order phase transitions between the vortex lattices with different orders of commensurability N is predicted.[11]

Oscillatory dependence of the critical current I_c on the parallel magnetic field owing to the commensurability effect has been observed on several kinds of multilayers: Nb/Ta (Ref. 3), Nb/Pd (Ref. 4), and Mo/Si (Ref. 5). It was shown that the I_c oscillations are accompanied by resistivity oscillations, and all features of the R vs. H and I_c vs. H curves correlate.[5] However, at low temperatures the zero-resistance regions that manifest the reentrance of superconductivity[5] appear instead of the resistance minima. The majority of the features of the nonmonotonic and reentrant behavior may be explained quantitatively in terms of the Ivlev–Kopnin–Pokrovskii theory.[10] The positions of the resistance minima and zero-resistance regions correspond to the stable states of the commensurate vortex lattices.[5]

At temperatures close to the transition temperature T_c not all of the above-mentioned effects have been observed, because the intrinsic pinning,[12] which creates large barriers for the transverse motion of the flux lines and gives rise to an effective locking of the vortices between the superconducting layers, becomes strong at temperatures sufficiently low that the condition $\xi_\perp(T) \lesssim s$ holds.[12,13] Here $\xi_\perp$ is the coherence length in the direction orthogonal to the layer planes.

It has been shown[14] that the intrinsic pinning causes another interesting phenomenon, namely a lock-in transition. Due to the anisotropy, at relatively small tilt angles the confinement of the vortices parallel to the layer planes becomes energetically more favorable than the creation of tilted vortices. The manner of the flux penetration in the oblique fields

is modified at angles which are close to $\theta = 0°$. Experimentally the lock-in transition is observed by several different methods. Among them are the measurements of the microwave dissipation at different orientations of **H**;[15] the lock-in transition is identified by the change in the dissipation mechanisms, which are controlled by the parallel and perpendicular components of the dc magnetic field, respectively. Evidence about the lock-in transition may be obtained from torque experiments[16–18] and from ac magnetic susceptibility measurements,[19] from magnetization,[20,21] and from resistive measurements.[22] A comparative analysis of all the methods used for determination of the lock-in transition is presented in Ref. 21. All these investigations have been performed on single crystals of high-temperature oxides and organic layered superconductors.

It is known that artificial superconducting superlattices consisting of conventional superconductor films and some insulating interlayers may perfectly imitate the properties of high-T_c compounds.[23–26] The cited works concern the flux line creep and the *H-T* phase diagram. Obviously, observation of the lock-in transition may be also expected in artificial superconducting multilayers. Here we report on finding the lock-in transition in Mo/Si superlattices (with a temperature of the superconducting phase transition of about 4 K).[27] For the study of this phenomenon we have used the resistive method described by Kwok *et al.*,[22] as well as a new method based on the effect of commensurability between intervortex distance and the superlattice wavelength. We believe that the latter method provides the clearest evidence of vortex locking between the layers in tilted fields as compared with all other methods mentioned above. The explicit temperature dependence of the critical angle for the lock-in transition is obtained for the first time.

SAMPLE PREPARATION AND EXPERIMENTAL PROCEDURE

The measurements were carried out on a Mo/Si multilayered sample with Mo layer thickness of 22 Å and Si layer thickness of 34 Å. The sample consists of 50 bilayers. The Mo/Si multilayer was prepared by two-magnetron sputtering onto a glass substrate at $T = 100\,°C$ in argon. The working pressure of argon in the deposition chamber was 3×10^{-3} torr. The initial vacuum was no worse than 10^{-6} torr.

Small-angle x-ray diffractometry was used for the determination of the superlattice period and for checking the degree of sample perfection. The number of satellite lines on the diffractograms for the samples investigated is 4, while for multilayers prepared in the same way with wavelengths equal to or exceeding 100 Å this number is about 10 or more. These data attest to the high regularity of the layering. The same conclusion follows from an electron microscopy investigation of the sample cross section. The latter also shows that the roughness of the interfaces does not exceed 7–8 Å. The multilayer period was determined with an accuracy of 0.1 Å.

The x-ray diffraction data showed that the silicon layers are amorphous and the molybdenum layers are microcrystalline, with a crystallite size of several nanometers. More de-
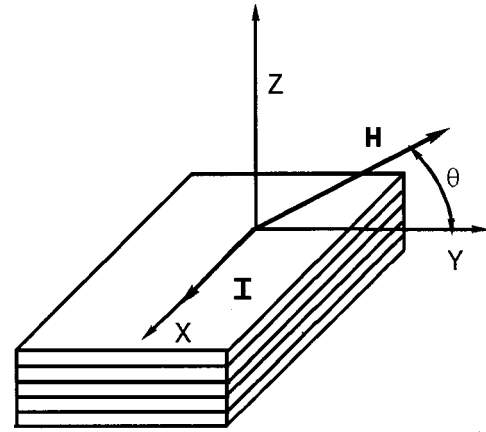

FIG. 1. Geometry of the experiment.

tails about the sample preparation and characterization may be found in Refs. 27–29.

The transport measurements were performed in a standard helium crystal equipped with a 5 T super-conducting coil. The geometry of the experiments is shown in Fig. 1. The orientation of the sample holder in the magnetic field was changed with the help of special rotation mechanism. The accuracy of the determination of the angle between the applied magnetic field **H** and the layer planes was no worse than 0.1°. During the rotation of the sample the transport current was always perpendicular to the applied magnetic field. The parallel orientation was identified by finding the minimum in the resistance. The stabilization of the temperature at a given point was about 10^{-3} K. The critical magnetic fields were defined in the resistive transitions with the use of the criterion $R = 0.5R_n$. The resistance measurements were carried out using the standard four-probe technique with a transport current of 1 mA.

EXPERIMENTAL RESULTS AND DISCUSSION

In Fig. 2a the typical dependences of the resistance on the parallel magnetic field at different temperatures are shown for a case of strong intrinsic pinning. At temperatures close to the transition temperature T_c all the resistive curves are smooth (they are outside the scope of this figure). Beginning from the temperature 3.5 K (the T_c for this sample is 3.67 K), minima appear on the R vs. $H_\parallel$ curves, and at still lower temperatures these minima are transformed to zero-resistance regions (Fig. 2b). These dependences closely correlate with the dependence of the critical current I_c on $H_\parallel$, as Fig. 2c shows. As was proved recently,[5] such nonmonotonic behavior of the critical current and resistivity and also the reentrance of superconductivity may be explained in terms of the commensurability effect that should be observed under the condition of strong intrinsic pinning. The locations of the R vs. $H_\parallel$ minima (and the I_c maxima, respectively) correspond to the stable states of the commensurate vortex lattices. For the parallel field the positions of the minima do not shift with temperature, as would be expected for the matching effect. The manifestations of the commensurability effects appear below some temperature T_0, where the condi-
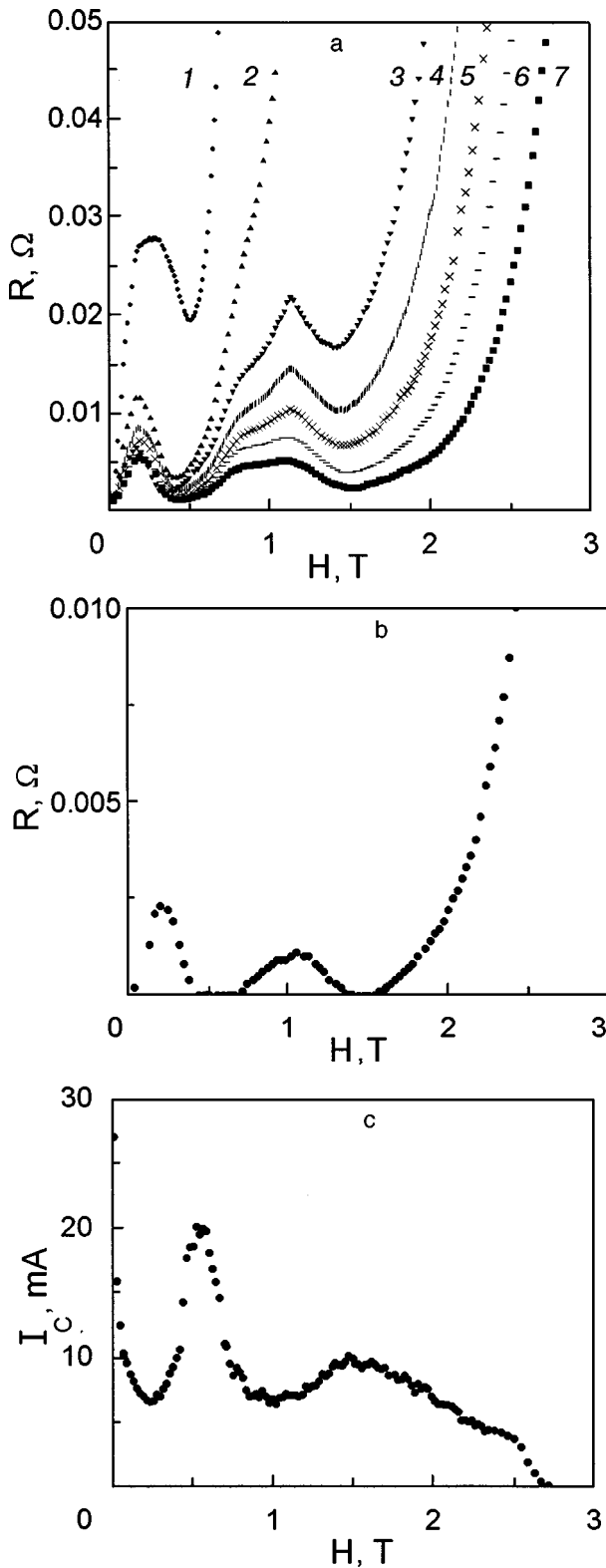
FIG. 2. Resistance as a function of the parallel magnetic field at different temperatures *T*, K: 3.504 (1); 3.478 (2); 3.467 (3); 3.462 (4); 3.459 (5); 3.453 (6); 3.447 (7) (a); at *T* = 3.44 K (b) Critical current as a function of the parallel magnetic field (c).
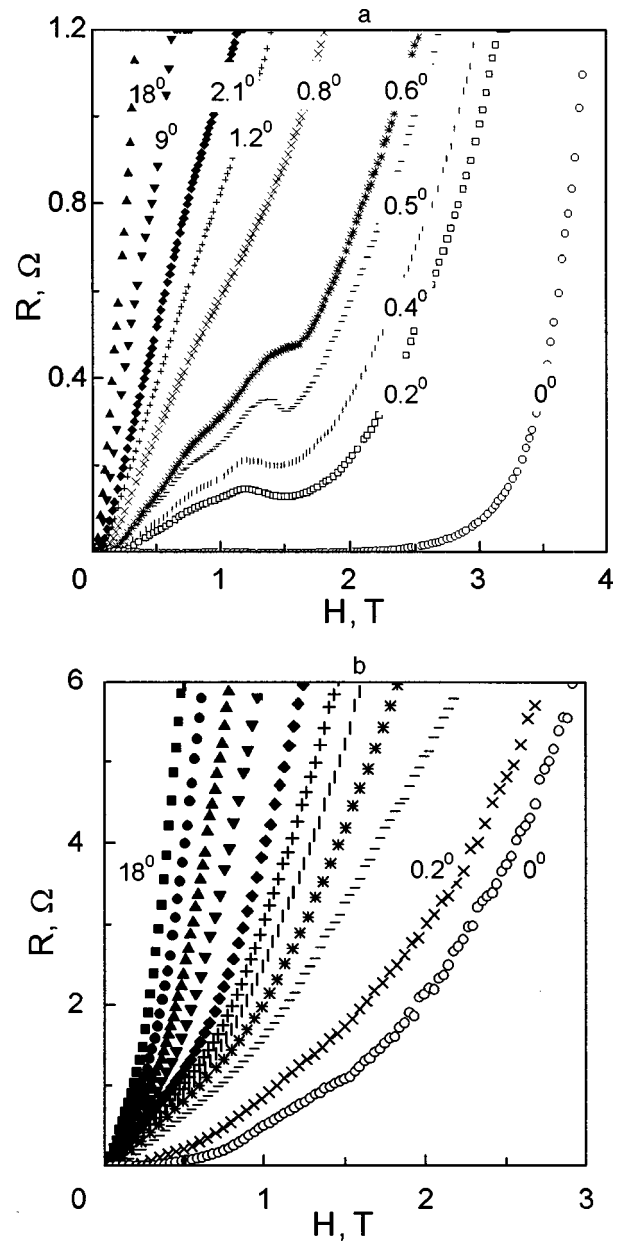

FIG. 3. Magnetic field dependences of the resistance at different orientations of the applied magnetic field at *T* = 3.44 K (a), and 3.503 K (b).

essentially different *R* vs. $H_\parallel$ curve patterns can be observed on the same sample, as was shown in Ref. 5. Obtaining one or another vortex arrangement depends on the magnetic history. In this paper we shall deal with only one of the possible kinds of *R* vs. $H_\parallel$ curve presented in Fig. 2.

If the lock-in transition exists in the system investigated, one should expect the appearance of resistivity minima at small tilt angles θ, as well (the angle $\theta = 0°$ for the magnetic field parallel to the layer planes). In the range of angles where the vortex lines are trapped between the superconducting layers, the position of the resistance minima is bound to remain constant because the VL structure stays unchanged. As Fig. 3a shows, this is indeed the case at sufficiently low temperatures. At larger angles the minimum disappears. The critical angle θ_c dividing the *R* vs. *H* curves with and without a minimum depends on temperature, as follows from Fig. 4.

tion $\xi_\perp < s/\sqrt{2}$ is met.[5] This temperature, as was mentioned above, is equal to 3.5 K. The data presented in Fig. 1 correspond to the stable states of commensurate VL configurations with $N = 1$ and $N = 3$. Other vortex arrangements with
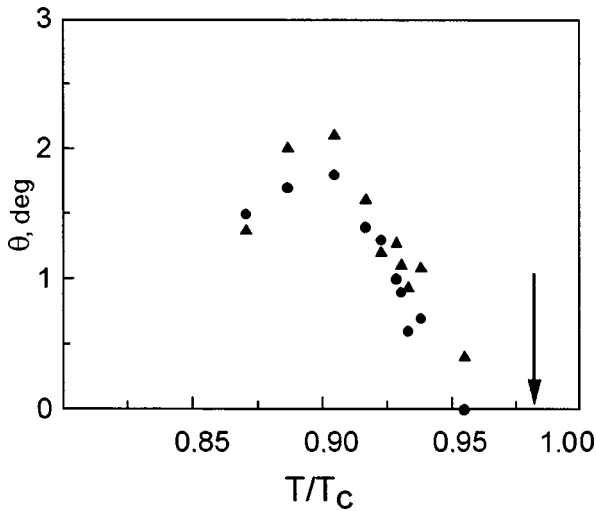
FIG. 4. The critical angle as a function of reduced temperature: obtained from the plots similar to Fig. 3a (●); determined in the way shown in Figs. 5 and 6 (▲). The arrow shows the cross-over temperature.

FIG. 5. Angular dependences of the resistance at different magnetic fields H, T: 0.2 (1); 0.3 (2); 0.4 (3); 0.5 (4).

At high temperatures there are no features on the R vs. $H_\parallel$ curves for $\theta = 0°$ or for the tilted fields either. The first slight kinklike hints appear at $T = 3.5$ K (Fig. 3b), and for this temperature θ_c is equal to zero with an accuracy of 0.1°.

In the paper of Kwok *et al.*[22] the lock-in transition was also observed on $YBa_2Cu_3O_x$ single crystals by the resistive method. A sharp drop of the resistance was found on the R vs. θ curves in the range of small angles and was convincingly interpreted by the authors as evidence of the lock-in transition. The critical angle θ_c in these experiments was about 0.3°, and it was practically independent of temperature. However, the latter statement cannot be considered as very reliable because the investigations were carried out in a very limited temperature range ($T/T_c = 0.993 - 1$). Probably the too-high slope $dH_{c\parallel}/dT|_{T_c}$ of the parallel critical fields has prevented those authors from going to lower temperatures.

A similar sharp drop in the resistance is observed in our experiments in the vicinity of the parallel orientation (Fig. 5; compare it with Fig. 2 in Ref. 22). It corresponds to the fast increase of the critical magnetic field in the same range of angles (see Fig. 6, curve 4). As Figs. 5 and 6 show, the H_{c2} vs. θ curves allow one to determine θ_c as well as the R vs. θ curves do. Curves of $H_{c2}(\theta)$ for different temperatures are presented in Fig. 6. The values of θ_c obtained from these plots are displayed in Fig. 4 along with those obtained from the plots similar to Fig. 3a. It is seen that the θ_c values determined by the two methods differ insignificantly.

According to the theoretical results of Feinberg and Villard,[14] for $H_{c1} \ll H \ll H_{c2}$ the region of field orientations for which the flux lines are trapped parallel to the layers (i.e., the critical angle θ_c) should depend on the barrier height associated with the intrinsic pinning, on the anisotropy parameter γ, and on the magnetic field intensity. The value of the critical angle is determined by the expression[14]

$$\cos(90° - \theta_c) = \frac{1}{\pi}\left[2a_1 \frac{H^*}{H}\left(1 + \gamma^2 \frac{H^*}{H}\right)\right]^{1/2}. \quad (1)$$
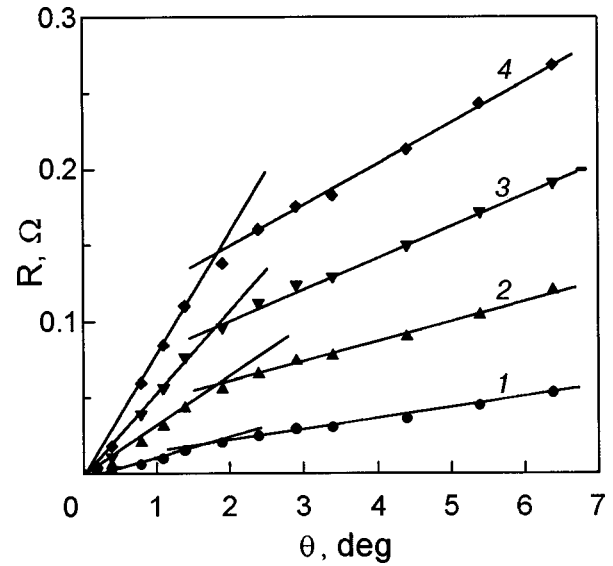
Here the field H^* is of the order of the first critical field H_{c1}; the value a_1 characterizes the barrier height ($a_1(T) = \exp(-c\xi(T)/s)$; c is some numerical constant),

$$\gamma = (M/m)^{1/2} = (dH_{c\parallel}/dT)|_{T_c}/(dH_{c\perp}/dT)|_{T_c}.$$

As the above formula shows, the value of the critical angle θ_c separating the two ranges of angles, the one in which the vortices are parallel to the layers and the one in which the direction of the induction vector B is tilted with respect to the layers, is mainly determined by the barrier height. The value of $a_1(T)$ grows with decreasing temperature. If the critical angle is determined from the H_{c2} vs. θ curves, like those in Fig. 6, the variation of H with the change of the temperature, according to formula (T), may influence the θ_c value, too. This may lead to a decrease of θ_c at low temperatures. However, the characteristic magnetic field $H^* \approx H_{c1}(T)$ also in-
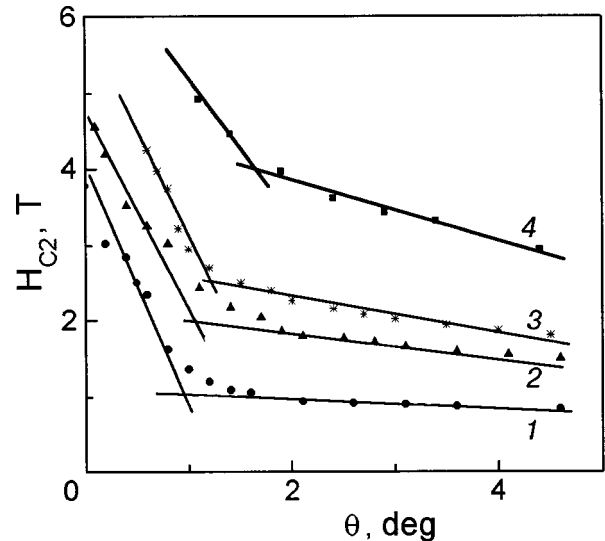

FIG. 6. Angular dependences of the parallel upper critical field at different temperatures T, K: 3.441 (1); 3.362 (2); 3.318 (3); 3.252 (4).

creases at low T. Thus, at first glance, the influence of the H^*/H factor is not so essential as that of $a_1(T)$.

The lock-in transition may be observed in the quasi-two-dimensional state, where substantial modulation of the vortex core energy in the direction orthogonal to the layers exists.[12] This means that one can observe this transition only at temperatures which are less than the crossover temperature

$$T_{cr} = T_c(1 - 2\xi_\perp^2(0)/s^2).$$

Indeed, the critical angle goes to zero at a temperature lower than T_c (Fig. 4). The crossover temperature for this sample is shown by an arrow. The onset of the lock-in transition is observed just below this temperature. As Fig. 4 shows, the critical angle increases as T is lowered, and only at the lowest temperature of the measurements is the tendency for diminishing θ_c observed. This latter tendency may be associated with the competing effect of the barrier height $a_1(T)$ and magnetic field. At sufficiently low temperatures the variation of the coherence length $\xi(T)$ slows down, and magnetic field enhancement may begin to play the dominant role.

The authors are now investigating the lock-in effect on superlattices with different anisotropy parameters. The results of this study will be published elsewhere.

In summary, the lock-in transition has been observed for the first time on artificial periodic layered systems (Mo/Si) including a conventional superconductor as one of the components. Previously it was shown that the new method of investigation of the VL structure in layered superconductors, which is based on the commensurability effect, works fairly well in the case when the magnetic field is parallel to the layers. Here we have shown that this method is also valid for tilted fields at relatively small misalignment between **H** and the layers. We believe that the data about the locking of vortices obtained from the R vs. H curves are direct, in distinction to all the other, indirect methods mentioned in the Introduction. For the first time we have obtained the explicit temperature dependence of the critical angle for the lock-in transition. An additional important conclusion which follows from our experiments is that, due to the lock-in effect, some deviation from a precisely parallel orientation does not lead to errors in the determination of the characteristic fields corresponding to the stable states of the commensurate vortex lattices.

*E-mail: juzephovich@ilt.kharkov.ua

[1] J. Campbell, M. M. Doria, and V. G. Kogan, Phys. Rev. B **38**, 2439 (1988).
[2] H. Raffy, J. C. Renard, and E. Guyon, Solid State Commun. **11**, 1679 (1972).
[3] P. R. Broussard and T. H. Geballe, Phys. Rev. B **37**, 68 (1988).
[4] C. Coccorese, C. Attanasio, L. V. Mercaldo, M. Salvato, L. Maritato, J. M. Slaughter, C. M. Falco, S. L. Prischepa, and B. I. Ivlev, Phys. Rev. B **57**, 7922 (1998).
[5] N. Ya. Fogel, M. Yu. Mikhailov, Yu. V. Bomze, and O. I. Yuzephovich, Phys. Rev. B **59**, 3365 (1999).
[6] M. Oussena, P. A. J. de Groot, R. Gagnon, and L. Taillefer, Phys. Rev. Lett. **72**, 3606 (1994).
[7] S. Ami and K. Maki, Prog. Theor. Phys. **53**, 1 (1975).
[8] B. I. Ivlev and N. B. Kopnin, Phys. Rev. Lett. **64**, 1828 (1990).
[9] B. I. Ivlev and N. B. Kopnin, J. Low Temp. Phys. **80**, 161 (1990).
[10] B. I. Ivlev, N. B. Kopnin, and V. L. Pokrovsky, J. Low Temp. Phys. **80**, 187 (1990).
[11] L. Bulaevskii and J. R. Clem, Phys. Rev. B **44**, 10234 (1991).
[12] M. Tachiki and S. Takahashi, Solid State Commun. **70**, 291 (1989).
[13] M. Tachiki and S. Takahachi, Solid State Commun. **72**, 1083 (1989).
[14] D. Feinberg and C. Villard, Phys. Rev. Lett. **65**, 919 (1990).
[15] H. Enriquez, N. Bontemps, P. Fournier, A. Kapitulnik, A. Maignan, and A. Ruyter, Phys. Rev. B **53**, 14757 (1996).
[16] D. E. Farrell, S. Bonham, J. Foster, Y. C. Chang, P. Z. Jiang, K. G. Vandervoort, D. J. Lam, and V. G. Kogan, Phys. Rev. Lett. **63**, 782 (1989).
[17] The anomalies in torque behavior observed at small angles in YBa$_2$Cu$_3$O$_7$[16] were explained by Bulaevsky[18] in terms of the lock-in effect.
[18] L. N. Bulaevskii, Phys. Rev. B **44**, 910 (1991).
[19] P. A. Mansky, P. M. Chaikin, and R. C. Haddon, Phys. Rev. Lett. **70**, 1323 (1993).
[20] S. Kolesnik, T. Skoskiewich, J. Jgalson, and Z. Tarnowski, Phys. Rev. B **54**, 13319 (1996).
[21] Yu. V. Bugoslavsky, A. A. Zhukov, G. K. Perkins, and A. D. Caplin, Phys. Rev. B **56**, 5610 (1997).
[22] W. K. Kwok, U. Welp, V. M. Vinokur, S. Fleshler, J. Downey, and G. W. Grabtree, Phys. Rev. Lett. **67**, 390 (1991).
[23] W. R. White, A. Kapitulnik, and M. R. Beasley, Phys. Rev. Lett. **66**, 2826 (1991).
[24] W. R. White, A. Kapitulnic, and M. R. Beasley, Phys. Rev. B **50**, 6303 (1994).
[25] P. Koorevaar, P. H. Kes, A. E. Koshelev, and J. Aarts, Phys. Rev. Lett. **72**, 3250 (1994).
[26] N. Ya. Fogel, V. G. Cherkasova, O. A. Koretskaya, and A. S. Sidorenko, Phys. Rev. B **65**, 85 (1997).
[27] E. I. Buchstab, V. Yu. Kashirin, N. Ya. Fogel, V. G. Cherkasova, V. V. Kondratenko, A. I. Fedorenko, and S. A. Yulin, Fiz. Nizk. Temp. **19** 704 (1993) [Low Temp. Phys. **19**, 506 (1993)].
[28] N. Ya. Fogel, E. I. Buchstab, A. S. Pokhila, A. I. Erenburg, and V. Langer, Phys. Rev. B **63**, 71 (1996).
[29] M. Yu. Mikhailov, O. I. Yuzephovich, A. S. Pokhila, Yu. V. Bomze, N. Ya. Fogel, I. M. Dmitrenko, S. A. Yulin, A. S. Sidorenko, O. B. Moldovan, and E. I. Buchstab, Fiz. Nizk. Temp. **25** 850 (1993) [Low Temp. Phys. **25**, 635 (1999)].

Swihart waves and surface plasmons in a parallel-plate superconducting transmission line

G. A. Melkov* and Yu. V. Egorov

T. Shevchenko Kiev National University, ul. Vladimirskaya 64, 01033 Kiev, Ukraine

The electromagnetic waves propagating inside a parallel-plate transmission line are investigated. In the case of a finite penetration depth of the electromagnetic field into the metal, a longitudinal electric E wave propagates in the the line instead of a transverse electromagnetic wave. At small thicknesses of the dielectric this wave goes over to a Swihart wave, and at large thicknesses of the dielectric it is converted into a surface wave (plasmon). It is shown that there exists an optimum thickness of the superconducting film coating the parallel-plate transmission line, for which the electromagnetic wave experiences the maximum slowing down. Using waveguides for surface waves, one can construct surface-wave microwave resonators. These resonators have a highly uniform microwave current distribution and, have a high concentration of microwave current in the superconducting film, and they are simple to fabricate. © *2000 American Institute of Physics.* [S1063-777X(00)00502-8]

INTRODUCTION

A parallel-plate line (Fig. 1) is a convenient single-mode model for real microstrip transmission lines, as it admits an analytical investigation of the waves in such lines. It was for a parallel-plate line that Swihart waves were observed instead of transverse electromagnetic waves in the case of a finite penetration depth λ of the electromagnetic field into the metal.[1]

For example, for identical superconducting films *1* and *2*, $b_1 = b_2 = b$, the propagation constant for Swihart waves was given in the classical monograph of Van Duzer and Turner[2] as

$$\beta_s^2 = k^2 \varepsilon \left(1 + \frac{2\lambda_L}{d} \coth \frac{b}{\lambda_L} \right), \tag{1}$$

where $k = \omega/c$, d is the thickness of the dielectric, ω is the frequency of the electromagnetic field, c is the speed of light in vacuum, and λ_L is the London penetration depth; formula (1) is valid for $kd\sqrt{\varepsilon} \ll 1$. It is seen from (1) that because of the penetration of the field into the superconductor, the propagation constant for a Swihart wave is larger than the propagation constant $k\sqrt{\varepsilon}$ for an electromagnetic wave in the dielectric, and that the difference becomes greater as the film thickness b is reduced. For $b \ll \lambda_L$, however, formula (1) becomes invalid, since for $b = 0$ the constant $\beta_s \to \infty$, but this is just the simple case of an open planar two-dimensional dielectric waveguide, which has a finite propagation constant $\beta_d < k\sqrt{\varepsilon}$.[3] According to Ref. 3, for $b_1 = b_2 = 0$ and $kd\sqrt{\varepsilon} \ll 1$ we have

$$\beta_d^2 = k^2 \left[1 + \frac{k^2 d^2}{4} \left(1 - \frac{1}{\varepsilon} \right)^2 \right]. \tag{2}$$

We see that under no circumstances does formula (1) reduce to (2), and it must therefore be refined for $b \to 0$. The case of thin superconducting films is extremely interesting for practical application, since a decrease in the thickness of the films is accompanied by an increase in their kinetic inductance, which is fundamental to the working principles of superconductor-based parametric and nonlinear devices.[4] However, this inductance does not increase to infinity, as is implied by (1), but to some maximum value, which would be useful to find for many technical applications.

Besides Swihart waves, a finite penetration depth λ leads to the onset of surface electromagnetic waves, i.e., surface plasmons propagating along metallic surfaces, which have been well studied from the microwave to the optical regions.[5,6] At the other extreme from the Swihart case, $kd\sqrt{\varepsilon} \gg 1$, the propagation constant for plasmons can be written as[5]

$$\beta_p^2 = k^2 \varepsilon (1 + k^2 \varepsilon \lambda^2), \tag{3}$$

where λ is the complex penetration depth of the electromagnetic field into the metal.

In this paper we show that Swihart modes and surface plasmons are different limiting cases ($kd\sqrt{\varepsilon} \ll 1$ and $kd\sqrt{\varepsilon} \gg 1$) of a unified Swihart–plasmon wave that propagates in
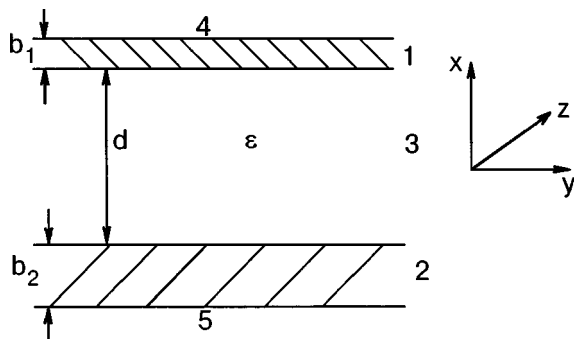

FIG. 1. Parallel-plate transmission line: metal films (*1,2*); dielectric with dielectric constant ε (*3*); free space (*4,5*).

the general case in waveguides with a finite conductivity of the walls. Figure 2 shows a schematic illustration of the electric field lines corresponding to these limiting cases. For $kd\sqrt{\varepsilon}\ll1$ [Fig. 2b] there exists a Swihart wave which for $\lambda=0$ (ideally conducting metal) goes over to an ordinary transverse electromagnetic wave [Fig. 2a]. For $kd\sqrt{\varepsilon}\gg1$ [Fig. 2c] surface plasmons propagate above the metal surface; they have no analog at zero penetration depth of the field into the metal, i.e., they do not exist in the case of infinite conductivity. Finally, the general case of Swihart–plasmon modes, which is realized for arbitrary $kd\sqrt{\varepsilon}$, is illustrated in Fig. 2d. As d increases, so does the number of electric field lines that are closed on the same metal surface from which they originate. The Swihart wave goes over smoothly to a surface plasmon, the electric field of which is completely concentrated around either of the two metal surfaces, whereas for the Swihart wave the electric field is distributed symmetrically around both surfaces. At zero penetration depth of the field into the metal, the Swihart–plasmon wave, like the purely Swihart wave, goes over to a transverse electromagnetic wave.

Thus our task in this paper is to investigate waves in a parallel-plate waveguide for arbitrary relationships among its parameters b_1, b_2, d, ε, and λ.

GENERAL DISPERSION RELATION

In the general case, the parallel-plate line shown in Fig. 1 admits the existence of longitudinal electric and longitudinal magnetic waves, the E and H modes, respectively.[5,6] We restrict analysis to only the E modes, since both the Swihart waves and surface plasmons are E modes which, in the case of infinite conductivity of the metal, go over to transverse electromagnetic waves. Furthermore, the H mode, unlike the lower E mode, has a critical wavelength $\lambda_{cr}\sim2d$ and cannot exist in microelectronic structures for $kd\sqrt{\varepsilon}\ll1$.
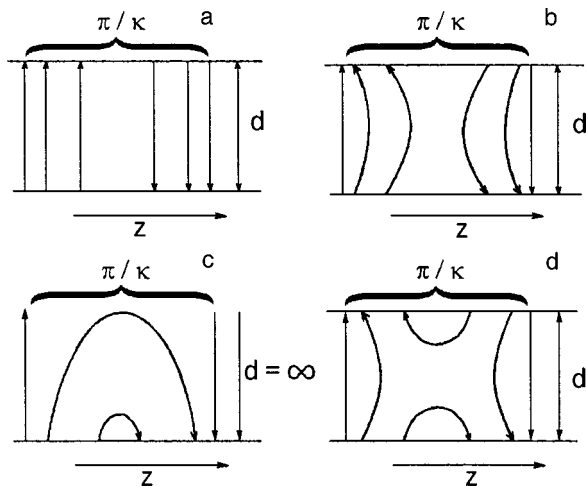

FIG. 2. Patterns of electric field lines in a parallel-plate transmission line in different limiting cases: transverse electromagnetic wave, $\lambda=0$ (ideally conducting metal) (a); Swihart wave, $\lambda\neq0$, $kd\sqrt{\varepsilon}\ll1$ (b); surface electromagnetic wave (plasmon), $\lambda\neq0$, $kd\sqrt{\varepsilon}\gg1$ (c); Swihart–plasmon wave, $\lambda\neq0$ (d).

We shall seek the solution in the form of harmonic waves propagating along the z axis, i.e., the electric and magnetic fields E, $H\sim\exp(j\omega t-j\beta z)$. Assuming, in addition, that the fields are uniform along the transverse axis y, we obtain the following system of equations describing the waves in the parallel-plate line shown in Fig. 1:

$$\left(\frac{\partial^2}{\partial x^2}+k_i^2\right)E_z^i=0;\quad i=1,...,5,\tag{4}$$

where k_i is the transverse propagation constant in the corresponding medium i. In free space $k_4^2=k_5^2=-\alpha^2=k^2-\beta^2$, and in a dielectric $k_3^2=k^2\varepsilon-\beta^2$. In superconducting media *1* and *2* the transverse propagation constant is ordinarily expressed in terms of the complex pentration depth $\lambda_i^2=-1/k_i^2$ (Ref. 7). In the case of type-II superconductors such as HTSCs, λ_i is determined not only by the London penetration depth λ_L but also by the presence of normal electrons, by the magnetic field B, by thermodynamic fluctuations, etc. Here we shall use an expression for λ_i obtained by Coffey and Clem[7] with allowance for the normal electrons and magnetic flux vortices:

$$\lambda_i^2=\frac{\lambda_{Li}^2-(j/2)\,\delta_{\nu i}^2}{1+2j\lambda_{Li}^2/\delta_{ni}^2},\tag{5}$$

where λ_{Li} is the london penetration depth in the ith medium and in general depends on the temperature and magnetic field, $\lambda_L=\lambda_L(t,B)$ (Ref. 7); $t=T/T_c$, where T_c is the critical temperature;

$$\delta_\nu^2=\frac{2B\Phi_0[\zeta+(\omega\tau)^2+j(1-\zeta)\omega\tau]}{\mu_0\omega\,\eta[1+(\omega\tau)^2]};$$

μ_0 is the magnetic permeability of the vacuum; η is the viscosity of the magnetic flux; Φ_0 is the magnetic flux quantum; $\zeta=I_0^{-2}(\nu)$, where $I_k(x)$ is the kth-order modified Bessel function of the first kind; $\nu=U/2k_BT$; U is the height of the potential barrier for magnetic flux vortices; k_B is Boltzmann's constant;

$$\tau=\frac{\eta}{k_p}\frac{I_0^2(\nu)-1}{I_0(\nu)I_1(\nu)};$$

and, k_p is the elastic constant of the vortex lattice (the Labusch parameter). In the absence of magnetic flux vortices, $\delta_\nu=0$, ignoring the magnetic flux creep ($\nu\gg1$) leads to $\zeta=0$ and $\tau=\eta/k_p$.

The normal conductivity in (5) is represented by the term containing $\delta_n^2=2\rho_n/\mu_0\omega$, where ρ_n is the resistivity of the normal electron liquid, which, like λ_L, depends on T and B: $\rho_n=\rho_n(t,B)$, as is discussed in detail in Ref. 7.

Formula (5) for the penetration depth is both for an ordinary, nonsuperconducting metal and for a superconductor at a temperature T above the transition temperature T_c. In the latter case on can just set $\lambda_{Li}=\infty$.[7]

The solution of system (4) in the different regions $i=1,2,...5$ has the form

$$i=1, \quad \frac{d}{2} \leqslant x \leqslant \frac{d}{2}+b_1, \quad E_z a_1 e^{x/\lambda_1}+c_1 e^{-x/\lambda_1},$$

$$i=2, \quad -b_2-\frac{d}{2} \leqslant x \leqslant -\frac{d}{2}, \quad E_z=a_2 e^{x/\lambda_2}+c_2 e^{-x/\lambda_2}$$

$$i=3, \quad -\frac{d}{2} \leqslant x \leqslant \frac{d}{2}, \quad E_z=a_3 \sin(k_3 x)+c_3 \cos(k_3 x),$$

$$\tag{6}$$

$$i=4, \quad x \geqslant \frac{d}{2}+b_1, \quad E_z=a_4 e^{-\alpha x},$$

$$i=5, \quad -b_1-\frac{d}{2} \leqslant x, \quad E_z=a_5 e^{\alpha x}.$$

From the continuity condition for the tangential components of the electric and magnetic fields at all the boundaries, $x=(-d/2)-b_2, \ -d/2, \ d/2, \ (d/2)+b_1$, one can obtain the following dispersion relation for the parallel-plate line shown in Fig. 1:

$$\tan k_3 d = \frac{\Theta_1+\Theta_2}{\Theta_1\Theta_2-1}, \tag{7}$$

where

$$\Theta_{1,2}=\frac{k^2 \varepsilon \lambda_{1,2}}{k_3} \frac{\coth(b_{1,2}/\lambda_{1,2})-(k^2\lambda_{1,2}/\alpha)}{1-(k^2\lambda_{1,2}/\alpha)\coth(b_{1,2}/\lambda_{1,2})}. \tag{8}$$

In the symmetric case ($b_1=b_2=b$; $\lambda_1=\lambda_2=\lambda$; $\Theta_1=\Theta_2=\Theta$), Eq. (7) simplifies to

$$\tan \frac{k_3 d}{2}=-\Theta, \tag{9}$$

$$\Theta=\frac{k^2 \varepsilon \lambda}{k_3} \frac{\coth(b/\lambda)-(k^2\lambda/\alpha)}{1-(k^2\lambda/\alpha)\coth(b/\lambda)}. \tag{10}$$

Equations similar to (7)–(10) have been considered repeatedly in the literature, but they have been investigated only for $kd\sqrt{\varepsilon} \ll 1$, i.e., for the case of Swihart waves, and, besides, they, like Eq. (1), were not set up to be valid in the limit $b \to 0$ (see, e.g., Ref. 9).

Equations (7)–(10) describe a Swihart–plasmon electromagnetic wave existing between two conducting planes. The pattern of electric field lines obtained from these equations is shown in Fig. 2d. We shall show below that in different limiting cases these equations describe both a Swihart wave and a wave of surface plasmons (for $kd\sqrt{\varepsilon} \ll 1$ and $kd\sqrt{\varepsilon} \gg 1$, respectively). It is only in these simple cases that the propagation constant has the simple form (1)–(3); in arbitrary cases either an approximate solution or a numerical analysis of the dispersion relations must be used.

LIMITING CASES

1. Swihart waves, $kd\sqrt{\varepsilon} \ll 1$

We have the following equation for determining the propagation constant β:

$$\beta^2=k^2\varepsilon\left[1+\frac{\lambda_1}{d}f(b_1,\lambda_1)+\frac{\lambda_2}{d}f(b_2,\lambda_2)\right], \tag{11}$$
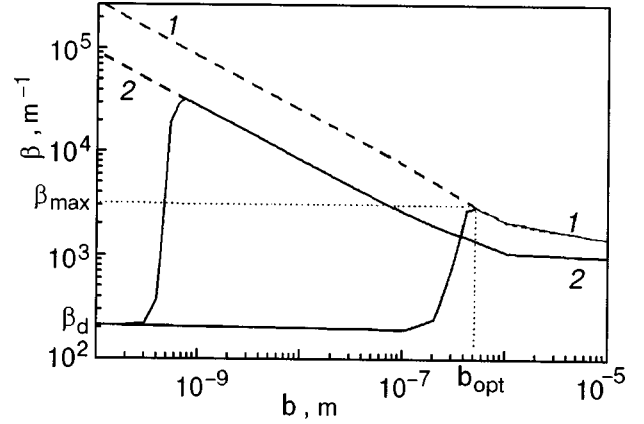

FIG. 3. Dependence of the propagation on β of a Swihart wave on the superconducting film thickness for different temperatures: $T=T_c=91$ K (*1*); $T=90$ K (*2*). The dashed and solid curves were calculated according to formulas (13) and (11), respectively; $d=1$ μm, $\varepsilon=9.8$; see text for the parameters of the superconducting film.

where $f(b,\lambda)$ is a function describing the influence of the finite thickness of the superconducting film:

$$f(b,\lambda)=\frac{\coth(b/\lambda)-(k^2\lambda/\sqrt{\beta^2-k^2})}{1-\coth(b/\lambda)(k^2\lambda/\sqrt{\beta^2-k^2})}. \tag{12}$$

For $b/\lambda \gg 1$ the function $f(b,\lambda)=1$; in the case

$$k^2\lambda \coth(b/\lambda) \ll \sqrt{\beta^2-k^2} \tag{13}$$

the function $f(b,\lambda)=\coth(b/\lambda)$, and expression (11) reduces to the form

$$\beta^2=k^2\varepsilon\left[1+\frac{\lambda_1}{d}\coth\left(\frac{b_1}{\lambda_1}\right)+\frac{\lambda_2}{d}\coth\left(\frac{b_2}{\lambda_2}\right)\right], \tag{14}$$

which is analogous to expression (1) for the propagation constant β_s of a Swihart wave if the London penetration depth λ_L in that expression is replaced by the complex penetration depth λ from Eq. (5), which takes into account the influence of the normal electrons and magnetic flux vortices. Then Eq. (14), unlike Eq. (1), leads to a complex value for the propagation constant, which reflects the fact that active losses arise in the transmission line.

Condition (13), and, with it, formula (14) are valid down to film thicknesses $b \geqslant 10^{-2}\lambda$, i.e., practically always. It is only near T_c (for $(T_c-T) \ll T_c$) that Eq. (11) must be used instead of (14). This is plainly seen from Fig. 3, which shows the results of a calculation of the propagation constants β for Swihart waves as functions of the superconducting film thickness b for two temperatures, T_c and T_c-1 K. In all the calculations here and below we have taken the following values for the parameters of the HTSC films: $T_c=91$ K, $\lambda_L(0,0)=2.5\times10^{-7}$ m, $\rho_n(0,0)=1\times10^{-6}$ $\Omega\cdot$m. According to Fig. 3, at a temperature only 1 K below T_c one may use formula (14) to film thicknesses down to a few nanometers. As the frequency increases, the region of T and b values in which formula (14) is valid becomes smaller: for $f=100$ GHz in the region of liquid-nitrogen temperatures this formula is valid only for $b \geqslant 0.1$ μm. We see from Fig. 3 that there exists an optimum thickness b_{opt} of the HTSC
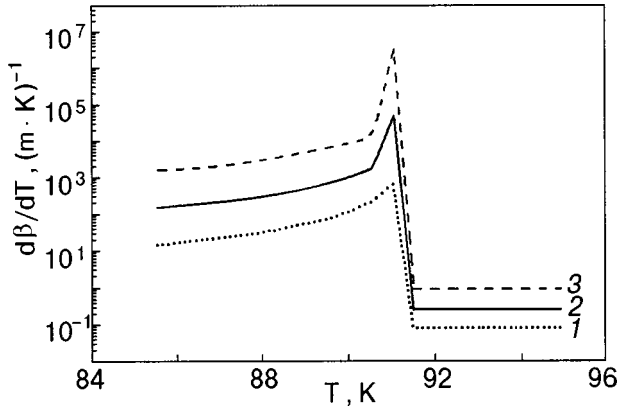
FIG. 4. Temperature dependence of the change $\partial\beta/\partial T$ of the propagation constant of a Swihart wave for various frequencies f, GHz: 1 (*1*), 10 (*2*), 100 (*3*); $d=1$ μm, $\varepsilon=9.8$, $b=0.1$ μm.
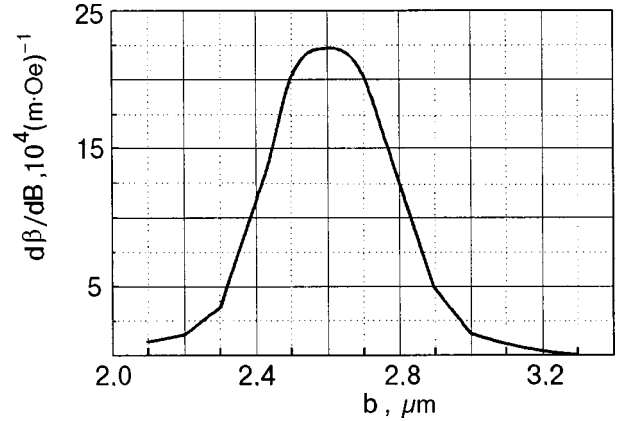

FIG. 5. Change $\partial\beta/\partial B$ of the phase constant with magnetic field as a function of the thickness $b_1=b_2=b$ of the superconducting films; $d=1$ μm, $f=10$ GHz, $T=90.9$ K, $\varepsilon=9.8$.

films for which the propagation constant of the Swihart wave reaches its maximum value β_{max}; for $b<b_{opt}$ the propagation constant falls off rapidly to the value for a planar dielectric waveguide, β_d [Eq. (2)].

The presence of superconducting films causes β_s to depend on various kinds of external influences.[9] By a suitable choice of the parameters of the transmission line one can optimize the line from the standpoint of creating parametric devices, controllable phase shifters, and highly sensitive superconducting temperature and magnetic field sensors. Systems with very thin superconducting films have been analyzed previously. For example, it was shown in Ref. 8 that the controllability of a microwave system containing a thin superconducting film also has a maximum as the film thickness is decreased, but this maximum arose not because of accurate allowance for the influence of the film thickness but rather was due to allowance for the finite width of the film. At a film width of 25 μm, as in our case, one has $b\sim10^{-2}\lambda$.

Figure 4 shows the temperature dependence of the rate of change $\partial\beta/\partial T$ of the phase constant for several different frequencies ($f=1$, 10, and 100 GHz). We see that near T_c the value of $\partial\beta/\partial T$ can reach very high values $[10^6(\text{m}\cdot\text{K})^{-1}]$, which correspond to phase shifts $\sim10^8$ deg/K.

Figure 5 shows the rate of change of the phase constant near T_c upon changes in the magnetic field, $\partial\beta/\partial B$, as a function of the HTSC film thickness. According to this figure, $\partial\beta/\partial B$ has a resonance dependence on the film thickness, with the maximum occurring precisely at $b=b_{opt}$. The temperature rate of change of the propagation constant, $\partial\beta/\partial T$ (see Fig. 4) also has a maximum near $b=b_{opt}$, i.e., both here and for determining $\partial\beta/\partial B$, one must use formula (11) to obtain correct results.

2. Surface plasmons, $kd\sqrt{\varepsilon}\gg1$

The propagation constant has the form

$$\beta^2=k^2\varepsilon(1+k^2\varepsilon\lambda^2f^2b/\lambda). \tag{15}$$

As in the case of Swihart waves, when condition (13) is satisfied, one has $f(b/\lambda)=\coth(b/\lambda)$ and

$$\beta^2=k^2\varepsilon[1+k^2\varepsilon\lambda^2\coth^2(b/\lambda)]. \tag{16}$$

As one would expect, Eqs. (15) and (16) go over to Eq. (3) for $b\gg\lambda$.

Equations (15) and (16), like (11) and (14), are valid for both normal metals and superconducting films. In actuality the waves in these two cases do not have any fundamental differences: the penetration depth λ and, with it, the propagation constant β are complex quantities $\lambda=\lambda'+j\lambda''$, $\beta=\beta'-j\beta''$. It is only for an ideal superconductor having no normal electrons, i.e., at $T=0$, that $\lambda=\lambda_L$ and the damping coefficient $\beta''=0$. In the general case one can therefore state that the existence of surface plasmons (like that of Swihart waves) requires not the damping of waves in the metal, as is correctly asserted in the study of normal metals,[5] but rather the presence of a finite penetration depth λ of electromagnetic waves into the metal: the larger the value of λ, the greater the slowing of the wave, and the more strongly it is ''squeezed'' toward the metal. While for a normal metal the penetration depth and the damping are uniquely related, for superconductors there is no such connection.

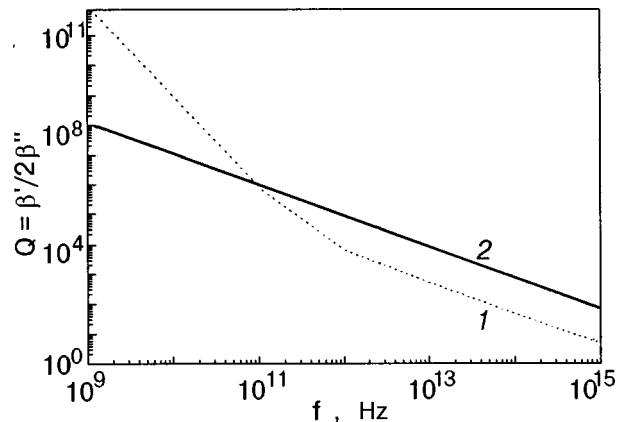Figure 6 shows the frequency dependence of the Q factor $Q=\beta'/2\beta''$ for surface electromagnetic waves (plas-

FIG. 6. Frequency dependence of the Q factor for surface plasmons propagating above a HTSC film (*1*) and above a copper film (*2*); $b=10$ μm, $T=77$ K, $\varepsilon=1$.

mons) propagating above a HTSC film and above a copper film. We see that the Q factor is larger all the way to the region of infrared wavelengths, and this is conducive to the successful application of surface plasmons in nonlinear optics.[6] Superconducting films, because of the stronger frequency dependence of the damping, have advantages over films of normal metals only in the microwave region, for the parameters we have chosen and for $f < 90$ GHz (see Fig. 6). However, even at higher frequencies, all the way up to 10^{12} Hz, their Q factor is much greater than that for microstrip lines and hollow waveguides. It is therefore extremely promising to use surface plasmons for making Josephson devices for the terahertz frequency range. There one will have low losses combined with a high amplitude of the microwave current flowing along the surface of the superconducting film through the Josephson contacts, in which the effect of nonlinear phenomena is proportional to the current amplitude.

The propagation constant of surface plasmons, like that of Swihart waves, can be altered by the application of a static magnetic field, but the change in this constant is much smaller for surface plasmons on account of their much smaller slowing in comparison with Swihart waves. In fact, it follows from a comparison of (11) and (15) that the additional contribution to the propagation constant in the case of Swihart waves is proportional to λ/d, whereas for surface plasmons it is $\sim k^2\lambda^2 \ll \lambda/d$. Therefore, for the sake of brevity, we shall therefore omit consideration of this effect.

3. Swihart–plasmon waves

The expressions obtained above for Swihart waves (11) and surface plasmons (15) are valid in the limiting cases $kd\sqrt{\varepsilon} \ll 1$ and $kd\sqrt{\varepsilon} \gg 1$, respectively. In general one must use the dispersion relation (7), which is a transcendental equation and admits exact analysis only by numerical methods. With some loss of accuracy, however, one can make a simplification of relation (7) for arbitrary kd as well. For this one must make use of the fact that the transverse propagation constant in the dielectric layer (see Fig. 1), $k_3 = (k^2\varepsilon - \beta^2)^{1/2}$, becomes an imaginary quantity when the electromagnetic field penetrates into the metallic walls. Then the tangent on the left-hand side of (7) goes over to the hyperbolic tangent, which for arbitrary values of the argument can be represented in the form $\tanh x \approx x/(1+x)$. This relation is exact for $x \to 0$ and $x \to \infty$, and the maximum error at $x \sim 1$ is not more than 35%. As a result, we have the following approximate expression for the propagation constant of Swihart–plasmon waves, which is valid for arbitrary thicknesses d of the dielectric:

$$\beta^2 = k^2\varepsilon\left\{1 + \frac{2\lambda}{d}f(b,\lambda) + k^2\varepsilon\lambda^2 f^2(b,\lambda)\right.$$
$$\left.\times\left[\frac{1}{2} + \left(\frac{1}{4} + \frac{2}{k^2\varepsilon d\lambda}f^{-1}(b/\lambda)\right)^{1/2}\right]\right\}.$$

As it should, this expression reduces to Eqs. (11) and (15) in the limiting cases $kd\sqrt{\varepsilon} \ll 1$ and $kd\sqrt{\varepsilon} \gg 1$, respectively.

4. Dielectric image waveguide

Image waveguides are widely used in integrated optics,[6] and there have been attempts to use them in the microwave range as well.[10] The simplest image waveguide is a waveguiding dielectric layer on a metal surface. Of course, any HTSC film grown on a dielectric substrate is a natural image waveguide. Here the wave propagates mainly in the substrate, periodically reflecting off the superconducting film and the dielectric–air boundary.

To go from a parallel-plate transmission line (see Fig. 1) to an image waveguide, we can just set $b_1 = 0$. We then obtain a waveguide consisting of a dielectric layer of thickness d on a metal slab of thickness b_2.

The propagation constant of a dielectric image waveguide can be obtained from Eqs. (7) and (8) with $b_1 = 0$. In the most interesting case, when $kd\sqrt{\varepsilon} \ll 1$ and condition (13) is satisfied, one has

$$\beta^2 = k^2\left\{1 + k^2\left[d\left(1 - \frac{1}{\varepsilon}\right) + \lambda\coth\left(\frac{b}{\lambda}\right)\right]^2\right\}. \tag{17}$$

Of course, in the absence of the dielectric substrate ($\varepsilon = 1$ or $d = 0$) expression (17) goes over to the propagation constant for surface plasmons (16) in vacuum above a metal surface. When a substrate is present the wave properties for an image waveguide are determined by both the parameters of the dielectric and the parameters of the metal film [respectively the first and second terms in the square brackets in formula (17)]. In the majority of real cases the contribution of the dielectric is substantially greater than the influence of the penetration depth of the electromagnetic field into the metal, and the properties of the surface electromagnetic waves in an image waveguide with a HTSC are practically no different from those for a dielectric waveguide. The only exception is at temperatures close to T_c, when the role of the second term in square brackets in (17) can grow strongly. We note that in comparing formulas (2) and (17) for $\lambda = 0$ it is necessary to double the height d of the waveguide in Eq. (2), since there an isolated dielectric waveguide was being considered, while in Eq. (17) it was a waveguide on a metal substrate, which, because of reflection effects, doubles the height of the waveguide, and its properties will be the same as for an isolated waveguide with twice the height.[3]

SURFACE WAVE RESONATORS

A piece of waveguide bounded in the direction of wave propagation is a resonator whose resonance frequency is determined by the length l of the piece. This statement also applies in full measure to surface waves — surface plasmons, waves in an image waveguide, etc. Thus a resonator can be a separate metal slab (or film) on a dielectric substrate, a film on a substrate with an external dielectric attached to it (a sandwich), etc.[11] Let us discuss some of the features of such resonators.

1. The resonant length l_{res} of the resonator will differ substantially from the values required by the condition $l_{\text{res}} = n\pi/\beta$ because the field goes beyond the confines of the resonator out its ends. Effects of this kind will be extremely strong on account of the small differences of the propagation

constants β of the surface waves from the propagation constant of electromagnetic waves in free space (see Eq. (16), for example). In addition, a real resonator has a finite width, and, as a result, the fields penetrate to the opposite side of the metal film not only on account of penetration of the field into the metal but also as a result of the bending of the magnetic field lines around the metal surface. For this reason the resonant length of a half-wave resonator can be almost one-fourth less than would be required by formula (15) or (17).[11] An exact calculation of the resonant frequencies of a resonator must be done in the many-wave approximation[11] and not the single-wave approximation, as in the present paper.

Up till now we have been talking about half-wave resonators in which both ends of the resonator are bordered by free space. If one end of the resonator is in contact with a metal surface, such as a wall of the waveguide in which the resonator is placed, then the specular reflection of the fields at the metal can bring about the formation of a quarter-wave resonator. Its resonant length is close to a quarter wavelength or to a multiple of this: $l_{\text{res}} = (2n-1)\pi/2\beta$. In a quarter-wave resonator the same effects tending to shorten the resonant length are present as in a half-wave resonator.

2. The Q factor Q of the resonator should be substantially higher than that of microstrip resonators but considerably less than for cavity resonators. The maximum Q factor for present-day HTSC films in the three-centimeter range is $Q \leqslant 10^5$ (Ref. 11). Because the surface character of the wave, the electromagnetic field is concentrated near the superconducting film, and that makes for a large surface current in it, as the loss is proportional to the square of the surface current. The situation is made even more complicated by the circumstance that the surface-wave resonator is open, and the field, although damped exponentially, can reach nearby metal surfaces such as the walls of the waveguide. This can lead to a further decrease in the Q factor to 10^4 or less. The metal surfaces have a particularly large effect on the Q factor for a quarter-wave resonator: these surfaces are necessary to its operation and the main source of losses. Therefore the Q factor of a quarter-wave resonator for surface waves in the three-centimeter range is $Q \leqslant 10^3$.

However, in spite of the low Q factor, surface-wave resonators for the microwave region also have a number of advantages. Foremost among them is the high value of the surface current, which is the cause of the low Q factor. Because there are no nearby metal surfaces, this current is highly uniform over the whole surface of the film: the non-uniformity from the middle of the film to the edges is only a fraction of a percent.[11] This makes surface-wave resonators promising for the excitation of arrays of Josephson contacts, e.g., for creating Josephson generators.

Another important advantage is the simplicity of construction and the strong coupling of a surface-wave resonator with transmission lines. The resonator is simply a HTSC film of the necessary dimensions on a dielectric substrate. To couple this resonator with transmission lines does not require any special transitions, as is necessary, e.g., for the excitation of a rectangular waveguide by a microstrip line. The pattern

of field lines in a surface-wave resonator is extremely close to that for the fundamental mode of a rectangular waveguide. The resonator can be excited by simply placing it in a waveguide in such a way that the z axis of the resonator (see Fig. 1) lies along the electric field lines of the waveguide.[11] At the upper edge of the millimeter and submillimeter wavelength ranges the relatively high Q factor and simplicity of construction make surface-wave resonators the best choice for integrated applications.

CONCLUSION

We have investigated the electromagnetic waves propagating in a parallel-plate transmission line consisting of a dielectric layer of thickness d covered top and bottom with films of a normal or superconducting metal. In the case of a finite penetration depth of the electromagnetic field into the metal, a longitudinal electric E mode rather than a transverse electromagnetic mode propagates in such a line. For $kd\sqrt{\varepsilon} \ll 1$ this mode goes over to a Swihart wave, and in the opposite limiting case $kd\sqrt{\varepsilon} \gg 1$ it goes over to a surface wave — a surface plasmon propagating along one of the metal surfaces. Here $k = \omega/c$ is the wave number of the electromagnetic wave. The surface plasmon is squeezed toward the metal surface as a result of the slowing of the wave when its field penetrates into the metal. The slowing and, hence, the concentration of the waves near the metal surface can be enhanced by coating the metal with a thin dielectric layer ($kd\sqrt{\varepsilon} \ll 1$). In that case one will have a surface-wave image waveguide. The surface waves both above an isolated metal and above a metal coated with a dielectric layer have low losses and can be used successfully at frequencies all the way up to the optical range. The electromagnetic waves above a superconductor are not fundamentally different from those above a normal metal. It should be noted only that in the case of a normal metal there is a unique relation between the damping, slowing, and penetration depth of the electromagnetic field into the metal. In the case of a superconductor there is only a relation between the penetration depth and the slowing, while the losses are determined by the presence of normal electrons, and here it is in principle possible (for an ideal superconductor at zero temperature) to have a situation in which there are no losses whatsoever but there is significant slowing, as happens in Swihart waves [see Eq. (1)].

There is an optimum thickness of the superconducting films covering a parallel-plate transmission line such that the slowing of the electromagnetic wave is maximum. In that case one also observes a maximum reaction of the propagation constant to external influences — changes in temperature, static magnetic fields, etc. This reaction can reach high values, and this makes superconducting transmission lines promising for constructing efficient parametric devices, controllable phase shifters, and highly sensitive temperature and magnetic field sensors.

Surface-wave waveguides can be used to make surface-wave microwave resonators, which are pieces of these waveguides with certain lengths. These resonators have a high uniformity and a high concentration of the microwave current in the superconducting film. Furthermore, they are

simple to make and have a field distribution in them which is close to that in a rectangular waveguide, which makes for a large coupling coefficient with such waveguides.

All of this makes superconducting surface-wave resonators very promising for use in microwave devices (Josephson generators, filters) at wavelengths all the way down to the submillimeter range.

*E-mail: melkov@boy.rpd.univ.kiev.ua

[1] J. S. Swihart, J. Appl. Phys. **32**, 461 (1961).
[2] T. Van Duzer and C. W. Turner, *Principles of Superconductive Devices and Circuits* [Elsevier, New York (1981); Radio i Svyaz', Moscow (1984).
[3] I. F. Vzyatyshev, *Dielectric Waveguides* [in Russian], Sov. Radio, Moscow (1970).
[4] J. H. Thompson, IEEE Trans. Magn. **MAG-27**, 2817 (1991).
[5] L. A. Vanshein, *Electromagnetic Waves* [in Russian], Radio i Svyaz', Moscow (1988).
[6] M. J. Adams, *Introduction to Optical Waveguides* [Wiley, New York (1981); Radio i Svyaz', Moscow (1984).
[7] M. W. Coffey and J. R. Clem, Phys. Rev. B **17**, 9872 (1992).
[8] K. K. Likharev, Izv. Vyssh. Uchebn. Zaved., Radiofiz. **14**, 909 (1971).
[9] S. A. Zhou, J. Supercond. **8**, 113 (1995).
[10] J. A. Paul and Y. W. Chang, IEEE Trans. Microwave Theory Tech. **MTT-26**, 751 (1978).
[11] G. A. Melkov, Y. V. Egorov, A. N. Ivanjuta, and V. Y. Malyshev, *Surface Wave HTS Resonators, MSMW Symposium Proceedings*, Kharkov, Ukraine (1998), p. 625.

Translated by Steve Torstveit

Spin polarization of quasiparticle states in *S/F* structures with a finite transparency of the *SF* interface

E. A. Koshina and V. N. Krivoruchko*

A. A. Galkin Donetsk Physics and Technology Institute, National Academy of Sciences of Ukraine, ul. R. Lyuksemburg 72, 340114 Donetsk, Ukraine
(Submitted July 27, 1999)
Fiz. Nizk. Temp. **26**, 157–163 (February 2000)

The proximity effect between a massive superconductor (*S*) and a mesoscopic layer of a normal ferromagnetic metal (*F*) is investigated for arbitrary transparency of the *SF* interface and arbitrary value of the proximity effect. For the case of high transparency of the *SF* interface and a low value of the proximity effect, the spatial distribution of the order parameter in the *S* layer and the densities of quasiparticle states at the interface for the *S* and *F* layers are found analytically as functions of the exchange field. It is shown that in mesoscopic *S/F* structures the single-particle excitations are polarized in both the *F* and *S* metals. © *2000 American Institute of Physics.* [S1063-777X(00)00602-2]

Recent studies[1–5] have convincingly demonstrated that superlattice structures of a ferromagnet (*F*) with a superconductor (*S*) have qualitatively different behavior, depending on the relative values of such parameters as the transparency of the *SF* interface, the strength of the proximity effect, the value of the exchange field, the relative degree of kinetic and diffusional character of the motion of quasiparticles, etc. When these properties of the system are correctly taken into account, one can explain qualitatively (and in a number of case predict) such novel effects as oscillations of the critical temperature of the superconducting transition in *S/F* multilayers, the periodically reentrant superconductivity of *SF* superlattices, etc.[2–5] Bimetal *S/F* structures also have a diversity of physical properties. For example, recent experiments[6,7] with *S/F* contacts (with the ferromagnetic metals Ni, Co, Fe, NiMnSb, $Ni_{0.8}Fe_{0.2}$, and $La_{0.7}Sr_{0.3}MnO_3$) have shown that Andreev reflection is strongly suppressed as the spin polarization of the electrons on the Fermi surface increases. At the same time, it has been found[8] that in *S/F/S* contacts with a finite transparency of the interface and a superparamagnetic state of the *F* layer (Gd), the Andreev reflection can be substantially enhanced by applying an external magnetic field (i.e., by increasing the spin order of the *F* layer). A strong mutual influence of magnetism and superconductivity is also observed in *S/F* nanostructures.[9]

The theory of tunnel junctions of the *SNINS* or *SNIS* types (*N* is a normal nonmagnetic metal, and *I* is an insulator) with arbitrary transparency of the *SN* interface has now attained a significant level of development (see, e.g., Refs. 10 and 11); nevertheless, a general theory of tunnel contacts in the case when the normal metal is ferromagnetic does not exist. The fundamental difference between nonmagnetic and ferromagnetic normal metals lies in the spin polarization of the conduction electrons in the *F* layer. As in *S/F* structures, because of the proximity effect with the *S* layer, superconducting correlations are also induced in the *F* layer, but the exchange polarization of the electrons on the Fermi surface

alters the pairing conditions. Two groups (subbands) of electrons arise in the *F* layer: Cooper pairs form quasiparticles consisting of the states $\{\mathbf{p}\uparrow,(-\mathbf{p}+\Delta\mathbf{p})\downarrow\}$ and of the states $\{\mathbf{p}\downarrow,(-\mathbf{p}-\Delta\mathbf{p})\uparrow\}$, where $\Delta p\sim H_{exc}/v_F$, H_{exc} is the exchange field in energy units, and v_F is the Fermi velocity. If the spin–orbit scattering of the electrons is small enough, the pairs from different spin subbands essentially do not mix.[11,12]

In this paper we develop a theory of the proximity effect for layered *S/F* systems with a massive *S* layer and a thin (mesoscopic) *F* layer, and with an arbitrary transparency of the *SF* interface. General relations are given by which one can reduce the problem of the proximity effect to one of solving the Usadel equations for the *S* layer with appropriate boundary conditions. Using the general expressions obtained, we investigate analytically the proximity effect in an *S/F* bilayer with a high transparency of the interfaces between layers. We find the density of states and the spatial distribution of the order parameter in the *S* and *F* metals, and we discuss effects connected with the exchange polarization of conduction electrons on the Fermi surface in the *F* metal. In particular, we show that for a finite transparency of the interface between the *S* and *F* layers a spin splitting of the density of quasiparticle states is observed in the *S* layer as well.

1. Let us consider the proximity effect in a bilayer consisting of a massive superconductor of thickness d_S and a thin ferromagnet of thickness d_F. The boundary of the *F* and *S* metals will be assumed flat; its transparency can be arbitrary. Suppose that the conditions of the ''dirty'' limit are satisfied for the *S* and *F* metals, and that the critical temperature T_C of the superconducting transition for the *F* metal is zero. We shall assume that the region $x\geq 0$ is occupied by the *S* metal, a layer $-d_F\leq x<0$ is occupied by the *F* metal, and that all quantities depend only on the *x* coordinate, which is along the normal to the interfacial surface. Below we shall consider a case of greater theoretical interest, viz.,

$$d_S\gg\xi_S, d_F\ll\min(\xi_F,\xi); \qquad (1)$$

$$\xi_S = \left(\frac{D_S}{2\pi T_C}\right)^{1/2} \quad \text{and} \quad \xi_F = \left(\frac{D_F}{2H_{exc}}\right)^{1/2}, \quad \xi = \left(\frac{D_F}{2\pi T_C}\right)^{1/2}$$

are the effective coherence lengths of the S and F metals (for the ferromagnetic metal the choice of a ''convenient'' coherence length depends on the relative values of the critical temperature T_C of the S metal and the parameter H_{exc}), $D_{S,F}$ are the diffusion coefficients of the F and S metals, and $\hbar = k_B = 1$. The first condition in (1) allows us to neglect the decrease in the critical temperature of the S/F bilayer in comparison with the critical temperature of the massive S metal, and the second condition allows us to treat all the quantities as spatially independent within the F layer.

As we know, the superconductivity of ''dirty'' metals is conveniently described by the quasiclassical Usadel equations. For the case when all quantities depend on a single coordinate x and the spin–orbit scattering can be neglected, the general form of the Usadel equations for a single subband of a superconducting ferromagnetic metal is as follows (see, e.g., Ref. 13):

$$-\frac{D_F}{2}\frac{d}{dx}\left(G_{F\uparrow\uparrow}\frac{d}{dx}\widetilde{F}_{F\uparrow\downarrow} - \widetilde{F}_{F\uparrow\downarrow}\frac{d}{dx}\widetilde{G}_{F\downarrow\downarrow}\right)$$

$$= -\widetilde{\omega}\widetilde{F}_{F\uparrow\downarrow} + \frac{\Delta_F}{2}(G_{F\uparrow\uparrow} + \widetilde{G}_{F\downarrow\downarrow}), \tag{2}$$

$$-\frac{D_F}{2}\frac{d}{dx}\left(\widetilde{G}_{F\downarrow\downarrow}\frac{d}{dx}F_{F\uparrow\uparrow} - F_{F\downarrow\uparrow}\frac{d}{dx}G_{F\uparrow\uparrow}\right)$$

$$= -\widetilde{\omega}F_{F\downarrow\uparrow} + \frac{\Delta_F^*}{2}(G_{F\uparrow\uparrow} + \widetilde{G}_{F\downarrow\downarrow}), \tag{3}$$

$$G_{F\uparrow\uparrow}\widetilde{G}_{F\downarrow\downarrow} + F_{F\downarrow\uparrow}\widetilde{F}_{F\uparrow\downarrow}^+ = 1. \tag{4}$$

Here $G_{\sigma\sigma'}(x,\omega)$, $F_{\sigma\sigma'}(x,\omega)$ and $\widetilde{G}_{\sigma\sigma'}(x,\omega)$, $\widetilde{F}_{\sigma\sigma'}(x,\omega)$ are the Green functions integrated over energy and averaged over the Fermi surface; they are defined in the standard way (see, e.g., Ref. 14):

$$G_{\uparrow\uparrow}(1,2) = -\langle\hat{T}_\tau\Psi_\uparrow(1)\Psi_\uparrow^+(2)\rangle,$$

$$F_{\downarrow\uparrow}(1,2) = \langle\hat{T}_\tau\Psi_\downarrow^+(1)\Psi_\uparrow^+(2)\rangle,$$

$$\widetilde{G}_{\downarrow\downarrow}(1,2) = -\langle\hat{T}_\tau\Psi_\downarrow^+(1)\Psi_\downarrow(2)\rangle,$$

$$\widetilde{F}_{\uparrow\downarrow}(1,2) = \langle\hat{T}_\tau\Psi_\uparrow(1)\Psi_\uparrow(2)\rangle, \quad \text{etc;}$$

$\widetilde{\omega} = \omega + iH_{exc}$, $\omega = \pi T(2n+1)$, $n = 0,\pm 1,\pm 2...$ are the Matsubara frequencies, $\Delta(x)$ is the order parameter; $\Psi_\sigma(1)$, $\Psi_\sigma^+(1)$ are the Heisenberg operators. We note that in the general case the exchange field breaks the symmetry of the system with respect to rotation in spin space both in the F layer and, on account of the proximity effect, in the S layer. It can be shown, however,[13,15] that for singlet pairing and in the absence of spin–orbit scattering and external magnetic fields, the whole system of Usadel equations decomposes into two equivalent subgroups, which go over to each other under interchange of the indices $\uparrow\leftrightarrow\downarrow$ and reversal of the sign of the exchange field, $H_{exc}\leftrightarrow -H_{exc}$. Assuming that the indicated conditions are met, we shall henceforth drop the spin indices in Eqs. (2)–(4).

For the S layer the Usadel equations have the standard form (see, e.g., Ref. 14). We shall assume below that for a nonsuperconducting F metal the bare value of the order parameter $\Delta_F^0 = 0$, but that $F_F \neq 0$ on account of the proximity effect with the superconductor. It is convenient to take into account the normalization of the Green function explicitly and to introduce (in analogy with Ref. 16) modified Usadel functions $\Phi_{S,F}$ defined by the relations $G = \omega/(\omega^2 + \Phi\widetilde{\Phi})^{1/2}$, $F = G\Phi/\omega$, etc. The system of Usadel equations now becomes:

for the S metal

$$\Phi_S = \Delta_S + \xi_S^2\frac{\pi T_C}{\omega G_S}[G_S^2\Phi_S']',$$

$$G_S = \frac{\omega}{(\omega^2 + \Phi_S\widetilde{\Phi}_S)^{1/2}}, \tag{5}$$

$$\Delta_S\ln(T/T_C) + 2\pi T\sum_{\omega>0}[(\Delta_S - \Phi_S G_S)/\omega] = 0; \tag{6}$$

for the F metal

$$\Phi_F = \xi^2\frac{\pi T_C}{\widetilde{\omega}G_F}[G_F^2\Phi_F']', \quad G_F = \frac{\widetilde{\omega}}{(\widetilde{\omega}^2 + \Phi_F\widetilde{\Phi}_F)^{1/2}}. \tag{7}$$

The equations for the functions $\widetilde{\Phi}$ have a form analogous to (5)–(7). In Eq. (7) we have used the effective coherence length ξ of a normal nonmagnetic metal with a diffusion coefficient D_F; this effective coherence length, which we have defined in Eq. (1), is convenient to use instead of ξ_F for analysis of the limit $H_{exc}\to 0$. In these equations we have used a prime to denote differentiation with respect to the coordinate x. We note that for $H_{exc}\neq 0$ the functions $\Phi_{S,F}(\omega)$ lose symmetry with respect to a change in the sign of the energy variable ω. This is one of the ways in which an S/F bilayer differs from a S/N bilayer.

Equations (5)–(7) must be supplemented by the boundary conditions for the functions Φ_S and Φ_F. It follows from Eq. (5) that in the interior of the S layer

$$\Phi_S(\infty) = \Delta_S(\infty) = \Delta_0(T), \tag{8}$$

where $\Delta_0(T)$ is the order parameter of a spatially homogeneous superconductor at temperature T in the BCS theory. At the outer boundary of the ferromagnet the boundary condition is $\Phi_F'(-d_F) = 0$. The boundary conditions at the interface between the ferromagnet and superconductor need to be discussed in some detail; ordinarily such boundary conditions are imposed for the functions G and F and for the case $T\to T_C$ without discussion (see, e.g., Refs. 11 and 12). Meanwhile, the conventional way of writing the boundary conditions presupposes that a number of physical conditions are met which may not hold for all real S/F contacts.

2. We obtain the boundary conditions on the Usadel equations for the SF interface at arbitrary temperatures $T \lesssim T_C$ by the same approach as was used in Ref. 17 to find the boundary conditions at an interface between two superconductors. The first condition on the Usadel equations ensures continuity of the supercurrent flowing through the SF

boundary at any value of the interfacial transparency (see, e.g., Eq. (15) of Ref. 17). It is easy to see that, when the normalization (4) is taken into account, the matrix expression (15) in Ref. 17 only needs to be written for the nonzero off-diagonal components:

$$p_F^2 l_F \left(F_F \frac{dG_F}{dx} - G_F \frac{dF_F}{dx} \right) \bigg|_{x=0}$$
$$= p_S^2 l_S \left(F_S \frac{dG_S}{dx} - G_S \frac{dF_S}{dx} \right) \bigg|_{x=0},$$

where $p_{F,S}$ are the momenta of the electrons at the Fermi surface, and $l_{F,S}$ are the electron mean free paths for the F and S layers, respectively. Going over to the modified Usadel functions $\Phi_S = \omega F_S / G_S$ and $\Phi_F = \tilde{\omega} F_F / G_F$, we obtain the following form for the first boundary condition on these functions at the SF interface:

$$\frac{1}{\tilde{\omega}} \gamma \xi G_F^2 \Phi_F' \bigg|_{x=0} = \frac{1}{\omega} \xi_S G_S^2 \Phi_S' \bigg|_{x=0}. \tag{9}$$

Here $\gamma = \rho_S \xi_S / \rho_F \xi$ is the proximity effect parameter, which characterizes the intensity of the superconducting correlations induced in the F layer on account of its proximity to the S layer; $\rho_{S,F}$ are the resistivities of the S and F metals in the normal state.

The second boundary condition takes into account the effects of a finite transparency of the SF interface (see, e.g., Eq. (22) of Ref. 17). As in the case of the first boundary condition, the matrix equation (22) of Ref. 17 needs to be written only for the nonzero off-diagonal components:

$$l_F \left(F_F \frac{dG_F}{dx} - G_F \frac{dF_F}{dx} \right) \bigg|_{x=0}$$
$$= \frac{3}{4} \left\langle \frac{x_F \delta}{R} \right\rangle (F_F G_S - F_S G_F) \bigg|_{x=0},$$

where δ is the transparency of the SF interface; $R = 1 = \delta$ is the coefficient of reflection of electrons from the interface, and $x_F = p_F / p_F^x$. For modified Usadel functions the second boundary condition at the SF interface becomes

$$\xi \gamma_{BF} G_F \Phi_F' \big|_{x=0} = \tilde{\omega} G_S (\Phi_S / \omega - \Phi_F / \tilde{\omega}) \big|_{x=0}, \tag{10}$$

where $\gamma_{BF} = \frac{2}{3} \langle x_F \delta / R \rangle^{-1} l_F / \xi$ is a parameter that takes into account the effects of a finite transparency of the interface. For $\gamma_{BF} = 0$, i.e., for a totally transparent boundary ($\delta = 1$), condition (10) goes over to $\Phi_S / \omega = \Phi_F / \tilde{\omega}$.

Relations (9) and (10) generalize the problem of the proximity effect for arbitrary transparency of the NS interface[10,16] to the case when the normal metal is a ferromagnet. An additional physical condition for the validity of relations (9) and (10) in comparison with an N metal is the assumption that the exchange splitting of the subbands, $p_F^{\pm} = \sqrt{2m}\sqrt{E_F \pm H_{exc}}$ is substantially smaller than the Fermi energy E_F, i.e., $H_{exc} \ll E_F$ (m is the effective mass of an electron). In this case the difference in the densities of states and transparencies of the SF interface for electrons with opposite spin orientations can be neglected. In such ferromagnetic metals as Ni, Gd, etc. the polarization of the electrons at low temperatures is not more than 10%, and the experimental results on the induced superconductivity in films of these ferromagnets mesh quite well with the ''conventional'' ideas about the proximity effect.[18,19] In the ferromagnetic phase of perovskite lanthanum manganates the spin polarization of the charge carriers has already reached nearly 100% at liquid-nitrogen temperatures (see, e.g., Ref. 20), and the value of the spin splitting of the Fermi surface is not small. Curiously, experimental studies of proximity structures between a superconductor and a material exhibiting colossal magnetoresistance have revealed some unusual properties (see, e.g., Refs. 21 and 22).

3. Let us show that the study of the induced superconductivity in S/F structures with a thin F metal [d_F satisfies condition (1)] can be reduced to consideration of a boundary-value problem for the S layer. Indeed, the differential equation (7) can be solved by iteration with respect to the parameter d_F / ξ. To a first approximation one can neglect the nongradient term and, taking into account that $\Phi_F'(-d) = 0$, we obtain $\Phi_F = $ const. In the next approximation in d_F / ξ we find, after linearizing Eq. (7),

$$\Phi_F'(x) = \frac{\tilde{\omega} \Phi_F(0)(x+d)}{\xi^2 \pi T_C G_F}. \tag{11}$$

Here in the integration we have again taken into account the condition that $\Phi_F'(-d) = 0$. Determining $\Phi_F'(x=0)$ from Eq. (11) and substituting it into boundary conditions (9) and (10), we obtain the boundary condition for the function Φ_S:

$$\xi_S G_S \Phi_S' \big|_{x=0}$$
$$= \gamma_M \tilde{\omega} \Phi_S \bigg/ \left[\pi T_C \left(1 + \frac{2 G_S \gamma_B \tilde{\omega}}{\pi T_C} + \frac{\tilde{\omega}^2 \gamma_B^2}{(\pi T_C)^2} \right)^{1/2} \right] \bigg|_{x=0} \tag{12}$$

and an equation determining the unknown value of the function Φ_F at $x = 0$:

$$\Phi_F(0) = G_S \Phi_S \bigg/ \left[\omega \left(\frac{\gamma_B}{\pi T_C} + \frac{G_S}{\tilde{\omega}} \right) \right] \bigg|_{x=0}. \tag{13}$$

Here $\gamma_M = \gamma d_F / \xi$, $\gamma_B = \gamma_{BF} d_F / \xi$. In the particular case $\gamma_B = 0$ (complete transparency), Eqs. (12) and (13) take the form $\xi_S G_S \Phi_S' \big|_{x=0} = \gamma_M \tilde{\omega} \Phi_S / (\pi T_C) \big|_{x=0}$ and $\omega \Phi_F(0) = \tilde{\omega} \Phi_S(0)$, respectively. The spatial dependence of the functions in the F layer, which is of mesoscopic thickness $d_F \ll \xi$, can of course be neglected. As a result, the problem of the proximity effect for a massive superconductor with a thin layer of a ferromagnet reduces to solving equations (5) and (6) for the S layer with the boundary conditions (8) and (12) and to Eq. (13). The latter determines the modified Usadel function Φ_F characterizing the superconductivity induced in the F layer on account of the proximity.

The degree to which the S and F layers influence each other depends on the parameters γ_M and γ_B and the value of the exchange interaction H_{exc}. In the general case the problem can be solved only by numerical methods, but in a number of particular limiting cases it admits analytical solution. Below we present the results of an analytical investigation of

a bilayer with a small proximity effect parameter and a high transparency of the SF interface: $\gamma_M \ll 1$, $\gamma_B \ll 1$.

4. In the limit $\gamma_M \ll 1$, $\gamma_B \ll 1$, it follows from condition (12) in the zeroth approximation in γ_M that $\xi_S \Phi'_S(0) = 0$ for $\omega \ll \Omega_\gamma \approx \pi T_C / \gamma_M$. Since the self-consistency equation (6) converges for $\omega \ll \Omega_C \approx \pi T_C$ ($\Omega_C \ll \Omega_\gamma$), one can assume that in this approximation the functions Φ_S and Δ_S are spatially homogeneous: $\Phi_S(x) = \Delta_S(x) = \Delta_0$, $\omega \ll \Omega_\gamma$. In this same approximation, by substituting the explicit form of the function G_S into Eq. (13) we obtain for the function Φ_F

$$\Phi_F(0) = \Delta_0 \tilde{\omega} / (\gamma_B \tilde{\omega} \beta^2 + \omega),$$

where $\beta = [(\omega^2 + \Delta_0^2)^{1/2} / (\pi T_C)]^{1/2}$.

Thus in the zeroth approximation in γ_M the function Φ_F falls off as γ_B increases (as the transparency decreases); the jump in the order parameter at the interface, $\Phi_S(0) - \Phi_F(0)$, increases.

In the next approximation in γ_M, by linearizing the Usadel equation (5) for $\Phi_S(x)$ and making use of the fact that $\Phi_S(\infty) = \Delta_0$, we obtain the general solution of equation (5) in the form $\Phi_S(x) = \Delta_0 + C \exp(-\beta x / \xi_S)$, where $C = \text{const}$. Substituting this solution into the boundary condition (12), we obtain a solution for $\Phi_S(\omega, x)$ in the form

$$\Phi_S(\omega, x) = \Delta_0 \left[1 - \frac{\gamma_M \beta \tilde{\omega} \exp(-\beta x / \xi_S)}{\gamma_M \beta \tilde{\omega} + \omega A} \right], \tag{14}$$

where

$$A \equiv A(\omega) = \left[1 + \frac{\gamma_B \tilde{\omega}}{(\pi T_C)^2} \left(\frac{2\omega}{\beta^2} + \gamma_B \tilde{\omega} \right) \right]^{1/2}.$$

Using Eq. (14) for $x = 0$ and relation (13), we find an expression for $\Phi_F(\omega, 0)$:

$$\Phi_F(\omega, 0)$$

$$= \frac{\Delta_0 \pi T_C A}{\pi T_C A \omega / \tilde{\omega} + \gamma_M \beta \pi T_C + \gamma_B [(\omega A + \gamma_M \beta \tilde{\omega})^2 + \Delta_0^2 A^2]^{1/2}}. \tag{15}$$

It follows from this relation that as either γ_B or the suppression parameter γ_M increases, the function Φ_F falls off, just as in the case of an S/N bilayer[16] or an S/S' bilayer.[10] For $H_{exc} \to 0$ the quantity $\tilde{\omega} \to \omega$, and the solution (14) reproduces all the results obtained in Refs. 10 and 16 for an S/N bilayer with $\gamma_M \ll 1$, $\gamma_B \ll 1$. In the case of a completely transparent interface ($\gamma_B = 0$) the solution of the Usadel equations becomes

$$\Phi_S(\omega, x) = \Delta_0 \left(1 - \frac{\gamma_M \beta \tilde{\omega} \exp(-\beta x / \xi_S)}{\gamma_M \beta \tilde{\omega} + \omega} \right).$$

Then the superconductivity induced in the F layer is characterized by a function $\Phi_F(0) = \Delta_0 \tilde{\omega} / (\gamma_M \tilde{\omega} \beta + \omega)$, which falls off as the parameter γ_M increases.

Knowing the function $\Phi_S(\omega, x)$, we can use Eq. (6) to calculate the spatial behavior of the parameter $\Delta_S(x)$ that determines the energy gap in the S layer:

$$\Delta_S(x) = \frac{2\pi T \sum_{\omega > 0} \Phi_S(\omega, x) G_S(\omega, x) / \omega}{\ln(T / T_C) + 2\pi T \sum_{\omega > 0} 1 / \omega}. \tag{16}$$
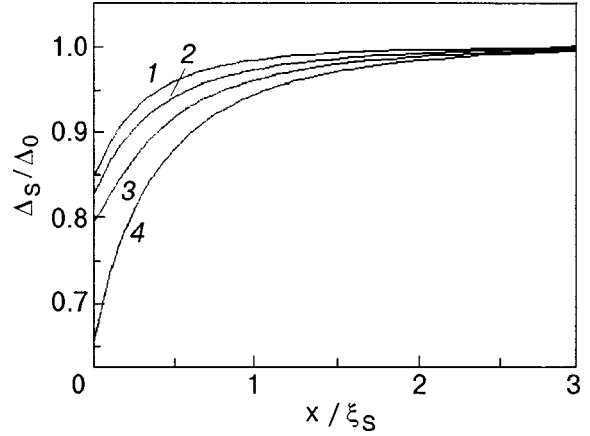

FIG. 1. Spatial dependence of the order parameter in the S layer $\Delta_S(x)$ near the SF interface for $\gamma_M = 0.1$, $\gamma_B = 0.1$ and for different values of the exchange field $H_{exc} / \pi T_C = 0$, 3, 5, and 10 (curves 1, 2, 3, and 4, respectively), $T / T_C \ll 1$. The order parameter in the F layer, $\Delta_F(x)$, in this approximation is constant and equal to the value at the interface, $\Delta_S(0)$.

The summation over frequencies in Eq. (16) is cut off by the Debye frequency ω_D. Figure 1 shows the curves of the spatial dependence of $\Delta_S(x)$ for $\gamma_M = 0.1$, $\gamma_B = 0.1$ at low temperatures for various values of the exchange interaction parameter H_{exc}. As in the case of S/N and S/S' bilayers, the BCS value of the order parameter is reached at a distance into the S layer of the order of several ξ_S. We see from Fig. 1 that the value of the order parameter near the SF interface, $\Delta_S(0)$, decreases with increasing exchange interaction: in accordance with Eq. (14), one can speak of ''induced'' exchange correlations in the S layer, which destroy Cooper pairs. At equal values of the exchange interaction parameter H_{exc} the order parameter $\Delta_S(0)$ at the SF interface decreases with increasing transparency of the boundary, which leads to a decrease in the jump of the amplitude of the Cooper pairs in going from the S to the F layer. The behavior here is completely analogous to the situation in an SN system (see Refs. 10 and 16). At small values of the parameter γ_M a decrease in the transparency of the boundary (i.e., an increase in the parameter γ_B) will lead to a sharp increase in the jump of the order parameter of the system at the boundary.

5. Let us use the expressions obtained above to investigate the influence of the exchange field on the density of states in the S and F layers. The densities of states for quasiparticles in the S and F layer, by definition, are given by

$$N_{S,F}(\varepsilon, x = 0) = \text{Re}\{ G_{S,F\uparrow\uparrow}(\varepsilon, 0) + G_{S,F\downarrow\downarrow}(\varepsilon, 0) \}$$

$$= N_{S,F\uparrow}(\varepsilon, 0) + N_{S,F\downarrow}(\varepsilon, 0). \tag{17}$$

For our case, that of finite transparency, the densities of states at the SF interface are different in the F and S layers. Using Eq. (14) for $x = 0$ and Eq. (15), we obtain the following expressions for the Green functions of a specified spin subband in the S and F layers at the SF interface:

$$G_{S\uparrow\uparrow}(\omega, 0) = (\omega A + \gamma_M \beta \tilde{\omega}) \mathcal{R}^{-1}(\omega),$$

$$G_{F\uparrow\uparrow}(\omega, 0) = \frac{\omega A + \tilde{\omega}[\gamma_M \beta + \gamma_B \mathcal{R}(\omega)]}{\{\Delta_0^2 A^2 + [\omega A + \tilde{\omega}(\gamma_M \beta + \gamma_B \mathcal{R}(\omega))]^2\}^{1/2}},$$
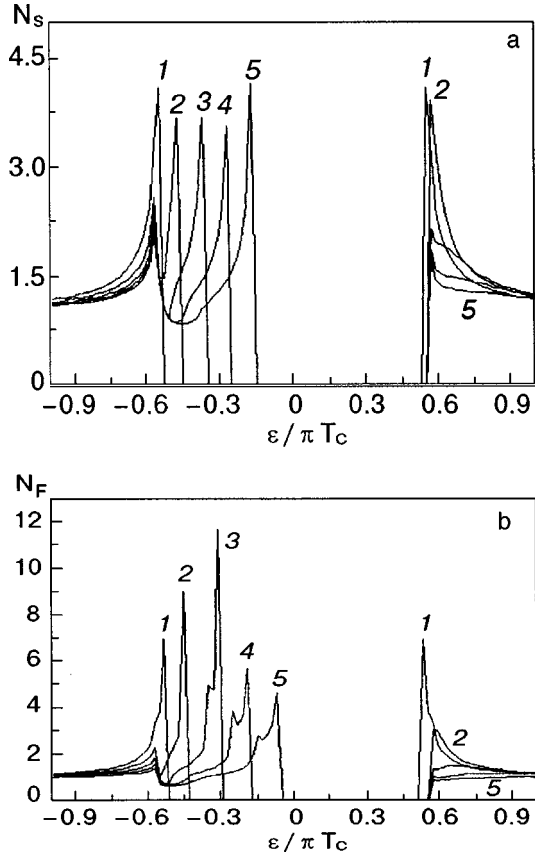
FIG. 2. Densities of quasiparticle states with a specified spin orientation in the S (a) and F (b) layers of an S/F sandwich for $\gamma_M = 0.1$, $\gamma_B = 0.1$, and various values of the exchange field $H_{exc}/(\pi T_C) = 0$, 1, 2, 3, and 4 (curves *1*, *2*, *3*, *4*, and *5*, respectively); $T/T_C \ll 1$.

where $\mathcal{R}(\omega) = \{\Delta_0^2 A^2 + (\omega A + \widetilde{\omega} \gamma_M \beta)^2\}^{1/2}$, and $A \equiv A(\omega)$ is defined according to (14). By performing an analytical continuation of the functions $G_{S\uparrow\uparrow}(\omega,0)$ and $G_{F\uparrow\uparrow}(\omega,0)$ onto the complex plane by means of the substitution $\omega \rightarrow -i\varepsilon$, we can obtain the explicit form of the expressions for the densities of states at the interface for each of the spin subbands: $N_{S\uparrow}(\varepsilon,0)$, $N_{S\downarrow}(\varepsilon,0)$ and $N_{F\uparrow}(\varepsilon,0)$, $N_{F\downarrow}(\varepsilon,0)$. The resulting expressions, which are too awkward to present here, imply that for $H_{exc} \neq 0$, $\gamma_M \neq 0$, and $\gamma_B \neq 0$ the density of quasiparticle states is spin-split in both the S and F layers: Re $G_{S,F\uparrow\uparrow} \neq$ Re $G_{S,F\downarrow\downarrow}$. This is because of the initial exchange splitting of the Fermi surface in the F metal, which is manifested in the characteristics of the united system—the F/S bilayer. The symmetry of the density of states with respect to the energy variable is also lost: Re $G_{S,F\uparrow\uparrow}(\varepsilon>0) \neq$ Re $G_{S,F\downarrow\downarrow}(\varepsilon<0)$, although the total density $N_{S,F}(\varepsilon)$ in (17), as is readily seen, is symmetric.

Figure 2 shows the curves of the densities of states for one of the subbands in the F layer and S layer, $N_{F\uparrow}(\varepsilon,0)$ and $N_{S\uparrow}(\varepsilon,0)$, as functions of the energy for $T \ll T_C$, $\gamma_M = 0.1$, $\gamma_B = 0.1$ and for different values of the exchange energy H_{exc} (the values of H_{exc} and ε are normalized to πT_C). As we see from Fig. 2, the exchange interaction leads to spin-splitting of the density of quasiparticle states not only in the F layer but also in the S layer; as we have said, this is due to the exchange splitting of the Fermi surface in the F metal. For

$H_{exc} \neq 0$ there are three features in the density of states $N_{F\uparrow}(\varepsilon,0)$ in the energy region $\varepsilon < 0$. One of them corresponds to the BCS value $|\varepsilon| = \Delta_0(T)$ and is less pronounced than in the nonmagnetic case (cf. with curve *1* for $H_{exc} = 0$). The second is due to the presence of the true gap $|\varepsilon| = \Delta_S(T)$ in the spectrum of single-particle excitations and reflects the renormalization of the gap in the S layer on account of the proximity effect. As the exchange interaction is increased in strength, the gap $\Delta_S(T)$ decreases in absolute value, and the height of the spikes at $|\varepsilon| = \Delta_0(T)$ falls off. Finally, the feature at the lowest values of $|\varepsilon|$ corresponds to $\Delta_F(T)$, i.e., to the induced value of the gap in the F layer. In the region of positive energies $\varepsilon > 0$ we observe one BCS singularity which is smeared out as the exchange is increased.

6. We have investigated the superconducting proximity effect in S/F structures having arbitrary transparency of the SF interface and arbitrary value of the proximity effect between a massive superconductor and a ferromagnet of mesoscopic thickness. Both metals correspond to the "dirty" limit. Analytical solutions were obtained for the case of high transparency of the interface and a low proximity effect. The density of single-particle states and the spatial dependence of the order parameter in the S and F metals are calculated as functions of the strength of the exchange field, the transparency of the interface, and the value of the proximity effect. We showed that in mesoscopic S/F structures the density of single-particle states is spin-polarized in both the F and S metals. We assume that it is particularly important to take the spin polarization of the density of states into account when interpreting the properties of $F/S/F$ tunnel contacts with a thin layer of the S metal. This type of tunnel contacts is now considered promising for use as the functional elements of a new type of magnetoresistive devices whose magnetoresistive and superconducting properties can be controlled by an applied voltage.[23]

[1] B. Y. Jin and J. B. Ketterson, Adv. Phys. **38**, 189 (1989).
[2] Z. Radovic, M. Ledvij, L. Dobrosaljevic-Grudjic, A. I. Buzdin, and J. R. Klem, Phys. Rev. B **44**, 759 (1991).
[3] P. Koorevaar, Y. Suzuki, R. Coehoorn, and J. Aarts, Phys. Rev. B **49**, 441 (1994).
[4] Th. Muhge, K. Westerholt, H. Zabel, N. N. Garif'yanov, Yu. V. Goryunov, I. A. Garifullin, and G. G. Khaliullin, Phys. Rev. B **55**, 8945 (1997).
[5] Yu. N. Proshin and M. I. Khusainov, Zh. Éksp. Teor. Fiz. **113**, 1708 (1998) [JETP **86**, 930 (1998)].
[6] R. J. Soulen Jr., J. M. Byers, M. S. Osofskey, B. Nadgorny, T. Ambrouse, S. F. Cheng, P. R. Broussard, C. T. Tanaka, J. Novak, J. S. Moodera, and J. M. D. Coey, Science **282**, 85 (1998).
[7] S. C. Upadhyay, A. Palanisami, A. N. Louie, and R. A. Buhrman, Phys. Rev. Lett. **81**, 3247 (1998).
[8] O. Bourgeois, P. Gandit, J. Lezuer, R. Melin, A. Sunce, X. Grison, and J. Chussy, cond-mat/9901045 (Jan. 1999).

[9] V. T. Petrashov, I. A. Sosnin, I. Cox, A. Parsons, and C. Troadec, cond-mat/9903237 (Mar. 1999).

[10] A. A. Golubov, E. P. Houwman, J. G. Gijsbertsen, V. M. Krasnov, J. Flokstra, H. Rogalla, M. Yu. Kupriyanov, Phys. Rev. B **51**, 15174 (1997).

[11] E. A. Demler, G. B. Arnold, and M. R. Beasley, Phys. Rev. B **55**, 15174 (1997).

[12] J. Aarts, J. M. E. Greers, E. Bruck, A. A. Golubov, and R. Coehoorn, Phys. Rev. B **56**, 2779 (1997).

[13] L. N. Bulaevskii, A. I. Buzdin, M. L. Kulic, and S. V. Panyukov, Adv. Phys. **34**, 175 (1985).

[14] A. M. Svidzinskiĭ, *Spatially Nonuniform Problems of the Theory of Superconductivity* [in Russian], Nauka, Moscow (1982).

[15] G. Eilenberger, Z. Phys. **190**, 142 (1966); **214**, 195 (1968).

[16] A. A. Golubov and M. Yu. Kupriyanov, Zh. Éksp. Teor. Fiz. **96**, 1420 (1989) [Sov. Phys. JETP **69**, 805 (1989)].

[17] M. Yu. Kupriyanov and V. F. Lukichev, Zh. Éksp. Teor. Fiz. **94**, 139 (1988) [Sov. Phys. JETP **67**, 1163 (1988)].

[18] P. M. Tredrow and R. Meservey, Phys. Rev. B **7**, 318 (1973).

[19] J. J. Hauser, H. C. Theueser, and N. R. Werthamer, Phys. Rev. B **142**, 118 (1996).

[20] Y. Okimoto, T. Katsufuji, T. Ishikawa, A. Urushibara, T. Arima, and Y. Tokura, Phys. Rev. Lett. **75**, 109 (1995).

[21] M. Kasai, Y. Kanke, T. Ohno, and Y. Kozono, J. Appl. Phys. **72**, 5344 (1992).

[22] Z. V. Dong, R. Ramesh, T. Venkatesan, M. Johnson, Z. Y. Chen, S. P. Pai, V. Tauansky, R. P. Sharma, R. Shreekala, C. J. Lobb, and K. L. Green, Appl. Phys. Lett. **71**, 1718 (1997).

[23] S. Takahashi, H. Imamura, and S. Maekawa, Phys. Rev. Lett. **82**, 3911 (1999).

Translated by Steve Torstveit

LOW-DIMENSIONAL AND DISORDERED SYSTEMS

Surface polaritons in a finite superlattice with a displaced layer in a quantizing magnetic field

N. N. Beletskiĭ and Yu. V. Bludov*

Institute for Radio Physics and Electronics, National Academy of Sciences of Ukraine, ul. Akad. Proskury 12, 61085 Kharkov, Ukraine
(Submitted June 18, 1999; revised September 16, 1999)
Fiz. Nizk. Temp. **26**, 164–172 (February 2000)

A theoretical study is made of surface polaritons (SPs) in a weakly disordered superlattice consisting of a finite number of infinitely extended two-dimensional electron layers (2DELs) placed in an external static quantizing magnetic field directed perpendicular to the 2DELs. The filling factor of the Landau levels is assumed to be the same in all the 2DELs. The disorder in the superlattice consists in having one of the interior 2DELs displaced from the position of periodicity by a certain distance Δ. The dispersion and energy characteristics of SPs are investigated in the case when a finite superlattice is embedded in a uniform dielectric medium. It is shown that under conditions of the integer quantum Hall effect, all the characteristics of the SPs are represented by quantized values. It is found that in a finite, weakly disordered superlattice there exists a local SP mode whose properties differ substantially from those of the usual SP modes in a finite ordered superlattice. The conditions under which the phase and group velocities of the SPs in a finite, weakly disordered superlattice can be substantially lower than in an isolated 2DEL are determined. It is found that when dissipation is taken into account, a new SP mode arises in a weakly disordered superlattice—an additional SP whose properties depend strongly on the electron momentum relaxation frequency ν and on the displacement Δ. © *2000 American Institute of Physics.* [S1063-777X(00)00702-7]

1. INTRODUCTION

Surface polaritons (SPs) in semiconductors with a superlattice (SL) have some interesting properties. These have been investigated previously in ordered (periodic) SLs: infinite,[1–4] semi-infinite,[5–7] and finite.[8–12] There has also been research interest in weakly disordered superlattices (WDSLs), which have only a small disruption of the periodicity. This disruption may be due to the presence of one or several layers which either have a different concentration of charge carriers (a ''defect'' layer) or have been displaced from the position of periodicity by a certain distance Δ.

Surface polaritons have been investigated in infinite,[13–16] semi-infinite,[17,18] and finite[16,19–21] WDSLs. The systems considered include WDSLs with a single ''defect'' layer,[13,15–20] finite WDSLs with two outermost ''defect'' layers,[21] and also an infinite WDSL with a single layer displaced from the position of periodicity.[14,15] It was shown in those papers that the spectrum of SPs in an WDSL differ substantially from the spectrum of SPs in ordered superlattices (OSLs). For example, in these systems there exists a local mode of SPs, the electromagnetic field of which is localized in the region where the periodicity of the SL is disrupted. This local mode can be higher or lower in frequency than the other SP modes in the WDSL, depending on whether the ''defect'' layer has a higher (enrichment layer) or lower (depletion layer) electron concentration than the other layers. In addition, it has been shown[14,15] that in an infinite WDSL containing a single displaced layer there can exist local SP modes whose dispersion curves lie outside the existence region of SPs in an infinite OSL.

In this paper we investigate SPs in a WDSL consisting of a finite number of two-dimensional electron layers (2DELs), one of which is displaced from its position of periodicity by a distance Δ. We show that under conditions of the integer quantum Hall effect (IQHE) all the characteristics of the SPs in a finite WDSL are represented by quantized values. We find that the SP spectrum in a WDSL has a local SP mode whose electromagnetic field is localized in the region of the displaced 2DEL. We find that near the cyclotron resonance, $\omega \sim \Omega$ ($\Omega = eB/m^*c$ is the electron cyclotron frequency, B is the magnetic field, e and m^* are the charge and effective mass of the electron, and c is the speed of light), the group velocity of the SPs undergoes jumps as the external magnetic field is varied, the value of the jumps being determined by the fine structure constant $\alpha = e^2/\hbar c$, the interlayer distance d, the displacement Δ, and the dielectric constants of the media making up and surrounding the WDSL. We also show in this paper that when the dissipation in the WDSL is taken into account, a new SP mode appears—an additional SP—whose properties are largely determined by the electron momentum relaxation frequency ν in the 2DEL and by the value of Δ.
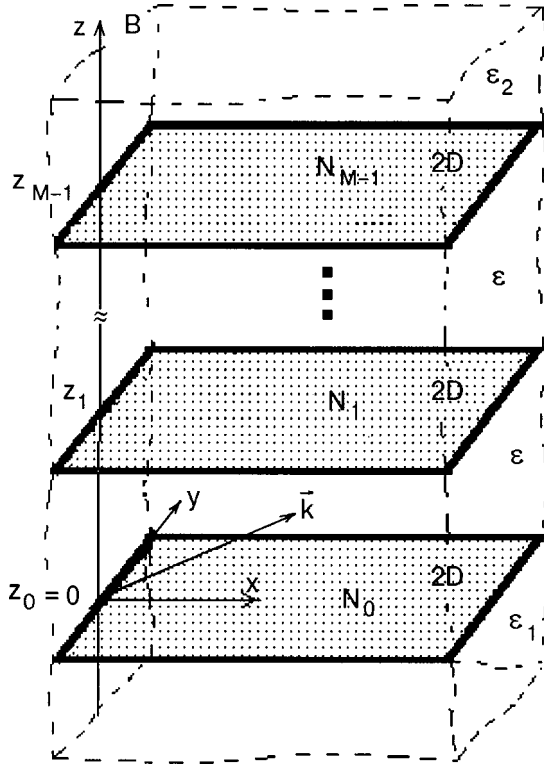
FIG. 1. Superlattice consisting of a finite number M of two-dimensional electron layers embedded in a dielectric medium with dielectric constants ε (for $0 < z < z_{M-1}$), ε_1 (for $z < 0$), and ε_2 (for $z > z_{M-1}$).

2. DISPERSION RELATION

Let us consider the SL in Fig. 1, which consists of a finite number M of infinitely extended 2DELs with Landau level filling factors N_m ($N_m = 2\pi l^2 n_m$, $l = (c\hbar/eB)^{1/2}$ is the magnetic length, and n_m is the electron density in the mth 2DEL $m = 0,1,\ldots M-1$), which lies in the plane $z = z_m$. The static quantizing magnetic field **B** is directed perpendicular to the 2DEL along the z axis. We shall assume that the region of space $0 < z < z_{M-1}$ is filled with a dielectric with a dielectric constant ε, while the semi-infinite media at $z < 0$ and $z > z_{M-1}$ are dielectrics with dielectric constants ε_1 and ε_2, respectively (an $\varepsilon_1 - \varepsilon - \varepsilon_2$ geometry).

The solutions of Maxwell's equations for the TM and TE modes have the following form:

TM modes:

$0 < z < z_{M-1}$

$$H_y(k,\omega,z) = B_+^m e^{p(z-z_m)} + B_-^m e^{-p(z-z_m)},$$

$$E_x(k,\omega,z) = -i\frac{cp}{\omega\varepsilon}[B_+^m e^{p(z-z_m)} - B_-^m e^{-p(z-z_m)}],$$

$z < 0$

$$H_y(k,\omega,z) = A_1 e^{p_1 z}, \quad E_x(k,\omega,z) = -i\frac{cp_1}{\omega\varepsilon_1}A_1 e^{p_1 z},$$

$z > z_{M-1}$

$$H_y(k,\omega,z) = A_2 e^{-p_2(z-z_{M-1})},$$

$$E_x(k,\omega,z) = i\frac{cp_2}{\omega\varepsilon_2}A_2 e^{-p_2(z-z_{M-1})};$$

TE modes:

$0 < z < z_{M-1}$

$$E_y(k,\omega,z) = D_+^m e^{p(z-z_m)} + D_-^m e^{-p(z-z_m)},$$

$$H_x(k,\omega,z) = i\frac{cp}{\omega}[D_+^m e^{p(z-z_m)} + D_-^m e^{-p(z-z_m)}],$$

$z < 0$

$$E_y(k,\omega,z) = C_1 e^{p_1 z}, \quad H_x(k,\omega,z) = i\frac{cp_1}{\omega}C_1 e^{p_1 z},$$

$z > z_{M-1} \quad E_y(k,\omega,z) = C_2 e^{-p_2(z-z_{M-1})},$

$$H_x(k,\omega,z) = -i\frac{cp_2}{\omega}C_2 e^{-p_2(z-z_{M-1})},$$

where

$$p = \sqrt{k^2 - \omega^2\varepsilon/c^2}, \quad p_i = \sqrt{k^2 - \omega^2\varepsilon_i/c^2},$$

$$i = 1,2; \quad m = 0,1,\ldots,M-2.$$

As the boundary conditions we use the continuity of the tangential component of the total electric field of the TE and TM modes at the boundaries $z = z_m$ ($m = 0,\ldots,M-1$). In addition, we shall assume that at these boundaries the tangential components of their total magnetic field undergo jumps due to the presence of currents in the 2DEL.

The use of the above-indicated boundary conditions on the interior boundaries $z = z_m$ ($m = 1,\ldots,M-2$) gives the following equations for the unknowns D_+^m, D_-^m, B_+^m, B_-^m, A_1, A_2, C_1, and C_2;

$$B_+^m - B_-^m - (B_+^{m-1}e^{pd_m} - B_-^{m-1}e^{-pd_m}) = 0, \tag{1}$$

$$D_+^m + D_-^m - (D_+^{m-1}e^{pd_m} + D_-^{m-1}e^{-pd_m}) = 0, \tag{2}$$

$$D_+^m - D_-^m - (D_+^{m-1}e^{pd_m} - D_-^{m-1}e^{-pd_m})$$

$$= -i\frac{4\pi\omega}{c^2 p}\sigma_{yy}^{(m)}(D_+^m + D_-^m) - \frac{4\pi}{\varepsilon c}\sigma_{yx}^{(m)}(B_+^m - B_-^m),$$
$$\tag{3}$$

$$B_+^m + B_-^m - (B_+^{m-1}e^{pd_m} + B_-^{m-1}e^{-pd_m})$$

$$= i\frac{4\pi p}{\omega\varepsilon}\sigma_{xx}^{(m)}(B_+^m - B_-^m) - \frac{4\pi}{c}\sigma_{xy}^{(m)}(D_+^m + D_-^m). \tag{4}$$

At the $z = 0$ boundary we have the following system of equations:

$$A_1 = \frac{\varepsilon_1 p}{p_1 \varepsilon}(B_+^0 - B_-^0), \quad C_1 = D_+^0 + D_-^0, \tag{5}$$

$$D_+^0 - D_-^0 - \frac{p_1}{p}C_1 = -i\frac{4\pi\omega}{c^2 p}\sigma_{yy}^{(0)}(D_+^0 + D_-^0)$$

$$-\frac{4\pi}{\varepsilon c}\sigma_{yx}^{(0)}(B_+^0 - B_-^0), \tag{6}$$

$$B_+^0 + B_-^0 - A_1 = i\frac{4\pi p}{\omega\varepsilon}\sigma_{xx}^{(0)}(B_+^0 - B_-^0)$$

$$-\frac{4\pi}{c}\sigma_{xy}^{(0)}(D_+^0 + D_-^0). \qquad (7)$$

Finally, at the boundary $z = z_{M-1}$ we find

$$A_2 = -\frac{\varepsilon_2 p}{p_2\varepsilon}(B_+^{M-2}e^{pd_{M-1}} - B_-^{M-2}e^{-pd_{M-1}}),$$

$$C_2 = D_+^{M-2}e^{pd_{M-1}} + D_-^{M-2}e^{-pd_{M-1}}, \qquad (8)$$

$$D_+^{M-2}e^{pd_{M-1}} - D_-^{M-2}e^{-pd_{M-1}} + \frac{p_2}{p}C_2$$

$$= i\frac{4\pi\omega}{c^2 p}\sigma_{yy}^{(M-1)}(D_+^{M-2}e^{pd_{M-1}} + D_-^{M-2}e^{-pd_{M-1}})$$

$$+ \frac{4\pi}{\varepsilon c}\sigma_{yx}^{(M-1)}(B_+^{M-2}e^{pd_{M-1}} - B_-^{M-2}e^{-pd_{M-1}}), \qquad (9)$$

$$B_+^{M-2}e^{pd_{M-1}} + B_-^{M-2}e^{-pd_{M-1}} - A_2$$

$$= -i\frac{4\pi p}{\omega\varepsilon}\sigma_{xx}^{(M-1)}(B_+^{M-2}e^{pd_{M-1}} - B_-^{M-2}e^{-pd_{M-1}})$$

$$+ \frac{4\pi}{c}\sigma_{xy}^{(M-1)}(D_+^{M-2}e^{pd_{M-1}} + D_-^{M-2}e^{-pd_{M-1}}), \qquad (10)$$

where $d_m = z_m - z_{m-1}$.

In Eqs. (3), (4), (6), (7), (9), and (10) $\sigma_{\alpha\beta}^{(m)}(\omega)$ are the components of the conductivity tensor of the 2DEL ($\alpha,\beta = x,y$), for which we shall use the expressions obtained in Refs. 22 and 23 in the absence of spatial dispersion ($kl \ll 1$):

$$\sigma_{xx}^{(m)}(\omega) = \sigma_{yy}^{(m)}(\omega) = \frac{e^2}{h}\frac{N_m\gamma}{1+\gamma^2},$$

$$\sigma_{xy}^{(m)}(\omega) = -\sigma_{yx}^{(m)} = \frac{e^2}{h}\frac{N_m}{1+\gamma^2}. \qquad (11)$$

Here $\gamma = (\nu - i\omega)/\Omega$, and ν is the electron momentum relaxation frequency in the 2DEL.

As we know, the linear homogeneous system of equations (1)–(10) has a solution only if its determinant is equal to zero. Thus the dispersion relation that we seek, which describes the propagation of SPs in a finite SL, can be written in the form

$$\begin{vmatrix} G_1 & G_2 & G_3 & G_4 \\ P_1 & P_2 & P_3 & P_4 \\ e^{pd_{M-1}}(1+\varphi) & e^{-pd_{M-1}}(1-\varphi) & -2\varepsilon b_{M-1}e^{pd_{M-1}} & -2\varepsilon b_{M-1}e^{-pd_{M-1}} \\ 2b_{M-1}e^{pd_{M-1}} & -2b_{M-1}e^{-pd_{M-1}} & e^{pd_{M-1}}(1+\psi) & -e^{-pd_{M-1}}(1-\psi) \end{vmatrix} = 0. \qquad (12)$$

Here

$$\varphi = \theta_2 + 2a_{M-1}, \quad \psi = \mu_2 - 2s_{M-1},$$

$$G_i = (1 - \theta_1 - 2a_0)F_{1i} + (1 + \theta_1 + 2a_0)F_{2i}$$
$$+ 2\varepsilon b_0(F_{3i} + F_{4i}),$$

$$F_i = 2b_0(F_{2i} - F_{1i}) + (1 - \mu_1 + 2s_0)F_{3i} - (1 + \mu_1 - 2s_0)F_{4i},$$

$$\theta_1 = \frac{\varepsilon_1 p}{p_1\varepsilon}, \quad \theta_2 = \frac{\varepsilon_2 p}{p_2\varepsilon}, \quad \mu_1 = \frac{p_1}{p}, \quad \mu_2 = \frac{p_2}{p},$$

$$a_m = i\frac{2\pi p}{\omega\varepsilon}\sigma_{xx}^{(m)}, \quad s_m = i\frac{2\pi\omega}{c^2 p}\sigma_{xx}^{(m)}, \quad b_m = \frac{2\pi}{\varepsilon c}\sigma_{xy}^{(m)}.$$

The general transfer matrix of a SL has the form $\hat{F} = \Pi_{m-1}^{M-2}\hat{T}_m$, where

$$\hat{T}_m = \begin{pmatrix} e^{-pd_m}(1-a_m) & a_m e^{-pd_m} & \varepsilon b_m e^{-pd_m} & \varepsilon b_m e^{-pd_m} \\ -a_m e^{pd_m} & e^{pd_m}(1+a_m) & \varepsilon b_m e^{pd_m} & \varepsilon b_m e^{pd_m} \\ -b_m e^{-pd_m} & b_m e^{-pd_m} & e^{-pd_m}(1+s_m) & s_m e^{-pd_m} \\ b_m e^{pd_m} & -b_m e^{pd_m} & -s_m e^{pd_m} & e^{pd_m}(1-s_m) \end{pmatrix}.$$

In the case when the SL consists of two 2DELs ($M = 2$) embedded in a homogeneous dielectric medium ($\varepsilon_1 = \varepsilon_2 = \varepsilon$, the $\varepsilon - \varepsilon - \varepsilon$ geometry), the dispersion relation (12) agrees with the dispersion relation (3.11) obtained in Ref. 23.

3. NUMERICAL RESULTS

Let us consider a finite WDSL in which all of the 2DELs have the same Landau-level filling factors ($N_0 = N_1 = \ldots = N_{M-1} = N$), and one of the interior 2DELs ($m = 1,\ldots,M - 2$) is displaced relative to the position of periodicity by a distance Δ. We write the expression for the distance d_m between 2DELs in a WDSL in the following way: $d_m = \Delta(\delta_{m,q} - \delta_{m,q+1}) + d$. Here $\delta_{m,q}$ is the Kronecker delta, d is the distance between 2DELs in the OSL, $q = 1,\ldots,M-2$ is the number of the displaced 2DEL. As a model for the 2DEL we take a GaAs/Al$_x$Ga$_{1-x}$As heterostructure with an effective carrier mass $m^* = 0.068m_0$ (m_0 is the free electron mass) and a dielectric constant $\varepsilon = 12$.

Figure 2 shows the SP spectrum (heavy solid curves) in a finite WDSL with $M = 5$, $\Gamma = 0$ ($\Gamma = \nu/\Omega$ is the dimensionless electron momentum relaxation frequency), $\delta = 0.1$ ($\delta = \Omega d/c$ is the dimensionless distance between neighboring 2DELs in the ordered periodic SL), $\tilde{\Delta} = 0.05$ ($\tilde{\Delta} = \Omega\Delta/c$ is the dimensionless displacement), and $N = 10$ for the $\varepsilon - \varepsilon - \varepsilon$ geometry in the case when $q = 1$. Plotted along the ordinate is the dimensionless frequency ω/Ω, and along the abscissa is the dimensionless wave number ck/Ω. For comparison, the thin solid curves $1' - 5'$ are the dispersion curves describing the propagation of SPs in an OSL with $\delta = 0.1$ and the same parameters as for the WDSL under study. Also shown in Fig. 2 is the dispersion curve 6 for SPs in an isolated 2DEL with $N = 10$, while the dashed line 7 is the light line $\omega = kv_d$ ($v_d = c/\sqrt{\varepsilon}$ is the speed of light in the dielectric filling the WDSL).

As we see in Fig. 2, in the long-wavelength region the SP spectrum in the WDSL is almost no different from the SP spectrum in the OSL. This is due to the fact that at large wavelengths the electromagnetic field of the SPs is weakly "pinned" to the 2DEL, and the position of the 2DEL in the WDSL does not materially affect the SP spectrum. At the
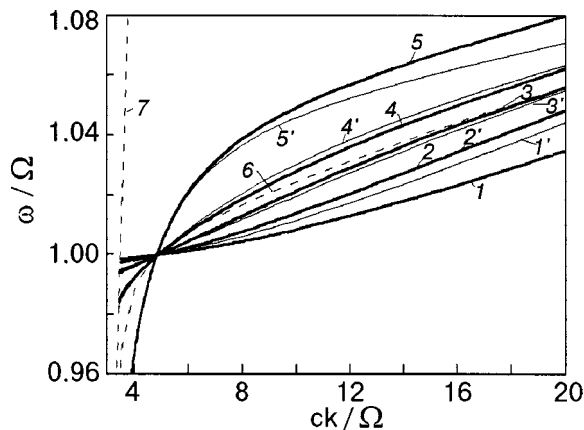
FIG. 2. Spectrum of SPs in a finite WDSL for $\varepsilon_1 = \varepsilon_2 = \varepsilon = 12$, $N = 10$, $\delta = 0.1$, $\tilde{\Delta} = 0.05$, $\nu = 0$, $M = 5$, and $q = 1$.

same time, in the short-wavelength region the difference in the specific spectra in the weakly disordered and ordered superlattices becomes more noticeable. Here the dispersion curves 5 and $5'$, corresponding to SPs with an in-phase oscillation of the electromagnetic field in all the 2DELs, in the long-wavelength limit ($k(M - 1)d \ll 1$) approach the dispersion curve for SPs in an isolated 2DEL with an effective Landau-level filling factor $N_{\rm eff} = MN$. In the low-frequency region ($\omega \ll \Omega$) the phase velocity of the SPs corresponding to dispersion curves 5 and $5'$ is practically equal to v_d. In the vicinity of the cyclotron resonance, however, the phase and group velocities of the SPs decrease sharply, and at frequencies in the region $\omega > \Omega$ they become slow waves. We note that in the case under study the dispersion curve 5 lies at higher frequencies than dispersion curve $5'$. We see from Fig. 2 that the SPs corresponding to dispersion curves $1-4$ and $1' - 4'$ have the following characteristic features. First, they all exist only in the vicinity of the cyclotron resonance and have an end point of termination of the spectrum, $p = 0$, lying on the light line 7. Second, their group velocity is substantially lower than the group velocity of the SPs corresponding to dispersion curves 5 and $5'$. In addition, the dispersion curve 1 (we shall show below that it corresponds to a local SP mode) lies at lower frequencies than dispersion curve $1'$. We note that in the limit $dp \to \infty$, when the neighboring 2DELs do not influence one another, all of the dispersion curves asymptotically approach the dispersion curve for SPs in an isolated 2DEL with $N = 10$ (curve 6).

Let us examine in more detail the dependence of the SP spectrum on the value of the displacement of the 2DEL in the WDSL. This dependence is shown in Fig. 3 for $M = 5$, $N = 10$, $\delta = 0.1$, $\Gamma = 0$, $ck/\Omega = 10$, $\varepsilon = 12$ in the case of the $\varepsilon - \varepsilon - \varepsilon$ geometry for three different choices of the displaced 2DEL, at positions $q = 1$ (a), $q = 2$ (b), and $q = 3$ (c). The dimensionless frequency ω/Ω is plotted along the ordinate, and the dimensionless displacement $\tilde{\Delta} = \Omega\Delta/c$ along the abscissa. We see that the frequency of the SPs corresponding to dispersion curve 1 decreases with increasing $|\tilde{\Delta}|$. We note that the behavior of dispersion curve 1 does not depend on the number of the displaced 2DEL (on the value of q). At the same time the properties of the SPs corresponding to dispersion curve 5 depend strongly on q. For example, for $q = 2$ the SP frequency increases monotonically with increasing $|\Delta|$. For $q = 1$, however, the SP frequency as a function of $\tilde{\Delta}$ has a minimum at $\tilde{\Delta} \approx -0.03$. For $q = 3$ this minimum occurs at $\tilde{\Delta} \approx 0.03$. At the same time, for $q = 2$ the SP frequency (dispersion curves $2-4$) depends weakly on $\tilde{\Delta}$. Analogous behavior is found for the dispersion curves 2 ($\tilde{\Delta} > 0$) and 3 ($\tilde{\Delta} < 0$) for $q = 1$. For $q = 3$ the dispersion curves 2 ($\tilde{\Delta} < 0$) and 3 ($\tilde{\Delta} > 0$) also depend weakly on $\tilde{\Delta}$. We note that the frequency of SPs corresponding to dispersion curve 4 can increase (for $q = 1$) or increase (for $q = 3$) with increasing $\tilde{\Delta}$.

Let us now consider the distribution of the average energy flux of the electromagnetic field of SPs in a finite WDSL. Figure 4 shows the distribution of the x component of the Poynting vector $S_x(z) = (c^2/8\pi)(\mathbf{E} \times \mathbf{H}^*)_x$ for several
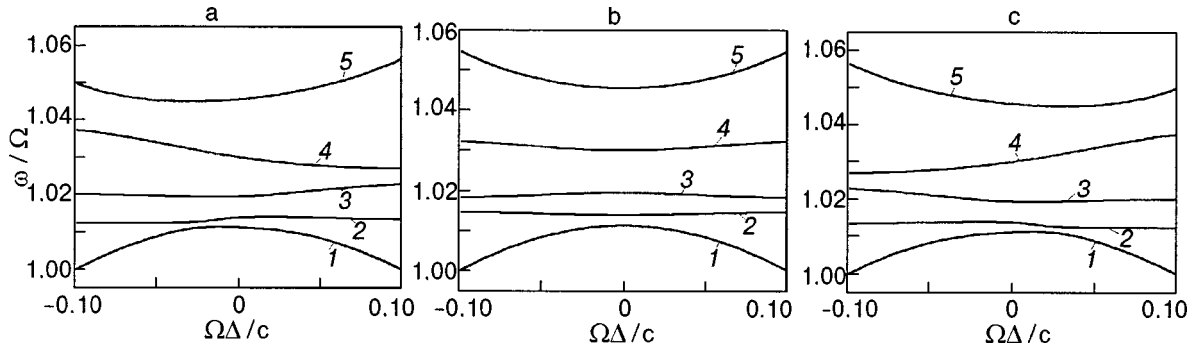
FIG. 3. Dependence of the SP frequency on the displacement Δ in a finite WDSL for $ck/\Omega = 10$, $\varepsilon_1 = \varepsilon_2 = \varepsilon = 12$, $N=10$, $\delta = 0.1$, $\nu = 0$, and $M=5$ for three different choices of the displaced 2DEL, at positions $q=1$ (a), 2 (b), and 3 (c).

SP modes with $ck/\Omega = 10.0$, $\tilde{\Delta} = 0.05$: $q=1$, $\omega/\Omega = 1.00846$ (a), $q=2$, $\omega/\Omega = 1.01438$ (b), and $q=3$, $\omega/\Omega = 1.01976$ (c). Plotted along the abscissa is the dimensionless distance $\chi = zc/\Omega$, and along the ordinate is the dimensionless x component of the Poynting vector $S_x(\chi)/S_x \times (+0)$. The vertical dot-and-dash lines indicate the positions of the 2DELs in the WDSL. The dashed curve in Fig. 4c shows the distribution of $S_x(\chi)/S_x(+0)$ in the OSL.

It is seen in Fig. 4a that practically all of the flux of electromagnetic energy for the SP mode corresponding to dispersion curve *1* (the local SP mode in the WDSL) is concentrated in the smallest gap between 2DELs in the WDSL. This circumstance explains the weak dependence of the frequency of the local SP mode on the number of the displaced 2DEL in the WDSL. Figure 3b and 3c shows the distribution of the energy flux for dispersion curves *2* ($q=2$) and *3* ($q=3$), which coincide with the corresponding dispersion curves for SPs in the OSL. For $q=2$ (Fig. 4b) the main part of the flux of electromagnetic field energy of the SPs is localized in the region $0 < z < d$ (far from the displaced 2DEL). For this reason the value of the displacement Δ does not have a substantial influence on the spectrum of the SP mode corresponding to dispersion curve *2*. For $q=3$ (Fig. 4c) the distribution of the energy flux in the WDSL in the region $z < 3d$ practically coincides with the energy flux distribution in the OSL. We note that in the region $z > 3d$ the value of $S_x/S_x(+0)$ in the OSL exceeds the value of $S_x/S_x(+0)$ in the WDSL. Here, however, the main part of the flux of elec-

tromagnetic field energy of the SPs in the WDSL is concentrated in the region $z < 3d$, and the value of the displacement Δ has almost no influence on the spectrum of the given SP mode.

Let us now examine the influence of dissipation in the 2DEL on the dispersion properties of the SPs. We shall assume that the wave number k is real-valued, while the frequency is complex ($\omega = \omega' + i\omega''$). In this case the variable $p = p' + ip''$ also becomes a complex quantity, and the existence condition for SPs, $\mathrm{Re}\, p = p' > 0$, holds for any values of k (including $k=0$). Figure 5 shows the curves of the dimensionless frequency $\omega'(k)/\Omega$ (solid curves) and dimensionless damping $\omega''(k)/\Omega$ (dashed curves) of SPs as functions of the dimensionless wave number ck/Ω in a finite WDSL with $M=5$, $N=10$, $\delta = 0.1$, $\tilde{\Delta} = 0.05$, and $\varepsilon = 12$ in the $\varepsilon - \varepsilon - \varepsilon$ geometry for $q=1$ and two values of the dimensionless electron momentum relaxation frequency Γ: $\Gamma = 0.1$ (a) and $\Gamma = 0.2$ (b).

We see from Fig. 5a that in the presence of dissipation in the 2DEL the SP spectrum contains, along with the ordinary modes (dispersion curves *1–5*) that exist in the WDSL even in the absence of dissipation, an additional surface polariton (ASP) that corresponds to the dispersion curve *6*. The existence of the ASP when dissipation in the 2DEL is taken into account can be explained by the following circumstance. In the $\Gamma = 0$ case two types of polaritons can exist in the WDSL: surface polaritons (discussed above), which exist under the condition $p^2 > 0$, and bulk polaritons, which exist
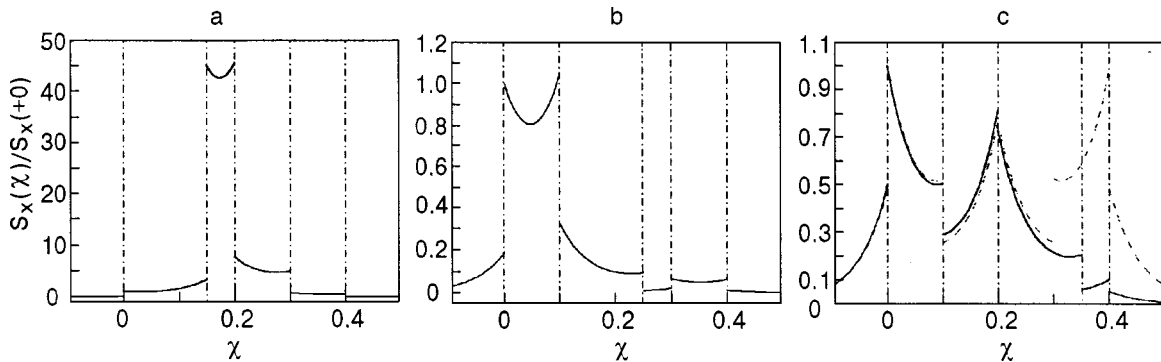

FIG. 4. Distribution of the x component of the Poynting vector $S_x(\chi = \Omega z/c)$ for $ck/\Omega = 10.0$, $\tilde{\Delta} = 0.05$, and several SP modes: $q=1$, $\omega/\Omega = 1.00846$ (a), $q=2$, $\omega/\Omega = 1.01438$ (b), and $q=3$, $\omega/\Omega = 1.01976$ (c).
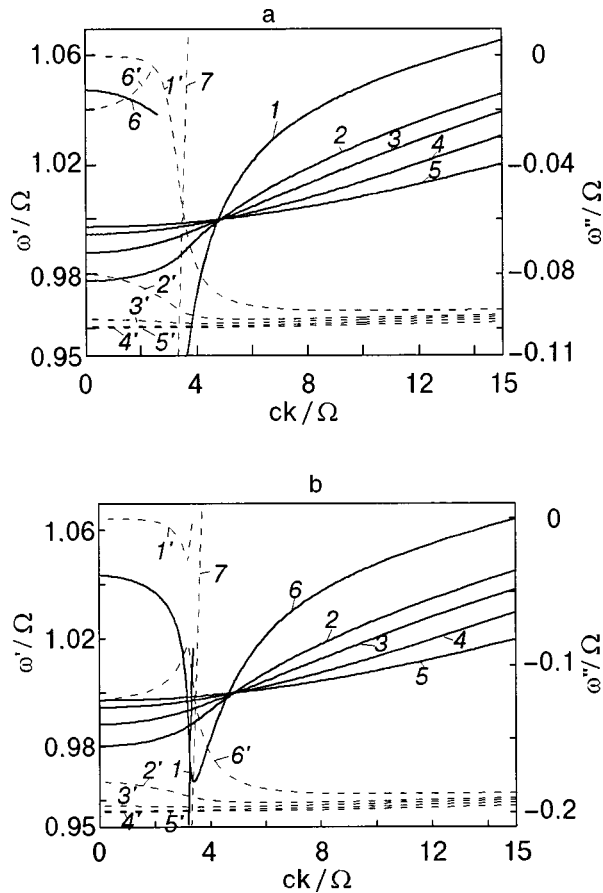
FIG. 5. Spectrum of SPs in a finite WDSL for $\varepsilon_1 = \varepsilon_2 = \varepsilon = 12$, $N = 10$, $\delta = 0.1$, $\tilde{\Delta} = 0.05$, $M = 5$, and $q = 1$ for the cases $\Gamma = 0.1$ (a) and $\Gamma = 0.2$ (b).

FIG. 6. Frequency of the additional surface polariton (ASP) versus the displacement Δ in a finite WDSL for $ck/\Omega = 1.0$, $\varepsilon_1 = \varepsilon_2 = \varepsilon = 12$, $N = 10$, $\delta = 0.1$, $\Gamma = 0.1$, and $M = 5$.

under the condition $p^2 < 0$. When dissipation is taken into account ($\Gamma \neq 0$), the variable p becomes a complex quantity, and the polaritons existing in the WDSL are therefore neither purely surface nor purely bulk. The additional SP is a "quasisurface" polariton, which is "pinned" to the 2DEL owing to the presence of dissipation. Its electromagnetic field is weakly "pinned" to the 2DEL, and in the absence of dissipation it would be a bulk polariton.

It should be noted that the ASP exists only to the left of the light line $\omega' = ck/\sqrt{\varepsilon}$ (dashed line 7). The ASP has an end point of termination of the spectrum which is determined by the condition $p' = 0$. We note that in the entire existence region of the ASP its electromagnetic field is weakly "tied" to the 2DEL, since $p' \ll p''$. At the end point of the spectrum, $p' = 0$, the electromagnetic field of the ASP becomes delocalized. At the same time, the electromagnetic field of an ordinarily SP is strongly "tied" to the 2DEL, since for them $p' \gg p''$. To the left of the light line, however, the electromagnetic field of ordinary SPs also becomes weakly "pinned" to the 2DEL.

Let us discuss the damping of ordinary SPs in more detail (curves $1'$–$5'$). First, in the vicinity of the cyclotron resonance the damping of mode 1 (curve $1'$) increases sharply and reaches a value of the order of Γ. Second, the damping corresponding to dispersion curves 2–5, is practically constant and approximately equal to Γ for all values of the wave numbers. At the same time, the damping of the
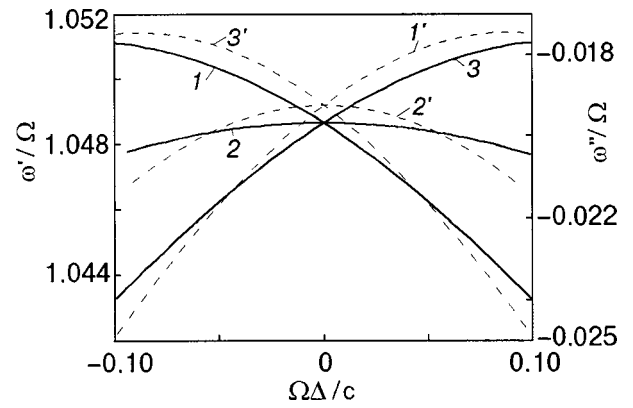
ASP (dispersion curve $6'$) gradually decreases with increasing k, going to zero and at the end point $p' = 0$ of the ASP spectrum.

As Γ increases, the SP spectrum in the WDSL is substantially restructured (Fig. 5b). For example, the fastest SP mode splits into two branches. One of them (dispersion curve 1) practically coincides with the light line and has an end point of the spectrum $p' = 0$. The second branch of SPs in the vicinity of the cyclotron resonance merges with the ASP, forming a continuous dispersion curve 6. This dispersion curve has a minimum near the light line. Here the damping of the fastest SP mode increases sharply in the vicinity of the cyclotron resonance (curve $1'$ is transformed into curve $6'$) and becomes approximately equal to Γ. As Γ increases further, the end point of the spectrum termination point $p' = 0$ for dispersion curve 1 is shifted to lower frequencies, and the minimum on the dispersion curve 6, formed by the merging of the ASP and the slow part of the fastest mode, becomes smoother.

Let us discuss in more detail how the spectrum and damping of the ASP change as the value of the displacement of the 2DEL is varied (at a constant wave number k). Figure 6 gives the corresponding dependence for the case when $ck/\Omega = 1.0$, $N = 10$, $\delta = 0.1$, $\varepsilon = 12$, $\Gamma = 0.1$, and three values of q: 1 (curves 1 and $1'$), 2 (curves 2 and $2'$), and 3 (curves 3 and $3'$). For $q = 1$ the frequency of the ASP (solid curve 1) decreases monotonically as Δ increases, while the damping (the dashed curve $1'$) has a minimum at $\tilde{\Delta} \approx 0.875$. At the same time, for $q = 3$ the frequency of the ASP (curve 3) increases with increasing Δ, and the minimum of the damping curve 3 occurs at $\tilde{\Delta} = -0.875$. We note that for $q = 2$ the curves of the frequency and damping of the ASP have a qualitatively different character: with increasing $|\Delta|$ the frequency of the ASP decreases, while the damping increases.

We emphasize that all of the above-described characteristics of SPs in a finite WDSL are quantized quantities, since the function $N(B)$ under conditions of the IQHE is a steplike function of magnetic field. For this reason the group velocity of the SPs undergoes jumps whose value is determined by the fine structure constant α, the dielectric constants ε, ε_1, and ε_2, and the interlayer distance d and the displacement Δ.

4. CONCLUSION

In summary, the properties of SPs in a finite WDSL under conditions of the integer quantum Hall effect have the following characteristic features. First, all of the dispersion and energy characteristics of the SPs are quantized quantities. Second, in the vicinity of the cyclotron resonance the phase velocity of the SPs decreases sharply, while the group velocity of the SPs undergoes jumplike changes as the magnetic field is changed. The value of the jumps in the SP group velocity is determined by the fine structure constant α, the dielectric constants of the weakly disordered superlattice, the interlayer distance d, and the displacement Δ. Third, the SP spectrum contains a local mode whose electromagnetic field is localized in the gap between the displaced 2DEL and the 2DEL nearest to it. Here the larger the displacement of the 2DEL, the lower the values of the phase and group velocities of the local SP mode in the weakly disordered superlattice.

When the dissipation in the WDSL is taken into account, a new, ''additional'' SP (ASP) arises. The properties of the ASP depend strongly on the value of Γ and the displacement Δ. The dispersion curves of the ASP lie to the left of the light line and have an end point of the spectrum, at which their field becomes delocalized. With increasing Γ the dispersion curve of the ASP merges with the fastest mode of the ordinary SPs. Furthermore, the properties of the ASP depend strongly on the position of the displaced 2DEL in the WDSL. The shorter the distance between one of the outermost 2DELs in the WDSL and the 2DEL adjacent to it, the higher the frequency of the ASP and the greater its damping.

In conclusion, we note that the SPs in finite WDSLs have low phase and group velocities at frequencies of the order of the cyclotron resonance and higher, and for this reason they can be used to make various devices of modern nanoelectronics. For example, the fact that the phase velocity of a SP is small (especially for the local SP mode) can be exploited for the amplification of electromagnetic waves in semiconductor structures by transferring to it the energy of a beam of charged particles (by the principle of the traveling wave tube). Furthermore, the size of the damping and the spectral features of the ASP might be used for the experimental determination of the electron momentum relaxation frequency in 2DELs and the value of the filling factor of the Landau levels.

*E-mail: bludov@ire.kharkov.ua

[1] S. A. Korzh and A. M. Kosevich, Fiz. Nizk. Temp. **7**, 1382 (1981) [Sov. J. Low Temp. Phys. **7**, 669 (1981)].
[2] A. Fetter, Ann. Phys. (N.Y.) **81**, 367 (1973); **88**, 1 (1974).
[3] S. Das Sarma J. J. Quinn, Phys. Rev. B **25**, 7603 (1982).
[4] W. L. Bloss and E. M. Brody, Solid State Commun. **43**, 523 (1982).
[5] G. F. Giuliani and J. J. Quinn, Phys. Rev. Lett. **51**, 919 (1983).
[6] R. E. Camley and D. L. Mills, Phys. Rev. B **29**, 1695 (1984).
[7] R. F. Wallis, R. Szenics, J. J. Quinn, and G. F. Giuliani, Phys. Rev. B **36**, 1218 (1987).
[8] J. K. Jain and P. B. Allen, Phys. Rev. Lett. **54**, 947 (1985).
[9] B. L. Johnson, J. T. Weiler, and R. E. Camley, Phys. Rev. B **32**, 6544 (1985).
[10] E. L. Albuquerque, P. Fulco, G. A. Farias, M. M. Auto, and D. R. Tilley, Phys. Rev. B **43**, 2032 (1991).
[11] B. L. Johnson and R. E. Camley, Phys. Rev. B **38**, 3311 (1988).
[12] M. S. Kushwaha, Phys. Rev. B **36**, 4807 (1987).
[13] W. L. Bloss, J. Appl. Phys. **69**, 3068 (1991).
[14] W. L. Bloss, Phys. Rev. B **44**, 1105 (1991).
[15] V. A. Kosobukin, Fiz. Tverd. Tela (Leningrad) **28**, 1964 (1986) [Sov. Phys. Solid State **28**, 1099 (1986)].
[16] V. M. Gvozdikov, Fiz. Nizk. Temp. **16**, 1156 (1990) [Sov. J. Low Temp. Phys. **16**, 668 (1990)].
[17] P. Hawrylak and J. J. Quinn, Solid State Commun. **59**, 781 (1986).
[18] E. L. Albuquerque, Solid State Commun. **91**, 251 (1994).
[19] J. K. Jain and S. Das Sarma, Phys. Rev. B **35**, 918 (1987).
[20] H. K. Sy and T. S. Chua, Phys. Status Solidi **176**, 131 (1993).
[21] H. K. Sy and T. C. Chua, Phys. Lett. A **169**, 99 (1994).
[22] I. E. Aronov and N. N. Beletskii, J. Phys.: Condens. Matter **8**, 4919 (1996).
[23] I. E. Aronov, N. N. Beletskii, G. P. Berman, and A. R. Bishop, Phys. Rev. B **56**, 10392 (1997).

Translated by Steve Torstveit

Weak localization of low-frequency sound in a quasi-one-dimensional crystal

E. P. Chulkin

Physicotechnical Institute, ul. Kirova 132, 426001 Izhevsk, Russia

A. P. Zhernov* and T. N. Kulagina

Kurchatov Institute Russian Science Center, Institute of Superconductivity and Solid-State Physics, 123182 Moscow, Russia
(Submitted June 23, 1999)
Fiz. Nizk. Temp. **26**, 173–175 (February 2000)

A study is made of the damping coefficient for sound in a dielectric chain crystal containing isotopic impurities at low temperatures $T \leqslant 0.1\Theta_D$ (Θ_D is the Debye temperature). It is shown that in the case of strong disorder, effects due to weak localization of the phonon modes have a substantial influence on the propagation of sound. © *2000 American Institute of Physics.* [S1063-777X(00)00802-1]

1. It was pointed out in Refs. 1–3 that quasilocal levels do not appear in the vibrational spectrum of low-dimensional crystal lattices with diagonal disorder (i.e., with heavy isotopic impurities), unlike the case for weakly anisotropic crystals. Consequently, for the phonon modes in low-dimensional lattices an important role can be played by coherent backscattering processes in the weak localization regime.[4,5] In a recent paper[6] we analyzed the influence of such processes on the frequency and temperature behavior of the damping coefficient of low-frequency sound in layered compounds.

In the present paper we report the results of a study of chainlike compounds. We note that chain crystals can support the existence of specific acoustical modes with displacement vectors oriented parallel and perpendicular to the weakly coupled chains. The vibrational modes of the first type are longitudinally polarized excitations (*l* modes). The modes of the second type are the so-called bending excitations (*b* modes).[7,8] Over a rather wide interval of low frequencies a strongly anisotropy chain crystal can exhibit quasi-one-dimensional dynamical properties. Such modes have been observed, e.g., in experiments on the elastic scattering of neutrons and the low-temperature specific heat in the quasi-one-dimensional compounds $(TaSe_4)_2I$ and $(Ta_{1-x}Nb_xSe_4)_2I$ (Refs. 9 and 10).

For the sake of definiteness we shall assume that the lattice of the quasi-one-dimensional crystal is tetragonal, with unit cell parameters a and b. The interaction efficiency between atoms in the basal plane $xy(\parallel)$ is assumed to be weaker than that along the axes of the chain, $z(\perp)$. For simplicity we also assume that the matrices of the force parameters are diagonal with respect to the Cartesian indices. In this situation there are three characteristic force parameters, which satisfy the inequalities

$$|\Phi_{zz}^{0s_\parallel}| \ll |\Phi_{xx}^{0s_\parallel}| \ll |\Phi_{xx}^{0s_\perp}|. \tag{1}$$

These force parameters correspond to three characteristic frequencies: $\omega_1^2 \ll \omega_2^2 \ll \omega_3^2$. Here the dispersion relations for acoustical longitudinal and bending vibrational modes are:

$$\omega_l^2(\mathbf{k}) = \frac{\omega_\perp^2 b^2 k_\perp^2}{2} + \omega_\parallel^2 \left(\sin^2 \frac{ak_x}{2} + \sin^2 \frac{ak_y}{2} \right), \tag{2}$$

$$\omega_b^2(\mathbf{k}) = \omega_1^2 a^2 k_\perp^2 + \frac{\omega_3^2 b^4 k_\perp^4}{\pi} + \omega_2^2 \left(\sin^2 \frac{ak_x}{2} + \sin^2 \frac{ak_y}{2} \right), \tag{3}$$

where $\omega_3 \approx \omega_\perp$ and $\omega_1 \approx \omega_\parallel$.

2. Let us immediately turn to the question of the absorption of low-frequency sound in chainlike compounds with diagonal disorder. We consider the situation in which when determining the ''bare'' single-particle lattice Green functions constructed for the operators of the dynamic atomic displacements for phonon modes, one can neglect the standard anharmonic interaction of the phonons in comparison with their elastic scattering on defects. For the spatial Fourier components of the Green function we have[8]

$$\bar{G}_{\mathbf{k}}^{+\,\prime j}(\omega) \approx \left(\omega^2 - \omega^2(\mathbf{k}) - i\frac{\omega}{\tau_i^j(\omega)} \right)^{-1},$$

$$\frac{1}{\tau_i^j(\omega)} = \frac{\pi}{2} c\varepsilon^2 \omega^2 g_j(\omega). \tag{4}$$

In Eq. (4) c is the concentration of isotopic defects ($c \ll 1$), $\varepsilon = (M_d - M_0)/M_0$, where M_d and M_0 are the masses of the defect and host atoms (here $M_d \gg M_0$), and $g_j(\omega)$ is the spectral partial density-of-phonon-states function.

According to what we have said, the condition $\tau_N^j \gg \tau_i^j(\omega_T)$, where τ_N^j is the relaxation time associated with normal anharmonic processes. Here we have set the characteristic phonon energy $\omega_T \approx kT/\hbar = \beta^{-1}$.

The above inequality is equivalent to the condition

$$c\varepsilon^2 \gg kT/M_0 v^2 = (10^{-5} - 10^{-4})T, \tag{5}$$

where v is the mean sound velocity.

To determine the temperature-dependent part of the damping coefficient for low-frequency sound (such that $\omega\tau_i^j(\omega_T) \ll 1$), we must find the imaginary part of the polarization operator Π^j of the single-particle lattice Green func-

tion with allowance for the anharmonic interaction of phonons. It can be shown that in the approximation of cubic anharmonicity (see Ref. 6)

$$\operatorname{Im}\Pi^j = \operatorname{Im}\Pi_1^j + \operatorname{Im}\Pi_2^j. \tag{6}$$

The first term describes the correction to the phonon damping on account of the standard anharmonic interaction between acoustical phonons. The second term is due to the interaction of the acoustical mode with the two-phonon coherent states that arise in the weak localization regime.[11,12] Here we have

$$\operatorname{Im}\Pi_1^j(\mathbf{k},\omega) \approx \frac{2\,\widetilde{\gamma}_3^2 \omega \omega_j^2(\mathbf{k})}{T}\sum_{\mathbf{k}_1}\ \omega_j^2(\mathbf{k}_1) n(\omega_j(\mathbf{k}_1))$$

$$\times (n(\omega_j(\mathbf{k}_1))+1)\,\tau_i^j(\omega_j(\mathbf{k}_1)), \tag{7}$$

$$\operatorname{Im}\Pi_2^j(\mathbf{k},\omega) \approx \frac{\widetilde{\gamma}_3^2 b\,\omega \omega_j^2(k)}{2\pi T}\ \int_{\omega_j^0}^{\omega_j^*}\frac{d\omega}{2\pi}\,n(\omega)(n(\omega)+1)$$

$$\times \frac{\omega^2 \tau_i^j(\omega)}{[D_\parallel^{0j}(\omega) D_\perp^{0j}(\omega)]^{1/2}}, \tag{8}$$

$\widetilde{\gamma}_3$ is the effective anharmonicity of the force constant, and $n(\omega)$ is the equilibrium Planckian distribution function of the phonons. In addition, $D_{\parallel(\perp)}^{0j}$ are the tensor components of the bare diffusion coefficient for phonons of the jth polarization:

$$\{D_\parallel^{0j}, D_\perp^{0j}\} = \frac{1}{4\pi g_j(\omega)}\sum_{\mathbf{k}}\ \left\{\frac{\partial \omega_j^2(\mathbf{k})}{\partial k_\parallel}, \frac{\partial \omega_j^2(\mathbf{k})}{\partial k_\perp}\right\}$$

$$\times \bar{G}_{\mathbf{k}}^{(j)+}(\omega)\bar{G}_{\mathbf{k}}^{(j)-}(\omega)$$

($\bar{G}^{+,-}$ are the retarded and advanced Green functions, respectively). Finally, the frequency $\omega_j^0 = \sqrt{2}\omega_{\parallel(2)}$ appearing in Eq. (8) separates the regions of quasi-three-dimensional (a small region of frequencies near zero) and quasi-one-dimensional behavior of the acoustical vibrational spectrum. The frequency ω_j^* determines the threshold of mobility of phonons and is found by setting the true static diffusion coefficient to zero.

It should be emphasized that in the limit of small $\mathbf{k}$ the sum in (7) diverges. It becomes finite if the anharmonic interaction of thermal phonons is taken into account. The mechanism of sound absorption described by expression (7) is important in the intermediate temperature region, where the scattering of thermal phonons is sensitive to defects. As to the expression for $\operatorname{Im}\Pi_2^j$ in the form (8), it is valid in the frequency interval $2\omega_{\parallel(2)}^2 \ll \omega^2 < \omega_{\perp(3)}^2$ in which the dispersion relations (2) and (3) display quasi-one-dimensional behavior. In the derivation of Eq. (8) it was also assumed that the ''coupling'' parameter of the chains, $\omega_{\parallel(2)}$, satisfies the condition $\omega_{\parallel(2)}\tau_i^{l(b)}(\omega) < 1$.

3. The temperature-dependent part of the damping coefficient for sound with the jth polarization can be written as follows with the use of Eqs. (6)–(8):

$$\Gamma^j = \Gamma_1^j + \Gamma_2^j \approx \operatorname{Im}\Pi_1^j(\omega_j(k)) + \frac{\operatorname{Im}\Pi_2^j(\omega_j(\mathbf{k}))}{2\omega_j(\mathbf{k})},$$

where it is understood that $\omega \approx \omega_j(\mathbf{k})$.

To compare the relative contribution of the weak localization effect to the sound damping, let us examine the ratios of Γ_1^j and Γ_2^j. From (7) and (8) we have

$$\frac{\Gamma_2^l}{\Gamma_1^l} \approx c\varepsilon^2 \frac{T}{\Theta_l}\left(\frac{T}{\omega_\parallel}\right)^2, \quad \frac{\Gamma_2^b}{\Gamma_1^b} \approx c\varepsilon^2 \frac{T}{\Theta_b}\left(\frac{T}{\omega_2}\right)^{3/2}, \tag{9}$$

where Θ_j is the Debye temperature of the jth vibrational mode.

Let us now examine expression (9). If the measure of the defect density in the crystal has a value $c\varepsilon^2 \leq 1$ and if $\omega_{\parallel(2)}$ and ω_2, which characterize the intensity of the interaction of the chains, are less than T, then in the low-temperature region $T \leq 0.1\Theta_j$ it is possible to have a situation where $\Gamma_2^j \geq \Gamma_1^j$. In other words, the temperature behavior of the sound damping coefficient is determined by processes of coherent backscattering of thermal phonons.

We note in conclusion that we only know of experimental data on the absorption of sound for the relatively regular quasi-one-dimensional compound $(TaSe_4)_2I$ and the lightly doped system $(Ta_{1-x}Nb_xSe_4)_2I$ (Ref. 13). For comparison of the qualitative results of the theory with experiment, data will be needed for substantially disordered chain crystals.

*E-mail: zhernov@kurm.polyn.kiae.su

[1] D. M. Bercha, M. N. Botvinko, L. Yu. Germanskaya, and M. A. Ivanov, Fiz. Nizk. Temp. **12**, 282 (1986) [Sov. J. Low Temp. Phys. **12**, 162 (1986)].

[2] M. A. Ivanov and Yu. V. Skripnik, Fiz. Tverd. Tela (Leningrad) **32**, 2965 (1990) [Sov. Phys. Solid State **32**, 1722 (1990)].

[3] M. A. Ivanov, A. M. Kosevich, E. S. Syrkin, I. A. Gospodarev, Yu. V. Skripnik, and S. B. Feodos'ev, Fiz. Nizk. Temp. **19**, 434 (1993) [Low Temp. Phys. **19**, 305 (1993)].

[4] A. P. Zhernov and E. P. Chulkin, Fiz. Tverd. Tela (St. Petersburg) **40**, 132 (1998) [Phys. Solid State **40**, 118 (1998)].

[5] A. P. Zhernov and E. P. Chulkin, Zh. Éksp. Teor. Fiz. **113**, 930 (1998) [JETP **86**, 507 (1998)].

[6] E. P. Chulkin, A. P. Zhernov, and T. N. Kulagina, Fiz. Nizk. Temp. **25**, 1218 (1999) [Low Temp. Phys. **25**, 912 (1999)].

[7] I. M. Lifshits, Zh. Éksp. Teor. Fiz. **22**, 475 (1952).

[8] A. M. Kosevich, *Physical Mechanics of Real Crystals* [in Russian], Naukova Dumka, Kiev (1981).

[9] J. E. Lorenzo, R. Currat, A. J. Dianoux, P. Monceau, and F. Levy, Phys. Rev. B **53**, 8316 (1996).

[10] J. E. Lorenzo, R. Currat, P. Monceau, B. Hennion, H. Berger, and F. Levy, J. Phys.: Condens. Matter **10**, 5039 (1998).

[11] A. P. Zhernov and E. P. Chulkin, Zh. Éksp. Teor. Fiz. **109**, 602 (1996) [JETP **82**, 321 (1996)].

[12] A. P. Zhernov and E. P. Chulkin, Phys. Status Solidi B **193**, 67 (1996).

[13] M. Saint-Paul, S. Holtmeier, P. Monceau, R. Currat, and F. Levy, J. Phys. C **8**, 2021 (1996).

Translated by Steve Torstveit

Influence of intrinsic point defects on the electrophysical properties of NbSe₃

A. A. Mamaluĭ, T. N. Shelest, and Kh. B. Chashka

*Kharkov State Polytechnical University, ul. Frunze 21, 310002 Frunze, Ukraine**
(Submitted July 20, 1999; revised August 19, 1999)
Fiz. Nizk. Temp. **26**, 176–180 (February 2000)

The temperature dependence of the electrical resistivity of quasi-one-dimensional NbSe₃ is investigated in the interval 78–550 K in the thermodynamic equilibrium and nonequilibrium states. At temperatures of 300–550 K one observes an exponential deviation from the linear dependence on account of the formation of thermodynamic equilibrium Se vacancies. The influence of intrinsic defects (vacancies) on the properties of NbSe₃ at 78–300 K is investigated by the quenching method. For samples with excess vacancies an anomalously large deviation from the Matthiessen rule (up to 150%) is observed. © *2000 American Institute of Physics.* [S1063-777X(00)00902-6]

INTRODUCTION

Thermodynamic equilibrium vacancies in crystals are a traditional subject for experimental and theoretical research.[1–4] Despite the large number of papers on this subject, however, some of the ideas about the behavior of vacancies under different conditions and the influence of vacancies on the various properties of crystals still remain in dispute.

The formation of vacancies in a state of thermodynamic equilibrium in a highly perfect lattice most often occurs by the Schottky mechanism,[5] when an atom hops from a subsurface lattice site onto the surface by a thermodynamically active process, followed by migration of the vacant site (vacancy) in the bulk of the crystal. Besides the surface, various structural macrodefects (dislocations, pores, grain boundaries) can also serve as sources and sinks for vacancies. Since the relaxation of the lattice consists in the dilatation of the nearest-neighbor atoms toward the vacancy (the ''inhomogeneous'' part of the relaxation) and the extension of the entire lattice (the ''homogeneous'' part), the net change in the volume of the metallic crystal depends importantly on the nature of the sources and sinks. However, this extremely important issue is addressed in only a comparatively small fraction of the experimental papers on vacancies in crystals (see, e.g., Refs. 6 and 7).

In the case of metals the introduction of vacancies is equivalent to the introduction of an electropositive substitutional impurity with an effective valence that takes into account the volume changes. The presence of vacancies leads to corresponding changes in the number of carriers per lattice site and in the Fermi energy, which is reflected in the kinetic, thermodynamic, and superconductive properties. The changes in the vibrational spectrum of a crystal in the presence of vacancies apparently reduce to a ''softening'' of the spectrum, i.e., to an increase in the low-frequency density of states on account of the decrease in density; this agrees qualitatively with the observed values of the entropy of vacancy formation and with experiments on the influence of vacancies on T_c in metals.[7–9]

For crystals with a marked anisotropy of the binding energy, i.e., in crystals of low-dimensional systems, the relaxation of a lattice containing vacancies must also be anisotropic. For quasi-one-dimensional crystals the relaxation of the lattice might be equivalent to a uniaxial extension, which can lead to destruction of the stability of the lattice. Unfortunately, we know of no studies on the behavior of vacancies in low-dimensional systems, even though interest in this topic has risen sharply in connection with the discovery of high-temperature superconductivity.

In this paper we report the first experimental study of the temperature dependence of the electrical resistivity of the well-known quasi-one-dimensional system[10] of NbSe₃ single crystals in the temperature range 78–550 K in both the equilibrium and nonequilibrium (after rapid quenching from high temperatures) states.

EXPERIMENTAL PROCEDURES

Quasi-one-dimensional NbSe₃ (Ref. 10) consists of chains of trigonal prisms of selenium atoms with a niobium atom at the center of each prism. The weakness of the coupling between chains makes this a quasi-one-dimensional compound. The single-crystal samples of niobium triselenide NbSe₃ were grown by the method of chemical gas-transport reactions.[11]

For the measurements the single-crystal samples of NbSe₃ $(0.02–0.05 \times 0.01–0.005 \times 10 \text{ mm})$ were placed on a Sitall devitrified glass substrate on which current and potential leads had been deposited. Electrical contacts were formed by applying a conducting silver paste.

For the experiments in the low-temperature region (78–300 K) we used the measurement cell described in Ref. 12 and a standard platinum resistance thermometer. The temperatures were stabilized to within $\pm 2 \times 10^{-2}$ K or better. At temperatures of 300–550 K the substrate and sample were placed, together with a Chromel–Alumel thermocouple, in a quartz ampoule which, as necessary, could be filled with an inert gas (helium) or evacuated. The quartz ampoule contain-

ing the sample and thermocouple was placed in an oven. During the measurements in the interval 300–550 K the temperature was stabilized to within ± 5 K.

We obtained the temperature dependence of the resistivity of the quasi-one-dimensional single crystal $NbSe_3$ in the interval 78–550 K in thermodynamic equilibrium and nonequilibrium states. The resistance was measured in direct current along the b axis, i.e., along the $NbSe_3$ chains, by a null scheme using the standard four-probe technique. The value of the transport current I was chosen so as to avoid cutoff of the charge density waves and ranged from 10 μA to 2.6 mA.

The samples were quenched both by rapid immersion in alcohol at 293 K and also in air. The base (initial) annealed state was attained by a slow cooling from high temperature at a rate of $dT/dt < 10^{-2}$ K/s. The procedure of annealing after quenching was carried out in isothermal and isochronous modes with holds of the quenched sample at 320–400 K.

EXPERIMENTAL RESULTS AND DISCUSSION

To shed light on the question of whether it is possible to form a thermodynamic equilibrium concentration of vacancies in low-dimensional systems, we did a series of experiments on $NbSe_3$ samples to study the temperature dependence of the electrical resistivity on heating at temperatures from 300 to 550 K. The typical temperature dependence of the resistivity during heating in air is shown in Fig. 1a. In the region 300–420 K a linear temperature dependence of the resistivity is observed, while above T_0 ($T_0 = 420$ K) there is a substantial exponential deviation from the linear dependence.

It should be noted that in a number of cases the size and character of the deviations from the linear dependence were noticeably altered. This was ordinarily observed at a sample temperature $T_1 \gtrsim 500$ K and was manifested in an extremely strong scatter of the resistivity values. Varying the composition of the heating medium (vacuum, air, gaseous helium) had only a slight effect on the size of the deviation and the value of the temperature at which the deviation began ($T_0 = 420 \pm 10$ K). The temperature T_1 above which the scatter was observed was also practically constant. The presence of the scatter is apparently due to local melting of the crystal or to the fluctuational formation of large coagulates of defects. It cannot be ruled out that nonstoichiometric selenium vacancies are formed as a result of the emergence of Se atoms to the surface and their subsequent evaporation. In principle there could also be a contribution due to intercalation of the gas from the heating medium, but holding the samples for several hours in the media used did not produce any systematic changes in the $R(T)$ curves. We note that when the sample was heated to temperatures $T > T_1$ the behavior of the temperature dependence of the resistivity was ordinarily irreversible on heating and cooling. In the region $T_0 < T < T_1$ the change of the resistivity with temperature was reversible.

It is known that for three-dimensional metallic systems at pre-melting temperatures an exponential deviation of the properties from a linear temperature dependence is observed
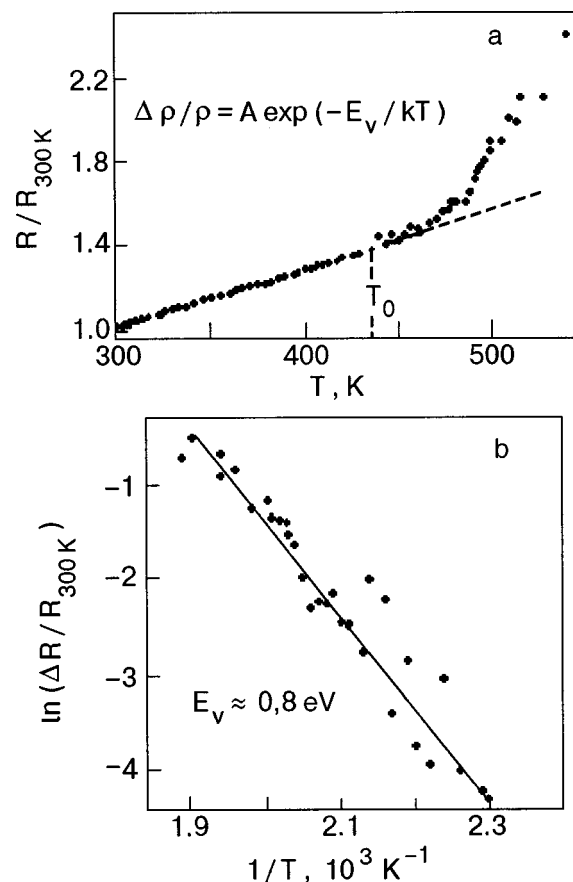

FIG. 1. Temperature dependence of the resistance (a) and the relative increment in resistance in semilogarithmic coordinates (b) for samples of single-crystal $NbSe_3$ in the region 300–550 K.

on account of the formation of thermodynamic equilibrium vacancies.[1-4] It is natural to suppose that the deviation from a linear temperature dependence of the resistivity of $NbSe_3$ in the present study is due to the formation of thermodynamic equilibrium vacancies.

Figure 1b shows a semilogarithmic plot, $\ln(\Delta\rho/\rho) = f(1/T)$, of the dependence of the resistivity obtained in the present study. It is clear that the deviation from a linear temperature dependence has an exponential character, as is typical for thermally activated processes. The activation energy is $E_v = 1 \pm 0.2$ eV. The error was determined by the scatter of the data of different experiments.

An estimate of the energy of vacancy formation E_v in a simple approximation of the binding energy shows that the exponential deviation from linearity in the temperature dependence of the resistivity of quasi-one-dimensional $NbSe_3$ is predominantly due to the formation of thermodynamic equilibrium selenium vacancies.

To investigate the influence of intrinsic point defects (vacancies) on the properties of the $NbSe_3$ crystal at comparatively low temperatures we performed quenching as follows. A sample was held in the oven for 1 hour at $T_q = 323$, 373, and 463 K, and then taken out into the air or immersed in alcohol. The rate of cooling was $\leqslant 10^2$ K/s.

In experiments on the quenching of high-temperature thermodynamic equilibrium lattice defects it is essential to
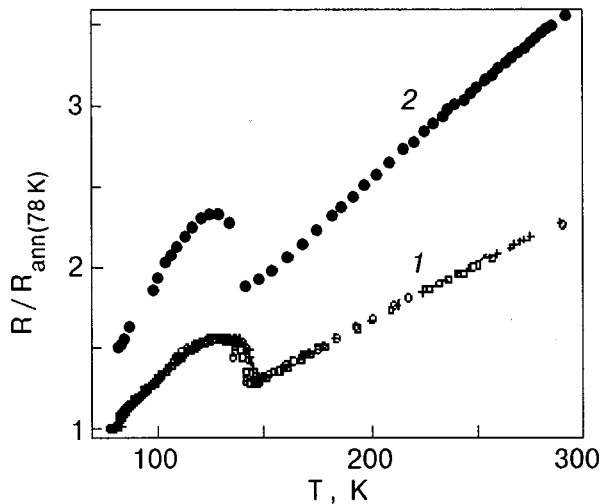
FIG. 2. Temperature dependence of the resistance of NbSe$_3$ samples in the thermodynamic equilibrium (*2*) and nonequilibrium (*1*) states in the interval 78–300 K: annealed (○); quenched from temperatures T_q, K: 327 (+), 373 (□), 463 (●).

follow correct cooling procedures. The rate of quenching must not exceed a maximum rate set by the onset of appreciable thermal stresses. Ordinarily in correctly performed experiments, after the fixing of the high-temperature concentration and distribution of vacancies in the sample (see below) and the subsequent restoration of the sample (by annealing at higher temperatures $T \approx T_D$) the physical properties being investigated undergo reversible changes. In this study we rarely observed a reversible recovery of the resistivity of the NbSe$_3$ samples. The residual resistivity after restoration of the sample was as high as 10% of the quenching-related increase. In the case of quenching from $T_q > T_1$ the reversible part of the resistivity was not more than 60%, which is consistent with the conjecture that stable macrodefects (coagulates) are formed in this temperature region or, possibly, that a local melting of the lattice occurs, which corresponds to the results in Ref. 13.

Figure 2 shows the temperature dependence of the resistivity of samples in the quenched and annealed states in the interval 78–300 K. On all of the curves obtained in the temperature region 78–145 K there is a characteristic phase transition of the charge-density wave type. For the annealed samples the charge-density wave is realized at $T_{CDW} = 145$ K, which agrees with the known values ($T_{CDW} = 145$ K).[10]

Curve *1* in Fig. 2 was obtained for an annealed sample of NbSe$_3$ (○) and for samples quenched from 323 and 373 K. These temperatures were chosen lower than the temperature at which the defect-induced deviation from a linear temperature dependence of the resistivity begins (Fig. 1). We see that the results are in good agreement, which attests to the correctness of the quenching (since there is practically no contribution from quenching stresses). Curve *2* was obtained for quenching from $T_q = 463$ K. It is characterized by a larger value of the resistivity at $T = 78$ K, a larger slope of the rectilinear part than on curve *1*, an appreciable lowering of the value of T_{CDW} ($\Delta T = -2$ K), and a larger value of the

''amplitude'' of the change in resistivity at the charge-density wave.

Analysis of the contribution of vacancies to the temperature dependence of the resistivity $\rho(C,T)$ is conveniently done in terms of the deviation from the Matthiessen rule (see, e.g., Ref. 14):

$$\rho(C,T) = \rho_{id}(T) + \rho_0(C) + \Delta(C,T), \tag{1}$$

where $\rho_{id}(T)$ is the resistivity of an ideal sample, $\rho_0(C)$ is the residual resistivity of the sample, and $\Delta(C,T)$ is a function describing the temperature and concentration dependence of the deviation from the Matthiessen rule.

When measurements are made on the same sample, the following relation can be used to good accuracy (less than 1% error):

$$\frac{\Delta(C,T)}{\Delta\rho_{78}} = \frac{\Delta R_T - \Delta R_{78}}{\Delta R_{78}}, \tag{2}$$

where ΔR_T is the difference of the resistances of the quenched and annealed sample at temperature T, and ΔR_{78} is that at 78 K. The accuracy of this relation is limited by the fact that it neglects the influence of the change in the dimensions of the sample containing vacancies in comparison with the sample without vacancies.

Figure 3 shows the temperature dependence of the function $\Delta(C,T)/\Delta\rho_{78}$ for the NbSe$_3$ sample after quenching from 463 K. One notices the positive value of $\Delta(C,T)$ in the entire temperature region and the presence of a maximum at 130 K (the maximum is shifted relative to the maximum on curves *1* and *2* (Fig. 2). For $T > 140$ K the deviation from the Matthiessen rule (DMR) increases practically linearly with temperature. The DMR is anomalously large in comparison with the deviations ordinarily observed in three-dimensional metals and reaches 150% at $T = 293$ K.

Since the electronic spectrum of quasi-one-dimensional single-crystal NbSe$_3$ is anisotropic, one can assume that the deviation from the Matthiessen rule is predominantly due to a lifting of the anisotropy of the electron distribution function in the scattering of conduction electrons on vacancies
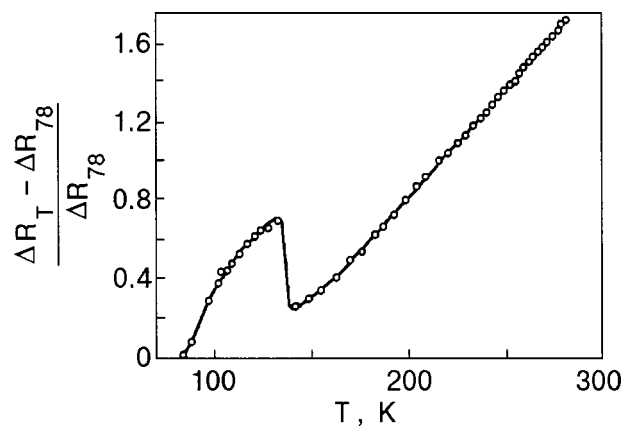

FIG. 3. Deviation from the Matthiessen rule in quenched ($T_q = 463$ K) samples of NbSe$_3$.

and to the valence effect arising as a result of the difference in the valence of the ''impurity'' and host atoms, as was shown in Refs. 3 and 4.

CONCLUSION

We have investigated experimentally the temperature dependence (at 78–550 K) of the resistivity of the quasi-one-dimensional single crystal $NbSe_3$ along the chains for thermodynamic equilibrium and nonequilibrium vacancy concentrations. In the temperature region 300–550 K an exponential deviation from the linear temperature dependence is observed at $T > T_0$ ($T_0 = 420 \pm 10$ K), which is due to the formation of thermodynamic equilibrium Se vacancies. The activation energy of Se vacancies was 1 ± 0.2 eV.

We found that the fixing of the high-temperature concentration of vacancies leads to a substantial change in the temperature dependence of the resistivity of $NbSe_3$, and this is manifested in large values of the deviation from the Matthiessen rule (up to 150%). For quenching from $T_q < T_0$ the heat treatment had no influence on the temperature dependence of the resistivity.

*E-mail: krio@kpi.kharkov.ua

[1] A. C. Damask and G. J. Dienes, *Point Defects in Metals* [Gordon and Breach, New York (1963); Mir, Moscow (1966)].

[2] R. Lannoo and J. Borgoin, *Point Defects in Semiconductors I* [Springer-Verlag, New York (1981); Mir, Moscow (1984)].

[3] W. A. Harrison, *Pseudopotentials in the Theory of Metals* [Benjamin, New York (1966); Mir, Moscow (1968)].

[4] W. A. Harrison, ''The theory of interatomic potentials in solids,'' in *Interatomic Potentials and Simulation of Lattice Defects* (Battelle Institute Materials Science Colloquia (6th), Seattle, Wash., June 14—16, 1971), edited by P. C. Gehlen, J. R. Beeler, and R. I. Jaffe, Plenum Press, New York (1972) [Usp. Fiz. Nauk **108**, 270 (1972)].

[5] G. Schottky, Z. Phys. **159**, 584 (1960).

[6] R. O. Simmons and R. W. Ballufi, Phys. Rep. **129**, 1533 (1963).

[7] A. A. Mamalui, V. A. Pervakov, and V. Y. Khotkevich, Phys. Status Solidi **29**, 21 (1975).

[8] A. A. Mamaluĭ and S. O. Ovcharenko, Fiz. Tverd. Tela (Leningrad) **31**, 171 (1989) [Sov. Phys. Solid State **31**, 1934 (1989)].

[9] A. A. Mamaluĭ, V. A. Pervakov, and V. I. Khotkevich, Fiz. Nizk. Temp. **1**, 318 (1975) [Sov. J. Low Temp. Phys. **1**, 156 (1975)].

[10] P. Monceau (ed.), *Electronic Properties of Inorganic Quasi-One-Dimensional Compounds*, Vol. 2, Reidel, Dordrecht–Boston–Lancaster (1985).

[11] Kh. B. Chashka, V. A. Bichko, M. A. Obolenskiĭ, R. Hasan, V. I. Beletskiĭ, and Fiz. Nizk. Temp. **24**, 47 (1998) [Low Temp. Phys. **24**, 35 (1998)].

[12] A. A. Mamaluĭ and A. N. Medyanik, Prib. Tekh. Éksp. , No. 5, 217 (1981).

[13] K. Svoboda, A. Zettl, and M. S. Sherwin, Solid State Commun. **70**, 859 (1989).

[14] R. J. Berry, Phys. Rev. **6**, 2994 (1972).

Translated by Steve Torstveit

Commensurate–incommensurate phase transitions for multichain quantum spin models: exact results

A. A. Zvyagin*

B. Verkin Institute for Low Temperature Physics and Engineering of the National Academy of Sciences of Ukraine, 47 Lenin Ave. Kharkov, 61164, Ukraine

The behavior in an external magnetic field is studied exactly for a wide class of multichain quantum spin models. It is shown that the magnetic field together with the interchain couplings cause commensurate–incommensurate phase transitions between the gapless phases in the ground state. The conformal limit of these models is studied and it is shown that the low-lying excitations for the incommensurate phases are not independent, because they are governed by the same magnetic field (chemical potential for excitations). A scenario for the transition from one to two space dimensions for the exactly integrable multichain quantum spin models is proposed, and it is shown that the incommensurate phases in an external magnetic field disappear in the limit of an infinite number of coupled spin chains. The similarities in the external field behavior for the quantum multichain spin models and a wide class of quantum field theories are discussed. The scaling exponents for the appearance of the gap in the spectrum of low-lying excitations of the quantum multichain models due to the relevant perturbations of the integrable theories are calculated. © *2000 American Institute of Physics.*
[S1063-777X(00)01002-1]

1. INTRODUCTION

There has recently been considerable interest in low-dimensional quantum-correlated spin and electron systems. These systems, especially one-dimensional (1D), manifest the specific features of, e.g., magnetic behavior at low temperatures, which are absent for the standard, conventional 3D magnetic systems. Spin systems usually manifest 1D behavior at temperatures higher than the temperature of the 3D magnetic ordering but lower than the maximum characteristic energy of the interaction between spins, i.e., in our case the intrachain spin–spin coupling. The origin of such specific features is the enhancement of the quantum fluctuations of the 1D systems due to the peculiarities of the 1D density of states together with the quantum nature of spins.

Moreover, during the last decade a large number of new quasi-1D spin compounds have been created and studied experimentally. These compounds manifest at low temperatures the properties of a single quantum spin chain or several quantum spin chains weakly coupled to each other.[1,2] It is strongly believed that this class of compounds will provide new information on the transition from 1D to 2D in quantum many-body physics. This is very important, because the 2D quantum many-body physics has been a challenge for both theorists and experimentalists since the beginning of the study of low-dimensional quantum systems. On the other hand, the advantage of the 1D theoretical studies is the possibility of obtaining exact solutions by using nonperturbative methods, which are difficult to apply for the higher-dimensional quantum many-body models. The results of the exact calculations of the 1D models can serve as testing grounds for the use of perturbative and numerical methods in more realistic situations.

Recently several exactly solvable models[3–5] have been introduced, in which the zigzag-like interaction between two quantum spin chains was studied exactly using the Bethe ansatz technique.[6] This method is widely known by now, see, e.g., the recent monograph[7] and references therein. The Bethe ansatz method permits exact calculation of the static characteristics of quantum many-body systems, such as the ground state behavior, the influence of an external magnetic field, and the thermodynamic features of the temperature dependence of the specific heat, magnetic susceptibility, etc. These results should apply to more-realistic systems, but it is not obvious how the interactions between the chains modify the answers. The mean-field-like approximations for the interchain couplings are not sufficient, because the mean field approach in any version already implies the existence of a (sometimes hidden) order parameter. It is, unfortunately, also unclear whether the numerical calculations, which can be directly applied for quantum many-body systems of very small sizes, by now (using at most, several tens of sites) describe well the properties of real systems, in which, even in quasi-1D ones, the number of sites is at least of order 10^8. On the other hand, it must be admitted that some features of the exactly solvable 1D models are far from what is observed experimentally, but these unrealistic features of the 1D models are known and simple to recognize.

The behavior of multichain spin systems in an external magnetic field is especially interesting (see, e.g., Refs. 5, 8–10) because of (i) the possibility of experimental observations due to recent progress in high-magnetic-field measurements, and (ii) very interesting theoretically predictable ef-

fects which are possible to recognize in experiments, such as phase transitions in the external magnetic field. However, several important issues are far from being resolved in the quantum two-chain spin models. For example, there are three questions that need to be answered: (1) Are the properties of those exactly solvable two-chain spin models unique or is it possible to say something about the more general class of two-chain quantum spin models? (2) How are the multichain quantum models connected to the 2D many-body systems, i.e., what is the scenario of the transition from 1D to 2D when one increases the number of coupled chains while keeping the conditions of integrability? (3) What will happen with the behavior of the nonintegrable multichain spin models if one goes beyond the frame-work of integrability, i.e., by adding some perturbations to the exactly solvable model? (For example, Ref. 10 implies that it is namely the spin chirality, which separately breaks the time-reversal and parity symmetries in the two-chain integrable model,[11] that is the reason for the emergence of the additional phase transitions in an external magnetic field for the two-chain spin-1/2 model as compared to the single-chain system.)

The goal of this paper is to answer these questions. First, we revisit the exactly integrable two-chain spin-1/2 model and show that the inclusion of magnetic anisotropy of the ''easy-plane'' type, for which the system stays in the quantum critical region, will not drastically change the behavior in an external magnetic field but will shift the critical values of the magnetic fields and intrachain couplings at which the phase transitions occur and will affect the critical exponents. We will show that these two-chain spin models share the most important features of the behavior in an external field with the wide class of $(1+1)$ quantum field theories. Next, we will introduce the higher-spin versions of the two-chain spin models, e.g., investigating the important class of 1D two-chain quantum ferrimagnets with different spin values at the sites of each chain. We will also investigate the behavior of the exactly solvable multichain spin models in an external magnetic field and show how the additional phase transitions arising due to the increasing number of chains vanish in the quasi-2D limit. Finally, we will show how the relevant deviations from integrability, e.g., the absence of terms in the Hamiltonian which separately break the parity and time-reversal symmetries, give rise to gaps in the spectra of low-lying excitations of multichain quantum spin systems, and we will calculate the scaling exponents for the gaps.

The paper is organized as follows. In Sec. 2 we revisit the exactly solvable two-chain uniaxial spin model[4] to remind the reader of the main steps of the Bethe ansatz. The investigations[9,10] of isotropic spin-1/2 two-chain models are generalized in this section for the case of uniaxial magnetic anisotropy. The calculations in this section are rather simple, but we will write them in detail because they provide the basis for the more nontrivial generalizations of this class of models, and will be used in the following sections. In Section 3 we point out the similarities between the behavior of the uniaxial two-chain quantum spin models and a class of quantum field theories (QFT) in an external magnetic field, predicting new phases for the QFT. In Sec. 4 we introduce the $SU(2)$ generalization of the integrable two-chain model

for higher values of the site spins (possibly different) in each chain, i.e., a quantum ferrimagnet. We point out the similarities of the quantum ferrimagnet with QFT in the case of a nonzero Wess–Zumino term and predict new phases for the latter in an external magnetic field. We derive integral equations for the critical exponents. In Sec. 5 we consider the multichain quantum spin model and discuss how the external field behavior of the integrable multichain models is changed when the number of chains is increased while preserving the exact solvability. In Sec. 6 we briefly sketch how the deviations from integrability change the magnetic and low-temperature properties of this class of multichain quantum spin systems. We close with a discussion of the main results and some conclusions.

2. TWO-CHAIN UNIAXIAL QUANTUM SPIN MODEL

A common property of some of the Bethe ansatz solutions is the presence of shifts θ_j of the spectral parameter λ for the associated transfer matrix of an algebraic version of the Bethe ansatz (the quantum inverse scattering method (QISM[7]). Those shifts also appear in the Bethe ansatz equations (BAE) for the quantum numbers called rapidities, which parametrize the eigenfunctions and eigenvalues of the Hamiltonians. Hence, the distributions of the rapidities are also affected by the shifts. An interesting property is connected with those shifts: depending on their values and the external magnetic field, even for (quasi)particles of the same type, additional minima may appear in distributions of the rapidities. These additional minima also result in nonmonotonic behavior of the dispersion relations of the low-lying excitations. Also, they provide additional Dirac seas for low-lying excitations, changing the structures of the physical ground states of the models. These additional minima determine the special behavior of the models in an external magnetic field.[3,5,9,10] In particular, the appearance of new phases and new phase transitions is due to the emergence of these new minima in the distributions of the quantum numbers.

To set the stage, let us first remind the reader about the main steps of the QISM. The common feature of the Bethe-ansatz-solvable models is the factorization of the monodromy matrix (the ordered product of all two-particle scattering matrices, which depend on some spectral parameter).[7] Exact (Bethe ansatz) integrability requires exclusively elastic scattering between (quasi)particles. For such theories the two-particle scattering matrices and L operators satisfy the Yang–Baxter relation.[7,12] In turn, the factorization of the monodromy matrices guarantees that they satisfy the Yang–Baxter equations, too. The transfer matrices of the associated statistical problem are traces over some additional, auxiliary subspace of monodromy matrices.[7] The most important feature of transfer matrices with different spectral parameters is their commutativity. A necessary and sufficient condition for this is the validity of the Yang–Baxter equations for the two-particle scattering matrices and hence for the monodromy matrices. The commutativity of the transfer matrices implies that one can construct an infinite number of integrals of motion, which commute with one another and with the transfer matrix. Therefore the exact integrability is proved.

Usually the structure of these integrals of motion is determined by their locality. For instance, the best-known of series of integrals of motion is the series of derivatives with respect to the spectral parameter of the logarithm of a transfer matrix taken at some special value of the former.[7] Locality means that for the first derivative of the logarithm of the transfer matrix (usually called the Hamiltonian of the lattice system) only short-range particle–particle interactions contribute.

In this paper we will see that namely the aforementioned shifts of the spectral parameters yield new phases in the ground state behavior in an external magnetic field for a wide class of exactly solvable models, quantum spin multichain models, and QFT. We will show that in the conformal limit these phases of the lattice models correspond to one Wess–Zumino–Witten (WZW) model or to several of them with dressed charges (proportional to the compactification radii) of scalar or matrix types for each of the phases, respectively.

Let us start with the form of the Bethe ansatz equations (BAE) for the set of rapidities $\{u_\alpha\}_{\alpha=1}^M$. In this paper we will concentrate only on the critical, easy-plane type of magnetic anisotropy for the antiferromagnetic spin multichain models, $0 \leqslant \gamma \leqslant \pi/2$ ($\gamma = \pi/q$, where q is an integer parametrizing the magnetic anisotropy), and the repulsive interactions in QFT. This corresponds to hyperbolic or rational solutions of the Yang–Baxter equations for the two-particle scattering matrices, or to $U(1)$ and $SU(2)$ symmetries of the scattering processes, respectively. For the simplest case of one shift θ, which pertains to the two-chain quantum spin models and to most QFT, the BAE have the form (here we use the more general hyperbolic parametrization first; for the rational limit see below)[4]

$$\prod e_1^{N_\pm}(u_\alpha \pm \theta) = e^{i\pi M} \prod_{\beta=1,\beta \neq \alpha}^M e_2(u_\alpha - u_\beta), \quad (1)$$

where $N_\pm$ are the numbers of sites in each of the spin chains; $e_n(x) = \sinh(x + i\gamma n/2)\sinh(x - i\gamma n/2)^{-1}$; and M is the number of down spins. The shift θ determines the interchain coupling constant for two-chain quantum spin-1/2 models.[4,11,13] Please note that the Bethe ansatz equations are just the quantization conditions for the rapidities, which parametrize the eigenwaves and eigenvalues of the many-body quantum model. The Hamiltonian is the first derivative of the logarithm of the transfer matrix (note that the transfer matrix of the two coupled spin chains in this integrable model is the product of the two standard transfer matrices of each chain with the spectral parameters $\lambda \pm \theta$:[11]

$$\hat{H}_{1/2} = \frac{1}{\sinh^2 \theta + \sin^2 \gamma} \sum_n (\cos \gamma \sinh^2 \theta(\mathbf{S}_{n,1} \cdot \mathbf{S}_{n+1,1}$$

$$+ \mathbf{S}_{n,2} \cdot \mathbf{S}_{n+1,2}) \, 2 \sin^2 \gamma \hat{I} \mathbf{S}_{n,1} \cdot (\mathbf{S}_{n,2} + \mathbf{S}_{n+1,2})$$

$$\times 2 \sin \gamma \sinh \theta(\hat{J}\mathbf{S}_{n+1,2} - \hat{J}\mathbf{S}_{n,1}) \cdot [\mathbf{S}_{n+1,1} \times \mathbf{S}_{n,2}]), \quad (2)$$

where

$$\hat{I} = \mathrm{diag}(\cosh \theta, \cosh \theta, \cos \gamma)$$

and $\hat{J} = \mathrm{diag}(\cos \gamma, \cos \gamma, \cosh \theta)$, $\mathrm{diag}(a,b,c)$ is a 3×3 diagonal matrix, and $[\times]$ denotes the vector product. Please note that the sum runs over n to N_+ for the chain with spins $S_{n,1}$ and to N_- for the chain with spins $S_{n,2}$. The parameter θ determines the intrachain coupling in our two-chain spin model. For $\theta = 0$ the Hamiltonian and BAE coincide with the ones for the single easy-plane antiferromagnetic spin-1/2 chain of length $N_+ + N_-$ with only nearest-neighbor interactions in it. The eigenvalue of the Hamiltonian (energy) is parametrized as a function of the rapidities as follows:

$$E = \sin \gamma \sum_\pm \sum_{\alpha=1}^M N_\pm [e_1(u_\alpha \pm \theta) + e_1^{-1}(u_\alpha \pm \theta)] + E_0, \quad (3)$$

where E_0 is the energy of the vacuum (ferromagnetic) state (with $M = 0$). The isotropic SU-symmetric antiferromagnetic quantum spin two-chain model[9,10,11,13] can be obtained from the uniaxial ($U(1)$-symmetric) one in Eqs. (1)–(3) by the simple change of variables in the limit: $u_\alpha \to \gamma u_\alpha$, $\lambda \to \gamma\lambda, \theta \to \gamma\theta, \gamma \to 0$. (The last limit corresponds to the rational, $SU(2)$-symmetric solution of the Yang–Baxter equations for the two-particle scattering matrices.) The two-chain isotropic ($SU(2)$-symmetric) spin-1/2 Hamiltonian obtained in this limit from Eq. (2) takes the form[4,9,10,11,13]

$$\hat{H}_{\mathrm{is}} = \left(\frac{1}{1+\theta^2}\right) \sum_n (\theta^2(\mathbf{S}_{n,1} \cdot \mathbf{S}_{n+1,1} + \mathbf{S}_{n,2} \cdot \mathbf{S}_{n+1,2}) + 2\mathbf{S}_{n,1}$$

$$\cdot (\mathbf{S}_{n,2} + \mathbf{S}_{n+1,2}) + 2\theta(\mathbf{S}_{n+1,2} - \mathbf{S}_{n,1}) \cdot [\mathbf{S}_{n+1,1}\mathbf{S}_{n,2}]). \quad (4)$$

The summations over n run to $N_\pm$ for each kind of spin, respectively. Note that for $\theta \to \infty$ Eq. (4) and the BAE recover the Hamiltonian and BAE of two decoupled spin-1/2 chains of lengths $N_\pm$ with the only nearest-neighbor interactions in each of the chains.

The solution to the BAE (1) is usually obtained in the thermodynamic limit ($N_\pm, M \to \infty$, with the ratio $M/(N_+ + N_-)$ fixed). Here instead of the discrete set of rapidities one introduces the distribution of a continuous density of rapidities. The ground state corresponds to the solutions of the BAE with negative energies, i.e., it is connected with the filling up of the Dirac sea(s) for the model. For the easy-plane antiferromagnetic two-chain spin-1/2 model the ground state corresponds to the filling of the Dirac sea for real rapidities, i.e., no spin bound states have negative energies. In the thermodynamic limit the real roots of Eq. (1) are distributed continuously over some intervals, which determine the Dirac seas of the model. The set of integral equations for the dressed densities of the rapidities $u_\alpha(\rho(u))$ and dressed energies of the low-lying quasiparticles ($\varepsilon(u)$) are (see, e.g., Ref. 7 for the standard procedure of deriving these integral equations from the BAE and Refs. 11 and 13 for the isotropic two-chain spin-1/2 model)

$$\rho(u)+\int_{(Q)}dv\,K(u-v)\rho(v)=\sum_{\pm}\frac{N_{\pm}}{N}\rho_{\pm}^{0} \qquad (5)$$

and

$$\varepsilon(u)+\int_{(Q)}dv\,K(u-v)\varepsilon(v)=h-\sum_{\pm}\frac{N_{\pm}}{N}\varepsilon_{\pm}^{0}, \qquad (6)$$

where the kernels of the integral equations are

$$K(u)=\frac{\partial\ln e_{2}(u)}{\partial u}=\frac{\sin(2\gamma)}{2\pi[\cosh(u)-\cos(2\gamma)]}, \qquad (7)$$

and h is an external magnetic field. The values

$$\rho_{\pm}^{0}(u)=\frac{\partial\ln e_{1}(u\pm\theta)}{\partial u}\equiv\frac{\partial p_{\pm}^{0}(u)}{\partial u}$$

$$=\frac{\sin\gamma}{2\pi[\cosh(u\pm\theta)-\cos\gamma]} \qquad (8)$$

are bare densities of the rapidities, and

$$\varepsilon_{\pm}^{0}(u)=h-\frac{\sin^{2}\gamma}{\cosh(u\pm\theta)-\cos\gamma} \qquad (9)$$

are bare energies (here ''bare'' corresponds to non-interacting particles, and the interaction ''dresses'' them as usual[7]). The integrations are performed over the domain (Q), determined in such a way that the dressed energies inside these intervals are negative. The limits of integration are determined by the zeros of the dressed energies and are the Fermi points for each sea. Analysis of the integral equations (5) and (6) in an external magnetic field shows that in general, for some values of θ and h, there can be one Dirac sea (it corresponds to one minimum of the bare densities of the rapidities and, hence, to one minimum of the bare energy). On the other hand, for higher values of θ and for some domain of h, two Dirac seas of the same type (gapless, see below) of excitations are possible (for two minima of the bare energies of the rapidities and thus two minima of the bare density). Note that for $\theta\to\infty$ at fixed $N_{\pm}$ all the roots of the integral BAE separate into two sets of ''right-'' and ''left-moving'' seas, centered at $\pm\theta$, respectively.

Here we briefly revisit the analysis of Refs. 9 and 10, but for the case of the uniaxial two-chain model. Analytical solutions to Eqs. (5) and (6) can be easily obtained in closed form in the limit of zero field and equal lengths of the chains $N_{+}=N_{-}$. The simplest nontrivial exited quasiparticle (spinon) is a hole in the Dirac sea for real rapidities, with the quasimomentum

$$p(u_{0})=2\arctan\left(\frac{\sinh(\pi u_{0}/\gamma)}{\cosh(\pi\theta/\gamma)}\right), \qquad (10)$$

where u_{0} is the spinon's rapidity. Note that for topological reasons such particles have to exist in pairs for the $SU(2)$-symmetric case, etc.[14,15] The energy of this spinon is given by

$$\varepsilon(u_{0})=-\sin\gamma\frac{\partial p(u_{0})}{\partial u_{0}}. \qquad (11)$$

It can be rewritten as a function of the quasimomentum, i.e., in the form of the commonly used dispersion relation

$$\varepsilon(p)=\frac{\pi}{\gamma}\sin\gamma\tanh\frac{\pi\theta}{\gamma}\sin\frac{p}{2}\left[\cos^{2}\frac{p}{2}+\sinh^{-2}\frac{\pi\theta}{\gamma}\right]^{1/2}. \qquad (12)$$

A spinon corresponds in the usual Bethe ansatz classification[7] of BAE solutions to a string of length 1. Naturally Eq. (1) have string solutions of higher lengths too. Other spin excitations can be obtained as combinations of spinon quasiparticles and higher-length strings with different rapidities. However, spinons here are picked out because only their dressed energies may be negative, i.e., only spinons may form Dirac seas of the ground state of the model.

One can see that the dispersion relation (12) of the low-lying excitation of the easy-plane two-chain spin-1/2 antiferromagnetic model is factorized into two parts: a gapless part at $p=0$, π and a gapped one at $p=\pi/2$ (cf. Refs. 9 and 10). The former corresponds to the oscillations of the magnetization, while the latter is connected with the oscillations of the staggered magnetization.[9] An analysis similar to the analysis of the solutions of Eqs. (5) and (6) for nonzero magnetic field $h\neq0$ (here we point out that according to the very accurate analysis in Ref. 16 the solution of the integral BAE in the first-order approximation reproduces correctly both the low- and high-coupling asymptotic behavior) shows that: (i) the dressed energy of a spinon as a function of the dressed quasimomentum has only one extremum, a maximum at $p=\pi/2$ for $\theta<\theta_{c}$, and (ii) for $\theta>\theta_{c}$ there are two maxima and one minimum (situated at $p=\pi/2$). At the (tri)critical point θ_{c}, the minimum disappears and the two maxima merge into a flatter one (at $p=\pi/2$). In the limit $\theta\to\infty$ the minimum is transformed into a cusp. It reveals that the gap of the staggered magnetization vanishes in this limit of two independent spin chains. This simple picture helps us to understand what happens if one switches on an external magnetic field h. Besides the usual phase transition to the ferromagnetic (spin-polarized) phase at

$$h_{s}=\sum_{\pm}\frac{N_{\pm}}{N}\varepsilon_{\pm}^{0}(0), \qquad (13)$$

there is an additional transition between two phases. One of these corresponds to one Dirac sea of spinons (at small θ), while the other one is connected with two Dirac seas for the same kind of spinons (at large θ). It can also be seen from the right-hand side of Eqs. (5) and (6) for the densities and dressed energies that the bare density and bare energy (corresponding to terms which do not depend on $\rho(u)$ and $\varepsilon(u)$) have either one or two minima, respectively. Hence, they reproduce the same property in the dressed characteristics: the interaction simply ''dresses'' the (quasi)particles, as usual, but the ''dressing'' does not affect the picture qualitatively. The new critical field value can be approximated by $h_{c}=(\pi/\gamma)\sin\gamma\cosh^{-1}(\pi\theta/\gamma)$ in the first-order approximation.[9] In this approximation the tricritical point is the root of the equation $1=\sinh(\pi\theta_{c}/\gamma)$. At this point two second-order phase transition lines h_{s} and h_{c} join. Hence, the

easy-plane magnetic anisotropy in the antiferromagnetic two-chain model does not change qualitatively the ground state behavior in the external magnetic field (cf. Refs. 9 and 10). However it changes the critical values of the magnetic field and the intrachain coupling. The difference between the two (gapless) phases is obvious: the first phase corresponds to a Néel-like antiferromagnetic ground state for spins in both chains (along the zigzag line), while the second phase is connected with Néel-like antiferromagnetic ground states in each of the chains, i.e., effectively to two magnetic sublattices in the two-chain model.

That is why our simple model explains in which domains of parameters the two-chain spin system behaves like a one-sublattice quantum easy-plane antiferromagnet, and where it behaves like a two-sublattice one. Note also that the phase transitions studied here are manifestations of the commensurate–incommensurate phase transitions for spin systems. One can obviously see this, because the intrachain coupling for two spin chains can be interpreted as the next-nearest-neighbor spin interactions for a single spin chain of higher length $N_+ + N_-$. Here the magnetic couplings are spin-frustrated, and so the emergence of the incommensurate magnetic states is understandable.

As a consequence of the conformal invariance of $(1+1)$-dimensional quantum systems, the classification of universality classes is simple in terms of the central charge (conformal anomaly C) of the underlying Virasoro algebra.[17] The critical exponents in a conformally invariant theory are the scaling dimensions of the operators within the quantum model. They can be calculated by considering the finite-size (mesoscopic) corrections for the energies and quasimomenta of the ground state and low-lying excited states. Conformal invariance formally requires all gapless excitations to have the same velocity (Lorentz invariance). The complete critical theory for systems with several gapless excitations with different Fermi velocities is usually given as a semidirect product of these independent Virasoro algebras.[18] Here we briefly sketch the procedure and write the results for the finite-size corrections to the energy, following the standard procedure (see, e.g., Ref. 18). One can see that for $\theta < \theta_c$ and for $\theta > \theta_c$, $h < h_c$, the conformal limit of our uniaxial two chain spin-1/2 model corresponds to one level-1 Kac–Moody algebra (one WZW model of level 1 with the conformal anomaly $C = 1$). The finite-size correction to the energy is rather standard (cf. Ref. 18):

$$E_{fs}(N_+ + N_-) = -\frac{\pi}{6} v_F + 2\pi V_F (\Delta_l + \Delta_r), \qquad (14)$$

where v_F is the Fermi velocity of the spinon, and the conformal dimensions of the primary operators are (please note that the lower indices denote the conformal dimensions for right- and left-moving quasiparticles, at the right and left Fermi point, respectively)

$$2\Delta_{l,r} = \left(\frac{\Delta M}{2z} \pm z\Delta D\right)^2 + 2n_{l,r}, \qquad (15)$$

where ΔM is an integer denoting the change of the number of particles induced by the primary operator; ΔD is an inte-

ger (half-integer) denoting the number of transferred particles from the right to the left Fermi point (backscattering processes); and $n_{l,r}$ are the numbers of particle–hole excitations of right- and left-movers. The values of the quantum numbers are restricted by $\Delta D = \Delta M/2$ (mod 1). The dressed charge $z = \xi(Q)$ is the solution of the (standard) integral equation[18]

$$\xi(u) + \int_{(Q)} dv\, K(u-v)\xi(v) = 1 \qquad (16)$$

taken at the limits of integration (these are the Fermi points, symmetric with respect to zero). In this phase there is only one region of integration over v. The dressed charge is a scalar. The behavior of our class of models in this phase in the conformal limit is rather standard[18]. The correlation functions decay asymptotically $\propto (x - v_F t)^{-\Delta_l}(x + v_F t)^{-\Delta_r}$. The choice of the appropriate quantum numbers of excitations ΔM, ΔD, and $n_{l,r}$ is determined for the leading asymptotic terms of the correlators by taking the possible numbers with the smallest exponents.

For $\theta > \theta_c, h > h_c$, however, the conformal limit of the easy-plane two-chain spin-1/2 model corresponds to the semidirect product of two level-1 Kac–Moody algebras, both with conformal anomalies $C = 1$, i.e., to two WZW models both of level 1.[9,10] The Dirac seas (i.e., the possible spinons with negative energies) are in the intervals $[-Q^+, -Q^-]$ and $[Q^-, Q^+]$ (minima in the distributions of rapidities at $\mp \theta$). This can be interpreted as symmetrically distributed (around zero) Dirac seas of ''particles'' for $[-Q^+, Q^+]$ and the Dirac sea of ''holes'' for $[-Q^-, Q^-]$. In fact the valley in the density distribution for ''particles'' and the maximum for ''holes'' are in one-to-one correspondence with the maxima and minimum of the dispersion relation for spinons. The second critical field h_c in this language corresponds to the van Hove singularity of the empty band of ''holes.'' Naturally, the Fermi velocities of ''particles,'' are positive, $v_F^+ = (2\pi\rho(Q^+))^{-1}\varepsilon'(u)|_{u=Q^+}$, while the Fermi velocities of ''holes'' are negative, $v_F^- = -(2\pi\rho(Q)^-)^{-1}\varepsilon'(u)|_{u=Q^-}$. The finite-size corrections to the energy for this case are

$$E_{fs}(N_+ + N_-) = -\frac{\pi}{6}(v_F^+ + v_F^-) + 2\pi(v_F^+(\Delta_l^+ + \Delta_r^+)$$
$$+ v_F^-(\Delta_l^- + \Delta_r^-)), \qquad (17)$$

where the dispersion relations for ''particles'' and ''holes'' are linearized about the Fermi points for each Dirac sea. The conformal dimensions of the primary operators are (the upper indices denote Dirac seas; the lower indices denote right and left Fermi points of each of these two Dirac seas; cf. Ref. 10 for the isotropic spin-1/2 two-chain model):

$$2\Delta_{l,r}^{\mp} = \left[\frac{(x_{-\pm}\Delta M^+ - x_{+\pm}\Delta M^-)}{2\det\hat{x}}\right.$$
$$\left.\mp\frac{(z_{-\pm}\Delta D^+ - z_{+\pm}\Delta D^-)}{2\det\hat{z}}\right]^2 + 2n_{l,r}^{\mp}, \qquad (18)$$

where the minus sign between the terms in square brackets corresponds to the right-movers and the plus sign to the left-

movers. Here $\Delta M^{\pm}$ denote the differences between the numbers of particles excited in the Dirac seas of ''particles'' and ''holes'' labeled by the upper indices. $\Delta D^{\pm}$ denote the numbers of backward scattering excitations, and $n_{l,r}^{\pm}$ are the numbers of particle–hole excitations for right-and left-movers of each of the Dirac seas (for ''particles'' and ''holes''). Please note that $\Delta M^{\pm}$ and $\Delta D^{\pm}$ are not independent. Their values are restricted by the following relations: $\Delta M^{+}-\Delta M^{-}=\Delta M$ and $\Delta D^{+}-\Delta D^{-}=\Delta D$, where ΔM and ΔD determine in a standard way the changes of the total magnetization and the total momentum of the system, respectively, due to excitations. Please note that in Refs. 10 and 19 these restrictions were missing; this resulted in, for example, the invalid statement that four independent low-lying backscattering excitations are possible. However one can see that only two of them are really independent. The same is true for excitations that change the total magnetization of the system: there are only two independent of four possible such excitations. This is a direct consequence of the fact that only one magnetic field determines the filling of the two Dirac seas for ''particles'' and ''holes'' or, in other words, two the two Dirac seas for spinons at $\pm\theta$.

The dressed charges $x_{ik}(Q^k)$ and $z_{ik}(Q^k)(i,k=+,-)$ are matrices in this phase. They can be expressed by using the solution of the integral equation[18,20]

$$f(u|Q^{\pm})=\left(\int_{-Q^{+}}^{Q^{+}}-\int_{-Q^{-}}^{Q^{-}}\right)K(u-v)f(v|Q^{\pm})$$

$$=K(u-Q^{\pm}) \qquad (19)$$

with[18]

$$z_{ik}(Q^k)=\delta_{i,k}+(-)^k\frac{1}{2}\left(\int_{Q^i}^{\infty}-\int_{-\infty}^{-Q^i}\right)dv\,f(v|Q^k),$$

$$x_{ik}(Q^k)=\delta_{i,k}-(-)^k\int_{-Q^i}^{Q^i}dv\,f(v|Q^k). \qquad (20)$$

Note that the dressed charges depend on the value of the magnetic anisotropy γ via the kernels, while they depend indirectly on the value of the intrachain coupling constant θ, only via the limits of integration. In the first-order approximation one can write the solutions as

$$x_{ik}(Q^k)\approx\delta_{i,k}-(-)^k\int_{-Q^i}^{Q^i}dv\,K(v-Q^k)+\dots$$

and

$$z_{ik}(Q^k)\approx\delta_{i,k}+(-)^k(1/2)\left(\int_{Q^i}^{\infty}-\int_{-\infty}^{-Q^i}\right)dv\,K(u-Q^k)+\dots$$

The Dirac sea for ''holes'' disappears, naturally for $h\to h_c,\theta\to\theta_c$. The slopes of the dressed energies of ''particles'' and ''holes'' at the Fermi points of the Dirac seas (Fermi velocities) differ in general from each other. Therefore we have a semidirect product of two algebras. Hence, in this region the dressed charges are 2×2 matrices. This means that the conformal limit of the easy-plane two-chain spin-1/2 model corresponds to one or two WZW theories, depending on the values of the intrachain coupling, magnetic anisotropy, and magnetic field. At the critical line h_c the

Dirac sea of ''holes'' disappears as well as the components of the dressed charge matrix $\hat{x}$ (with square-root singularities of the critical exponents for the correlation functions). Note that the dressed charge z becomes $z=(2x)^{-1}$ at the phase transition line h_c. This corresponds to the disappearance of one of the WZW CFT. Unfortunately, it is impossible to obtain an analytical solution to Eq. (19) in closed form for a finite interchain coupling θ. Naturally, in the limiting cases of two independent chains of lengths $N_{\pm}$, $\theta\to\infty$ and a single chain of length $N_{+}+N_{-}$, $\theta=0$, the solutions of Eqs. (16), (19), and (20) coincide with the well-known solutions (see Ref. 18). The correlation functions of the uniaxial two-chain spin-1/2 model decay algebraically in this phase $\propto(x-v_F^+t)^{-\Delta_l^+}(x-v_F^-t)^{-\Delta_l^-}(x+v_F^+t)^{-\Delta_r^+}(x+v_F^-t)^{-\Delta_r^-}$ with the minimal exponents of the possible quantum numbers of excitations $\Delta M^{\pm}$, $\Delta D^{\pm}$, and $n_{l,r}^{\pm}$. We point out once more that the same magnetic field plays the role of a chemical potential for the ''particles'' and ''holes,'' or for the spinons of both Dirac seas in the second phase, and hence this choice of minimal quantum numbers is constrained.

We must point out here that there is a crucial difference between our situation and the case of dressed charge matrices appearing for systems with the internal structure of bare particles[18]. There the two Dirac seas of the ground states are connected with different kinds of excitations, e.g., holons and spinons for the repulsive Hubbard model, or Cooper-like singlet pairs and spinons for the supersymmetric t-J model. They correspond to two different kinds of Lagrange multipliers, chemical potentials, and magnetic fields. Thus the lowlying excitations of the conformal theories in the spin and charge sectors of these correlated electron models are practically independent of each other (spin-charge separation). Note that the spin and charge sectors are connected via the off-diagonal elements of the dressed charge matrix, though. This is a consequence of the fact that, say, holons or unbound electrons carry both charge and spin. On the other hand, two Dirac seas appear for the same kinds of particles for the models studied in this paper, which are also connected with the same magnetic field governing the filling of both Dirac seas. These seas appear due to two minima in the bare energy distribution and correspond to nonzero shift θ in the Bethe ansatz equations. In other words, the two Dirac seas are determined by the interchain coupling and appear if the values of the coupling and external magnetic field are higher than the threshold values θ_c and h_c, respectively. We believe that such a threshold behavior does not depend on the integrability of the model and is a generic feature for any multi-chain quantum spin models.

The low-temperature Sommerfeld approximation shows that, as usual, the low-temperature specific heat off the critical lines is proportional to T. On the critical lines the van Hove singularities produce $\sqrt{T}$ low-temperature behavior of the specific heat, while at the tricritical point we have $T^{1/4}$ behavior.

What are the changes due to the different lengths of the chains $N_{+}\neq N_{-}$? One can see obviously that the values of the spinon momentum, energy, and velocity (which was v

$=(\pi/\gamma)\sin\gamma\tanh(\pi\theta/\gamma))$ become functions of $N_+ - N_-$. For example, the velocity renormalizes as $v \to v[1 + (N_+ - N_-)^2 \tanh^2(\pi\theta/2\gamma)/N^2]^{-1}$. This introduces dependences of the critical values θ_c and h_c (as well as of the saturation field h_s) on the difference $N_+ - N_-$. Also, the Fermi velocities and Fermi points for finite-size corrections become dependent on this difference. One can in principle consider different coupling constants $J_\pm$ for each of the chains (over-all multipliers[21]). This produces renormalizations similar to the effect of $N_+ \neq N_-$, i.e., the velocity, for example, renormalizes as $v \to J_+ v[1 + (J_-/J_+)^2 \tanh^2(\pi\theta/2\gamma)]^{-1}$.

3. CONNECTIONS TO THE QUANTUM FIELD THEORIES

The studies presented in the previous section, being rather standard (note, though, some important new features which were absent in the previous studies,[4,9,10,11,13,19] such as the dependence of the critical values of the interchain coupling and external magnetic field on the magnetic anisotropy parameter and on the difference in the lengths of the chains, also the important restrictions on the quantum numbers of low-lying conformal excitations). However, we will use the results of that Section for novel studies for a wider class of exactly solvable models in Secs. 3–5. For instance, in this Section we point out the important similarities in the behaviors of the two-chain quantum spin model considered in the previous section and several models of QFT.

Really, when examining Eq. (1), one can see that these Bethe ansatz equations coincide with the equations which describe the behavior of the spin (color) sector of some QFT. $N_\pm$ corresponds to the numbers of (bare) particles with positive and negative chiralities. For example, for the chiral-invariant Gross–Neveu (CIGN) model[14,22] we have to put $\gamma \to 0$ (i.e., the $SU(2)$-symmetric case, equivalent to the $SU(2)$-symmetric Thirring model), and $\theta = (1 - g^2)/2g$, where g is the coupling constant of the chiral invariant Gross-Neveu QFT.[14] As to the Lagrange multiplier h, it can play the roles of either an external magnetic field or the chemical potential, or an external topological field dual to the topological Noether current in QFT. Here we point out that in fact in QFT the theorists are interested in physical particles, which have a finite mass (gap). In the chiral-invariant Gross-Neveu model the gap of the staggered oscillations of the two-chain quantum spin model plays the role of the physical mass of the particle (spinor).[13,14] As to the (gapless) oscillations of the magnetization of the two-chain spin model, we point out that they are consequences of the lattice and play the role of the massless fermion doublers of the lattice QFT.[23] The results of the previous section mean that the behavior of the chiral-invariant Gross-Neveu model (or $SU(2)$-symmetric Thirring model) in an external magnetic field depends strongly on the coupling constant θ (or equivalently on g). For $\theta < \theta_c$ the conformal limit of the QFT corresponds to one level-1 WZW model with the conformal dimension $C = 1$. However, for $\theta > \theta_c(-\theta_c - \sqrt{\theta_c^2 + 4} < 2g > -\theta_c + \sqrt{\theta_c^2 + 4})$ the conformal limit of this QFT in an external magnetic field corresponds to the semidirect product of two level-1 WZW models with the conformal dimensions $C = 1$. Two kinds of conformal points for this QFT have been

mentioned already[24] in a slightly different context. They were connected with one WZW theory or two WZW theories, coupled via a current–current interaction. This is related to right–left symmetry of the chiral invariant Gross–Neveu QFT (see also Refs. 32 and 33 for the case of the QFT for the principal chiral field).

Note that the condition $h > h_c$ in the QFT means that the magnetic field is larger than the mass of the physical particle (color spinor). In this sense, in the region of magnetic field values $h < h_c$ the results of the QFT (see, e.g., Ref. 22) predict zero magnetization; however, a different lattice regularization, similar to the lattice scheme used in the previous Section, predicts a nonzero magnetization of the chiral-invariant Gross–Neveu model in this region. This is an indirect effect of the fermion doublers. In other words, it is connected with the well-known mapping of the lattice (e.g., Thirring) model under regularization onto two continuum QFT either both bosonic (the free bosonic and sine-Gordon QFT[25]), or both fermionic (a free one and the continuum massive Thirring model). There are necessarily two such theories because of the Nielsen–Ninomiya fermion doublers: remember that we have started from a lattice.[23]

For other models of QFT the lattice regularization procedure[26–28] has been used. Here θ plays the role of the cutoff for keeping the mass of the physical particle finite. For example, for the $U(1)$-symmetric Thirring QFT[23,29] one can use the results of the previous section with the limit $\theta \to \infty$ taken after the thermodynamic limit ($L, N_\pm, M \to \infty$ with their ratios fixed, L is the size of the box). In this case one can obviously obtain the conformal limit of the theory with nonzero physical masses of the particles. Naturally, in the limit $\theta \to \infty$ one is always, in the presence of an external magnetic field, in the phase with two Dirac seas. Here the latters correspond to the right- and left- moving particles (with positive and negative chiralities). Actually here our point of view coincides with that of the field theorists. Recently it was shown[30] that for the $(1+1)$-dimensional sine-Gordon model the lattice regularization scheme in the ''light-cone'' approach gives results similar to ours for the conformal limit of the model. It was shown there that at the UV fixed point the conformal dimensions of the sine-Gordon model are determined by two $U(1)$ charges of excitations (the usual one and the chiral charge). The chiral charge corresponds to the number of excitations transferred from one Dirac sea to the other, similar to our results (note that the above-mentioned lattice-regularized sine-Gordon case corresponds in our notation to $\theta \to \infty$, where the integral equations for the particles with the positive and negative chiralities are totally decoupled). We point out here, that such behavior is not unexpected, because the sine-Gordon QFT belongs to the same class of models studied in our paper, i.e., its Bethe ansatz description features a shift of rapidities in the Bethe ansatz equations in the lattice-regularized theory.[30]

4. HIGHER SPIN (CHIRALITY) GENERALIZATIONS

For the higher spin generalizations of the Bethe ansatz theory presented in Sec. 2 we can write the BAE in the form

$$\prod_{\pm} e^{N_\pm}_{n_\pm}(u_\alpha \pm \theta) = e^{i\pi M} \prod_{\beta=1,\beta \neq \alpha}^{M} e_2(u_\alpha - u_\beta), \tag{21}$$

where $n_\pm = 2S_\pm$ are the values of the spins in each chain or the colors of the bare particles in QFT. The eigenvalue of the transfer matrix can be written as

$$\Lambda(\lambda) = \prod_{\alpha=1}^{M} \frac{\sinh(\lambda - u_\alpha + i\gamma/2)}{\sinh(u_\alpha - \lambda + i\gamma/2)}$$

$$+ e^{i\pi M} \prod_{\pm} \left(\frac{\sinh(\lambda \pm \theta)}{\sinh(i\gamma n_\pm/2 - \lambda \mp \theta)} \right)^{N_2}$$

$$\times \prod_{\alpha=1}^{M} \frac{\sinh(u_\alpha - \lambda + 3i\gamma/2)}{\sinh(\lambda - u_\alpha - i\gamma/2)}. \tag{22}$$

Similar new phases with one or two kinds of Dirac seas for similar kinds of low-lying excitations also exist for a number of models in which $n_\pm \neq 1$, e.g., for the higher-spin ($S > 1/2$) two-chain models with equal spins in each chain, $SU(n+1)$ CIGN QFT.[31] there $n_+ = n_- = n \neq 1$; for the principal chiral field models (nonlinear σ model) for CP-symmetric[32] (there $n_+ = n_- \to \infty$) and CP-asymmetric cases[33] (there $n_+ \neq n_-$, $(n_+ + n_-) \to \infty$, $(n_+ - n_-)$ fixed, i.e., the symmetry $SU(2) \times SU(2) \propto O(4)$; and for the $O(3)$-symmetric nonlinear σ model[34] as well as for spin-($S_+ \equiv 2n_+$)–spin-($S_- \equiv 2n_-$) two-chain models (quantum two-chain ferrimagnet). Note that for spins $S \neq 1/2$ the procedure of the construction of the Hamiltonian is more complicated, because it corresponds to the two-chain uniaxial generalization of the Takhtajan–Babujian model; see, e.g., Ref. 35. For the simplest case of isotropic exchange interactions between the spins and between the chains the Hamiltonian has the form

$$\mathcal{H} = \sum_n \{ \theta^2 (\mathcal{H}_{S_+,S_+,n_1,n_1+1} + \mathcal{H}_{S_-,S_-,n_2,n_2+1})$$

$$+ 2(\mathcal{H}_{S_+,S_-,n_1,n_2} + \mathcal{H}_{S_-,S_+,n_1,n_2+1})$$

$$+ [(\mathcal{H}_{S_+,S_+,n_1,n_1+1}$$

$$+ \mathcal{H}_{S_-,S_-,n_2,n_2+1}), (\mathcal{H}_{S_+,S_-,n_1,n_2}$$

$$+ \mathcal{H}_{S_-,S_+,n_1,n_2+1})] + 2i\theta[(\mathcal{H}_{S_+,S_+,n_1,n_1+1}$$

$$+ \mathcal{H}_{S_-,S_-,n_2,n_2+1}), (\mathcal{H}_{S_+,S_-,n_1,n_2}$$

$$+ \mathcal{H}_{S_-,S_+,n_1,n_2+1})] \}, \tag{23}$$

where $[...]\{[...]\}$ denote the (anti)commutator,

$$\mathcal{H}_{S_1,S_2,n,n+1} = \sum_{j=|S_1-S_2|+1}^{S_1+S_2} \sum_{k=|S_1-S_2|+1}^{j}$$

$$\times \frac{k}{k^2 + \theta^2} \prod_{l=|S_1-S_2|}^{S_1+S_2} \frac{x - x_l}{x_j - x_l}, \tag{24}$$

$x = \mathbf{S}_{1,n}\mathbf{S}_{2,n+1}$ and $2x_j = j(j+1) - S_1(S_1+1) - S_2(S_2+1)$. The summation over n runs to $N_\pm$ in each chain. One can obviously see that for $S_\pm = 1/2$ the Hamiltonian (23) recovers the isotropic antiferromagnetic spin-1/2 Hamiltonian (4) in-

vestigated in Sec. 2. For a single spin chain, $\theta = 0$, $N_+ = N_-$ the Hamiltonian coincides with the known Hamiltonian of alternating spin chains.[36–38] The Bethe-ansatz studies of the model for $n_\pm$ can be performed in complete analogy with the above-mentioned case $n_\pm = 1$, keeping in mind, of course, the main difference: for the $SU(2)$-symmetric or uniaxial higher-spin models the ground state corresponds to the filling up of the Dirac seas for spin strings of lengths $n_\pm$.[35] The well-known fusion scheme can be used for the case of a flavor-degenerate situation of the chiral invariant Gross–Neveu CIGN QFT, in the absence of flavor fields.[39] Note that, except for the $O(3)$-symmetric case, $\gamma = 0$ everywhere in the above-mentioned models of QFT. This corresponds to rational solutions of the Yang–Baxter equation for the two-particle scattering matrices. For the two spin chains the two-chain quantum ferrimagnet model corresponds to two Takhtajian–Babujian chains with different values of the site spins, coupled due to nonzero θ. The total quasimomentum and the energy of the system in the framework of the lattice (local) regularization scheme for some QFT can be written as[23]

$$-2a_t E = \sum_{\pm} \sum_{\alpha=1}^{M} \frac{\partial}{\partial u_\alpha} N_\pm \ln e_{n_\pm}(u_\alpha \pm \theta),$$

$$iaP = \sum_{\pm} \sum_{\alpha=1}^{M} N_\pm \ln e_{n_\pm}(u_\alpha \pm \theta), \tag{25}$$

where a and a_t denote the space and time lattice constants, respectively, and their ratio fixes the velocity of light ("light-cone" approach). The CP-symmetric (chiral invariant) case corresponds to the situation in which $n_+ = n_- = n$. The Dirac seas are related to the dressed (quasi)particles with negative energies (strings of length $n_\pm$). The behavior of the dispersion relation for excited particles in the CP-symmetric case ($n_+ = n_- = n$ and $N_+ = N_-$) is similar to Eq. (12): for instance, for the chiral-invariant Gross-Neveu QFT and principal chiral field model the right-hand side of Eq. (12) must be simply multiplied by $\sin(\pi r/n+1)/\sin(\pi/n+1)$, and the parameter θ in Eq. (12) has to be replaced by $(n+1)\theta/2$, where $r = 1,...,n$ is the rank of a fundamental representation of the $SU(n+1)$ algebra. All the previously mentioned characteristic features from the case $n_\pm = 1$ persist. The differences are in the levels of the Kac-Moody algebras in the conformal limit: the conformal anomalies are $C = 3n/(n+2)$. Now the conformal field theory is a semidirect product of a Gaussian ($C = 1$)[40] and a $Z(n)$ parafermion models:[41] the operators identified from the scaling behavior of states consisting only of Dirac sea strings (found from finite-size corrections) are found to be composite operators formed by the product of a Gaussian-type operator and the operator in the parafermionic sector. To find the nonzero contributions from parafermions (constant shifts) one can consider the states with strings of other lengths than the Dirac sea present.[42] For the scaling dimensions these shifts are $(2r - r^2)/(2n+4)$, $r = 1,2,...$

From now on we concentrate on the $n_+ \neq n_-$ situation. For the two-chain spin system the situation corresponds to the quantum ferrimagnet. Here we point out that due to the

zigzag-like interactions in the system and spin frustration the ferrimagnets of this class are in the singlet ground state (compensated phase) for $h=0$, unlike the standard classical ferrimagnets in uncompensated phases. The integral equations that determine the physical vacuum of the systems are similar to Eqs. (5) and (6). They reveal one or several minima of the corresponding distributions of dressed energies and densities with possible negative energy states, i.e., one or several Dirac seas:

$$\varepsilon_\tau(u) + \int dv K_{\tau\tau'}(u-v)\varepsilon_{\tau'}(v) = h\frac{N_\tau}{N}n_\tau + \sum_\pm \frac{N_\pm}{N}\varepsilon_{\tau,\pm}^0. \tag{26}$$

$$\rho_\tau(u) + \int dv K_{\tau\tau'}(u-v)\rho_{\tau'}(v) = \sum_\pm \frac{N_\pm}{N}\rho_{\tau,\pm}^0. \tag{26}$$

The index τ enumerates two possible Dirac seas and appears because $n_+ \neq n_-$, and the $\pm$ enumerate two possible minima due to the nonzero shift θ. The index τ was naturally absent for the CP-symmetric case $n_+ = n_-$. Note that for quantum two-chain ferrimagnets the investigated gapless phases in the ground state in an external magnetic field are similar to the spin-compensated and uncompensated phases. Thus the phase transition between those phases is similar in nature to the well-known spin-flop phase transition in the classical theory of magnetism. Note, though, that the spin-flop transition is of the first order (easy-axis magnetic anisotropy), while the transition under study is a second-order one (easy-plane anisotropy). The Fourier transform of the kernel is given by

$$2\coth(\omega/2)[\,\mathrm{diag}(e^{-n_+|\omega/2|}\cosh(n_+\omega/2), e^{-n_-|\omega/2|}$$
$$\times\cosh(n_-\omega/2)) - \hat\sigma_x(e^{-(n_+-n_-)|\omega/2|} - e^{-(n_++n_-)|\omega/2|})], \tag{27}$$

where $\mathrm{diag}(a,b)$ is 2×2 diagonal matrix and $\hat\sigma_x$ is the usual Pauli matrix. Note that after taking the limit $(n_+ + n_-) \to \infty$, which is the case of the CP-asymmetric case of the QFT for the principal chiral field, i.e., with the Wess-Zumino term,[33] the inverse kernel coincides formally (up to a constant multiplier) with the one for the case $n_+ = n_- = 1$. This indicates a global $O(4)(O(3))$ symmetry of the principal chiral field.[33] There may also be two different behaviors, corresponding to one or several Dirac seas for $n_+ \neq 1$ or $n_- \neq 1$. Naturally, in the conformal limit the associated WZW CFT have different conformal anomalies determined by $n_\pm : C_\pm = 3n_\pm/(n_\pm+2)$. For the determination of the Gaussian parts of the conformal dimensions of primary operators, Eqs. (18) can be used. One has to add the input from the parafermionic sectors, too.[41,42] The elements of the dressed charge matrices are the solutions of the following system of integral equations:

$$\xi_{\tau,\tau'}(u) + \sum_\pm \int dv K_{\tau'}(u-v)\xi_{\tau,\pm}(v) = \delta_{\tau,\tau'}, \tag{28}$$

in which the summation over $\pm$ is due to the two possible Dirac seas (two minima in the distribution of rapidities) at $\pm\theta$. For different values of the spins, $n_+ \neq n_-$, a transition between two different phases is induced by increasing an external magnetic field to some critical value, even in the absence of the shift θ.[37,38] This differs from the CP-symmetric case $n_+ = n_-$, where the phase transition is only connected with the nonzero value of the intrachain coupling parameter θ. For the CP-symmetric case, one or two Dirac seas of the same type of excitations exist due to the nonzero θ. But in the CP-asymmetric case the existence of two Dirac seas can be related to two different kinds of low-lying excitations (particles). They are strings of lengths n_+ and n_-, respectively. In this situation the dispersion relations may be independent (not only factorized as for the previous CP-symmetric cases). The (new) phase transition at h_c reveals the van Hove singularity of the empty Dirac sea for the longer strings. The spin saturation field h_s is connected with the empty Dirac sea of strings of the smaller length.

5. MULTICHAIN QUANTUM SPIN MODELS

It is worthwhile to mention that phase transitions in an external magnetic field, similar to the ones studied in this paper for uniaxial spin chains and QFT, have been already studied in 1D quantum alternating single spin chains,[37,38] spin-1/2 isotropic two-chain models,[9,10] and correlated electron models with the finite concentration of magnetic impurities.[43] The Bethe ansatz equations for those models are similar to the ones studied in the present paper, Eqs. (1) and (21). Note that the energies for spin models are defined (as usual for the lattice models) as the first logarithmic derivatives of the transfer matrices. The factorization of the dispersion relation for the lowest excitations (spinon) reveals essentially two kinds of magnetic oscillations: excitations of the magnetization, and oscillations of the staggered magnetization, i.e., the manifestation of essentially two magnetic sublattices. Naturally, the existence of the latters persists in the continuum limit of such systems, too (cf., for instance, the standard theory of antiferromagnetism). Two nonferromagnetic phases also reveal themselves in finite-size corrections to the energies of these quantum spin models. There, instead of a scalar dressed charge for the phase with one Dirac sea for spinons, 2×2 dressed charge matrices appear in the second phase, with two Dirac seas for spin strings of different lengths in an alternating spin chain[37,38] or for spinons of the same kind in zigzag-like coupled spin chains (see Refs. 9 and 10 for the isotropic two-chain spin-1/2 model).

The symmetry-breaking terms [the difference $(n_+ - n_-) = 2(S_1 - S_2)$, or nonzero θ] in BAE are actually the reason for the emergence of several gapless phases (or two Dirac seas) in the ground state in an external magnetic field. It is also interesting to note that a homogeneous shift of rapidities can be removed for one Dirac sea in the case of periodic boundary conditions by an appropriate unitary (gauge) transformation (shift of variables), e.g., $u_\alpha \to u_\alpha \pm \theta$. But in the case of open boundary conditions, the BAE take the form (for reasons of simplicity we write the free boundary situation only, without the external boundary potential):

$$\prod_{\pm} e_{n_{\pm}}^{2N}(u_{\alpha}\pm\theta)=\prod_{\pm}\prod_{\beta} e_2(u_{\alpha}\pm u_{\beta}). \qquad (29)$$

It is clear that for the open chain one cannot remove the shift θ of the rapidities u_{α} from one Dirac sea by a special choice of the gauge. From this point of view the latter case is close to the *CP*-symmetric situation in QFT.

One can see from the structure of the Hamiltonians that for the two-chain spin models the parameter θ characterizes the intrachain coupling for each chain (or the next-nearest-neighbor interaction in a single spin chain picture). It is obvious to introduce the series of $\{\theta_j\}_{j=1}^{J}$ (for each chain) and to construct the Hamiltonian of the exactly integrable multichain (J is the number of chains) spin model. For the simplest case with all $S=1/2$ isotropic antiferromagnetic chains, the Hamiltonian reads:[4]

$$\hat{H}_J=A\sum_n \left\{ \left[\prod_{i,k}(\theta_i-\theta_k)\right]\hat{P}_{S_{n,r}S_{n+1,r}} \right.$$
$$+\sum_{p<q}\frac{\Pi_{i,k}(\theta_i-\theta_k)}{(\theta_p-\theta_q)}[\hat{P}_{S_{n,q}S_{n+1,p}},\hat{P}_{S_{n,q}S_{n+1,q}}$$
$$+\hat{P}_{S_{n,p}S_{n+1,p}}]+\cdots+\left(\sum_{j=1}^{J}\hat{P}_{S_{nj}S_{nj+1}}-\hat{P}_{S_{n,J}S_{n,J+1}}\right.$$
$$\left.\left.+\hat{P}_{S_{nJ}S_{n+1,1}}\right)\right\}, \qquad (30)$$

where A is the normalization constant (which depends on θ_j); $\hat{P}_{S_aS_b}\propto(1/2)\hat{I}\otimes\hat{I}+2\mathbf{S}_a\otimes\mathbf{S}_b$ is the permutation operator; and $[.,.]$ denotes a commutator. Note that in the case of $J\neq 2$ the integrable model corresponds to the pair couplings not only between the nearest-neighbor spins but also to the next-nearest three-spin, etc., couplings. All those terms are only essential in quantum mechanics, because in classical physics they are total time derivatives[11] and do not change the equations of motion. The Bethe ansatz equations have the form

$$\prod_{j=1}^{J} e_1^{N}j(u_m+\theta_j-\theta_1)=e^{i\pi M}\prod_{k}^{M} e_2(u_m-u_k), \qquad (31)$$

where M is the total number of down spins and N_j is the number of sites in the jth chain. The previously studied situation $J=2$ corresponds to the shift of the variables $u_m \rightarrow u_m+\theta$ with $\theta_2-\theta_1=-2\theta$. Now $\theta_j-\theta_1$ determines the values of the intrachain couplings in chain j.

The analysis of the low-temperature thermodynamics of the multichain spin system is analogous to the $J=2$ case studied in Secs. 2–4. From the structure of the Bethe ansatz equations in the thermodynamic limit N_j, $M\rightarrow\infty$, with their ratios fixed, one can see that for the J-chain model (for different θ_j) there can exist, generally speaking, J phase transitions of the second order in the ground state in an external magnetic field. These are none other than the commensurate-incommensurate phase transitions for the quantum multichain spin model with different couplings between the chains. The values of the critical fields $h_{c_1},\dots,h_{c_{J-1}}$ and the

value of the magnetic field of the transition to the ferromagnetic state h_s depend on the set of θ_j, i.e., on the intrachain couplings (and also on the values of the magnetic anisotropy constants, which can be taken different for each chain; this does not destroy the integrability). The ferromagnetic state is gapped, while all other phases are gapless in the integrable multichain spin quantum model. There are also $J-1$ tricritical points at which the lines of the phase transitions h_{c_j} join the line of the spin saturation phase transition. Naturally, the phase that corresponds to the lowest value of the magnetic field, say $h<h_{c_1}$ for special values of θ_j (the condition is similar to $\theta<\theta_c$ for $J=2$), has in the conformal limit one scalar dressed charge. Hence, in the conformal limit our multichain spin model behaves as the level-1 WZW CFT. In the next phase the multichain quantum spin model behaves as the semidirect product of two WZW CFT, hence their dressed charges are 2×2 matrices, and so on, until the last gapless phase, which corresponds to the semidirect product of J WZW CFT with $J\times J$ dressed charge matrices. Note that J in this approach also denotes the number of possible Dirac seas (each of them is connected with the same magnetic field, so the excitations in each of them are not independent), and thus, with one-half of the number of Fermi points. In the limit $J\rightarrow\infty$ (i.e., quasi-2D spin system) one obtains the (2D) Fermi surface instead of the set of 1D Fermi points (the latter become distributed more closely to each other with the growth of J). In this limit the differences between θ_j tend to zero, and that is why the differences between θ_{c_j}, h_{c_j}, and also between h_{c_j} and h_s disappear, too. Therefore in this limit only h_s survives. This means that for the quasi-2D limit of such an integrable model of J coupled quantum spin chains with $J\rightarrow\infty$ we expect only two phases in the ground state in an external magnetic field: the ferromagnetic gapped one and the gapless phase, which in the conformal limit corresponds to one WZW CFT (with a single scalar dressed charge). The phase transition between these two phases in the ground state in an external magnetic field is of the second order.

6. BEHAVIOR OF THE NONINTEGRABLE MULTICHAIN SPIN SYSTEMS

So far we have studied only integrable multichain quantum spin models. We have shown that the commensurate-incommensurate phase transitions of the second order have to reveal themselves in an external magnetic on account of the intrachain interactions (or the next-nearest interactions in a single quantum spin chain picture). We have shown that the emergence of these phase transitions does not depend on the value of the site spins; they emerge in the presence of easy-plane magnetic anisotropy, which keeps the system in the critical (gapless) region. It is not clear, however, which features of the behavior of the integrable models with the ''fine-tuned'' parameters have to exist for more realistic multichain models, and what are the qualitative differences that are expected to exist between the integrable multichain models and real multichain spin systems.

We have to add one more thing to clarify the situation: we study (quasi)-1D spin quantum models, for which one

can use the Lieb-Schultz-Mattis theorem (and its generalizations).[8,44] However, it is obvious that due to the frustration of the interactions between neighboring spins and the presence of additional terms in the Hamiltonians which violate the time-reversal and parity symmetries in the systems (spin chiralities or spin currents), for all of the spin models studied in this paper one cannot satisfy the conditions of the theorem. Hence it cannot be applied (at least not directly). That is why for all the models studied there are no spin gaps (except for the trivial one for the spin-polarized ground state). (Here we are not talking about the gaps connected with the magnetic anisotropy but rather about the Haldane-like spin gaps[45] which appear even for the isotropic spin-spin interaction, and about fractional magnetization plateaus[8]). As we argued before,[11] it is the presence of the chiral spin terms (or the operators of the nonzero spin currents) in the Hamiltonian (which are total time derivatives and do not change the classical equations of motion but rather affect the topological properties, like the choice of the θ-vacuum in Haldane's approach) is the reason why the low-lying spin excitations (and particles for lattice QFT) for our class of models are gapless and our low-energy theories are conformal. It has to be mentioned that recent results of the perturbative RG analysis of the zigzag spin-1/2 chain without three-spin terms shows the tendency of the RG currents to flow to the state with the parity and time-reversal violation.[46] By the way, one can obviously see that the *XY* limit of the two-chain spin model does not correspond to the free fermion point of the exactly solvable model, and this agrees with the results of Ref. 46. Note, though, that in the latter it was erroneously concluded that the time-reversal and parity symmetries were violated by the two-chain zigzag spin Hamiltonian with only two-spin couplings (i.e., the nearest- and next-nearest-neighbor interactions in the single chain picture), without spin current terms in the Hamiltonian. Hence the symmetry of the state considered was lower than the symmetry of the Hamiltonian there.

Naturally, the relevant perturbations to our integrable models will immediately produce spin gaps. As usual, the algebraic (power-law) decay of the correlation functions in the ground state of the models considered in this paper determines the quantum criticality. This means that, starting from the (conformal) exact solutions obtained in this paper, one can argue that the response of the more realistic spin systems to perturbations can be evaluated by using perturbative methods, e.g., in a renormalization group framework. For example, let us study the effect of relevant perturbations to the Hamiltonians considered, $\hat{H}_r = \hat{H} + \delta\hat{H}_1$, where one can choose as $\hat{H}_r$, e.g., the standard Heisenberg or uniaxial Hamiltonians for several coupled quantum spin chains, and as $\hat{H}$ the hamiltonians of spin chains considered exactly in this paper for some values of θ, where the three-spin terms are relevant. The correction to the ground state energy and the excitation gap (mass of the particle in QFT) for the quantum critical system are $\Delta E \propto -\delta^{(d+z)/y}$ and $m \propto \delta^{1/y}$, respectively, where d is the dimension of the system, and z is the dynamical critical exponent. For the conformally invariant systems studied here one has $d = z = 1$. The application of the

standard scaling relations yields $y + x = 2(=z+d)$, where x is the scaling dimension, i.e., $x = 2\Delta_l + 2\Delta_r$, found in the previous sections (for the phases with the dressed charge matrices the summation over upper indices is meant). Hence the gap for the low-lying excitations (the mass of the physical particles in QFT) for the perturbed systems will be $m \propto \delta^{1/2(1-\Delta_l-\Delta_r)}$. Note that because of scaling, the behavior of the critical exponents (which are related to the exponents we introduced for the integrable multichain spin models) in the vicinities of the lines of phase transitions has to be universal, and this can be checked experimentally. We expect that the spin gap has to exist for values of the isotropic zigzag interchain coupling higher than or of the order of 0.5 for the two-chain spin-1/2 system,[9] where the three-spin couplings are relevant and the emergence of the spin gap is known exactly.[47]

Very recently, density matrix renormalization group numerical studies of the two-chain zigzag spin-1/2 model (without chiral three-spin terms in the Hamiltonian) were performed in Ref. 48. These numerical studies strongly support the picture proposed here (see also Ref. 9): the magnetization as a function of the magnetic field in the ground state reveals (i) one second-order phase transition (to the spin-saturation phase) for weak intrachain coupling, (ii) one more second-order phase transition between the magnetic (gapless) phases in the intermediate region of intrachain coupling, and (iii) in addition to those second-order phase transitions, one to the gapped phase with zero magnetization (plateau) at an intrachain coupling value of 0.5.

We should also mention that it is not the chiral spin terms (as implied in Ref. 10) but the intrachain coupling that is responsible for the commensurate–incommensurate phase transitions between the gapless phases in this class of models. As to the aforementioned spin currents, their ''fine-tuned'' values produce the cancellation of the spin gap for zero magnetic field[9]. We should also note that to our mind some features of the phase diagram obtained in Ref. 19 are artifacts of the small number of sites involved in the numerical calculations. In Fig. 5 of Ref. 19 in the regions $0.52 < \kappa < 0.6$ (corresponding to intrachain couplings, normalized to the value of the interchain interaction, in the range [0.54–0.75]) we can obviously see that when increasing the value of the magnetic field one goes from the gapped phase with zero magnetization into the gapless one with two Dirac seas of low-lying excitations, then reaches the gapless phase with one Dirac sea, then returns to the gapless phase with two Dirac seas, and finally reaches the spin-saturated phase. To our mind this return to the already passed phase is nonphysical. One can clearly see that the region of values of the intrachain couplings in which these strange returns happen is reduced in size when going from 16 sites in the numerical calculations to 20 sites. This confirms that the presently achieved sizes of the quantum systems for numerical calculations can produce even qualitatively invalid results, and therefore analytical calculations are necessary, too.

We point out that despite the fact that the relevant perturbations in general produce a gap for the low-lying excitations, one can apply the results of this paper to real gapless

multichain spin systems, too. For example, it was recently observed that even for the two-leg ladder system $SrCa_{12}Cu_{24}O_{41}$ the spin gap collapses under pressure.[49]

7. CONCLUDING REMARKS

In this paper, motivated by recent progress in the experimental measurements for multichain spin systems, we have theoretically studied the behavior in an external field of a wide class of multichain quantum spin models and quantum field theories. First, we have investigated the external field behavior of the exactly integrable two-chain spin-1/2 model and have shown that the inclusion of the magnetic anisotropy of the easy-plane type, for which the system stays in the quantum critical region, does not qualitatively change the behavior in an external magnetic field. However, we have shown that the magnetic anisotropy alters the critical values of the magnetic fields and intrachain couplings at which the phase transitions occur and affects the critical exponents. We have shown that the external-field-induced phase transitions we discussed are the commensurate–incommensurate phase transitions due to the next-nearest-neighbor two-spin interactions, which are present in these multichain models with zigzag-like couplings. We have pointed out that the low-lying excitations of the conformal limit of our class of multichain spin models are not independent in the incommensurate phase, because they are governed by the same magnetic field. We have shown that these two-chain quantum spin models share the most important features of the behavior in an external field with the wide class of $(1+1)$ quantum field theories.

We have introduced higher-spin versions of the two-chain exactly solvable spin models, e.g., we have investigated the important class of 1D two-chain quantum ferrimagnets with different spin values at the sites of each chain. Here we have shown that the phase transitions in an external magnetic field in this exactly solvable two-chain quantum ferrimagnet are similar in nature to the phase transitions between the spin-compensated and uncompensated phases in ordinary classical 3D ferrimagnets.

We have also studied the behavior of the multichain exactly solvable spin models in an external magnetic field and shown how the additional phase transitions arising due to the increasing number of chains vanish in the quasi-2D limit. Hence, to the best of our knowledge, we have proposed the first exact scenario of the transition from 1D to 2D quantum spin models in the presence of an external magnetic field. We have argued that the commensurate–incommensurate phase transitions in the multichain quantum spin models have to disappear in the limit of an infinite number of chains.

Finally, we have shown how the relevant deviations from integrability, i.e., the presence of three-spin (spin chiral) terms in the Hamiltonians which separately break the parity and time-reversal symmetries, give rise to gaps in spectra of the low-lying excitations of the multichain quantum spin systems, and we have calculated the critical scaling exponents for these gaps. We pointed out the qualitative agreement of our exact analytical calculations with recent numerical simulations for zigzag spin models.

*E-mail: zvyagin@ilt.kharkov.ua

---

[1] For a recent review on so-called ''ladder'' systems, see E. Dagotto and T. M. Rice, Science **271**, 618 (1996) and references therein.

[2] D. C. Johnston, J. W. Johnston, D. P. Goshorm, and A. P. Jacobson, Phys. Rev. B **35**, 219 (1987); Z. Hiroi, M. Azuma, M. Takano, and Y. Bando, J. Solid State Chem. **95**, 230 (1990); M. Azuma, Z. Hiroi, M. Takano, K. Ishida, and Y. Kitaoka, Phys. Rev. Lett. **73**, 3463 (1994); Y. Ajiro, T. Asano, T. Inami, H. Aruga-Katori, and T. Goto, J. Phys. Soc. Jpn. **63**, 859 (1994); G. Chaboussant, P. A. Crowell, L. P. Lévy, O. Piovesana, A. Madouri, and D. Mailly, Phys. Rev. B **55**, 3046 (1997); S. A. Carter, B. Batlogg, R. J. Cava, J. J. Krajewski, W. F. Peck, Jr., and T. M. Rice, Phys. Rev. Lett. **77**, 1378 (1996); G. Chamboursant, Y. Fagot-Revurat, M.-H. Julien, M. E. Hanson, C. Berthier, M. Horvatić, L. P. Lévy, and O. Piovesana, Phys. Rev. Lett. **80**, 2713 (1998); W. Shiramura, K. Takatsu, B. Kurniawan, H. Tanaka, H. Uekusa, Y. Ohashi, K. Takizawa, H. Mitamura, and T. Goto, J. Phys. Soc. Jpn. **67**, 1548 (1998).

[3] A. M. Tsvelik, Phys. Rev. B **42**, 779 (1990).

[4] V. Yu. Popkov and A. A. Zvyagin, Phys. Rev. Lett. **175**, 295 (1993).

[5] N. Muramoto and M. Takahashi, Preprint, cond-mat/9902007.

[6] H. Bethe, Z. Phys. **71**, 205 (1931).

[7] V. E. Korepin, N. M. Bogoliubov, and A. G. Izergin, *Quantum Inverse Scattering Method and Correlation Functions*, Cambridge University Press, Cambridge, 1993.

[8] M. Oshikawa, M. Yamanaka, and I. Affleck, Phys. Rev. Lett. **78**, 1984 (1997).

[9] A. A. Zvyagin, Phys. Rev. B **57**, 1035 (1998).

[10] H. Frahm and C. Rödenbeck, J. Phys. A **30**, 4467 (1997).

[11] A. A. Zvyagin, JETP Lett. **60**, 580 (1994); Phys. Rev. B **51**, 12579 (1995); A. A. Zvyagin and H. Johannesson, Europhys. Lett. **35**, 151 (1997).

[12] R. J. Baxter, *Exaxtly Solved Models in Statistical Mechanics*, Academic, Press, Orlando (1982).

[13] A. A. Zvyagin, JETP Lett. **63**, 204 (1996).

[14] N. Andrei and J. H. Lowenstein, Phys. Rev. Lett. **43**, 1698 (1979).

[15] L. D. Faddeev and L. A. Takhtadjan, Phys. Lett. A **85**, 375 (1981).

[16] K. Fabricius, A. Klüumper and B. M. McCoy, Preprint, cond-mat/9810278.

[17] A. A. Belavin, A. M. Polyakov, and A. B. Zamolodchikov, Nucl. Phys. B **41**, 333 (1984); J. L. Cardy, Nucl. Phys. B **270**, 186 (1986); H. W. J. Blöte, J. L. Cardy, and M. P. Nightingale, Phys. Rev. Lett. **56**, 742 (1986); I. Affleck, *ibid.* **56**, 746 (1986).

[18] H. J. de Vega and F. Woynarowich, Nucl. Phys. B **251**, 439 (1985); N. M. Bogoliubov, A. G. Izergin, and V. E. Korepin, Nucl. Phys. B **275**, 687 (1986); F. Woynarovich and H.-P. Eckle, J. Phys. A **20**, L97 (1987); *ibid.* **20**, L443 (1987); N. M. Bogoliubov, A. G. Izergin, and N. Yu. Reshetikhin, J. Phys. A **20**, 5361 (1987); A. G. Izergin, V. E. Korepin, and N. Yu. Reshetikhin, *ibid.* **22**, 2615 (1989); F. Woynarovich, H.-P. Eckle, and T. T. Truong, *ibid.* **22**, 4027 (1989); H. Frahm and V. E. Korepin, Phys. Rev. B **12**, 10553 (1990); N. Kawakami and S.-K. Yang, Phys. Rev. Lett. **65**, 2309 (1990); H.-P. Eckle and C. J. Hamer, J. Phys. A **24**, 191 (1991).

[19] H. Frahm and C. Rödenbeck, Preprint cond-mat/9812103.

[20] V. E. Korepin, Theor. Math. Phys. **41**, 953 (1979).

[21] S. Park and K. Lee, J. Phys. A **31**, 6569 (1998).

[22] G. I. Japaridze and A. A. Nersesyan, Phys. Lett. A **85**, 23 (1981).

[23] C. Destri and T. Segalini, Nucl. Phys. B **55**, 759 (1995).

[24] C. Destri and H. J. de Vega, Phys. Lett. B **201**, 245 (1988).

[25] A. Luther and V. J. Emery, Phys. Rev. Lett. **33**, 589 (1974).

[26] V. O. Tarasov, L. A. Takhtadzhyan, and L. D. Faddeev, Theor. Math. Phys. **57**, 1059 (1983).

[27] N. M. Bogolybov and A. G. Izergin, Theor. Math. Phys. **59**, 441 (1984).

[28] C. Destri and H. J. de Vega, J. Phys. A **22**, 1329 (1989).

[29] G. I. Japaridze, A. A. Nersesyan, and P. B. Wiegmann, Nucl. Phys. B **230**, 511 (1984).

[30] C. Destri and H. J. de Vega, Nucl. Phys. B **504**, 621 (1997).

[31] N. Andrei and J. H. Lowenstein, Phys. Lett. B **90**, 106 (1980).

[32] A. M. Polyakov and P. B. Wiegmann, Phys. Lett. B **131**, 121 (1983).

[33] A. M. Polyakov and P. B. Wiegmann, Phys. Lett. B **141**, 223 (1984).

[34] P. B. Wiegmann, Phys. Lett. B **141**, 217 (1984); *ibid.* **152**, 209 (1985).

[35] L. A. Takhtajan, Phys. Lett. A **87**, 479 (1982); H. M. Babujian, Nucl. Phys. B **215**, 317 (1983).

[36] H. J. de Vega and F. Woynarovich, J. Phys. A **25**, 4499 (1992).

[37] P. Schlottmann, Phys. Rev. B **19**, 9202 (1994).

[38] A. A. Zvyagin and P. Schlottmann, Phys. Rev. B **52**, 6569 (1995).

[39] P. P. Kulish, N. Yu. Reshetikhin, and E. K. Sklyanin, Lett. Math. Phys. **5**, 393 (1981).

[40] L. Kadanoff and A. C. Brown, Ann. Phys. (N.Y.) **121**, 318 (1979).

[41] A. B. Zamolodchikov and V. A. Fateev, Sov. Phys. JETP **62**, 215 (1985); D. Gepner and Z. Qiu, Nucl. Phys. B **285**, 423 (1987).

[42] A. N. Kirillov and N. Yu. Reshetikhin, J. Phys. A **20**, 1587 (1987); F. C. Alcaraz and M. J. Martins, *ibid.* **22**, 1829 (1989); H. Frahm and N.-C. Yu, *ibid.* **23**, 2115 (1990).

[43] P. Schlottmann and A. A. Zvyagin, Phys. Rev. B **56**, 13989 (1997).

[44] E. Lieb, T. Schultz, and D. Mattis, Ann. Phys. (N.Y.) **16**, 407 (1961); I. Affleck and E. H. Lieb, Lett. Math. Phys. **12**, 57 (1986).

[45] F. D. M. Haldane, Phys. Lett. A **93**, 464 (1983).

[46] A. A. Nersesyan, A. O. Gogolin, and F. H. S. Essler, Phys. Rev. Lett. **81**, 910 (1998).

[47] C. K. Majumdar and D. K. Ghosh, J. Math. Phys. **10**, 1388 (1969).

[48] K. Okunishi, Y. Hieida, and Y. Akutsu, Preprint, cond-mat/9904155.

[49] H. Mayaffre, P. Auban-Senzier, M. Nardone, D. Jerome, D. Poilblanc, C. Bourbonnais, U. Ammerahl, G. Dhalenne, and A. Revcolevschi, Science **279**, 345 (1998).

QUANTUM EFFECTS IN SEMICONDUCTORS AND DIELECTRICS

NMR study of the low-temperature phase of vanadium dioxide

L. A. Boyarskiĭ, S. P. Gabuda, and S. G. Kozlova

Institute of Inorganic Chemistry, Siberian Branch of the Russian Academy of Sciences,
Novosibirsk State University, pr. Ak. Lavrent'eva 3, 630090 Novosibirsk, Russia

The magnetic shielding and quadrupole interaction constants of ^{51}V nuclei in the low-temperature (nonconducting) phase of vanadium dioxide are determined by magnetic resonance on the ^{51V} nuclei. It is shown that the metal–insulator transition in VO_2 is accompanied by a change in the sign of the magnetic shielding constant and by an electronic transition $2V^{4+} \rightarrow V^{3+} + V^{5+}$, which is accompanied by a charge ordering in the cation sublattice. © *2000 American Institute of Physics.* [S1063-777X(00)01102-6]

INTRODUCTION

Transition metal oxides have been attracting research attention for a long time now. Of particular interest are the oxides of titanium and vanadium, whose $3d$ and $4s$ shells are strongly hybridized. These substances exhibit unusual electrical, optical, magnetic, and thermodynamic properties and undergo phase transitions. The most thoroughly studied are oxides of vanadium doped with alkali or transition elements (e.g., NaV_2O_5 [Refs. 1 and 2] or $V_{1-x}Nb_xO_2$ [Ref. 3], respectively). In the low-temperature, nonmetallic phases these compounds exhibit exotic properties due mainly to the nonuniform distribution of charge density and spin density in them. In particular, unusual antiferromagnetic structures are present in $(VO)_2P_2O_7$ (Ref. 4), and the properties of LiV_2O_4 are described in the framework of heavy-fermion concepts.[5]

However, there is a simpler structure that is also of interest: pure vanadium dioxide. It is known that below $T_c = 340$ K, VO_2 undergoes a first-order metal–insulator (or, according to other data, metal–semiconductor) phase transition. At the transition there is a change in lattice symmetry. The high-temperature, metallic phase of the tetragonal system has the rutile (TiO_2) structure. The low-temperature, nonconducting phase is monoclinic, with a crystal structure that is a slightly deformed version of the initial lattice, with distorted octahedral coordination of the vanadium ions. There is a doubling of the period and a modulation of the chains of vanadium ions along the c axis of the initial lattice, which corresponds to the a axis in the structure of the low-temperature phase. This results in the formation of V–V pairs with a somewhat shortened distance $d(V-V) = 2.62$Å within the pairs and a lengthened distance (3.17 Å) between the nearest vanadium ions of the neighboring pairs.

The available information about the magnetic properties of vanadium dioxide is inconsistent. It follows from Ref. 6 that the low-temperature phase is paramagnetic, with a small susceptibility that is practically independent of temperature. The growth in the susceptibility at helium temperatures observed in Ref. 6 was attributed to the presence of impurities in the sample. In Ref. 7, however, it is asserted that the susceptibility of the dioxide obeys the Curie law with an effective moment of $2\mu_B$, which corresponds to the trivalent vanadium ion. At the same time, in Ref. 8 a diamagnetic low-temperature phase of VO_2 is reported.

On account of the $3d$ electronic configuration of the V^{4+} ion, it would be natural to have spin paramagnetism. However, the mutually contradictory data obtained in reality suggest both the presence of impurity effects and a possible nonuniform distribution of the charge density. In particular, it seems likely that a pairing of the $3d^1$ electrons of the V^{4+} ions occurs. One of the possible pairing mechanisms may be based on the small-radius bipolaron concept proposed by Anderson.[9] In the polaron model, two electrons can be localized in the immediate proximity of each other on account of a strong local distortion of the crystal lattice. In particular, it has been shown[10] that in the mixed oxide $(Ti_xV_{1-x})O_2$ the ground state of the electron system evolves continuously with x from a superconducting state of the BCS type to an insulator state in which the Cooper pairs are localized in the form massive bipolarons.[9] It is entirely realistic to suppose that for pure binary VO_2 the insulator and weakly magnetic states are brought about by an analogous type of bipolaron mechanism of electron pairing. However, in that case the transition from the conducting to the insulating (semiconducting) state should be accompanied by the appearance of structurally inequivalent vanadium ions, a change in the charge distribution, and charge ordering in the system.

The NMR method holds great promise for investigating nonuniform charge-density distributions. Results have been published[11,12] for studies of the ^{51}V nuclei in VO_2 in relatively weak (up to 1.8 T) magnetic fields. It was shown that in the metallic phase, VO_2 exhibits an anomalous (diamagnetic) Knight shift of the NMR signal (i.e., in the direction of higher magnetic fields relative to the NMR signal of free ^{51}V nuclei). At the transition to the nonconducting phase of VO_2 the NMR signal undergoes a jump to lower magnetic fields, i.e., corresponding to paramagnetic shifts of the NMR. In

addition, it was found that the spectral band of the NMR in the nonconducting phase is split into two asymmetric lines; this was explained as being due to a sharp increase in the electric field gradient at the sites of localization of the vanadium ions. However, because of the insufficiently high magnetic fields used, it was not possible to investigate the contribution of a possible structural inequivalency of the vanadium ions.

EXPERIMENT

We undertook a study of the charge distribution and the electron–nuclear interactions in the nonconducting low-temperature phase of vanadium dioxide by the method of NMR on ^{51}V nuclei in both low and high (up to 9.4 T) magnetic fields. Since the phase transition entails a jump in the volume of the unit cell (by 8%), it is problematic to obtain single-crystal samples from the melt and preserve them in that state through the transition to normal conditions. We therefore limited the study to the characteristics of poly-crystalline VO_2. The powder samples were synthesized by a technique based on the solid-phase reaction $V_2O_3 + V_2O_5 \rightarrow 4VO_2$ (Ref. 13). According to the data of an x-ray phase analysis, the impurity content in the sample was not more than 1%. From an analysis of the stoichiometry of the samples in respect to the oxygen content, we obtained the formula $VO_{2.01 \pm 0.01}$.

For the measurements in fields from 1.4 to 1.8 T we used a wide-line spectrometer equipped with a cryostat for low-temperature studies, including at helium temperatures. The measurements in high magnetic fields ($B_0 = 9.4$ T) were done on a production-model Bruker MSL-400 multinuclear spectrometer, which comes equipped with a superconducting solenoid. To increase the signal/noise ratio the MAS technique was used (rapid spinning of the sample (up to 10 thousand rpm) at the ''magic'' angle $54°44'$ relative to the magnetic field direction). A study of the low-field NMR spectra in the temperature interval from 77 to 300 K did not reveal any substantial changes in the position and shape of the lines. At the same time, making low-temperature measurements with the use of the MAS technique is extremely difficult. We therefore used room-temperature data for our analysis. It should be noted once again that the point of the metal–insulator transition in vanadium dioxide lies considerably lower.

The number of integrations was ∼1000 at a pulse duration of 0.7 μs and a delay between pulses of 0.5 s; the duration of an integration was 80 h. Liquid $VOCl_3$ was used as an external reference standard for the measurements of the NMR shifts.

MEASUREMENTS IN A HIGH MAGNETIC FIELD

In a magnetic field of 9.4 T we obtained a multicomponent, asymmetric NMR spectrum of ^{51}V, with a width of up to 0.1 T (Fig. 1). The very large broadening of the spectrum is due to first-order quadrupole effects, which also complicate the analysis of the magnetic shielding effects (Appendices 1 and 2). Since the first-order effects lead to a symmetric broadening of the spectral bands, it is clear that the asym-
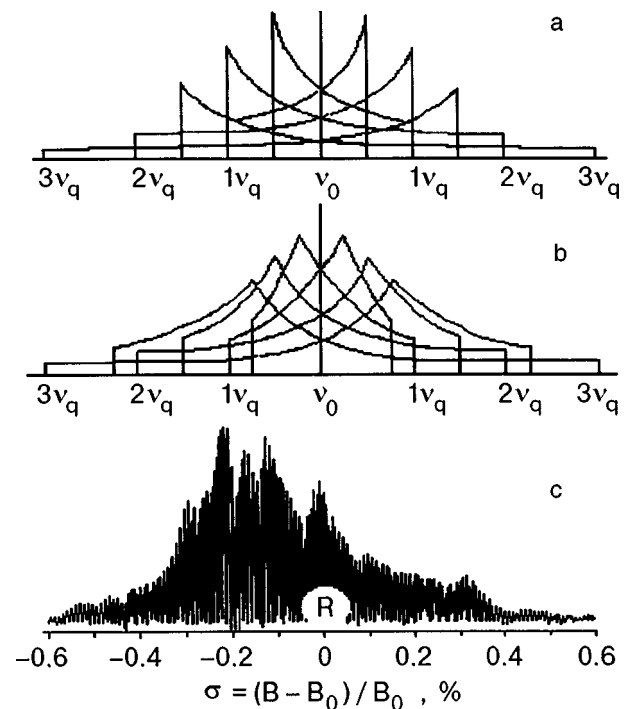

FIG. 1. Theoretical NMR spectra due to first-order quadrupole effects for nuclear spin 7/2 with different asymmetry parameters: $\eta = 0$ (a) and 0.5 (b); the experimental NMR spectrum of ^{51}V in VO_2 in a field $B_0 = 9.4$ T (c). R is the marker from $VOCl_3$.

metric spectrum observed in the experiment is the result of a superposition of two symmetric bands of different widths, shifted with respect to each other. A computer modeling of the spectrum confirmed this hypothesis and enabled us to separate the initial experimental spectrum into two lines of approximately equal intensity, shifted relative to each other by $0.25 \pm 0.01\%$ (Fig. 1). The results of this separation show that there are two structurally and chemically different positions of the vanadium ions, V(1) and V(2), in the low-temperature phase of VO_2. The parameters of the electric quadrupole interactions inferred from the analysis are presented in Table I and Fig. 2, together with the isotropic mean of the magnetic shielding of the vanadium nuclei.

From a comparison with the known spectroscopic data for vanadium compounds we can assign the NMR signal of

TABLE I. Quadrupole interaction and magnetic shielding parameters for $^{51}V(1)$ nuclei in the metallic and nonconducting phases of VO_2.

Phase of VO_2	Quadrupole coupling constant, MHz	Asymmetry parameter η	Nuclear shielding constant $\langle \sigma \rangle = (B - B_0)/B_0$, %
Metallic [Refs. 11 and 12]	4.90	0.9	+0.380
Nonconducting			
V(V)*	4.64	0.35	+0.002
V(V)**	4.31	0.35	+0.019
V(III)*	5.95	0.8	−0.249
V(III)**	5.75	0.5	−0.232

Note: The results of an analysis of the NMR spectra of ^{51}V in fields of 1.5 and 9.4 T are indicated by * and **, respectively.
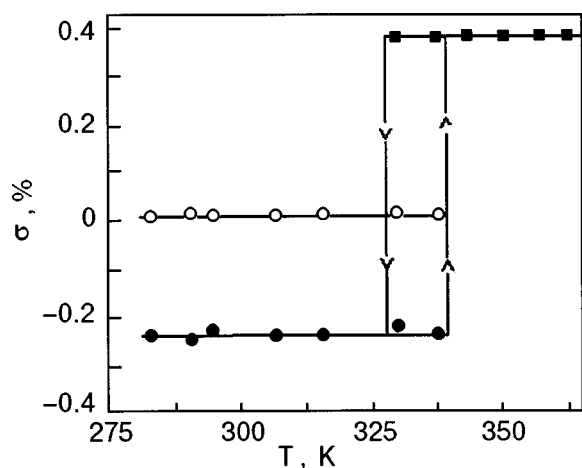
FIG. 2. Temperature dependence of the shielding constants of vanadium near T_c. In the low-temperature phase there are two constants, corresponding to two valence states of the vanadium ions, V^{3+} (○) and V^{5+} (●); in the high-temperature phase there is one constant, corresponding to V^{4+} (■).

V(1) to V^{5+} ions, and the V(2) signal to V^{3+}, with the respective electronic configurations $3d^2$ and $3d^0$, the first of which should be spin-paired (low-spin).

MEASUREMENTS IN LOW MAGNETIC FIELDS

To verify that we are justified in attributing the splitting of the NMR spectra of ^{51}V to the influence of second-order quadrupole effects, we measured the dependence of the doublet splitting on the magnitude of the magnetic field. It was expected, in the framework of the interpretation given in Refs. 12 and 14, that the value of the doublet splitting would be inversely proportional to the external magnetic field. In the experiment we obtained the following values of the splitting: $\Delta B = 34.7$ G at $B_0 = 14.94$ kG, and $\Delta B = 46.5$ G at $B_0 = 17.91$ kG. Thus the field dependence of ΔB observed in the experiment does not support that interpretation of the nature of the spectral splitting. Moreover, the slight growth of ΔB with increasing B_0 suggests an essentially magnetic nature of the splitting of the NMR spectrum of ^{51}V, due to the magnetic inequivalence of the vanadium ions in the nonconducting phase of VO_2.

Proceeding from the data of the high-temperature measurements, we analyzed the shape of the low-field NMR spectra (see Fig. 3 and Appendix 3). We assumed that the observed spectrum is a superposition of two lines described by the different shielding constants found above and with different parameters of the second-order quadrupole interaction (see Table I). We ignored the contributions due to effects of anisotropy of the magnetic shielding and to first-order quadrupole effects. The calculated spectra (Fig. 3) are in good agreement with those obtained in the experiment. The mean-square deviation of the experimental points from the calculated spectrum does not exceed 5%. It can also be noted that the proposed model, with two inequivalent vanadium ions, agrees with the experimental dependence of the doublet splitting on the magnitude of the external magnetic field.
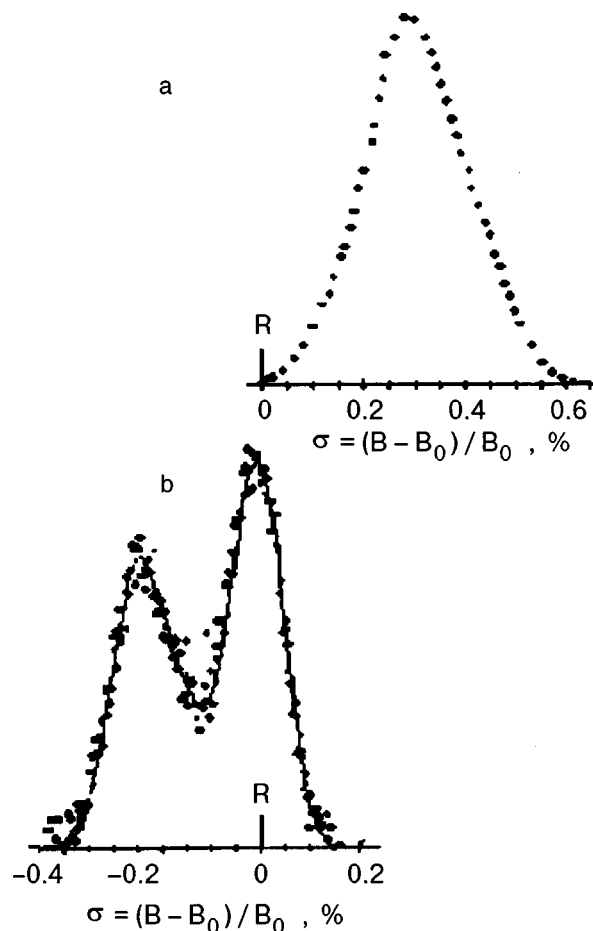

FIG. 3. Experimental (points) and calculated (continuous curve) NMR spectra of ^{51}V in VO_2 in a field $B_0 = 1.4$ T at $T > T_c$ (a: data of Refs. 11 and 12) and for $T < T_c$ (b: our data). The calculated spectrum for $T < T_c$ corresponds to two structurally inequivalent states of the vanadium ions, with the quadrupole and chemical interaction parameters listed in Table 1. R is the marker from $VOCl_3$.

To estimate the error due to neglect of the anisotropy of the magnetic shielding, we determined the characteristic width (of the order of 0.1%) of the central transition $1/2 \leftrightarrow -1/2$ in the high-field NMR spectrum of ^{51}V. For this transition there are no first-order quadrupole effects, and the second-order effects are negligible. It can therefore be assumed that its width is entirely due to the anisotropy of the magnetic shielding. From this we found that the error due to neglecting the anisotropy of the magnetic shielding in the low-field NMR spectra of ^{51}V can reach 3%. The results of a comparison of the data (see Table I) demonstrate good agreement of the parameters calculated for the two values of the magnetic field.

CONCLUSIONS

1. According to our data, the metal–insulator transition in vanadium dioxide is due to the electronic transition $2V^{4+} \rightarrow V^{3+} + V^5$, with the onset of two structurally and chemically different positions of the vanadium ions, V(III) and V(V). Essentially, the position V(III) is characterized by significant antishielding, amounting to -0.24%, and by an increased quadrupole interaction, both in comparison with

the conducting phase and in comparison with the position V(V) of the nonconducting phase. On a qualitative level, both of these facts can be explained by the expected effect of the onset of a bipolaron, as a strong local distortion of the lattice by the electrons. This conclusion is supported by the large values of the quadrupole coupling and magnetic shielding constants of the vanadium nuclei.

2. The anomalous (diamagnetic) Knight shift in the metallic phase of VO_2 is indicative of the predominance of the $s-d$ exchange polarization, for which the Hamiltonian of the interaction should have a negative sign, corresponding to an antiferromagnetic interaction. It can be assumed that the electron pairing mechanism in the low-temperature phase of VO_2 is genetically related to the electron exchange in the high-temperature metallic phase. It is extremely unusual that, in spite of the antiferromagnetic character of the electron–electron interaction, the low-temperature phase of VO_2 in low fields is apparently diamagnetic, and when the field is increased it goes over to an excited weakly paramagnetic state. It should be noted that a stable antiferromagnetic state arises in vanadium oxides in the presence of alkali-metal dopant ions.

3. The observed experimental facts can be more or less adequately interpreted in the framework of a polaron model. However, this approach cannot be considered as ultimately correct. One need only compare the development of the concepts of the transition in NaV_2O_5 crystals and in high-temperature superconductors. In the first case the customary ideas of a spin-Peierls transition have been called into question by Khomskiĭ,[2] who considers this transition to be charge-related. In the second case the theory has been advanced by intimately tying together the spin and charge subsystems. Mainly we have in mind the SO(5) theory developed by Zhang and Demler (see, e.g., Refs. 15 and 16). At the same time, we believe that the polaron models that have been proposed for high-temperature superconductors are far out on the fringe.

We do not rule out the likelihood that vanadium oxides, serving as a kind of model systems for far more complex cuprates, will also in time find a more realistic description. Today, however, we cannot say anything more definite than to propose that a complete study of both the spin and charge degrees of freedom is necessary.

APPENDIX 1

Quadrupole interaction and magnetic shielding of ^{51}V in VO_2

The effective Hamiltonian of the interaction of the nuclear spin ^{51}V ($I=7/2$) can be represented as the sum of three Hamiltonians:

$$H = H_Z + H_Q + H_{sh},$$

where $H_Z = -\mu B_0$ is the Hamiltonian of the Zeeman interaction of the magnetic moment $\mu = \gamma \hat{\mathbf{I}} h/2\pi$ of the vanadium nucleus in an external magnetic field B_0, and γ is the gyromagnetic ratio. In a system described by this Hamiltonian, the resonance frequency is determined by the condition

$$h\nu_0 = \mu B_0/I \quad \text{or} \quad \nu_0 = \gamma/2\pi B_0;$$

$$H_Q = [e^2 qQ/4I(2I-1)][3\hat{I}_Z^2 - \hat{I}^2 + 1/2\eta(\hat{I}_+^2 + \hat{I}_-^2)]$$

is the Hamiltonian of the interaction of the nuclear quadrupole moment Q with the electric field gradient (EFG) $eq = V_{zz}$, $\eta = |V_{xx} - V_{yy}|/V_{zz}$ is the asymmetry parameter of the EFG, where $V_{xx} \leq V_{yy} \leq V_{zz}$, $0 \leq \eta \leq 1$, $\hat{I}_\pm = \hat{I}_x \pm \hat{I}_y$ are components of the nuclear spin operator, and e is the charge of an electron. If the external magnetic field is high enough, $H_Z \gg H_Q$, then in the first order of perturbation theory the quadrupole interaction leads to splitting of the NMR spectrum of ^{51}V into $2I=7$ components positioned symmetrically about ν_0:

$$\nu_m = \nu_0 - \frac{3/4 e^2 qQ[3m^2 - I(I+1)]}{h[2I(2I-1)]}$$
$$\times (3\cos^2\theta - 1 + \eta\sin^2\theta\cos 2\varphi)$$

The angles θ and φ characterize the direction of the field B_0 in the principal axes of the EFG tensor; m is the magnetic quantum number ($m = I, I-1, \ldots, 1$). For a powder sample the spectrum is a family of broad lines. $H_{sh} = \mu\sigma B_0$ is the interaction Hamiltonian of the magnetic moment μ with the electrons of an ion in an external magnetic field B_0; σ is the magnetic shielding (chemical shift) tensor. In general σ can be separated into two parts: an isotropic part σ_{is}, and an anisotropic part σ_{anis}. The isotropic part σ_{is} leads to a shift of the NMR spectrum with respect to ν_0, whereas the anisotropic part σ_{anis} leads to a broadening of the spectrum:

$$\nu = \nu_0[1 - \sigma_{is} - \sigma_{anis}(3\cos^2\theta - 1 + \eta\sin^2\theta\cos 2\varphi)]$$

Ordinarily for vanadium nuclei the broadening of the spectra due to magnetic shielding is much less than the quadrupole broadening.

APPENDIX 2

Calculation of the high-field NMR spectra of ^{51}V in VO_2

Figure 1 shows the calculated NMR spectra of ^{51}V resulting from first-order effects with asymmetry parameters $\eta = 0$ and 0.5. In both cases the spectra are broad and symmetric. In order to obtain agreement between the calculated and observed spectra, we have proposed the existence of two different structural positions of the vanadium nuclei, which are characterized by different EFG tensors $q_{zz}(1)$ and $q_{zz}(2)$ and magnetic shielding tensors $\sigma(1)$ and $\sigma(2)$. To a first approximation we have neglected the anisotropic parts of the magnetic shielding σ_{anis}, since $\nu_0\sigma_{anis}(1,2) \ll e^2 q_{zz}Q$, and we have included only $\sigma_{is}(1)$ and $\sigma_{is}(2)$. In other words, we have modeled the real spectrum by a superposition of two different symmetric bands, shifted relative to each other. The computational procedure was based on a numerical modeling of the convolution integral of the two components with the

use of a Gaussian broadening function with two broadening parameters β_i for the two positions of the ^{51}V nuclei: $\beta_i = \beta(1)$ and $\beta(2)$:

$$F(\nu) = F_1(\nu) + F_2(\nu),$$

where

$$F_i(\nu) = (\beta_i \sqrt{\pi})^{-1} \sum_m \int \int \exp[-(\nu - \nu_{im})^2/$$

$$\beta_i^2] \sin \theta \, d\theta \, d\varphi,$$

$$\nu_{im} = (1 - \sigma_{iis}) \nu_0 - 1/4 \nu_{iQ}(2m-1)$$

$$\times (3 \cos^2 \theta - 1 + \eta_i \sin^2 \theta \cos 2\varphi),$$

$$\nu_{iQ} = 3e^2 q_{izz} Q / [2I(2I-1)h]^{-1}.$$

The optimum fitting parameters of the experimental spectrum to the calculated spectrum, $\sigma(1)$, $\sigma(2)$, $e^2 q_{zz}(1) Q/h$, and $e^2 q_{zz}(2) Q/h$, are presented in Table I.

APPENDIX 3

Calculation of the low-field NMR spectra of ^{51}V in VO$_2$

For $H_Z \gtrsim H_Q$ the description of the NMR spectra of ^{51}V by first-order quadrupole effects becomes inefficient, and one must include the second order of perturbation theory. In this case, taking the quadrupole interaction into account for each position of the nuclei leads to the following shift of the central component of the spectrum:

$$\nu_{i(1/2 \leftrightarrow 1/2)} = (1 - \sigma_{iis}) \nu_0 - (R_i/6\nu_0)$$

$$\times [A_i(\varphi) \cos^4(\theta) + B_i(\varphi) \cos^2(\theta) + C_i(\varphi)],$$

where

$$R_i = (3e^2 q_{zzi} Q / [2I(2I-1)h])^2 [I(I+1) - 3/4],$$

$$A_i(\varphi) = -27/8 + 9/4 \eta_i \cos 2\varphi - 3/8 \eta_i^2 \cos^2 2\varphi,$$

$$B_i(\varphi) = 30/8 - 1/2 \eta_i^2 - 2 \eta_i \cos 2\varphi + 3/4 \eta_i^2 \cos^2 2\varphi,$$

$$C_i(\varphi) = -3/8 + 1/3 \eta_i^2 - \eta_i/4 \cos 2\varphi - 3/8 \eta_i^2 \cos^2 2\varphi.$$

The experimental low-field NMR spectrum of ^{51}V was modeled by the convolution integral of the two components with the use of a Gaussian broadening function:

$$F(\nu) = F_1(\nu) + F_2(\nu),$$

$$F_i(\nu) = (\beta_i \sqrt{\pi})^{-1} \int \int \exp[-(\nu - \nu_i)^2/\beta_i^2] \sin \theta \, d\theta \, d\varphi.$$

The optimum parameters of the quadrupole interaction were determined from the condition of minimization of the function

$$\sum_i [F_{\exp}(\nu_i) + F(\nu_i)]^2 = \min.$$

[1] A. N. Vasil'ev, A. I. Smirnov, M. Isobe, and Y. Ueda, Phys. Rev. B **56**, 5065 (1997).
[2] M. V. Mostovoy and D. I. Khomskii, cond-mat/9806215.
[3] G. Villeneuve, A. Bordet, A. Casalot, J. P. Pouget, H. Launois, and P. Lederer, J. Phys. Chem. Solids **33**, 1953 (72).
[4] J. Kikuchi, K. Motoya, T. Yamauchi, and Y. Ueda, cond-mat/9902205.
[5] V. I. Anisimov, M. A. Korotin, M. Zölfl, T. Pruschke, K. Le Hur, and T. M. Rice, cond-mat/9903372.
[6] J. P. Pouget, P. Lederer, D. S. Schreiber, H. Launois, D. Wohlleben, A. Casalot, and G. Villeneuve, J. Phys. Chem. Solids **33**, 1960 (1972).
[7] H. Trarieux, J. C. Bernier, and A. Michel, Ann. Chim. (Paris) **4**, 183 (1969).
[8] R. N. Pletnev, L. V. Zolotukhina, and V. A. Gubanov, *NMR in Compounds of Variable Composition* [in Russian], Nauka, Moscow (1983).
[9] P. W. Anderson, Phys. Rev. Lett. **34**, 953 (1975).
[10] B. K. Chakraverty, Phys. Rev. B **17**, 953 (1978).
[11] J. Umeda, H. Kusumoto, K. Narita, and E. Yamada, J. Chem. Phys. **42**, 1458 (1965).
[12] G. F. Lynch, S. L. Segel, and M. Sayer, J. Magn. Res. **15**, 8 (1974).
[13] F. J. Morin, Phys. Rev. Lett. **3**, 34 (1959).
[14] G. Anderson, Acta Chem. Scand. **24**, 420 (1970).
[15] Shou-Cheng Zhang, cond-mat/9709289.
[16] E. Demler and Shou-Cheng Zhang, cond-mat/9806336

Translated by Steve Torstveit

PHYSICAL PROPERTIES OF CRYOCRYSTALS

Stimulation of argon desorption by an oxygen impurity

A. G. Belov,* E. M. Yurtaeva, and I. Ya. Fugol'

B. Verkin Institute for Low Temperature Physics and Engineering, National Academy of Sciences of Ukraine, pr. Lenina 47, 61164 Kharkov, Ukraine
(Submitted July 1, 1999; revised September 13, 1999)
Fiz. Nizk. Temp. **26**, 204–213 (February 2000)

The influence of an oxygen impurity on the efficiency of desorption of excited atoms and molecules from the surface of crystalline argon is investigated. A significant increase in the yield of desorbed particles is observed at an O_2 concentration of 1 at. % in the argon host matrix. It is shown that a xenon impurity does not have a similar effect. Possible mechanisms are proposed for the stimulation of argon desorption by impurity oxygen. One of them may involve the formation of argon microclusters around O^- ions near the surface of the crystal. Another mechanism may be due to an increase in the probability of recombination of Ar_2^+ with an electron on account of the hopping of the negative charge between the O_2^- and Ar_2^+ ions. © *2000 American Institute of Physics.* [S1063-777X(00)01202-0]

INTRODUCTION

The desorption of atoms and molecules from solid surfaces has become a topic of much wider research interest in recent years on account of the new desorption mechanisms involving the electronic excitation of crystals and the possibility of selectively studying these processes by means of synchrotron radiation.[1–12] Modern technology makes it possibility to measure the absolute efficiency of desorption, for which crystals of inert gases are model objects.[13,14] Of particular interest is the desorption of excited particles.

The luminescence spectra of desorbed Ar* atoms in the states $^1P_1$ and $^3P_1$ and also "hot" unrelaxed $Ar_2^{(v)}$ molecules in high vibrational states near the surface of crystalline argon have been recorded for various means of excitation: heavy ions,[3,9,15] electrons,[2,5,9,10,16] and photons of synchrotron radiation.[4,7,12,17] By now several processes responsible for the desorption of rare gas atoms (R) from a crystal have been identified. One of them is due to the localization of free excitons near the surface, with the release of a considerable energy E_{LR} to the lattice. The subsequent ejection of an excited atom Ar* occurs as a result of the deformation of the lattice due to the self-trapping (autolocalization) process. A second process involves the dissociative decay of argon molecules in highly excited vibrational states $Ar_2^{*(v)}$ near the surface of the crystal. Measurements made in Ref. 6 show that in the excitation of electrons with energy $E_e = 200$ eV the first process is almost an order of magnitude more efficient than the second.

Yet another "stimulator" of desorption is dissociative recombination of a self-trapped hole and an electron at the surface of the crystal.[3,17] The excess kinetic energy released in this process can cause ejection of an excited atom from the confines of the sample. Together with the desorption of neutral particles R found in the ground and excited states, the desorption of positively charged ions R^+ is also observed, and this suggests that charged excitations are participating in the process.[6]

The presence of impurity centers in crystals can appreciably alter the kinetics of electronic excitations, since they are efficient traps for both charged and excitonic excitations, which govern the desorption process. Research on the influence of impurities on the argon desorption efficiency has been reported in Refs. 15 and 16. In both cases high-energy particles were used for excitation of the crystals: He$^+$ ions[15] and electrons.[16] In measurement of the desorption efficiency the total yield of neutral particles (Ar+Ar*) was recorded, without discriminating the individual components. In Ref. 15 the luminescent intensity of the whole sample was also monitored, but it corresponded mainly to the strongest fundamental emission of Ar_2^* from the bulk, and not from the desorbed components. Although the overall result of both studies shows a decrease in the desorption efficiency when impurities are added to crystalline Ar, there were certain peculiarities observed when the impurity was oxygen. In particular, in Ref. 15 it was reported that the signal from desorbed argon dimers became stronger in the presence of an admixture of 5 at. % O_2, while a nitrogen impurity had no such effect. In Ref. 15 it was mentioned that the desorption yield in crystals coated with a film of oxygen sometimes gets stronger before decreasing to the normal value for the sputtering of the film. Neither paper discusses the causes of these effects. We also note that studies[18] have shown that the negatively charged atomic ions O^- are present in the flux of particles desorbed from argon crystals containing an oxygen impurity.

In the present study we have observed a significant enhancement of the desorption of excited atoms and molecules of argon in the presence of impurity oxygen. A xenon impurity causes no such effect and even tends to decrease the

desorption in the ternary mixtures $Ar+O_2+Xe$. Several explanations for the observed effect have been proposed, based on the conjecture that negative oxygen ions are formed in the argon matrix.

EXPERIMENTAL PROCEDURES

　　Studies of the bulk and desorbed components of the emission from pure Ar crystals and Ar crystals containing oxygen and xenon were carried out by the method of luminescence analysis under the excitation of the samples by monochromatic electrons with energy $E_e \approx 2$ keV. The current density was $j = 0.04$ mA/cm^2. Under these conditions the sample did not suffer appreciable erosion over the course of several hours. The electron stream was directed along the normal to the surface of the sample. The optical emission was recorded at an angle of $45°$. The crystals were grown by the gas-phase deposition at a condensation temperature $T_c = 30$ K and then were slowly cooled to $T = 5$ K. The polycrystals obtained were optically transparent. The gaseous argon was purified beforehand in a special apparatus utilizing liquid lithium at a temperature $T = 200 °C$. The oxygen concentration in the pure crystals did not exceed 10^{-4} at. %. The limiting oxygen concentration was 1 at. %. The xenon concentration was varied from 10^{-3} to 1 at. %. Optical studies were done in a flow-through helium cryostat with a substrate temperature that could be regulated over the interval 2.5–78 K. The emitted radiation was recorded in the vacuum ultraviolet region of the spectrum by means of a VMR-2 normal-incidence monochromator in the photon-counting mode. The spectral resolution was 0.05 nm. The working vacuum in the cryostat was maintained at a level of 10^{-10} bar.

RESULTS

　　Figure 1a shows the luminescence spectra in the region of the fundamental emission of Ar_2^* for a pure argon crystal and a crystal containing a 1 at. % oxygen impurity. The spectrum consists of molecular and atomic emission bands of excited centers found in the bulk of the sample and on its surface, and also in the gas phase near the sample. The luminescence of these centers located in the deep layers of the argon crystal corresponds to the well-known transition $Ar_2^*(M)$ $^{1,3}\Sigma_u^+ - {}^1\Sigma_g^-$, with a maximum at an energy E_M near 9.8 eV. The narrow band of atomic luminescence (c) is energetically closer to the forbidden transition $^3P_1 - {}^1S_0$ ($E_c = 11.52$ eV) and is probably due to defect sites of the lattice.[10] The inset shows an enlargement of the emission from the desorbed components, a, b, and W. The desorbed components of atomic origin, Ar^* (a and b), correspond to the transitions $^1P_1 - {}^1S_0$ and $^3P_1 - {}^1S_0$, with emission energies $E_a = 11.83$ eV and $E_b = 11.62$ eV. The emission from the desorbed molecules $Ar_2^{(v)}(W)$ is due to transitions from the high vibrational states $^{1,3}\Sigma_u^{+(v)}$ with energy $E_W = 11.52$ eV. The spectra correspond to the same excitation conditions. The main difference between them is in the relative intensity between the bulk and desorbed components (Fig. 1b). The effect of an oxygen impurity on the luminescence of the argon host is manifested in the quenching of the bulk molecular emission $Ar_2^*(M)$ and in the enhancement of
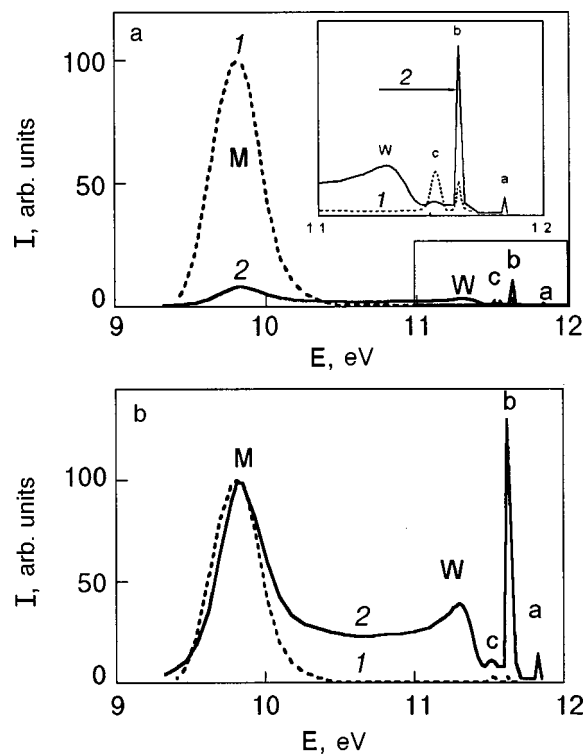

FIG. 1. a: Luminescence spectra of a pure argon crystal (*1*) and a crystal of argon containing 1 at. % O_2 (*2*). The inset shows an enlargement of the emission region of the desorbed components. b: The same spectra, normalized at the maximum to the intensity of the band M (Ar_2^*).

the intensity of the desorbed components a, b, and W. In the region of low oxygen impurity concentrations our data agree well with the results obtained by other authors.[1,10,12] At an oxygen concentration $C = 1$ at. % the ratios $\rho_b = I(b)/I(M)$ and $\rho_W = I(W)/I(M)$ increase significantly. Changing the O_2 impurity concentration led to changes in the intensities of the desorbed and bulk components of Ar_2^* as follows: $\chi_b = \rho_b(1\%)/\rho_b(10^{-4}\%) \approx 30$ and $\chi_W = \rho_W(1\%)/\rho_W(10^{-4}\%) \approx 80$. For the components c the relative intensity $I(c)/I(M)$ did not change appreciably.

　　In the next series of experiments we investigated the same ratios when a Xe impurity was added to the argon matrix. In the pure Ar crystal the ratio ρ_b did not change appreciably as the Xe concentration was increased, in spite of the fact that the M band is also quenched by impurity Xe (even more efficiently than in the case of an O_2 impurity). Figure 2a shows the spectra of pure argon and of argon containing a 0.1 at. % Xe impurity. The distortion of the shape of the Ar_2^* band is apparently due to the superposition of the $^1P_1 - {}^1S_0$ emission of the xenon atom in the matrix. Higher concentrations of Xe lead to the practically complete vanishing of the Ar_1^* emission. In Ar crystals containing 1 at. % O_2, even at a low concentration of impurity Xe, one observes a pronounced decrease of the relative intensities of the desorbed and bulk components. As an illustration of what we have said, Fig. 2b shows the normalized spectra of argon with an oxygen impurity and argon with impurities of oxygen and xenon in equal proportions.

　　Figure 3 shows the change in the relative intensities of the desorbed component b and the component c as the xenon
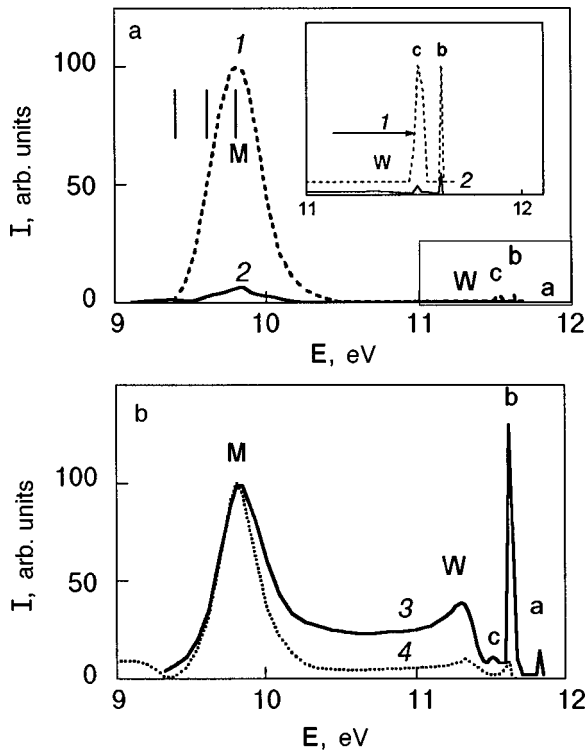
FIG. 2. Luminescence of structures: a—pure argon (*1*) and Ar+0.1 at. % Xe (*2*); b—Ar+1 at. % O$_2$ (*3*) and Ar+1 at. % O$_2$+1 at. % Xe (*4*). The vertical lines mark the positions of the emission bands of Xe in argon in the region of the $^1P_1-^1S_0$ transition.[21] The spectra in b are normalized at the maximum to the intensity of the band *M* (Ar$_2^*$).

concentration increases. At first the ratio $I(b)/I(M)$ decreases rapidly as Xe is added, and then it goes to saturation, while still remaining higher than in the pure crystal. The ratio $I(c)/I(M)$ remains practically unchanged.

Figure 4 shows the relative intensity of the desorbed *W* and bulk *M* molecular luminescence $I(W)/I(M)$ as a function of the Xe concentration. There is an obvious similarity to the behavior of the desorbed components of atomic and molecular origin. The dashed line is the value of $I(W)/I(M)$ in pure argon, which remains considerably lower than in the crystals containing impurity oxygen.

Certain differences in the energy positions of the maxima of the Ar$_2^*$ emission in crystals with different impurity concentrations were also observed. For $C=1$ at. % O$_2$ the maximum is shifted to higher energy by an amount $\Delta E_O \approx 0.04$ eV relative to the pure crystal. For an admixture of Xe, on the other hand, one observes a shift of the maximum of Ar$_2^*$ to lower energies, by an amount $\Delta E_{Xe} \approx 0.07$ eV.

To complete the picture we note that the spectrum of crystalline argon containing oxygen has bands due to the emission of the excimers ArO* and Ar$^+$O$^-$ (2.2 and 6.25 eV, respectively), and also the series of molecular emission bands O$_2^*$ (C$^3\Delta_u^+ \rightarrow X^3\Sigma_g$) in the region from 1.8 to 3 eV. The admixture of xenon effectively quenches this emission and gives rise to characteristic XeO* bands, the intensity of which increases with increasing Xe concentration and reaches a maximum at $C \approx 1$ at. % Xe. A more detailed description of these spectra was published in Ref. 19.
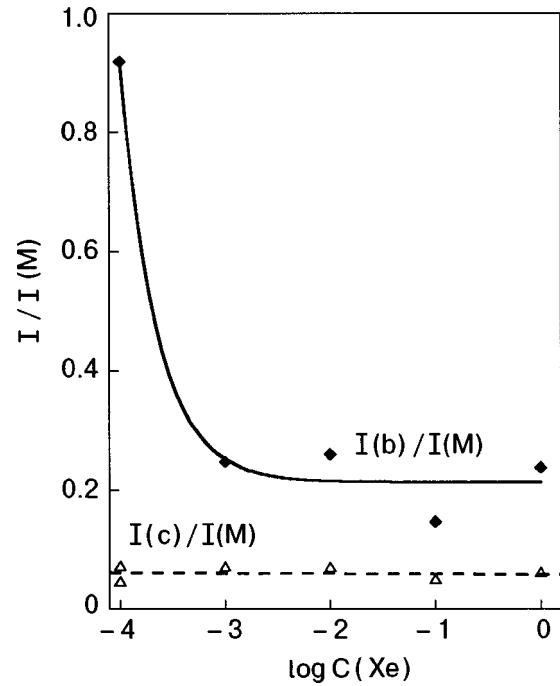

FIG. 3. Relative intensities $I/I(M)$ of the desorbed atomic luminescence *b* and the emission of an atomic defect center *c* versus the xenon concentration in a solution Ar+1 at. % O$_2$+Xe.

The change in the relative intensities $I(b)/I(M)$ of the desorbed and bulk components of Ar$_2^*$ as the O$_2$ concentration is changed is comparable to the corresponding characteristics for the relative intensity of the excimer luminescence of Ar$_2^+$O$^-$ (*H*) and Ar$_2^*$ (see Fig. 5a). As the oxygen concentration is increased, the ratio $I(H)/I(M)$, like $I(b)/I(M)$, increases significantly. We note, however, that for the atomic components *c* one does not observe any sub-
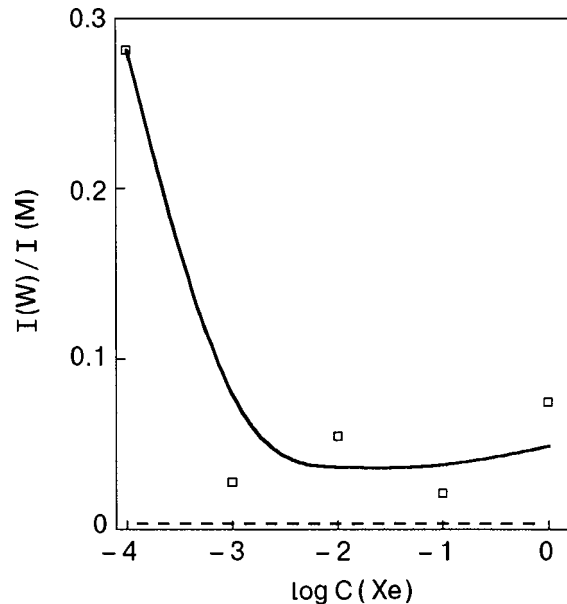

FIG. 4. Relative intensity of the desorbed molecular luminescence $I(W)/I(M)$ versus the Xe concentration in a solution Ar+1 at. % O$_2$+Xe. The dashed line indicates the value of $I(W)/I(M)$ in pure argon.
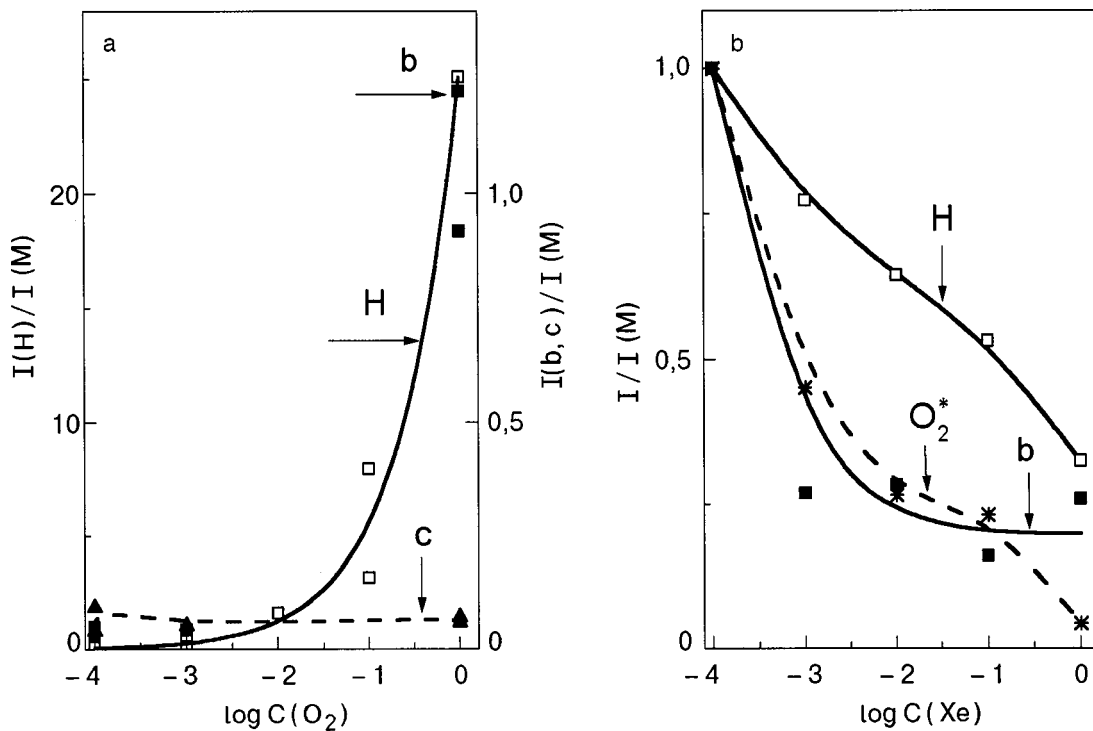
FIG. 5. a: Change in the relative intensities $I/I(M)$ of the emission from the desorbed atoms b (■), the atomic defect component c (▲), and excimers $Ar_2^+O^-$ (H) (□) as the oxygen concentration is increased. b: The relative intensities $I(b)/I(M)$ (■), $I(H)/I(M)$ (□), and $I(O_2^*)/I(M)$ (*) (the transition $C^3\Delta_u^+ \rightarrow X^3\Sigma_g$) as functions of the xenon concentration in crystals of Ar+1 at. % O_2.

stantial changes in the relative intensity $I(c)/I(M)$. On the other hand, the decrease in $I(H)/I(M)$ as Xe is added, although it correlates with $I(b)/I(M)$, nevertheless has a much flatter dependence (see Fig. 5b). The concentration dependence of $I(O_2^*)/I(M)$ is closer to $I(b)/I(M)$.

In addition to an enhancement of the desorption of argon we also observed enhancement of the desorption of xenon impurity centers as oxygen is added. Figure 6 shows two luminescence spectra of the Xe atom in a pure Ar host matrix and in a matrix containing 1 at. % O_2. The narrow peak 0 at $E = 8.44$ eV corresponds to the $^3P_1 - {}^1S_0$ transition of the free Xe atom, while the wider bands 1, 2, and d correspond to centers with varying degrees of deformation of the environment.[20]

DISCUSSION OF THE RESULTS

The set of experimental data indicate the enhancement of the desorption of excited atoms and molecules from the surface of crystalline argon at an oxygen concentration in it of 1 at. %. This enhancement is of both an absolute and a relative character, as is manifested in the significant increase of the ratios $I(b)/I(M)$ and $I(W)/I(M)$. The same is not true of the change in the atomic component c, the relative intensity of which, $I(c)/I(M)$, remains practically unchanged. The admixture of xenon into an argon crystal containing oxygen leads not only to an absolute quenching of the molecular emission but also to a relative decrease in the desorption, $I(b)/I(M)$ and $I(W)/I(M)$.

The observed effects do not have analogs in the framework of the desorption mechanisms that have been discussed up till now. Thermal stimulation processes in this case can-

not give a large contribution to the desorption yield, since the experiment was done at $T = 5$ K. The desorption due to inelastic scattering of high-energy electrons can give a certain
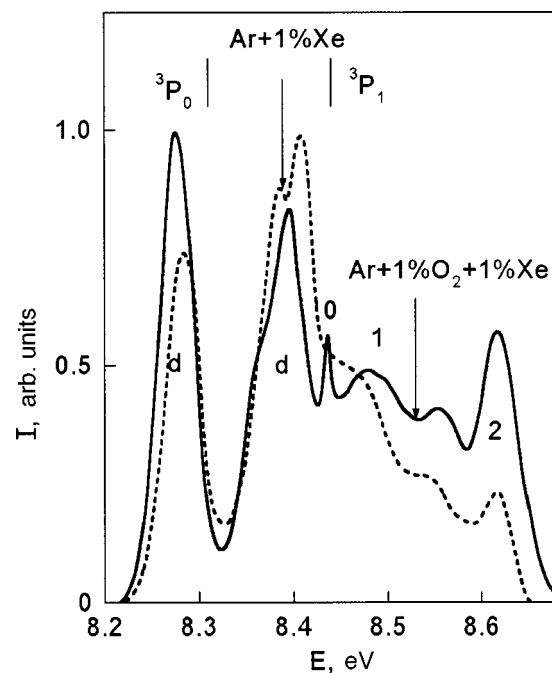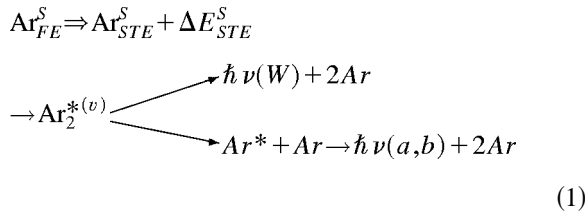

FIG. 6. Luminescence spectra of a Xe impurity atom in a pure Ar matrix (dashed curve) and in a matrix containing 1 at. % O_2 (solid curve). The peak 0 is the emission from the desorbed atom in the state $^3P_1$, while the wider bands 1, 2, and d correspond to centers with plastic, elastic, and defect deformations of the environment of the Xe atom in the Ar crystal. The spectra are normalized to the maximum intensity.

contribution to the observed emission, but it should be constant for any impurity concentration, since the energy of the exciting electrons does not change in the whole series of experiments. One can thus conclude that in the given case a fundamental role in the process of ejection of excited particles from the surface of the sample is played by the electronic excitations of the crystal.

Several channels for this desorption have now been established: 1) excitation of surface excitons; 2) migration of bulk excitons toward the surface of the sample; 3) recombination processes of the charged centers Ar_2^+ with electrons on the surface of the sample.[2,3,12]

When the surface excitons Ar_{FE}^S are localized at the surface, a cavity forms around the localized exciton Ar_{STE}^S as a result of the repulsive interaction, and an excess energy ΔE_{STE}^S is released. The subsequent desorption of the excited molecule (or atom) gives a large contribution to the emission from thin samples:[12]

$$Ar_{FE}^S \Rightarrow Ar_{STE}^S + \Delta E_{STE}^S$$

$$\rightarrow Ar_2^{*(v)} \begin{array}{l} \nearrow \hbar\nu(W)+2Ar \\ \searrow Ar^*+Ar\rightarrow\hbar\nu(a,b)+2Ar \end{array}$$

$$(1)$$

Even at the smallest sample thicknesses used in the experiment ($d\approx 5$ nm) the ratio $I(b)/I(M)=0.3$, i.e., it is 3 times as large as for a massive sample with $d\geqslant 100$ nm.[12] As we see in Fig. 1, the relative enhancement of the desorption in the presence of oxygen is much higher: $I(b)/I(M)\approx 1$, i.e., it is approximately 20 times as large as for a pure crystal. Under the conditions of our experiment, at an energy of the exciting electrons $E_e=2$ keV and $d\approx 5$ μm, the ratio $I(b)/K(M)=0.05$ for pure crystals. This is somewhat below the value $I(b)/I(M)=0.1$ obtained in other studies with the excitation of massive samples by lower-energy electrons or synchrotron radiation.[1,10,12] It should thus be concluded that the excitation of surface excitons does not play an appreciable role under the given experimental conditions, and we shall not consider it further.

The excitation of bulk excitons leads to desorption of the excited atoms only in the case when they reach the surface of the sample in the course of their migration. The excitation spectra of the W band show that the greatest contribution is given by excitons with $n=1,1'$ (Ref. 12). The calculation done in that paper corresponds to a diffusion length $l_0=20$ nm for the excitations responsible for the emission band of desorbed molecules, W. Furthermore, in the subsurface layers (at energies $E_e\sim 0.5$ keV) an additional contribution is given by mobile excitations with a small diffusion length $l_0=2$ nm. This value is comparable to the diffusional range of an exciton $\Gamma(3/2, 1/2)n=1$ for its emergence on the surface of the crystal ($l=5-10$ nm).[12] The mean free path $l_0=20$ nm is characteristic for "hot" excitons with kinetic energy greater than the height of the barrier to self-trapping of Γ excitons $n=1,1'$ or for excitons $n\geqslant 2$.

Let us now consider in more detail the processes of formation of the excitations responsible for desorption. The mean free path of a high-energy exciting electron with energy $E_e=2$ keV is $l\approx 5.5$ nm,[21] and the total depth of its penetration into the crystal is $L\approx 50$ nm.[22] From a comparison of l_0, l, and L one can conclude that the first excited centers formed in the electron irradiation of a crystal will, on average, be formed in the interior of the sample, at a distance of approximately 5 nm from the surface. Apparently the excitons with $n=1,1'$ from just this region of the crystal have the highest probability of emerging on the surface of the sample and subsequently leading to its desorption. The excitations formed at large depths can emerge on the surface if they have a sufficient store of kinetic energy. The probability of formation of such high-energy excitons in irradiation by electrons is quite large, since the energy-loss spectrum of an electron in argon has a maximum at 17.3 eV, i.e., at an energy 3 eV higher than the bottom of the conduction band of the crystal.[23] Unlike the case of photoexcitation, when a crystal is excited by high-energy electrons, the creation of electron–hole pairs is a much more probable process than the direct formation of an exciton. On the other hand, an energy of 17 eV is insufficient for the formation of a genetically unrelated electron–hole pair, which requires 24–27 eV.[21] Consequently, the fast recombination processes of genetically related pairs will lead to the formation of high-energy excitons. It can be concluded from what we have said that both low-energy excitons near the surface and high-energy excitons formed far in the interior of the sample can participate in the formation of desorbed excited particles.

The emergence of an exciton onto the surface is governed by its lifetime with respect to self-trapping and the probability of its trapping by structural disruptions or impurity centers. In general form for steady-state excitation conditions, this process can be represented in the framework of the kinetic equation for the diffusion of a free exciton:

$$\frac{dn_{FE}}{dt}=I_{FE}-n_{FE}\left(\frac{1}{\tau_{STE}}+\frac{1}{\beta_O N_O}\right)$$
$$-(k_O N_O+k_S N_S+k_d N_d)=0, \qquad (2)$$

where n_{FE} is the concentration of free excitons (FE) in the bulk of the sample; I_{FE} is the number of FEs generated per unit volume per unit time; τ_{STE} is the lifetime of a FE with respect to self-trapping; $1/\beta_O N_O$ is a parameter determining the lifetime of a FE with respect to the oxygen-impurity-stimulated formation of Ar_2^*; N_O, N_S, and N_d are the concentrations of oxygen impurity centers, surface atoms, and defects, and k_O, k_S, and k_d are the rate constants for the trapping of a free exciton by these centers, respectively.

Calculating these processes is, generally speaking, a complicated problem. However, in the limiting case of a high oxygen concentration the trapping of an exciton and the transfer of its energy to an impurity are the predominant processes. At 1 at. % O_2 the intensity of the emission from self-trapped $Ar_2^*(M)$ centers decreases by more than an order of magnitude. Here the intensity of the impurity luminescence increases significantly.[19] The probability that an exciton will emerge to the surface, grain boundaries, and defect sites of the lattice should decrease accordingly. The c band, which is possibly due to the emission from atoms in the immediate proximity of defects, grain boundaries, or the sur-

face of the sample behaves in just this way, in correlation with the change in the intensity of the M band. Consequently, the introduction of an oxygen impurity turns on some additional mechanisms which stimulate desorption. Since a xenon impurity in the Ar host does not cause radical changes in the relative intensity $I(b)/I(M)$, one can presume that oxygen has a specific effect on the desorption efficiency.

In our view, this may be due to the positive electron affinity of oxygen. We recall that for an oxygen atom the electron affinity $E_a = 1.465$ eV, while for oxygen molecules $E_a = 0.44$ eV. The argon crystal, in contrast, has a negative electron affinity, defined as $V_0 \equiv E_g - E_{th} = 0.3$ eV. (Here E_g and E_{th} are the width of the energy gap and the threshold energy for the production of photoelectrons, respectively.) Therefore the question of whether the negatively charged ions O^- or O_2^- can be stabilized inside the bulk of the sample requires careful analysis and additional experimental research. We note that in xenon the formation of stable complexes $Xe^+ + F^-$ can occur,[24] but for argon the their existence is improbable. This is because the electron affinity of fluorine ($E_a = 3.4$ eV) is considerably higher than that of oxygen, and V_0 for crystalline xenon has the opposite sign: $V_0 = -0.4$ eV. On the other hand, in argon there exists a rather efficient way of binding negative ions, by the formation of triatomic charge-transfer complexes of the type $Ar_2^+ O^-$ (Ref. 19). After emission to the ground state, the $Ar_2^+ O^-$ complex decomposes into neutral components.

In the subsurface layer the properties of the Ar matrix are altered. Studies have shown[25] that in this region of the crystal the sign of the electron affinity of Ar is changed to positive, and this may promote the formation of a stable ionic complex $Ar_n O^-$. Recent studies have demonstrated the possibility that stable clusters $Ar_n O^-$ can exist.[26] The formation of clusters with $n = 12$ was found to be the most probable. The total energy of stabilization of O^- in such a cluster is 0.63 eV. $Ar_{12} O^-$ clusters have an elevated temperature of the vibrational subsystem T_i. The calculation of Ref. 26 shows that $T_i \approx 20$ K for $n = 12$, while $T_i \approx 4$ K for $n \geq 15$. If such a complex is formed on the surface of the crystal, it can be a zone of weakened internal binding of the atoms. The excitation of such a complex by an exciton that has emerged onto the surface can lead to an increased probability of desorption in this region. $Ar_{12} O^-$ clusters are icosohedra, with the oxygen atom at the center.[26] On the surface of a macroscopic crystal this shape may be altered somewhat. In any case, however, it differs from the fcc structure, possibly being closer to hcp, which is preferable when an oxygen impurity is introduced.[27]

We should also mention that computer modeling of the displacements caused by a neutral oxygen impurity in the argon matrix indicates the possibility of such a restructuring.[28] A calculation shows that the oxygen atom in the ground state at a substitutional position distorts the surrounding lattice very little. The disruptions of the structure around an O atom found in an interstitial position has symmetry D_{4h} and form a tetrahedron in which the closest Ar atoms are displaced approximately 0.4 Å along a vertical axis passing through the oxygen atom and only 0.08 Å in the perpendicular direction. Since the O^- ion has close to a ^2P
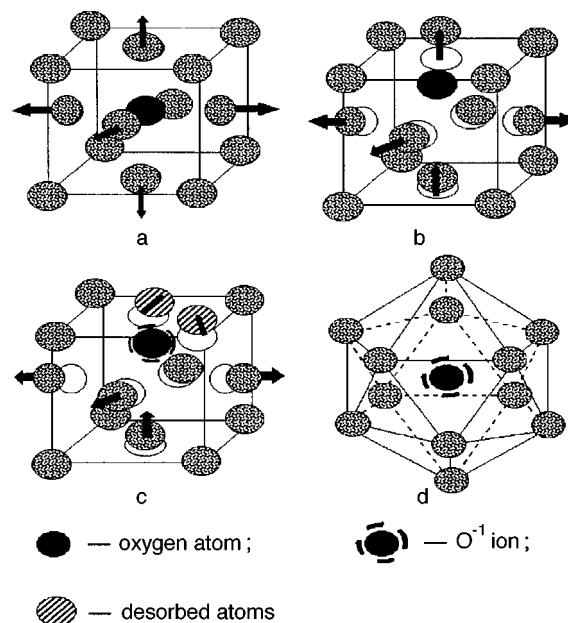

FIG. 7. Structure of the near environment of a neutral oxygen atom in an argon host matrix with an fcc structure, in the perturbed (a) and unperturbed (b) states, and of the O^- atom in the fcc lattice (c) and in an $Ar_{12} O^-$ cluster (d) (Ref. 26).

configuration, and the additional electron enhances the interaction, the deformation may be greater.
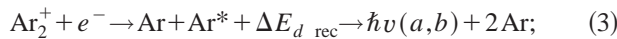
Figure 7 shows the near environment of a neutral oxygen atom in the fcc argon matrix in the perturbed and unperturbed states and also an O^- ion in a cluster. Such a structural rearrangement tends to weaken the binding and makes it easier to remove an Ar surface atom upon its excitation. The fact that the oxygen can remain in a lower-lying layer can account for the absence of luminescence of free O atoms. The proposed model finds agreement with the results of Ref. 18 on the observation of desorption of negatively charged O^- atoms from argon crystals containing an oxygen impurity.

At oxygen concentrations of less than 1 at. % in the argon matrix we did not observe the luminescence of the oxygen molecule O_2, because of its efficient dissociation in interactions with the high-energy excitons of the argon matrix.[29] Similarly, emission from individual O atoms was not observed, only from their compounds with argon: ArO^* and $Ar_2^+ O^-$. This attests to a sufficient degree of stabilization of the O atoms in interstitial positions of the lattice and to the high efficiency of their interaction with the neighboring argon atoms. The maximum intensity of the emission from oxides of argon is reached at an oxygen concentration $C \approx 0.1$ at. %. At $C = 1$ at. % O_2 a quenching of the emission from ArO^* and $Ar_2^+ O^-$ occurs on account of the rise of the molecular luminescence of O_2^*, i.e., the appearance of ''free'' oxygen centers. As we see from Fig. 5b, even small doses of xenon rapidly quench the desorption activity. In addition, the luminescence of ''free'' oxygen molecules, which can trap an electron, also decreases rapidly. At the same time, there is an increase in the intensity of the neutral ''bound'' excimers of oxygen with xenon: XeO^* and $Xe^+ O^-$. All these changes can be brought about by the lo-
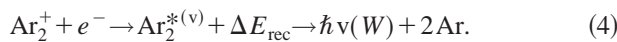
calization of excess oxygen centers near Xe impurity atoms, which have a higher chemical activity than Ar. In turn, the oxygen enhances the desorption of the nearby Xe atom, which lies on the surface (see Fig. 6).

The photoexcitation spectrum obtained in Ref. 12 for the *W* band coincides in its basic outlines with the photoexcitation of the bulk luminescence of Ar_2^*, but with a pronounced redistribution of the intensity in favor of surface excitons and the lowest bulk excitons with $n = 1$.[17] These states apparently give the main contribution to the formation of the states responsible for the *W*-band emission. In addition, the maximum near $2E_g$ is evidence that positive ions play an important role in the population of the excited molecular states $Ar_2^{*(v)}(W)$. As was shown in Ref. 12, it is due to dissociative recombination of a self-trapped hole with an electron near the surface of the sample. We note that the same maximum, corresponding to the formation of hole states, is also present in the excitation spectrum of Ar_2^* molecules in the bulk of the sample.

As compared to the case of photoexcitation, excitation of argon crystals by high-energy electrons has a higher efficiency in the energy region between the maxima just described, which lies approximately 3 eV above E_g and corresponds to the most probable creation of electron–hole pairs.[23] Since the self-trapping time of a hole is very short ($\tau \sim 10^{-12}$ s),[21] the transfer of energy toward the surface occurs via self-trapped molecular ions Ar_2^+. Let us therefore examine the influence of an oxygen impurity on the recombination mechanism of desorption:

$$Ar_2^+ + e^- \rightarrow Ar + Ar^* + \Delta E_{d\ rec} \rightarrow \hbar v(a,b) + 2\,Ar; \qquad (3)$$

or

$$Ar_2^+ + e^- \rightarrow Ar_2^{*(v)} + \Delta E_{rec} \rightarrow \hbar v(W) + 2\,Ar. \qquad (4)$$

The mobility of self-trapped holes is low in comparison with that of free excitons, and the probability of their emerging onto the surface is governed by the lifetime τ_{rec} of Ar_2^+ with respect to recombination with an electron. In turn, τ_{rec} depends on two factors: the initial concentration of charged states and the probability of their trapping by an impurity. The initial concentration of positive ions and electrons in a crystal is essentially determined by the conditions of excitation of the sample, which are kept the same for both the pure crystals and the crystals containing impurities. On the other hand, the trapping of Ar_2^+ at an impurity in the bulk of the sample should lead to a simultaneous decrease in the intensity of both the *M* and *W* bands. This clearly follows from the photoexcitation spectra of these bands, since the contribution of the ion part, which lies above E_g, to the total intensity of the spectrum for them is practically the same. An analogous conclusion was reached in Ref. 15 on the basis of a kinetic model of the trapping of holes at impurity centers. Thus neither of these factors could lead to enhancement of the desorption from the surface of the sample. A third factor that can increase the probability of emergence of positive Ar_2^+ ions onto the surface may be the accumulation of a nonequilibrium concentration of negative charges near the surface in the form of O^- or O_2^- ions. The onset of a local electric field between the oppositely charged ions can appre-

ciably increase the mobility of Ar_2^+ in the direction toward the surface. The subsequent recombination via the formation of intermediate unstable charge-transfer exciplex compounds can lead to the formation of excited $Ar_2^{(v)}$ molecules near the surface of the crystal:

$$Ar_2^+ + O_2^- \rightarrow \{Ar_2^+ O_2^-\}^* + \Delta E_{rec} \rightarrow Ar_2^{*(v)}$$
$$+ O_2 \rightarrow \hbar v(W) + 2\,Ar + O_2. \qquad (5)$$
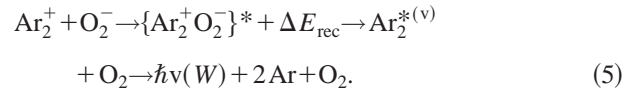
The energy ΔE_{rec} released in the process of recombination promotes the escape of excited atoms and molecules from the surface of the crystal. This mechanism of stimulation can give an additional contribution to the enhancement of the desorption of the excimers $Ar_2^{(v)}$. We note that the recombination of Ar_2^+ with an electron can also come about without the direct participation of oxygen in the process—as a result of the long-distance hopping of an electron between two ions of unlike charge. As was shown in Ref. 30, such a process can occur even at distances $r \approx 1.5$ nm, which is three times the lattice parameter of Ar. In this case oxygen serves only as a temporary trap for stabilization of the electron. Clearly the most important role here will be played by negatively charged molecules, since the binding energy of an electron with O_2^- is 1 eV smaller than with O^-.

Additional studies will be needed to check the proposed hypothesis, including simultaneous measurements of the optical and electrical characteristics of the crystal. There is also a need for more-detailed theoretical studies of the desorption efficiency on the basis of the kinetics of neutral and ionic excitations.

CONCLUSION

We have investigated the desorption of excited atoms and molecules from the surface of crystalline argon under the influence of electron irradiation. In crystals containing an oxygen impurity of around 1 at. % there is significant enhancement of the desorption of excited argon atoms and molecules in comparison with crystals of pure argon. The presence of a xenon impurity in the argon matrix does not cause a similar effect, although an enhancement of the desorption of Xe impurity atoms is observed in the presence of an oxygen impurity. We discussed some possible reasons for the increase in desorption yield stimulated by an O_2 impurity. We proposed two possible mechanisms involving the trapping of electrons at oxygen impurity centers and the formation of O^- and O_2^- ions. One of them would involve the structural rearrangement of the argon lattice near an O^- ion and the resulting decrease in the binding energy of the Ar surface atoms. The other would be due to an increase in the probability of recombination of Ar_2^+ with an electron on account of the transfer of negative charge between O_2^- and Ar_2^+ ions stabilized near the surface of the crystal.

*E-mail: belov@ilt.kharkov.ua

[1] E. Roick, R. Gaethke, P. Gurtler, T. O. Woodruff, and G. Zimmerer, J. Phys. C. **17**, 945 (1984).

[2] F. Coletti, J. M. Debever, and G. Zimmerer, J. Phys. (France) Lett. **45**, L467 (1984).

[3] C. T. Reinmann, R. E. Jonson, and W. L. Brown, Phys. Rev. Lett. **53**, 600 (1984); C. T. Reinmann, W. L. Brown, D. E. Grosjen, M. J. Nowakowski, and W. T. Buller, Phys. Rev. B **45**, 43 (1992).

[4] P. Feulner, T. Muller, A. Puschmann, and D. Menzel, Phys. Rev. Lett. **59**, 791 (1987).

[5] O. Ellegaard, R. Pedris, J. Schou *et al.*, Appl. Phys. A: Solids Surf. **46**, 305 (1988).

[6] I. Arakawa, M. Takahashi, and K. Takeuchi, J. Vac. Sci. Technol. A **7**, 2090 (1989).

[7] T. Kloiber and G. Zimmerer, Phys. Scr. **41**, 962 (1990).

[8] M. Joppien, F. Grotelushen, T. Kloiber, M. Lengen, T. Moller, J. Wormer, G. Zimmerer, J. Keto, M. Kykta, and M. C. Castex, J. Lumin. **48−49**, 601 (1991).

[9] A. G. Belov, V. N. Svishchev, and I. Ya. Fugol', Fiz. Nizk. Temp. **15**, 61 (1989) [Sov. J. Low Temp. Phys. **15**, 34 (1989)].

[10] E. V. Savchenko, I. Ya. Fugol', O. N. Grigorashchenko, S. A. Gubin, and A. N. Ogurtsov, Low Temp. Phys. **19**, 418 (1993).

[11] R. E. Jonson and J. Schou, Mat. Fys. Medd. Dan. Vid. Seldk. **43**, 403 (1993).

[12] O. N. Grigorashchenko, A. N. Ogurtsov, E. V. Savchenko, J. Becker, M. Runne, and G. Zimmerer, Surf. Sci. **390**, 277 (1997).

[13] J. Schow, P. Borgesen, O. Ellegaard, and H. Sorensen, Phys. Rev. B **34**, 93 (1986).

[14] T. Hirayama, A. Hayama, T. Koike, T. Kuninobu, I. Arakawa, K. Mitsuke, M. Sakurai, and E. V. Savchenko, Surf. Sci. **390**, 266 (1997); E. V. Savchenko, T. Hirayama, A. Hayama, T. Koike, T. Kuninobu, I. Arakawa, K. Mitsuke, and M. Sakurai, Surf. Sci. **390**, 261 (1997).

[15] C. T. Reimann, W. L. Brown, and R. E. Johnson, Phys. Rev. B **37**, 1455 (1988).

[16] E. Hudel, E. Steinacker, and P. Feulner, Phys. Rev. B **44**, 8972 (1991).

[17] A. N. Ogurtsov, E. V. Savchenko, J. Becker, M. Runne, and G. Zimmerer, J. Lumin. **76−79**, 478 (1998).

[18] L. Sanche, L. Parenteau, and P. Cloutier, J. Chem. Phys. **91**, 2664 (1989).

[19] A. G. Belov, I. Ya. Fugol', and E. M. Yurtaeva, Low Temp. Phys. **24**, 440 (1998).

[20] I. Ya. Fugol' and A. G. Below, Solid State Commun. **17**, 1125 (1975).

[21] N. Schwentner, E. E. Koch, and J. Jortner, *Electronic Excitations in Condensed Rare Gases*, Springer-Verlag, Berlin (1985).

[22] A. Adams and P. K. Hausma, Phys. Rev. B **22**, 4258 (1980).

[23] B. Sonntag, ''Dielectric and optical properties,'' in *Rare Gas Solids*, Vol. 2, edited by M. L. Klein and J. A. Venables, Academic Press, New York (1977).

[24] M. E. Fajardo and V. A. Apkarian, J. Chem. Phys. **89**, 4124 (1988).

[25] M. Michauld and L. Sanche, Phys. Rev. B **50**, 4725 (1994).

[26] S. T. Arnold, J. U. Hendricks, and K. H. Bowen, J. Chem. Phys. **102**, 39 (1995).

[27] H. Kiefte, M. J. Clouter, and E. Whalley, J. Chem. Phys. **81**, 1419 (1984).

[28] D. Maillard, J. Fournier, H. H. Mohammed, and C. Girardet, J. Chem. Phys. **78**, 5480 (1983).

[29] E. M. Yurtaeva, I. Ya. Fugol', and A. G. Belov, Fiz. Nizk. Temp. **16**, 101 (1990) [Sov. J. Low Temp. Phys. **16**, 54 (1990)].

[30] D. Paillard and J. M. Mestdagh, J. Chem. Phys. **91**, 6866 (1989)

Translated by Steve Torstveit

LOW-TEMPERATURE PHYSICS OF PLASTICITY AND STRENGTH

Low-temperature softening of β-tin single crystals on doping with substitutional impurities

V. P. Soldatov, V. D. Natsik,* A. N. Diulin, and G. I. Kirichenko

B. Verkin Institute for Low Temperature Physics and Engineering, National Academy of Sciences of Ukraine, pr. Lenina 47, 61164 Kharkov, Ukraine

The yield stresses of single crystals of solid solutions of β-tin with substitutional impurities of indium, cadmium, and zinc are measured over a wide interval of low temperatures (1.6–150 K). The low-temperature impurity softening effect is observed, which is manifested in a decrease in the yield stresses of the alloys in comparison with that of pure tin. The temperature and concentration boundaries of the existence region of this effect are established, and the dependence on the combined size and modulus misfit parameter between the atoms of tin and the impurities, which characterizes the strength of the impurity barriers for the motion of dislocations in the alloy, is determined. Analysis of the data obtained indicates a qualitative agreement of the observed regularities of the impurity softening effect and the behavior that follows from the model of Sato and Meshii, which takes into account the role of impurity atoms both as centers of nucleation of kinks on screw dislocations and as centers of opposition to the lateral dispersal of the kinks along the dislocation line. © *2000 American Institute of Physics.* [S1063-777X(00)01302-5]

INTRODUCTION

Impurity doping is one of the simplest ways of hardening metallic materials. As the concentration of the impurity atoms in a pure metal matrix is increased, their hardening influence is clearly manifested in the growth of one of the basic mechanical characteristics of a material–the yield stress. This tendency, which is the most important feature of the solid-solution hardening effect, is typical for a wide class of metallic materials and doping admixtures. Nevertheless, there is convincing experimental evidence that it breaks down; this is manifested in specific effects of impurity softening: for certain alloys based on metals with the bcc structure and under certain conditions, increasing the impurity concentration leads to a decrease in the yield stress instead of an increase. This phenomenon, which was first observed in iron–chromium alloys,[1] has subsequently been observed in several other bcc alloys, predominantly alloys of iron.[2–21] From the experimental data obtained to date one can sketch the broad outlines of the phenomenology of the effect:

—Impurity softening is inherent to solid solutions based on bcc metals, which are typified by high values of the yield stress and a high sensitivity of the latter to temperature;

—Impurity softening is observed in a bounded interval ΔT of moderately low temperatures, lying in the region $T < T_0$, where T_0 is the temperature of the transition from the athermal to the activational branch of the yield stress;

—The effect is caused by both interstitial and substitutional impurities, at concentrations $c \lesssim 1-2$ at. % .

Since the discovery of impurity softening there have been several hypotheses proposed to explain the nature of this effect. We shall discuss them in detail in the analysis of the results of the present study. Right now we will mention only the two circumstances that stimulated our present research. First, in spite of the active discussion of the problems of impurity softening, at present there is no unified opinion as to the physical nature of this effect. Second, the physical basis on which a number of the explanatory hypotheses rest is the idea that the impurities stimulate the nucleation of pairs of dislocation kinks, which govern the mobility of screw dislocations in the Peierls relief.[22–26] According to this idea, the impurity softening effect is the exclusive ''privilege'' of crystals in which the mobility of dislocations is governed by the restraining effect of the Peierls relief (so-called Peierls crystals). Experimental data on impurity softening have been obtained primarily for alloys of iron— typical Peierls crystals. Of course, to confirm the idea in question it will be necessary to make observations and detailed investigations of the impurity softening effect on a wider class of crystals of the Peierls type.

We have shown previously that the low-temperature plasticity of high-purity (99.9995%) single crystals of β-tin oriented for predominant slip in the $(100)\langle 010\rangle$ system is governed by the motion of screw dislocations through Peierls barriers.[27,28] Pure and lightly doped single crystals of β-Sn maintain an appreciable reserve of plasticity and a smooth character of the flow on cooling to helium temperatures. These properties make β-Sn single crystals distinctly promising objects for the observation of impurity softening effects. In this paper we investigate in detail the influence of

small concentrations of In, Cd, and Zn impurities on the temperature dependence of the yield stress of β-Sn single crystals oriented for slip along the $(100)\langle010\rangle$ system. In choosing In, Cd, and Zn as the doping admixtures we were guided by the following considerations: first, at low concentrations $c < -0.5$ at. % these impurities form disordered solid solutions of substitution with tin; second, they are substantially different from one another in the values of the size and modulus misfit in relation to tin.

In the following analysis of the temperature–concentration dependences obtained for the yield stress $\tau_0(T,c)$ of alloys based on β-Sn in the low-temperature region, we identify the anomalies that are characteristic for the impurity softening effect. We discuss how the value of this effect depends on the impurity concentrations and on the strengths of the impurity barriers that oppose the motion of dislocations. We discuss the agreement of the experimentally observed features of impurity softening with the hypotheses that have been proposed to explain it.

1. EXPERIMENTAL TECHNIQUE

1.1. Preparation and straining of the samples

Single crystals of tin alloys containing impurities of Cd, Zn, and In were grown by a modified Bridgman method in batches of 10 from one seed.[29] The initial components used to prepare the alloys contained not more than 10^{-5} at. % uncontrolled impurities. The solubility of Cd and Zn in solid tin is approximately 1 at. %, and that of indium, according to various published sources, fluctuates in the range $3-7$ at. %.[30] The impurity concentration in the alloys studied varied in the interval 0.005–0.53 at. %, and two of the levels (0.01 and 0.53 at. %) were the same for all three types of alloys. In accordance with the phase equilibrium diagrams, the grown single crystals were solid solutions of substitution.

The samples were double-bladed in shape, with a working part $25 \times 5 \times 1.5$ mm. They were strained by uniaxial extension in the creep mode using a weight method of loading. The longitudinal axis of the samples was in the $\langle110\rangle$ direction, so that a maximal shear stress would act in the $(100)\langle010\rangle$ slip system. A diagram of the loading of the samples is shown in Fig. 1 (inset): the load on the sample was changed in steps, which corresponded to stress increments $\delta\tau$ of the order of 0.2–0.4 MPa. The strain increments corresponding to each stress increment were measured with a precision inductive sensor and were automatically recorded on an electronic chart recorder to an accuracy of 5×10^{-5}. This loading regime gave an average rate of strain of the order of 5×10^{-5} s^{-1}. From the stress increments $\delta\tau$ and the corresponding strain increments $\delta\varepsilon$ we constructed hardening curves corresponding to the given average strain rate. These curves were used to determine the desired characteristic—the yield stress (the critical shear stress).

1.2. Determination of the yield stress

We took the value of the yield stress τ_0 to be the stress at which the initial segment of the strain curves $\tau(\varepsilon)$ begins to deviate from its linear trend (Fig. 1). This value is close to
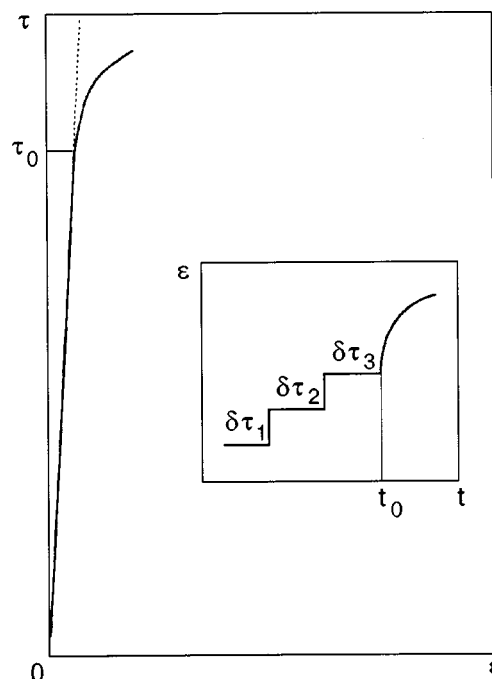

FIG. 1. Schematic illustration of a fragment of the strain curve $\tau(\varepsilon)$ (τ_0 is the yield point). The inset shows the strain diagram of the sample for a stepped loading of the crystal by stress increments $\delta\tau$ (t_0 is the time corresponding to the attainment of the yield stress).

the stress at which irreversible creep begins, which is determined from the change in the character of the $\delta\varepsilon(t)$ curves (Fig. 1, inset): for $\tau < \tau_0$ the curves of the strain increment have a Γ-shaped form, while for $\tau > \tau_0$ (the time t_0) a pronounced nonsteady stage appears on these curves, corresponding to developed plastic flow. These methods complement each other and enable one to correct the values obtained for τ_0 so as to determine them with the least error.

Another important circumstance in the recording of the yield stress is to take into account the scatter in the values of τ_0 due to the structural nonuniformity and small random deviations of the orientation of the axis of extension of the samples. The method used to grow the crystals made it possible to obtain more than 10 identical crystals of a specified shape and crystallographic orientation from a single seed; these crystals could be used as working samples without any additional mechanical treatment (cutting, grinding, and polishing). This method of obtaining the samples reduces to a minimum the influence of random factors on the value of the yield stress. To further reduce the role of these factors, we measured τ_0 at different temperatures on the same sample. The first measurement was done at the highest temperature in the interval of interest, and the sample was then unloaded, its temperature was lowered a relatively small amount, and it was again loaded to τ_0. This method made it possible to obtain the $\tau_0(T)$ curve on several samples of the same batch with a step of 1 K in the region below 4.2 K and with a step of 5–10 K above 4.2 K. In this way we obtained the temperature dependence of the yield stress $\tau_0(T)$ in the interval 1.6–150 K.
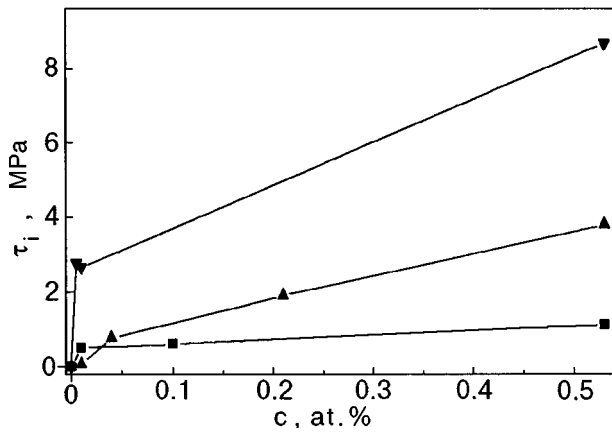
FIG. 2. Concentration dependence of the athermal component of the yield stress $\tau_i(c)$ at $T > 100$ K for alloys based on β-Sn: Sn–In (■); Sn–Zn (▼); Sn–Cd (▲).

2. EXPERIMENTAL RESULTS AND DISCUSSION

2.1. Temperature–concentration dependence of the yield stress of alloys and the softening effect

The yield stress of crystalline materials is customarily represented as a sum of the thermal (activational) component τ_a and an athermal compoenent τ_i, each of which also depends on the impurity concentration c:

$$\tau_0(T,c) = \tau_a(T,c) + \tau_i(c). \tag{1}$$

This division reflects the existence of two types of barriers to the slip of dislocations in the strained crystal: short-ranged, which are overcome by the dislocations with the help of thermal fluctuations, and long-ranged, forming an athermal (to an accuracy up to the temperature dependence of the elastic modulus) background of internal stresses.[31] According to a reliably established experimental fact, impurity softening is a feature of the activational component τ_a alone,[11,19] while the value of the internal stresses τ_i, as a rule, increase monotonically with increasing concentration of the doping impurities.

Our experimental temperature curves of the yield stress of pure β-tin and three alloys based on it, with different concentrations of the dopants, are in agreement with the ideas set forth above. The absolute values of $\tau_0(T,c)$ in the temperature interval 4.2–150 K for these alloys are given in a previously published paper,[32] where it was shown that above 80–90 K the yield stress τ_0, both for pure tin and for all the alloys investigated, has a rather wide interval of athermal behavior. The results of the present study confirm this observation. If the values of the yield stresses at $T > 100$ K are identified with the internal stresses $\tau_i(c)$, then one obtains for the concentration dependence of this quantity the curves shown in Fig. 2.

Against the background of the rising (on account of the doping) athermal component of the yield stress $\tau_i(c)$, the impurity softening effects are manifested in pure form in an analysis of the temperature–concentration curves of the difference $\tau_a(T,c) = \tau_0(T,c) - \tau_i(c)$. These curves are shown in Figs. 3–5 for the alloys studied. The curves in these figures were obtained by subtracting from the yield stress its
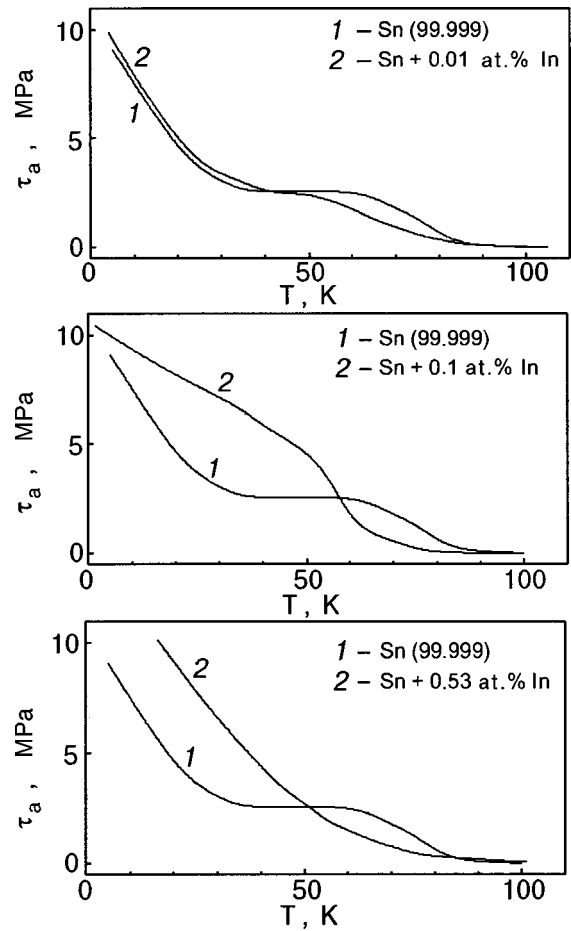

FIG. 3. Temperature dependence of the activational component of the yield stress for pure β-tin (*1*) and for alloys of β-tin with an indium impurity (*2*).

athermal component for $T > 100$ K. Along with the curves of $\tau_a(T,c)$, each of the figures shows the curve for the activational component of the yield stress for pure β-tin, $\tau_a(T,0)$. So as not to obliterate the fine details of the curves, we have left off the experimental data points through which these curves were drawn; the scatter of the experimental points is approximately the same as in Ref. 32. In Figs. 3–5 one can clearly see the temperature intervals ΔT_s within which $\tau_a(T,c) < \tau_a(T,0)$. The value of the softening effect, $\Delta\tau_s = \tau_a(T,0) - \tau_a(T,c) > 0$, and also the width and position of the interval ΔT_s on the temperature axis depend substantially on the type and concentration of the impurities (Fig. 6).

The above-described lowering of the activational component of the yield stress as a result of doping can be termed a relative softening effect. Meanwhile, there also exists an absolute softening effect: at sufficiently low values of the impurity concentration one can identify temperature intervals on which the total yield stress of the alloy lies below that of pure tin, i.e., $\tau_0(T,c) < \tau_0(T,0)$. An idea of the size of the absolute softening can be gotten from Fig. 7, which shows the concentration dependence of the athermal component $\tau_i(c)$ and the maximum values of the relative softening on the intervals ΔT_s: $\eta_s(c) = \max_T(\Delta\tau_s(T,c))$ (see Fig. 6): absolute softening corresponds to the inequality $\eta_s(c) > \tau_i(c) - \tau_i(0)$. It is seen in Fig. 7 that for the alloys Sn–In and
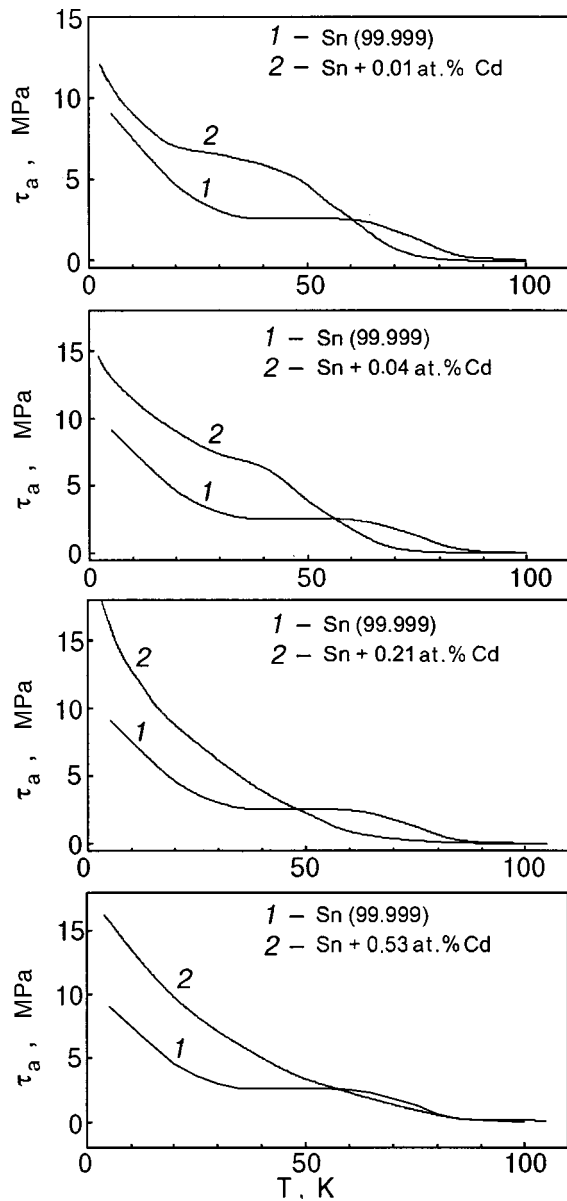
FIG. 4. Temperature dependence of the activational component of the yield stress for pure β-tin (*1*) and for alloys of β-tin with a cadmium impurity (*2*).
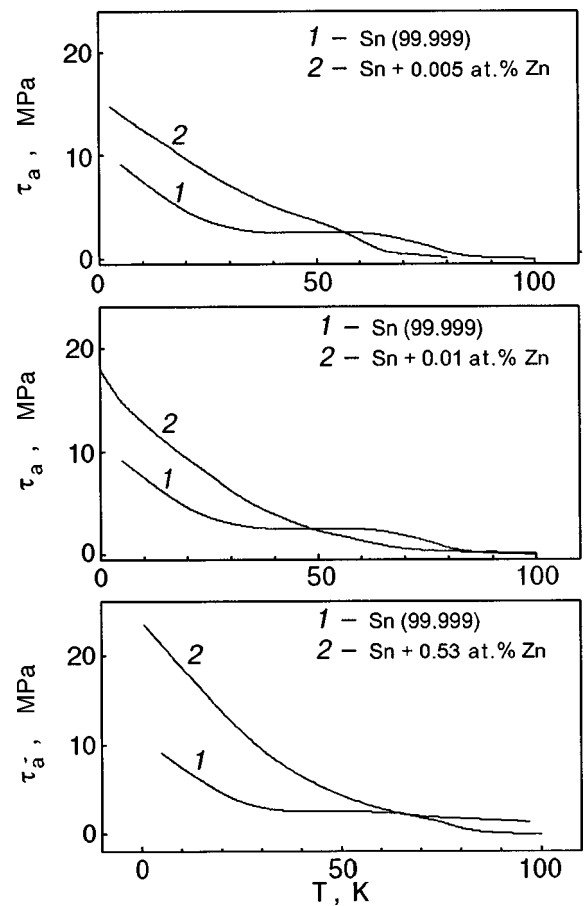

FIG. 5. Temperature dependence of the activational component of the yield stress for pure β-tin (*1*) and for alloys of β-tin with a zinc impurity (*2*).

Sn–Cd there exists an appreciable interval of impurity concentrations in which impurity softening of the activation component more than compensates the increase of the athermal component.

Thus the temperature–concentration curve of the yield stress of β-tin-based alloys in the low-temperature region qualitatively repeats the basic features observed in the study of bcc alloys, including the impurity softening effect of interest here.

Further discussion of the nature of the the physical mechanisms of the impurity softening effect will require experimental data on the temperature–concentration curves of one more important characteristic of the plasticity—the rate sensitivity of the deforming stress near the yield point, $d\tau/\delta\ln\dot\varepsilon$. In our experiments this quantity was investigated in detail for the alloy Sn–Cd (Fig. 8).

2.2. Temperature–concentration curve of the softening effect

Figure 6 shows the temperature dependence of the parameter $\Delta\tau_s$ for the investigated alloys. It is seen from these figures that the qualitative character of the softening effect is the same for all the alloys: the softening reaches a maximum in the temperature region 65–70 K and falls off smoothly to zero on both sides of the maximum, i.e., it exists in a finite temperature interval ΔT_s. The position of the maxima of $\Delta\tau_s$ on the temperature axis is nearly insensitive to the type of impurity, but it fluctuates by several degrees as the impurity concentration is varied. A more important effect is the influence of the type and concentration of the impurity on the width of the temperature interval ΔT_s in which the effect is manifested and on the height of the maxima of η_s, as is seen from Table I.

TABLE I. Influence of the type and concentration of the impurity on the parameters of the softening effect.

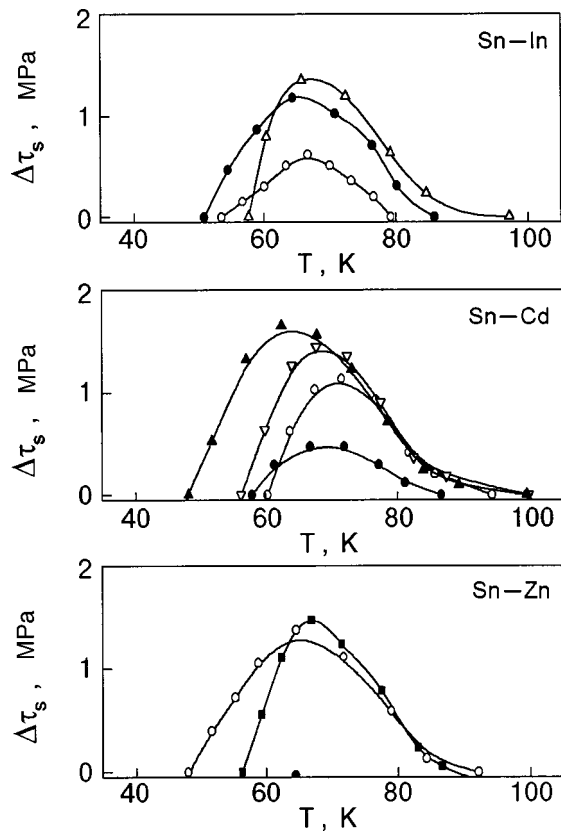| Alloy	ΔT_s, K	η_s, MPa	Alloy	ΔT_s, K	η_s, MPa
Sn+0.01 at.% In	50	0.6	Sn+0.53 at.% In	35	1.1
Sn+0.01 at.% Cd	33	1.1	Sn+0.53 at.% Cd	28	0.44
Sn+0.01 at.% Zn	30	1.3	Sn+0.53 at.% Zn	0	0

FIG. 6. Temperature dependence of the of the parameter $\Delta\tau_s$ in alloys of β-tin with impurities of indium, cadmium, and zinc, at. %: 0.005 (■); 0.01 (○); 0.04 (▽); 0.1 (△); 0.21 (▲); 0.53 (●).

The width of the interval ΔT_s decreases in the series from In to Zn, and this decrease is increasingly significant as their concentration in the alloy increases. Admixtures of cadmium occupy an intermediate position between indium and zinc in terms of their effects.

The curves of $\eta_s(c) = \max_T(\Delta\tau_s(T,c))$ (Fig. 7) are evidence of the nonmonotonic dependence of the size of the softening effect on the impurity concentration for all the alloys. However, the finer details of the dependence $\eta_s(c)$, e.g., the position of the maximum on the $\eta_s(c)$ curve, are sensitive to the type of dopant. In spite of the qualitative differences in the details, the concentration dependence of the value of the effect has a common trait for all three alloys—the presence of a maximum which is reached at different concentrations of the impurities, with a subsequent decrease of the effect at a different rate, depending on the impurity type. It can be supposed that for each type of impurity there exists a critical concentration c_{cr} above which the softening effect vanishes. For example, for the alloy Sn–Zn the vanishing of the effect is observed at $c_{cr} \approx 0.53$ at. % Zn, while a somewhat greater value of c_{cr} can be expected for the Sn–Cd alloys, and for Sn–In it can be around 1 at. %.

It is of interest to compare the values of the impurity softening effect at the same dopant concentrations in each alloy. As can be seen from Table I, at a low concentration the greatest softening effect is obtained for a Zn impurity, while at high concentrations it is obtained for In.
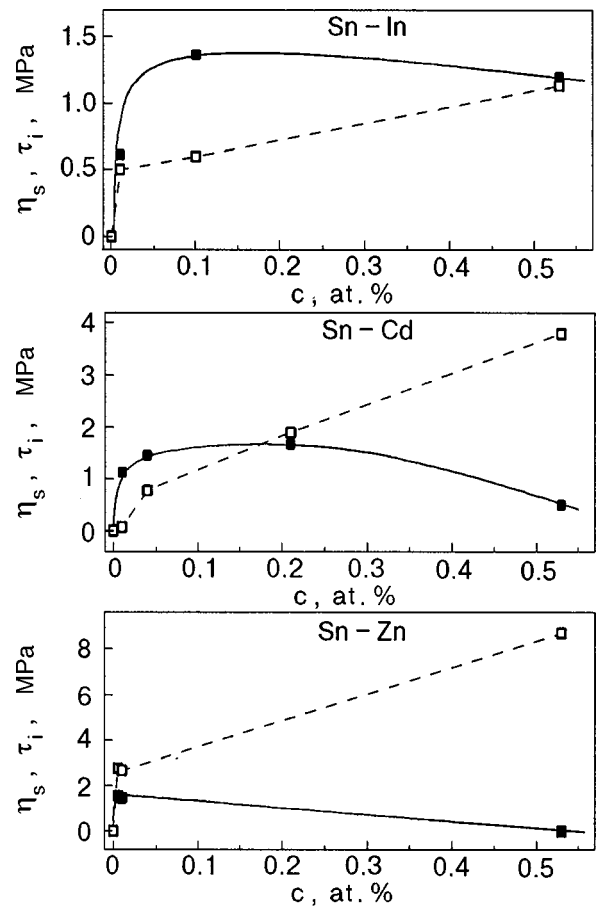

FIG. 7. Concentration dependence of the maximum values of the softening η_s (■) in comparison with the behavior of the athermal component of the yield stress τ_i (□).

3. DISCUSSION OF THE RESULTS

From the time of discovery of impurity softening there have been two main approaches to explaining the physical nature of this effect. According to the first approach, the effect can arise because of the interaction between dissolved atoms and residual impurities that are difficult to eliminate from the material by any methods of purification. In this
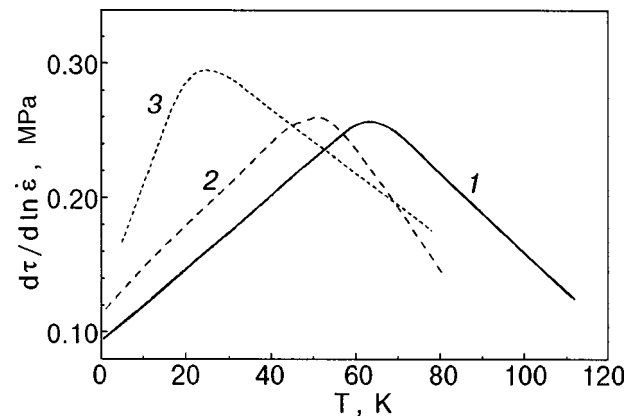

FIG. 8. Temperature dependence of the rate sensitivity of the yield stress for Sn–Cd alloys with cadmium concentrations of 0.01 (*1*), 0.21 (*2*), and 0.53 at. % (*3*).

mechanism the dissolved atoms act as a kind of adsorbent, purifying the surrounding region of the crystal from ''harmful'' (tending to harden the matrix of the original substance) impurities. Purification is achieved either on account of the chemical activity of the foreign atoms, which interact with the residual impurities and cause them to coagulate into larger particles, or on account of their regrouping by the elastic stress fields localized around the dissolved atoms.[1,2,9,12,15] In a number of papers the impurity softening effect is attributed to the influence of interstitial impurities on the density of mobile dislocations[8,9] or to the activation of cross slip by such impurities.[11]

   The second mechanism is based on the idea that the softening effect is an inherent property of Peierls crystals and arises from the specifics of the influence of impurity atoms on the motion of screw dislocations through the barriers of the Peierls potential relief.[5,7,18,19,23–26,33–35] The most important feature of this influence is a decrease (first predicted in Refs. 22 and 23) of the activation energy for nucleation of kink pairs on screw dislocations in the presence of a misfit defect. Kubin and co-workers,[25,35] working from data provided by *in situ* electron microscopy and ordinary tensile experiments, analyzed the softening effect in the Fe–C system and established that the presence of carbon atoms in iron leads to a discontinuous character of the motion of screw dislocations, lowering the activation energy by 1/3 from its value in pure iron. They proposed a model in which the mobility of screw dislocations in dilute bcc alloys is governed by a competition between two processes that occur in parallel—nucleation of normal (in the pure metal) and ''softened'' (when there are impurity atoms near the dislocation) kink pairs on the gliding screw dislocations. The first process dominates at low values of the impurity concentration, while the second dominates at higher concentrations. According to this model, the value of the softening effect is described in the corresponding concentration regions by the relations

$$\Delta\tau_s = \alpha c \, \frac{kT}{v} \qquad \text{for} \quad c < c_0,$$

$$\Delta\tau_s + \frac{3}{2} \frac{kT}{v} [\ln(c) + \beta] \quad \text{for} \quad c > c_0, \qquad (2)$$

where α and β are constants, and $c_0 \sim 10^{-4}$.

   It follows from expressions (2) that the temperature dependence of the softening effect $\Delta\tau_s(T)$ is determined by the temperature dependence of the rate sensitivity of the yield stress (the rate sensitivity is governed by the factor $kT/v = d\tau/d\ln\dot\varepsilon$, and the character of the concentration curves $\Delta\tau_s(c)$ changes from a linear dependence at low concentrations to a weak logarithmic dependence at high concentrations.

   We note that this model does not consider the influence of impurity atoms on the lateral (along the dislocation line) movement of the nucleated kinks. It was assumed that the lateral motion of kinks is completely free and for this reason do not bring any additional features into the mobility of dislocations on the whole. However, this assumption, which is indisputable for a pure material, is not obvious in the case of alloys. A study of this question by Sato and Meshii[24] showed
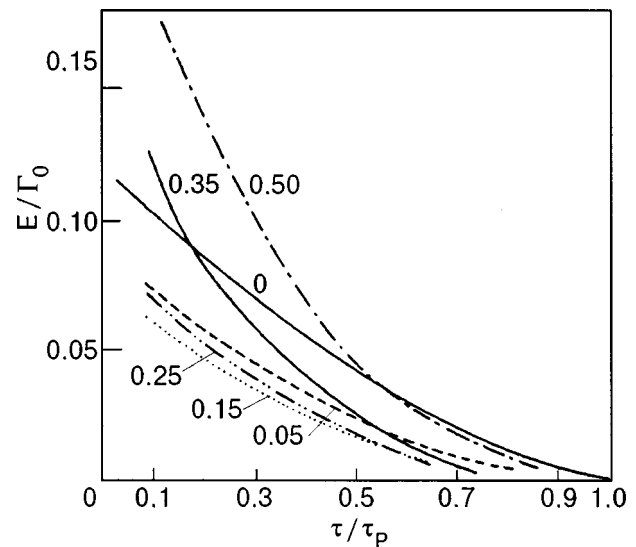

FIG. 9. Stress dependence of the activation energy for the motion of a screw dislocation in the combined field of the Peierls potential and of misfit defects. Γ_0 is the energy per unit length of the dislocation, and τ_P is the Peierls stress. The curves are labeled by the values of the maximum strain around a misfit center, a measure of its strength.[24]

that the centers of dilatation that promote the nucleation of kinks at the same time oppose their dispersal along the dislocation. Therefore, in the analysis of the mobility of dislocations in alloys of the Peierls type it is, generally speaking, necessary to take into account both modes of kink dynamics. It becomes particularly important to take the lateral motion of kinks into account when the height of the barriers that must be overcome by the kinks becomes comparable to the energy of nucleation of kink pairs. Subsequently, in a series of papers by Petukhov *et al.*,[36–38] it was attempted to obtain a unified description of the influence of impurity atoms on both the nucleation and the dispersal of kink pairs.

   One of the important conclusions of Ref. 24 is that there exists a certain critical value (strength) of the impurity barriers. This is illustrated in Fig. 9,[24] which shows the calculated results on the stress dependence of the activation energy necessary for the motion of a screw dislocation through the combined field of the Peierls potential and a misfit center for various values of the strength of the center. The calculation was done for spherical centers, and the strength parameter used was the maximum misfit strain around the center. It is seen that the activation energy (and with it, the macroscopic yield stress) is lowered in the presence of a misfit center and that the lowering effect is sensitive to the strength of the center. At a certain (critical) value of the strength the activation energy again begins to increase, and this corresponds to the decrease in the softening effect. The change in the concentration of misfit centers can give rise to a redistribution of the role of the processes of nucleation and dispersal of the kinks and can have a substantial influence on the behavior of the effect.

   Thus, together with the temperature and impurity concentration, the behavior of the softening effect should also be governed by a factor such as the strength of the impurity barriers.
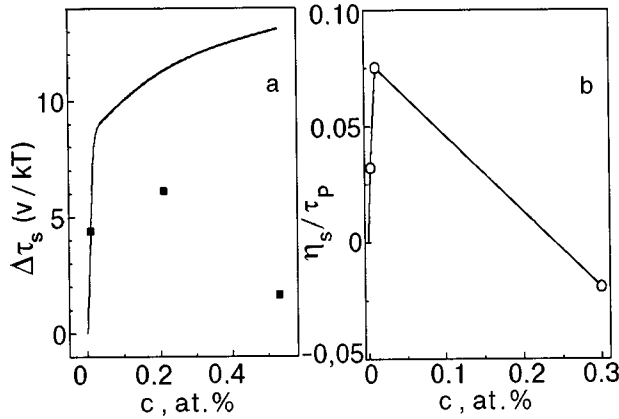
FIG. 10. Dependence of the parameter $\Delta\tau_s(v/kT)$ on the impurity concentration in the alloy: the solid curves are for the model of Kubin *et al.*;[25] the squares ■ show the experimental data obtained for Sn–Cd alloys (a). The concentration dependence of the maximum value of the softening, normalized to the Peiersl stress in the model of Sato and Meshii, constructed according to the data of Fig. 11a in Ref. 24 (b).
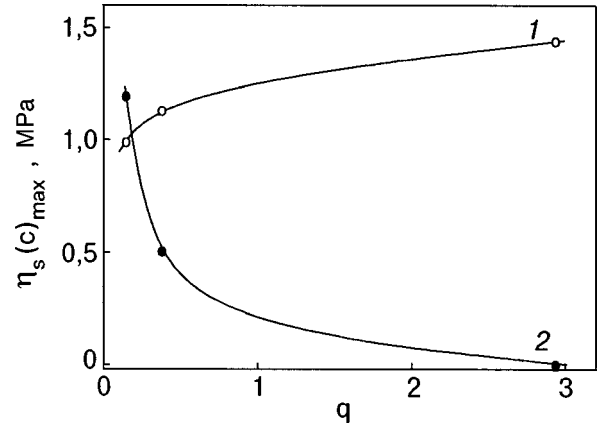

FIG. 11. Dependence of the maximum value of the impurity softening η_s on the combined misfit parameter q (the strength of the impurity barrier) in alloys with impurity concentrations c, at. %: 0.01 (*1*), 0.53 (*2*).

Let us now compare the results of our experiments with the conclusions obtained in an analysis of the models described above. In the framework of these models we have discussed only the influence of impurities on the activational component of the deforming stress; in the next Subsection we shall discuss only the parameters of the relative softening effect.

3.1. Temperature dependence of the effect

As can be seen from Fig. 6 and Table I, the softening effect is observed in a bounded interval of moderately low temperatures, outside of which the activational component of the yield stress of the alloy is higher than that of pure tin. This behavior of the effect is predicted by both the model of Sato and Meshii and the model of Kubin *et al.* One of the consequences of the Kubin model that is subject to experimental verification is the prediction that the temperature dependence of the softening effect should be the same as that of the rate sensitivity of the yield stress. We have checked whether this prediction holds for the case of the Sn–Cd alloy. It can be seen from a comparison of Fig. 6 and 8 that the positions of the maxima of these parameters on the temperature axis are strongly different, and that the difference increases as the impurity concentration increases, reaching 40 K for the alloy Sn+0.53 at. % Cd, for example.

It is possible that one of the causes of the disagreement of the experimental data and formula (2) is that the Kubin model does not take into account the role of impurity atoms as centers of opposition to the kinks in their lateral motion along the dislocation lines.

3.2. Concentration dependence of the effect

Figure 10 shows the types of concentration curves obtained from calculations in the models of Sato and Meshii[24] and Kubin *et al.*[25] We note for the sake of definiteness that the curve in Fig. 10b reflects the behavior of the relative value of the impurity softening effect, η_s/τ_P, obtained from the data of Fig. 11 of Ref. 24. The $\tau_0(T,c)$ curves in that

figure were calculated in Ref. 24 for a hypothetical alloy with a fixed value of the strength of the impurity barrier. The values of η_s/τ_P were found at the crossing points of the $\tau_0(T)$ curves with the straight line $T=\text{const}\approx70$ K.

Let us compare the curves in Figs. 10 and 7. The minimum impurity concentration in our alloys corresponded to the lower boundary of the concentration region in the Kubin model ($c_0\sim10-4$) above which the effect practically ceases to depend on the impurity concentration. This tendency, as we see from a comparison of Fig. 10a and Fig. 7, is not observed. All of the $\eta_s(c)$ curves for our alloys pass through a maximum and then undergo a more or less steep drop. At the same time, there is a satisfactory qualitative similarity between our experimental curves and the curve calculated for the Sato and Meshii model (see Fig. 10b).

3.3. Influence of the strength of the impurity barriers

The experimental data on the influence of this parameter on the softening effect are few and inconsistent. Some studies have found no connection between the size of the effect and the difference of the geometric and elastic parameters of the host and impurity atoms, which accords with the absence of a connection between the size of the effect and the strength parameter in Refs. 4 and 6, while in other studies the effect was found to be insensitive to the size of the misfit but its dependence on the modulus misfit was emphatically affirmed.[14] To elucidate the influence of this parameter on the softening effect in the alloys investigated in the present study, we adopted as a quantitative measure of the strength of the impurity barriers the quantity q introduced by Fleisher:[39]

$$q=|\delta_G-\alpha\delta_R|,$$

$$\delta_G=\frac{2(G_{\text{Sn}}-G_i)}{2G_{\text{Sn}}+|G_{\text{Sn}}-G_i|}; \quad \delta_R=\frac{R_{\text{Sn}}-R_i}{R_{\text{Sn}}}. \quad (3)$$

The symbol q denotes the combined misfit parameter (barrier strength), which takes into account the contribution to the strength of the interaction of the dislocation with impurity atoms from both the size and modulus misfits; G_{Sn} and

TABLE II. Values of the strength of the impurity barriers and the parameters used for calculating them.

Element	R, Å (Refs. 40, 41)	δ_R	$G = G_{44}$, GPa	δ_G	q
Sn (host)	1.62	0	28.2 (Refs. 41, 42)	0	0
In	1.66	0.024	8 (Ref. 41)	0.53	0.146
Cd	1.57	0.031	24.5 (Refs. 41, 43)	0.122	0.38
Zn	1.37	0.154	46 (Ref. 41)	−0.48	2.94

G_i are the shear moduli of tin and of the dopant material; R_{Sn} and G_i are the atomic radii of tin and of the dopant atom; and, the coefficient $\alpha = 16$ for screw and $\alpha = 3$ for edge dislocations.

In the analysis of the low-temperature plastic flow of pure β-Sn along the slip system $(100)\langle 010\rangle$ we established that it is brought about by the motion of screw dislocations through Peierls barriers.[27,28] This conclusion also applies to the low-temperature plasticity of the dilute alloys of tin with indium, cadmium, and zinc.[32] On the basis of these results we can calculate the values of the strength of the impurity barriers opposing the motion of the dislocations (see Table II).

Table II also give information about the atomic radii and shear moduli of the alloy components. It is seen that indium, cadmium, and zinc impurities in tin give rise to dislocation barriers of different strengths: the strongest are barriers formed by zinc atoms, and the weakest are formed by indium.

Figure 11 shows the maximum value of the impurity softening $\eta_s(c)$ in the interval ΔT_s as a function of the parameter q for two fixed impurity concentrations in the alloys: $c = 0.01$ and 0.53 at. %. These curves clearly indicate the presence of a link between the value of the effect and the strength of the impurity barriers, and the character of the relationship displays a strong dependence on the impurity concentration. Indeed, at a low concentration of impurity atoms the effect increases with increasing strength parameter, whereas at a high concentration it decreases with q. A simple analysis shows that the quantitative interrelationship between the parameter of the effect η_s and the strength parameter q is well approximated by a power law:

$$\eta_s(c, q) = A(c)q^n, \qquad (4)$$

in which the parameters A and n have different values at low and high impurity concentrations in the alloys. For example, $A = 1.3$, $n = 0.12$ for $c = 0.01$ at. % and $A = 0.2$ and $n = -1$ for $c = 0.53$ at. %.

Thus, depending on the concentration, the same impurity can act to soften or harden the host crystal. In the set of impurities investigated here, such a role is most characteristic for zinc atoms. It remains to be said that the observed feature in the behavior of the effect is predicted in the model of Sato and Meshii on the basis of a consistent incorporation of the dual role of the impurity atoms in the potential relief of a Peierls crystal—as centers of nucleation of paired kinks on screw dislocation, and as centers of opposition to their dispersal along the dislocation line. In particular, it follows

from this model that impurity atoms in high concentrations can lead to a softening effect only under the condition that the strength of the barriers created by them is rather low.

Thus we see from the above discussion that our experimental results are in qualitative agreement with the model developed in the paper by Sato and Meshii.[24]

CONCLUSION

1. Single-crystal samples of alloys of β-tin with impurities of indium, cadmium, and zinc exhibit a low-temperature impurity softening effect which is manifested in a decrease in the yield stress in the alloys as compared to pure tin. This effect is observed in bounded intervals of moderately low temperatures and concentrations.

2. We measured the temperature and concentration dependences of the impurity softening effect and compared them to those predicted in different theoretical models of the effect.

3. We established how the value of the effect depends on the combined size and modulus misfit parameter of the atoms of the host matrix and the substance dissolved in it (the strength of the impurity barriers). We showed that the interrelationship of these quantities is described by a power law with an exponent that depends on the impurity concentration in the alloy.

4. An analysis of the data obtained in this study showed that the interrelationships found are in good agreement with the behavior of the effect implied by the model of Sato and Meshii,[24] which takes into account the role of impurity atoms both as centers of nucleation of paired kinks on screw dislocations and as centers of opposition to their lateral motion along the dislocation line.

*E-mail: natsik@ilt.kharkov.ua

[1] G. E. Lacy and M. Gensamer, Trans. AIME **32**, 88 (1944).
[2] W. P. Ress, B. E. Hopkins, and H. R. Tilper, J. Iron Steel Inst., London **169**, 157 (1951).
[3] G. T. Horne, B. B. Roy, and H. W. Paxton, J. Iron Steel Inst., London **201**, 161 (1963).
[4] H. H. Kranzlein, M. S. Burton, and G. V. Smith, Trans. AIME **233**, 64 (1965).
[5] R. J. Arsenault, Acta Metall. **14**, 831 (1966).
[6] F. Bolling and R. H. Richman, Can. J. Phys. **45**, 541 (1967).
[7] T. E. Mitchel and P. L. Raffo, Trans. AIME **242**, 907 (1968).
[8] B. Harris, Phys. Status Solidi **29**, 383 (1968).
[9] B. W. Christ and G. V. Smith, Mem. Sci. Rev. Met. **65**, 208 (1968).
[10] Y. Nakada and A. S. Khe, Acta Metall. **16**, 903 (1968).
[11] B. W. Christ, R. P. Gamble, and G. V. Smith, Scr. Metall. **3**, 521 (1969).
[12] K. V. Ravi and R. Gibala, Scr. Metall. **3**, 547 (1969).
[13] P. L. Raffo, J. Less-Common Met. **17**, 133 (1969).
[14] B. Ram Roy, Scr. Metall. **3**, 531 (1969).
[15] K. V. Ravi and R. Gibala, Acta Metall. **18**, 623 (1970).
[16] T. E. Mitchell and R. L. Smialek, in *Proceedings of the 2nd International Conference on Strength of Metals and Alloys*, Asilomar (1970), p. 73.
[17] R. Gibala and T. E. Mitchell, Scr. Metall. **7**, 1143 (1973).
[18] D. J. Quesnel, A. Sato, and M. Meshii, Mater. Sci. Eng. **18**, 199 (1975).
[19] J. P. Cottu, J. P. Peyarade, P. Chomel, and P. Groh, Acta Metall. **26**, 1179 (1978).
[20] J. P. Peyarade, P. Groh, and J. P. Cottu, in *Proceedings of the 5th International Conference on Strength of Metals and Alloys*, Aachen (1979), p. 959.
[21] P. Chomel and J. P. Cottu, in *Proceedings of the 5th International Con-*

ference on Strength of Metals and Alloys, Aachen (1979), p. 1013.

[22] A. Urakami and M. E. Fine, in *Proceedings of the First International Conference on the Mechanical Behavior of Materials*, Kyoto, Japan (1971).

[23] B. V. Petukhov, Fiz. Tverd. Tela (Leningrad) **13**, 1445 (1971) [Sov. Phys. Solid State **13**, 1204 (1971)].

[24] A. Sato and M. Meshii, Acta Metall. **21**, 753 (1973).

[25] L. P. Kubin, F. Louchet, J. P. Peyrade, P. Groh, and P. Cottu, Acta Metall. **27**, 343 (1979).

[26] H. Suzuki, in *Dislocations in Metallurgy* (Vol. 4 of Dislocations in Solids), North-Holland, Amsterdam (1979), p. 191.

[27] G. I. Kirichenko, V. D. Natsik, and V. P. Soldatov, Fiz. Met. Metalloved. **63**, 386 (1987).

[28] V. D. Natsik, G. I. Kirichenko, V. V. Pustovalov, V. P. Soldatov, and S. É. Shumilin, Fiz. Nizk. Temp. **22**, 925 (1996) [Low Temp. Phys. **22**, 740 (1996)].

[29] Yu. G. Kazarov, in *Condensed Matter Physics* [in Russian], Kharkov (1973), issue 11, p. 100.

[30] M. Hansen and K. Anderko, *Constitution of Bindary Alloys*, 2nd ed. [McGraw-Hill, New York (1958); Mir, Moscow (1962)].

[31] A. Seeger, ''The mechanism of glide and work-hardening in face-centered cubic and hexagonal close-packed metals,'' in *Dislocations and Mechanical Properties of Crystals*, New York (1957), p. 275.

[32] A. N. Diulin, G. I. Kirichenko, V. D. Natsik, and V. P. Soldatov, Fiz. Nizk. Temp. **24**, 595 (1998) [Low Temp. Phys. **24**, 452 (1998)].

[33] R. J. Arsenault and Cadman, in *Defects and Defect Clusters in BCC Metals and their Alloys*, Nuclear Metallurgy, 1, p. 41 (1973).

[34] J. Diehl, M. Schreiner, S. Staiger, and S. Zwiesele, Scr. Metall. **10**, 949 (1976).

[35] L. P. Kubin and F. Louchet, Acta Metall. **27**, 337 (1979).

[36] B. V. Petukhov, Fiz. Met. Metalloved. **56**, 1177 (1983).

[37] B. V. Petukhov and Yu. I. Polyakov, Kristallografiya **38**(6), 4 (1993) [Crystallogr. Rep. **38**, 715 (1993)].

[38] B. V. Petukhov, Kristallografiya **41**(2), 197 (1996) [Crystallogr. Rep. **41**, 393 (1996)].

[39] R. L. Fleisher, Acta Metall. **9**, 996 (1961).

[40] W. B. Pearson, *The Crystal Chemistry and Physics of Metals and Alloys*, [Wiley–Interscience, New York (1972); Part 1, Mir, Moscow (1977)].

[41] G. V. Samson (ed.), *Properties of the Elements* (Part 1) [in Russian], Metallurgiya, Moscow (1976).

[42] A. A. Hendrickson and E. Fine, Trans. AIME **221**, 103 (1970).

[43] W. P. Mason (ed.), *Physics Acoustics: Principles and Methods*, [Academic Press, New York (1968); Mir, Moscow (1972)].

Translated by Steve Torstveit

BRIEF COMMUNICATIONS

High-frequency impedance of layered conductors in a high magnetic field

V. G. Peschanskiĭ*

Kharkov State University, pl. Svobody 4, 61007 Kharkov, Ukraine; B. Verkin Institute for Low Temperature Physics and Engineering, National Academy of Sciences of Ukraine, pr. Lenina 47, 61164 Kharkov, Ukraine

I. V. Kozlov and K. Jiasemides**

Kharkov State University, pl. Svobody 4, 61007 Kharkov, Ukraine
(Submitted July 19, 1999)
Fiz. Nizk. Temp. **26**, 225–227 (February 2000)

The propagation of electromagnetic waves in layered conductors is investigated theoretically for low temperatures, where it is extremely important to take into account the energy quantization of the charge carriers by the magnetic field. The quantum kinetic equation for the statistical operator is used to calculate the quantum oscillations of the surface impedance over a wide range of frequencies ω. © *2000 American Institute of Physics.*
[S1063-777X(00)01402-X]

In recent years there has been a rising interest in research on the physical phenomena occurring in conductors of organic origin, having a layered structure with a pronounced anisotropy of their metallic conductivity. These include a large family of charge-transfer complexes based on bis-ethylenedithio-tetrathiafulvalene (BEDT-TTF)$_2$X, where X is a set of various anions. The electrical conductivity along the layers in these complexes is 3–4 orders of magnitude higher than that along the normal **n** to the layers; this is clearly due to the sharp anisotropy of the velocity distribution of the charge carriers, $\mathbf{v} = \partial\varepsilon(\mathbf{p})/\partial\mathbf{p}$, on the Fermi surface $\varepsilon(\mathbf{p}) = \varepsilon_F$, i.e., their energy

$$\varepsilon(\mathbf{p}) = \sum_{n=0}^{\infty} \varepsilon_n(p_x, p_y)\cos(anp_z/\hbar) \tag{1}$$

depends only weakly on the momentum projection $p_z = \mathbf{p} \cdot \mathbf{n}$.

The quasi-two-dimensional character of the electron energy spectrum of layered conductors makes for an extremely clear manifestation of the quantum oscillations of the Shubnikov–De Haas and de Haas–Van Alfen effects. The Shubnikov–de Haas oscillations of the magnetoresistance have been observed in many organic layered conductors. Already there have been quite a few reports of experimental studies of the propagation of electromagnetic waves in ion–radical layers with a low-dimensional electron energy spectrum.[1–6] In this connection it is of interest to do a theoretical analysis of the quantum oscillation effects in alternating fields, since high-frequency phenomena are extremely informative and can be used successfully for a detailed study of the electronic structure of layered conductors and, in particular, the dispersion relation and the relaxation properties of the charge carriers.

Let us consider the propagation of electromagnetic waves along the normal to the layers in organic layered conductors with a quasi-two-dimensional electron energy spectrum, placed in a rather high magnetic field **H** such that the mean free path l of the charge carriers is much greater than the radius of curvature r of their trajectories. If the penetration depth of the electromagnetic wave into the conductor is less than the linear dimensions of the conductor, then the problem of the distribution of the electric field $\mathbf{E}(z)$ of the wave in the sample is similar to that of the propagation of the electromagnetic field in a half space $z \geq 0$ occupied by the layered conductor.

To find the current density

$$j = \text{Tr}(e\hat{\mathbf{v}}\hat{\rho}) \tag{2}$$

it is necessary to solve the quantum kinetic equation for the statistical operator $\hat{\rho} = \hat{\rho}^{(0)} + \hat{\rho}^{(1)}$, which in the case of a monochromatic wave of extremely low intensity has the form

$$\left[-i\omega + \frac{1}{\tau} + \frac{i}{\hbar}(\varepsilon_n - \varepsilon_{n'})\right]\rho_{nn'}^{(1)} + v_z\frac{\partial\rho_{nn'}^{(1)}}{\partial z}$$
$$= -\frac{\rho_n^{(0)} - \rho_{n'}^{(0)}}{\varepsilon_n - \varepsilon_{n'}}(e\mathbf{E}\cdot\mathbf{v})_{nn'}. \tag{3}$$

Here $\hat{\rho}^{(0)}$ is the statistical operator describing the equilibrium unperturbed state of the charge carriers; only the diagonal components of this operator are nonzero, and they are the Fermi distribution functions $\rho_0(\varepsilon_n(\rho_H))$, where $p_H = \mathbf{p} \cdot \mathbf{H}/H$.

In Eq. (3) we have kept only the terms linear in the small perturbation of the charge carriers by the electromagnetic wave. Solely for the sake of brevity in the calculations we have taken the quantum analog of the collision integral into

account in the relaxation-time approximation for the conduction electrons, i.e., as an operator multiplying the nonequilibrium part of the statistical operator $\hat{\rho}^{(1)}$ by the collision frequency $1/\tau$.

The constitutive relation (2) together with Mawell's equations

$$\text{curl } \mathbf{H} = 4\pi j/c - i\omega \mathbf{E}/c, \quad \text{curl } \mathbf{E} = i\omega(\mathbf{H} + 4\pi \mathbf{M}), \quad (4)$$

where $\mathbf{M}$ is the magnetization, form a complete system of equations for the problem of finding the electromagnetic field distribution in the conductor.

A more substantial simplification of the calculations of the impedance Z and electromagnetic field distribution in a conductor can be achieved if it is assumed that the quantized energy levels in the magnetic field $\mathbf{H} = (0,0,H)$ have the form

$$\varepsilon_n(p_z) = (n + 1/2)\hbar\Omega - \eta\varepsilon_F \cos(ap_z/\hbar), \quad (5)$$

where $\Omega = eH/mc$, c is the speed of light in vacuum, e is the charge of the electron, and the cyclotron effective mass m of the electron is independent of p_z; this takes place when the energy spectrum in the plane of the layers is isotropic.

The quasi-two-dimensionality parameter η of the conductor will be assumed not too small, so that

$$\frac{\hbar\Omega}{\varepsilon_F} \ll \eta \ll 1, \quad (6)$$

and a quasi-classical description of the electronic phenomena is valid.

By virtue of the symmetry of the problem, the electric field E_z is equal to zero, and the coupling of the current density with the electric field in the plane of the layers is easily found using the solution of the kinetic equation (3). We perform an even continuation of the electric field into the region of negative z and do a Fourier transform. If the surface of the sample ($z=0$) on which the wave is incident reflects the charge carriers in a specular manner, then the Fourier transforms of the current density $j_\alpha(k)$ and of the electric field $E_\beta(k)$ are connected by a local relation:

$$j_\alpha(k) = \sigma_{\alpha\beta}(k)E_\beta(k); \quad (\alpha,\beta) = (x,y). \quad (7)$$

In this case it is easy to find $E_\alpha(k)$ by some straightforward calculations and then, by doing the inverse Fourier transformation

$$E_\alpha(z) = \frac{1}{\pi} \int_0^\infty dk E_\alpha(k)\cos kz, \quad (8)$$

to find the distribution of the electric field of the wave in the conductor.

Quantum oscillation effects are due to the presence of features on the density of states of the charge carriers when their energy spectrum is quantized. Upon the summation in the collision integral over the states of the scattered electrons, these features inevitably manifest themselves,[7–10] leading to an oscillatory dependence of τ on $1/H$, viz.,

$$\frac{1}{\tau} = \frac{1}{\tau_0}\left[1 + \Psi\left(2\pi^2 \frac{T}{\hbar\Omega}\right)I_0\left(\frac{2\pi\varepsilon_F}{\hbar\Omega}\eta\right)\cos\left(\frac{\varepsilon_F}{\hbar\Omega}\right)\right], \quad (9)$$

where τ_0 is the nonoscillatory part of the relaxation time, T is the temperature in energy units, $\Psi(\xi) = \xi/\sinh\xi$, and $I_0(\xi)$ is the Bessel function.

When the surface impedance Z is calculated in the region of high frequencies ω of the electromagnetic wave, when $\omega\tau \gg 1$, the form of the collision integral in Eq. (3) is not so important, since the main approximation in the parameter $1/\omega\tau$ corresponds to the collisionless limit. In the low-frequency region ($\omega\tau \ll 1$), however, it is extremely important to take into account the quantum oscillations of the collision integral.

For $T \ll \hbar\Omega$ in a high magnetic field $\hbar\Omega \gg \omega\tau e^2 \eta\varepsilon_F/(mc^2 a)$, the quantum oscillations of the low-frequency ($\omega\tau \ll 1$) impedance Z_{osc} are determined mainly by oscillations of the collision integral, and $Z_{osc} \cong Z[\hbar\Omega/(\varepsilon_F\eta)]^{1/2}$.

As the frequency ω is increased, the contribution to Z_{osc} from oscillations of the collision integral compete with the magnetization oscillations, which in the collisionless limit completely determine Z_{osc}.

No fundamental difficulties arise in solving the problem for an arbitrary form of the quasi-two-dimensional electron energy spectrum. The competition of the various mechanisms of formation of quantum oscillation effects in a high-frequency field and the fine details of the dispersion relation for the charge carriers can be taken into account by means of an analysis of the phase relations in the presence of beats of the oscillations at small η.

*E-mail: vpeschansky@ilt.kharkov.ua
**Present address: Predikari 5, GR-111 41 Athens, Greece

[1] J. Singleton, F. L. Pratt, M. Doporto, T. J. B. M. Janssen, M. Kurmoo, J. A. A. J. Perenboom, W. Hayes, and P. Day, Phys. Rev. Lett. **68**, 2500 (1992).

[2] S. Hill, A. Ardavan, J. M. Schrawa, and J. Singleton, ''Fermi surface spectroscopy: a magnetic resonance approach,'' *Reports of the XXII International Conference on Low Temperature Physics*, Espoo–Helsinki, Finland (1999), Abstracts LT22, p. 399.

[3] S. V. Demishev, H. E. Sluchanko, A. V. Semeno, and N. A. Samarin, JETP Lett. **61**, 313 (1995).

[4] S. V. Demishev, A. V. Semeno, N. E. Sluchanko, N. A. Samarin, I. V. Voskoboinikov, V. V. Glushkov, J. Singleton, S. J. Blundell, S. O. Hill, W. Hayes, M. V. Kartsovnik, A. E. Kovalev, M. Kurmoo, P. Day, and N. D. Kushch, Phys. Rev. B **53**, 12794 (1996).

[5] A. Polisski, J. Singleton, and N. D. Kushch, Czech. J. Phys. **46**, Suppl. S5 (1996) (Proc. XXI Intern. Conf. on Low Temp. Phys. (LT 21), Prague, Aug. 8–14, 1996).

[6] S. V. Demishev, A. V. Semeno, N. E. Sluchanko, N. A. Samarin, I. B. Voskoboĭnikov, M. V. Kartsovnik, A. E. Kovalev, and N. D. Kushch, Zh. Éksp. Teor. Fiz. **111**, 979 (1997) [JETP **84**, 540 (1997)].

[7] M. Ya. Azbel', Zh. Éksp. Teor. Fiz. **34**, 1158 (1958) [Sov. Phys. JETP **7**, 801 (1958)].

[8] E. N. Adams and T. D. Holstein, J. Phys. Chem. Solids **10**, 254 (1959).

[9] A. M. Kosevich and B. B. Andreev, Zh. Éksp. Teor. Fiz. **38**, 882 (1960) [Sov. Phys. JETP **11**, 637 (1960)].

[10] Yu. A. Bychkov, Zh. Éksp. Teor. Fiz. **39**, 1401 (1960) [Sov. Phys. JETP **12**, 971 (1961)].

Translated by Steve Torstveit

QUANTUM LIQUIDS AND QUANTUM CRYSTALS

Motion of vortices in an annular region

T. I. Zueva*

B. Verkin Institute for Low Temperature Physics and Engineering, National Academy of Sciences of Ukraine, pr. Lenina 47, 51164 Kharkov, Ukraine

The vortex solutions of the nonlinear Schrödinger equation in a bounded region are analyzed. The asymptotic limit in which the dimensions of the vortex cores are much smaller than the distance between vortices is investigated. A system of equations describing the dynamics of vortices in the annular region (ring) between two coaxial cylinders is derived. It is shown that as the inner radius of the ring decreases, the system of equations reduces to the corresponding system on a disk, and as the gap decreases, the motion obtained is analogous to that in a rectilinear channel. An analytical solution of the equation is given for the case when there is only one vortex in the ring, and a numerical simulation of the motion of two vortices with arbitrary signs of the vortex strength is carried out for different initial positions of the vortices. © *2000 American Institute of Physics.* [S1063-777X(00)00102-X]

INTRODUCTION

Consider the functional

$$f(u) = \frac{\hbar^2}{2m} |\nabla u|^2 + \alpha |u|^2 + \frac{\beta}{2} |u|^4. \tag{1}$$

This functional represents the free energy density of a superfluid[1,2] (u is the wave function, $\hbar$ is Planck's constant, m is the mass of a helium atom, α, β are parameters that depend only on temperature T, and $\alpha < 0$). Minimizing f with respect to $\bar{u}$, we obtain the Euler–Lagrange equation in the form

$$\frac{\hbar^2}{2m} \Delta u - \alpha u \left(1 + |u|^2 \frac{\beta}{\alpha} \right) = 0,$$

where Δ is the Laplacian operator.

Changing to dimensionless variables (u', x') by setting $x = \xi x'$, $u = u_0 u'$, $u_0^2 = -\alpha/\beta$, where

$$\xi^2(T) = \frac{\hbar^2}{2m} |\alpha| \tag{2}$$

is the coherence length for He II, which determines the minimum length over which appreciable changes occur in $|u|$ (or ρ_S), i.e., ξ is equal to the radius a_0 of the vortex core.

$$\Delta' u' + u'(1 - |u'|^2) = 0. \tag{3}$$

Equation (3) is the so-called stationary Ginzburg–Landau equation. Two forms of stationary Ginzburg–Landau equations are treated in mathematical physics:

$$\Delta u + u(1 - |u|^2) = -i u_t, \tag{4}$$

$$\Delta u + u(1 - |u|^2) = u_t. \tag{5}$$

Equation (4) is the nonlinear Schrödinger equation, and Eq. (5) is the nonlinear heat flow equation.

An important feature of these equations is the existence of asymptotic solutions of the vortex type. The concept of vortices introduced in hydrodynamics can be applied for the description of features in various media. The motion of vortices is widely considered in the literature on magnets, superconductors, in charged fluids, and in superfluids.

In Refs. 3 and 4 it was shown that in the nonstationary case (5) (the nonlinear heat flow equations) the vortices behave like charged particles (vortices having the same sign of the vorticity repel one another, while vortices of unlike sign attract), whereas the vortex solutions of the nonlinear Schrödinger equation are similar to hydrodynamic vortices.

In this paper we use the procedure proposed in Ref. 4 to derive equations describing the motion of a vortex system. This procedure yields an asymptotic expression for the phase Φ of the wave function to arbitrary accuracy and reduces the problem of solving the Ginzburg–Landau equation to one of solving a boundary-value problem for Φ in a specified region. The choice of suitable boundary conditions (Dirichlet, Neumann, or mixed conditions) can significantly broaden the spectrum of problems that can be treated. In particular, the Neumann condition at a solid boundary is analogous to the condition of impermeability in hydrodynamics or to the condition that there be no currents flowing into or out of a superconductor. Dirichlet boundary conditions describe a contact between a superconductor and normal metal, while mixed boundary conditions are imposed in problems describing the behavior of a superconducting layer in a normal metal (see, for example, Ref. 5).

We consider the motion of vortices in superfluids (quantum fluids) in the absence of magnetic field in bounded regions—in particular, in the annular region between two coaxial cylinders, a region containing N vortices of vortex strength n_j, located at the positions $\xi_j = (\zeta_j, \eta_j)$,

$j=1,2,\ldots,N$. We consider the asymptotic limit when the dimensions of the vortex cores are much smaller than the distance between vortices.

The equations of motion for quantum vortices obtained in this paper are of the form

$$\dot{\xi}_j = 2\mathbf{K}^{(j)}, \quad j=1,2,\ldots,N, \tag{6}$$

$\mathbf{K}^{(j)}=\mathbf{K}^{(j)}(\xi_j;\xi_1,\xi_2,\ldots,\xi_N)$ is expressed in terms of the derivative of a complex potential $W(z)$ of the flow of an ideal fluid in the ring,[10] evaluated at the point where the jth vortex is located:

$$\mathbf{K}^{(j)} = (\operatorname{Re} W'(z_j), \ -\operatorname{Im} W'(z_j)),$$

where $z_j = \zeta_j + i\eta_j$ are the complex coordinates of the jth vortex.

This form of the equations is the same as that of the equations found in the literature for the description of magnetic vortices and vortices in other systems (see, for example, Refs. 6 and 7, even though they were obtained by a completely different method.

Analysis of these equations shows that the Schrödinger equation (4) actually does admit a solution in the form of vortices which behave like hydrodynamic vortices. In this paper we write explicit expressions for these equations in an annular region so that they can be solved numerically once the initial positions of the vortices are specified. We show that as the inner radius of the ring decreases, this solution reduces to the solution of the corresponding system on a disk, and as the gap decreases (i.e., for $R_2 - R_1 \ll R_1$) we obtain motion analogous to that in a rectilinear channel. We find an analytical solution to equations (6) when there is only one vortex in the ring, and we carry out a numerical simulation of the motion of two vortices for various initial positions of the vortices and arbitrary signs of their vortex strengths.

EQUATION OF MOTION OF A VORTEX

Let us consider the stationary Ginzburg–Landau equation

$$\Delta u + u(1 - |u|^2) = 0, \tag{7}$$

and its solutions of the form

$$u(\mathbf{x}) = U(r)\exp(i(n\theta + \theta_0)), \tag{8}$$

which are called *vortex solutions*. Here (r,θ) are the polar coordinates of $\mathbf{x}$: $\mathbf{x} = (r\cos\theta, r\sin\theta)$. For $r>0$ the function $U(r)$ satisfies the equation

$$U_{rr} + \frac{1}{r}U_r - \frac{n^2}{r^2}U + (1 - U^2)U = 0. \tag{9}$$

Let us now consider the nonlinear Schrödinger equation (4). We change to the new variables $\tilde{\mathbf{x}} = \varepsilon\mathbf{x}'$, $\tilde{t} = \varepsilon^2 t'$. As the small parameter ε we take the quantity ξ from Eq. (2), i.e., $\varepsilon = \xi$. In the new variables Eq. (4) becomes

$$\Delta u + \frac{1}{\varepsilon^2}u(1 - |u|^2) = iu_t. \tag{10}$$

The positions of the vortex is of order $O(\varepsilon)$, and the distance between vortices is of order $O(1)$, as in the original physical statement of the problem.

To obtain a system of equations describing the dynamics of the vortices, we follow the procedure proposed in Ref. 4.

Let us first consider the region outside of the vortex cores and construct an asymptotic solution of equation (10), treating the vortices as point singularities located at the points $\mathbf{x} = \xi_t(t)$. We call this the "exterior" solution and seek it in the form

$$u^\varepsilon(\mathbf{x},t) = u_0(\mathbf{x},t) + \varepsilon u_1(\mathbf{x},t). \tag{11}$$

It can be shown (see Appendix) that $|u_0| = 1$, so we can write $u_0 = e^{\Phi_0(\mathbf{x},t)}$. The phase $\Phi_0(\mathbf{x},t)$ of the wave function within the volume of the superfluid, except in the neighborhoods of the vortex cores, is a solution of the following boundary-value problem:

$$\begin{cases} \Delta\Phi_0 = 0, \\ \Phi_0(\mathbf{x},t) \to \theta_0 + n_j\theta, \quad \mathbf{x} \to \xi_j, \\ \dfrac{\partial\Phi}{\partial n} = 0 \quad \text{at the solid boundary} \end{cases} \tag{12}$$

and can be determined for a wide spectrum of regions. For an annular region $R_1 \leqslant r \leqslant R_2$ the solution Φ_0 was found as[10]

$$\Phi_0(z) = \operatorname{Re} W(z) = \operatorname{Re}\left\{ i\sum_{k=1}^{N} n_k\left[\ln\sigma\left(i\ln\frac{z}{z_k}\right)\right.\right.$$
$$\left.\left. -\ln\sigma\left(i\ln\frac{zz_k}{Z_{2,k}^2}\right) - \frac{2i\eta}{\omega_1}\ln\frac{r_k}{R_2}\ln z\right]\right\} + \text{const.} \tag{13}$$

Here $W(z)$ is a complex potential, $\sigma(z)$ is the Weierstrass sigma function with half-periods $\omega_1 = \pi$, $\omega_2 = i\ln(R_2/R_1)$, $\eta = \zeta(\omega_1)$, $\zeta(z)$ is the Weierstrass zeta function with the same half-periods,[11] $Z_{2,k} = R_2\exp i(\tilde{\theta}_k)$; the complex variable $z = r\exp(i\tilde{\theta})$ is measured from the center of the *ring*, so that the azimuthal angle $\tilde{\theta} = \tan^{-1}(y/x)$, and $\tilde{\theta}_k = \tan^{-1}(\eta_k/\zeta_k)$.

Expanding Φ_0 in a Taylor series around the jth vortex, we obtain an approximate expression for the phase of the wave function and, hence, for the wave function u_0 itself. This solution is

$$u_0 = e^{i\Phi_0} \approx e^{in_j\theta + i\theta_0}[1 + i\mathbf{K}^{(j)}\cdot\mathbf{r} + O(r^2)], \tag{14}$$

where

$$\mathbf{K}^{(j)} = \nabla\Phi_0 = (\operatorname{Re} W'(z_j), -\operatorname{Im} W'(z_j));$$

$$W'(z_j) = \frac{1}{z_j}\sum_{\substack{k=1 \\ k\neq j}}^{N} n_k\left[\zeta\left(i\ln\frac{z_j z_k}{Z_{2,k}^2}\right) - \zeta\left(i\ln\frac{z_j}{z_k}\right)\right]$$

$$+ \frac{n_j}{z_j}\zeta\left(2i\ln\frac{r_j}{R_2}\right) - \frac{2i\eta}{\omega_1 z_j}\sum_{k=1}^{N} n_k\ln\frac{r_k}{R_2}. \tag{15}$$

$$r = (x - \zeta_j(t), \ y - \eta_j(t)),$$

We now construct another solution of equation (10), setting

$$U^\varepsilon(\mathbf{x},t)=U_0\left(\frac{\mathbf{x}-\xi_j(t)}{\varepsilon}\right)+\varepsilon U_1\left(\frac{\mathbf{x}-\xi_j(t)}{\varepsilon}\right)+\dots$$

and seeking an approximate solution for large $\mathbf{X}=(\mathbf{x}-\xi_j(t))/\varepsilon$. This solution, which is possibly independent of the presence of boundaries of the region, can be found in a manner analogous to the solution of the problem for the nonlinear heat flow equation in an unbounded region[4] (see Appendix):

$$U(\mathbf{X},t)=e^{in j\theta+i\theta_0}\left[1+\frac{i\varepsilon}{2}(\dot\xi_j\mathbf{X})+O\left(\frac{1}{R_2}\right)\right.$$

$$\left.\times\left(1+\varepsilon\left(\dot\xi_j\cdot\frac{X}{R}\right)\right)\right]. \tag{16}$$

In order for solutions (14) and (16) to be mutually consistent, it is necessary that the leading terms of the expansion be equal for $\mathbf{r}=\varepsilon\mathbf{X}$, i.e.,

$$\mathbf{K}^{(j)}\cdot\varepsilon\mathbf{X}=\frac{1}{2}(\dot\xi_j\cdot\varepsilon\mathbf{X}),$$

which gives

$$\dot\xi_j=2\mathbf{K}^{(j)}. \tag{17}$$

This is the desired equation of motion for the jth vortex. By varying j from 1 to N, we obtain the equations of motion of all the vortices.

Knowing the particular form of the complex potential $W(z)$ in (13), one can obtain all the necessary information about the motion of vortices in rings of any dimensions.

Motion of vortices in cylinders and narrow rings

We shall show that for $R_1\to 0$ one obtains the motion of vortices in a cylinder. Indeed, since the half-period $|\omega_2|=\ln(R_2/R_1)$ is large in this case, the denominator of the ζ and σ functions $q=\exp(i\pi\omega_2/\omega_1)=R_1/R_2$ is small, the elliptic functions degenerate into the elementary functions:[11]

$$\zeta(u)=\frac{\eta u}{\omega_1}+\frac{\pi}{2\omega_1}\cot\frac{\pi u}{2\omega_1}$$

and the cotangents are easily evaluated:

$$\cot\left(\frac{i}{2}\ln\frac{z_jz_k}{Z_{2,k}^2}\right)=-\frac{z_j+Z_{2,k}^2/z_k}{z_j-Z_{2,k}^2/z_k},$$

$$\cot\left(\frac{i}{2}\ln\frac{z_j}{z_k}\right)=-\frac{z_j+z_k}{z_j-z_k}.$$

Then from expression (15) we get

$$W'(z_j)\approx\sum_{k=1}^{N}n_k\left[\frac{1}{z_j-z_k}-\frac{1}{z_j-Z_{2,k}^2/z_k}\right].$$

This is just the complex conjugate velocity of a fluid with N vortices in a cylinder.[8]

Another limiting case of interest is that of a narrow ring, $R_2-R_1\ll R_2$. Here $|\omega_1|\gg|\omega_2|$, and q is large. Using the homogeneity relation for the ζ functions[11]

$$\zeta(z|\omega_1,\omega_2)=i\zeta(iz|i\omega_1,\omega_2)=i\tilde\zeta(iz),$$

we arrive at the half-periods $\tilde\omega_1=\ln(R_2/R_1)$, $\tilde\omega_1=i\pi$, and the denominator q becomes small, so that the ζ functions again degenerate to cotangents:

$$\zeta\left(i\ln\frac{z_j}{z_k}\right)=-i\tilde\zeta\left(\ln\frac{z_j}{z_k}\right)\approx-\frac{i\tilde\eta}{\tilde\omega_1}\ln\frac{z_j}{z_k}$$

$$-\frac{i\pi}{2\tilde\omega_1}\cot\frac{\pi}{2\tilde\omega_1}\ln\frac{z_j}{z_k};$$

$$\zeta\left(i\ln\frac{z_jz_k}{Z_{2,k}^2}\right)=-i\tilde\zeta\left(\ln\frac{z_jz_k}{Z_{2,k}^2}\right)\approx-\frac{i\tilde\eta}{\tilde\omega_1}\ln\frac{z_jz_k}{Z_{2,k}^2}$$

$$-\frac{i\pi}{2\tilde\omega_1}\cot\frac{\pi}{2\tilde\omega_1}\ln\frac{z_jz_k}{Z_{2,k}^2}.$$

The tildes over the symbols mean that all quantities are evaluated at the new half-periods. In addition,

$$\eta=\zeta(\omega_1)=i\tilde\zeta(i\pi)=i\tilde\eta'.$$

After elementary calculations we obtain

$$W'(z)=\frac{1}{z}\sum_{k=1}^{N}\frac{i\pi n_k}{2\tilde\omega_1}\left[\cot\frac{\pi}{2\tilde\omega_1}\ln\frac{z_j}{z_k}-\cot\frac{\pi}{2\tilde\omega_1}\ln\frac{z_jz_k}{Z_k^2}\right]$$

$$+\frac{i}{z\tilde\omega_1}\sum_{k=1}^{N}n_k\ln\frac{R_2}{z_k}.$$

This is the complex conjugate velocity of a fluid in a narrow ring. To obtain the motion in a narrow rectangular channel, we conformally map the (cut) ring to a segment of a strip by means of the function $u=i\ln(z/R_2)$.

The ring maps into a horizontal strip between the straight lines $u=0$ and $u=-\ln(R_2/R_1)$. The velocity of fluid in the strip (channel) has the form

$$W'(u)=\frac{W'(z)}{u'(z)}=\frac{\pi}{2\tilde\omega_1}\sum_{k=1}^{N}n_k\left[\cot\frac{\pi}{2\tilde\omega_1}(u-u_k)\right.$$

$$\left.-\cot\frac{\pi}{2\tilde\omega_1}(u-u_k^*)\right]+C,$$

where

$$u_k=i\ln\frac{r_k\exp(i\theta_k)}{R_2};\quad u_k^*=i\ln\frac{R_2\exp(i\theta_k)}{r_k};$$

C is a constant flow.

Each term in the sum is the velocity of a fluid generated by an infinite Kármán vortex street,[14] where $2\tilde\omega_1=2\ln(R_2/R_1)$ is the distance between vortices. The narrowness of the channel means that these streets have practically no effect on one another, i.e., the distance between the streets is much greater than the distance between vortices within a street (this is ensured by the condition $|\tilde\omega_1|\ll|\tilde\omega_2|$).

Example 1. Let us investigate Eq. (17) in more detail for the particular case when there is one vortex moving in the ring.

Let there be a single vortex, located at the point

$z_1 = r_1 \exp(i\theta_1)$, in a ring $R_1 \leqslant r \leqslant R_2$.

For $N = 1$ we obtain from expressions (15) and (17)

$$W'(z_1) = \frac{n_1}{z_1} \zeta\left(2i \ln \frac{r_1}{R_2}\right) - \frac{2i \eta n_1}{\omega_1 z_1} \ln \frac{r_1}{R_2}.$$

Since, according to Ref. 11,

$$\zeta(z) = \frac{\eta z}{\omega_1} + \frac{\pi}{2\omega_1}\left[\cot\frac{\pi z}{2\omega_1} + 4\sum_{n=1}^{\infty} \frac{q^{2n}}{1-q^{2n}} \sin\frac{\pi n z}{\omega_1}\right],$$

for $\omega_1 = \pi$, $z_1 = 2i \ln(r_1/R_2)$ we obtain

$$\zeta_0(z_1) \equiv \zeta(z_1) - \frac{\eta z_1}{\omega_1} = \frac{1}{2}\cot\left[i \ln\left(\frac{r_1}{R_2}\right)\right]$$

$$+ 2\sum_{n=1}^{\infty} \frac{q^{2n}}{1-q^{2n}} \sin\left(2ni \ln\frac{r_1}{R_2}\right).$$

This gives

$$W'(z_1) = \frac{n_1}{z_1} \zeta_0(z_1).$$

We note that $\zeta_0(z_1)$ is an *imaginary*-valued quantity. Thus $W'(z_1) = (in_1/z_1)F(r_1)$, where $F(r_1)$ is a real-valued function of the vortex position r_1. Then

$$\mathbf{K}^{(1)} = (\mathrm{Re}\, W'(z_1), -\mathrm{Im}\, W'(z_1)) = \frac{n_1}{r_1} F(r_1)\hat{e}_\theta,$$

where $\hat{e}_\theta = (\sin\theta_1, -\cos\theta_1)$.

The equation of motion of the vortex takes the form

$$\dot{\xi}_j(t) = \frac{2n_1}{r_1} F(r_i)\hat{e}_\theta.$$

The velocity of the vortex is directed along a tangent to the circle on which the vortex is located. This is in agreement with the hydrodynamic theory of vortices: a vortex in a ring moves along a circle.[13]

Example 2. Let us analyze the motion of two vortices in a ring. We obtain the equations of motion of the two vortices from Eqs. (15) and (17) with $N = 2$.

These equations can be solved approximately by specifying the dimensions of the ring and the initial positions of the vortices, with the vortex strengths (n_1 and n_2) set equal to $+1$ or -1.

The solutions for a ring with an inner radius $R_1 = 0.5$ cm and outer radius $R_2 = 1.5$ cm were obtained by the Runge–Kutta method for various vortex strengths and various initial positions $\mathbf{x}_1$ and $\mathbf{x}_2$ of the vortices; they are illustrated in Figs. 1–5 (parts a, b, and c correspond to times $t_1 < t_2 < t_3$).

A ''vortex–vortex'' pair moves independently with a constant velocity along the same circle if at the initial time the vortices are located on the same circle and a sufficient distance apart (Fig. 1). If the vortices are initially located on different circles, then the vortex lying closer to the outer wall will move faster and will overtake the second vortex. At the time of overtaking the ''inner'' vortex describes a loop, while the ''outer'' vortex deviates slightly toward the center of the ring (Fig. 2).
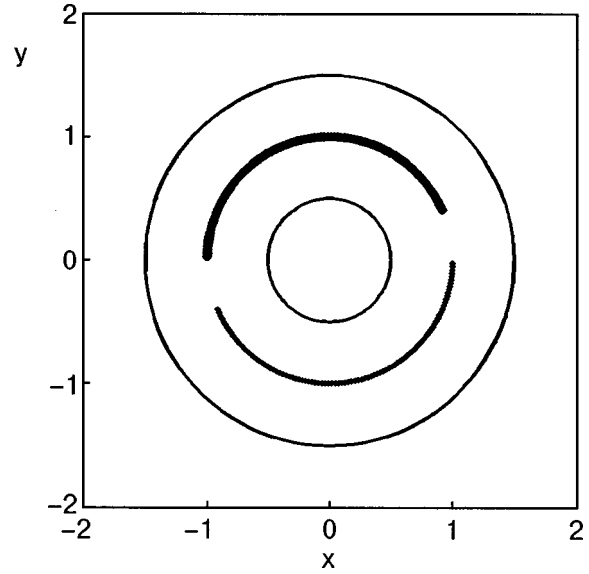

FIG. 1. Motion of a ''vortex–vortex'' pair ($n_1 = n_2 = 1$). The initial positions of the vortices are $\mathbf{x}_1 = (1,0)$, $\mathbf{x}_2 = (-1,0)$ (on the same circle). The vortices move along the circle independently of each other and at a constant velocity.

A ''vortex–antivortex'' pair moves mainly in opposite directions, but this is not simple motion along a circle. The vortex lying closer to the outer wall (the ''outer'' vortex) moves faster. If initially the vortices lie on different circles on different sides of the center, then as they approach each other the outer vortex slows down and the inner vortex changes its direction of motion, accelerates, and describes a complete revolution (Fig. 3). As it again approaches the outer vortex, it again slows down and changes direction, while the outer vortex accelerates and describes a revolution. Thus the inner vortex moves along a rather complex trajectory containing loops, while the outer vortex moves along a nearly circular trajectory, the motion of both vortices being very nonuniform in time.

If both vortices of a ''vortex–antivortex'' pair are initially located along one radius, then the vortices move in opposite directions, with the outer vortex having the higher velocity, but it slows down as it passes the other vortex. The inner vortex is deflected toward the center of the ring, describing a ''lobed'' trajectory (Fig. 4).

No less interesting is the motion of vortices of different sign initially located an appreciable distance apart on the same circle [Fig. 5a]. The vortices start to move toward each other, but after they have approached closely enough, they turn around [Fig. 5b] and move in the opposite directions, each along its own closed trajectory! [Fig. 5c].

CONCLUSION

We have implemented the method proposed in Ref. 4 for solving the Ginzburg–Landau equation in the nonstationary case [the Schrödinger equation (4)] for bounded regions. We have obtained a dynamical system of equations (17)—a system of ordinary differential equations—describing the motion of vortices. The right-hand sides of these equations are the gradients of the phase of the wave function of the con-
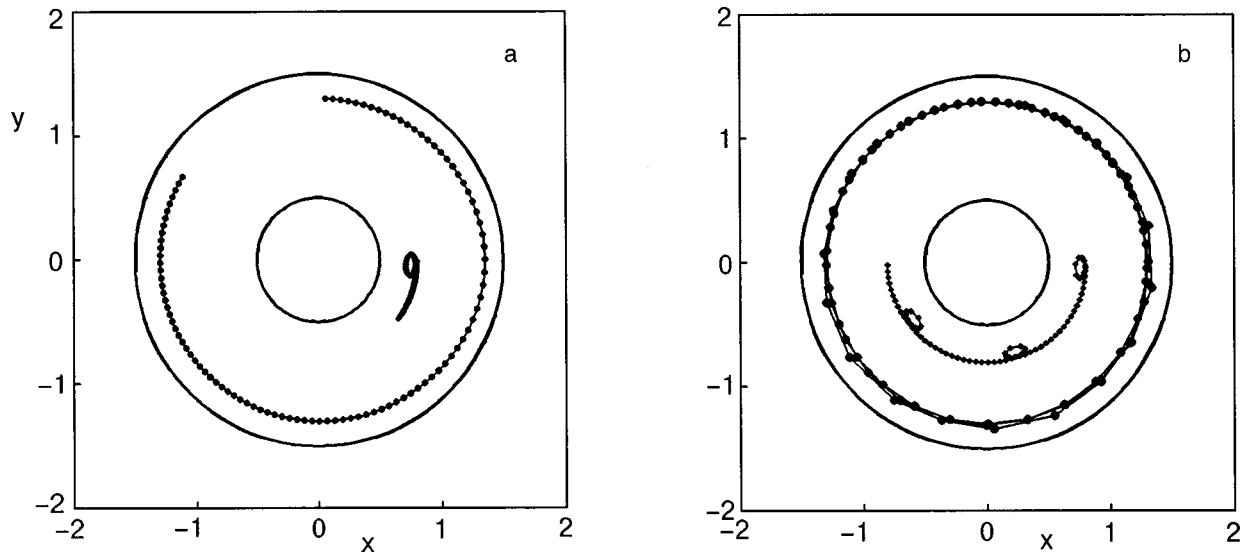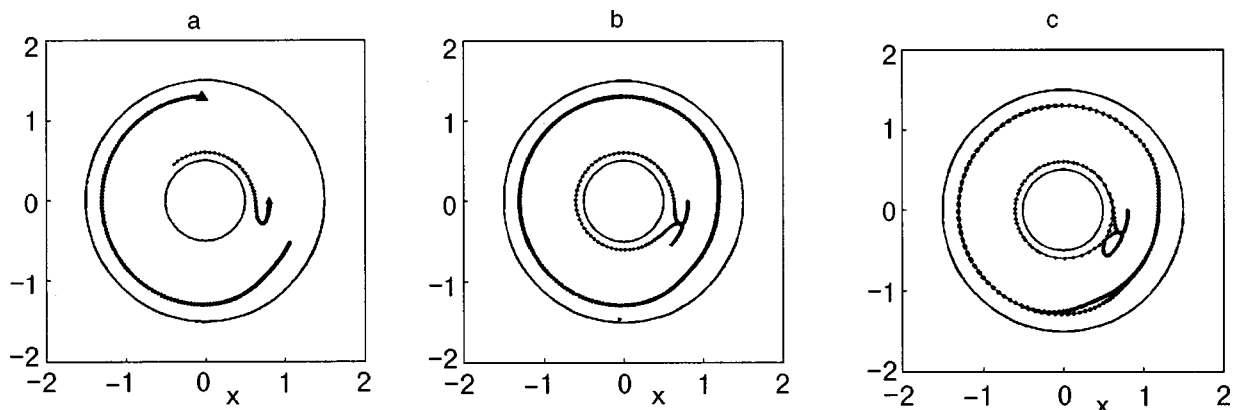
FIG. 2. Motion of a "vortex–vortex" pair ($n_1 = n_2 = 1$). The initial positions of the vortices are $\mathbf{x}_1 = (0.8, 0)$, $\mathbf{x}_2 = (0, 1.3)$. The vortices move in the same direction, and the second vortex (that closer to the outer wall) is moving faster. At the time of overtaking, the first vortex describes a loop, and then the motion along the circle continues.

densate, and for a superfluid can be expressed in terms of the derivative of a vector potential $W(z)$ of a fluid containing vortices; this vector potential depends on the shape of the region. We have given the explicit form of the complex potential for an annular region.

We have obtained an analytical solution of equation (17), which describes the motion of a single vortex in a ring, and we have investigated numerically the motion of a pair of vortices for various initial positions and strengths (signs) of the vortices. The trajectories of the vortices are shown in the figures.

APPENDIX

Derivation of the equations of motion of the vortices

The substitution of expansion (11) into Eq. (10) gives the following sequence of equations (the coefficients of equal powers of ε):

$$\varepsilon^{-2}: \quad u_0(1 - |\dot{u}_0|^2) = 0, \tag{A1}$$

$$\varepsilon^{-1}: \quad u_1 \bar{u}_0 + u_0 \bar{u}_1 = 0, \tag{A2}$$

$$\varepsilon^0: \quad -i u_{0t} = \Delta u_0 - |u_1|^2 u_0. \tag{A3}$$

From the first equation we immediate get $|u_0| = 1$, which gives $u_0 = e^{i\Phi_0(\mathbf{x}, t)}$.

From Eq. (A2) we get an equation relating the phase of the wave function u_0 with the modulus of the wave function u_1:

$$\Phi_{0t} = i\Delta\Phi_0 - (\nabla\Phi_0)^2 - |u_1|^2.$$

Since Φ_0 and $|u_1|$ are real-valued, this equation yields the following two equations:

$$\Delta\Phi_0 = 0, \tag{A4}$$

$$\Phi_{0t} = -(\nabla\Phi_0)^2 - |u_1|^2. \tag{A5}$$

FIG. 3. Motion of a "vortex–antivortex" pair ($n_1 = -n_2 = 1$). The initial positions of the vortices are $\mathbf{x}_1 = (0.8, 0)$, $\mathbf{x}_2 = (0, 1.3)$. The vortices start moving in opposite directions, but the second vortex moves faster (the initial positions of the vortices are indicated by triangles). As they approach each other, the second vortex slows down and the first changes direction and accelerates, describing a complete revolution. On the subsequent approach the pattern is repeated. Thus the inner vortex describes a complicated trajectory with loops, while the outer vortex moves nearly along the circumference, deviating slightly toward the center of the ring as it approaches the inner vortex.
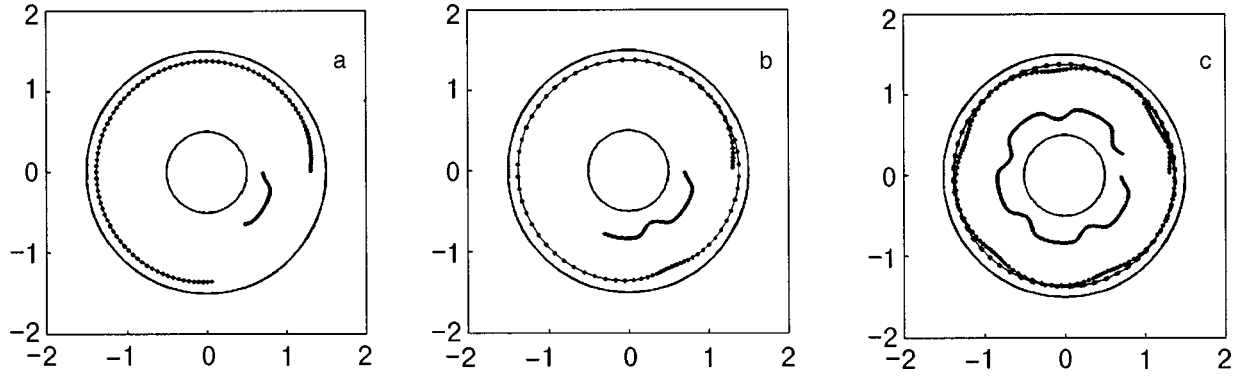
FIG. 4. Motion of a ''vortex–antivortex'' pair ($n_1 = -n_2 = 1$). The initial positions of the vortices are $x_1 = (0.7,0)$, $x_2 = (1.3,0)$ (on the same radius). The vortices move in opposite directions, the second vortex moving faster. Upon overtaking the first vortex, the second vortex slows down, while the first vortex deviates toward the center of the ring. One ''lobe'' of the trajectory of the first vortex corresponds to one revolution of the second vortex.

The first of these allows us to calculate Φ_0 (if suitable boundary conditions are specified), and the second enables us to find $|u_1|$ if Φ_0 is known.

Let us now find a solution of equation (A4) in the region outside the vortex cores, with the asymptotic boundary conditions at the cores

$$\Phi_0(\mathbf{x},t) \to n_j\theta + \theta_0, \quad \mathbf{x} \to \xi_j(t), \tag{A6}$$

where $\xi_j(t) = (\zeta_j, \eta_j)$ are the coordinates of the jth vortex, $\theta = \tan^{-1}[(y - \eta_j)/(x - \zeta_j)]$ is the azimuthal angle of the jth vortex, θ_0 is the phase shift, and $\theta_0 = \theta_0(\xi_1,\ldots,\xi_N)$.

Besides the conditions (A6) at the vortices, in a bounded region it is necessary to impose a condition at the boundary. Since the phase of the condensate wave function $\Phi(\mathbf{x},t)$ is related to the hydrodynamic velocity potential $\varphi(\mathbf{x},t)$ by the relation[9]

$$\varphi = \frac{\hbar}{m}\,\Phi,$$

one has $\mathbf{v} = \nabla\varphi = (\hbar/m)\nabla\Phi$, and the hydrodynamic condition of impermeability at a solid boundary, $\mathbf{v}\cdot\mathbf{n} = 0$, gives a Neumann boundary condition for Φ: $\partial\Phi/\partial n = 0$ at the boundary.

We thus have the following boundary-value problem for Φ_0:

$$\begin{cases} \Delta\Phi_0 = 0 & \text{in the region outside the vortex cores} \\ \Phi_0(\mathbf{x},t) \to n_j\theta + \theta_0, & \mathbf{x} \to \xi_j, \\ \dfrac{\partial\Phi_0}{\partial n} = 0 & \text{at the boundary.} \end{cases}$$

$$\tag{A7}$$

The solution of this problem can be found by the method of ''reflected vortices'' or by some other method. In particular, for an annular region $R_1 \leq r \leq R_2$ the velocity potential φ of an ideal fluid containing N vortices with vortex strengths n_k, located at the points $z_k = r_k \exp(i\tilde{\theta}_k)$, can be written in complex form.[10]

To obtain an approximate expression for Φ_0 in the neighborhood of the jth vortex, we note that for $z \to z_j$, only one term in the sum over k in (13) has a singularity, and that is the term corresponding to the vortex potential:

$$\Phi_0(z,t)\big|_{x \to \xi_j} = n_j \tan^{-1}\frac{y - \eta_j}{x - \zeta_j} = n_j\theta.$$

Consequently, in the neighborhood of the jth vortex, $\Phi_0(z,t)$ can be written in the form
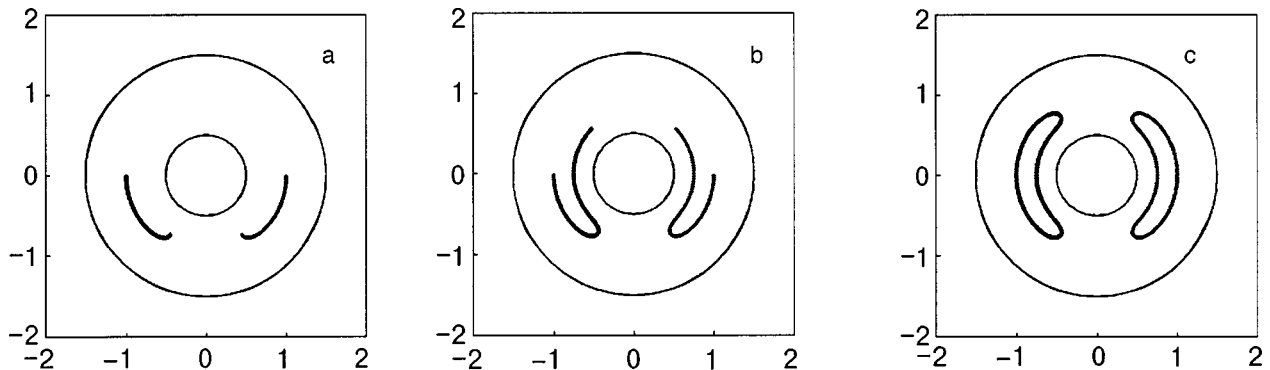
$$\Phi_0(z,t) = n_j\theta + \Phi_0^1(z,t)$$

FIG. 5. Motion of a ''vortex–antivortex'' pair ($n_1 = -n_2 = 1$). The initial positions of the vortices are $x_1 = (1,0)$, $x_2 = (-1,0)$ (on the same circle). The vortices move in opposite directions, each on its own closed trajectory, and never approach each other.

where $\Phi_0^1(z,t)$ is nonsingular at the point $z=z_j$ and can be expanded in a Taylor series about that point:

$$\Phi_0^1(z,t)=\Phi_0^1(z_j)+(\nabla\Phi_0^1)|_{z=z_j}\cdot(\mathbf{x}-\xi_j)+O(\mathbf{x}-\xi_j)^2.$$

The first term is the phase shift at the point $\xi_j(t)$: $\Phi_0^1(z_j)=\theta_0$.

Taking into account that

$$\nabla\Phi_0=(\operatorname{Re}W'(z),-\operatorname{Im}W'(z)),$$

and evaluating $W'(z_j)$ with the singular term excluded, we obtain expression (15). The wave function u_0 takes the form (14).

This is the ''exterior'' solution of the Schrödinger equation equation in the neighborhood of the jth vortex. The influence of the boundaries of the region is included in the term $\mathbf{K}^{(j)}$, which is calculated specifically for each region.

Let us find another solution to equation (4): we seek it in the form of a series,

$$U(\mathbf{x},t)=U_0(\mathbf{X})+\varepsilon U_1(\mathbf{X})+\ldots,$$

where we have introduced the notation

$$\frac{\mathbf{x}-\xi_j(t)}{\varepsilon}=\mathbf{X},$$

or, in polar coordinates, $\mathbf{X}=(R\cos\theta,R\sin\theta)$.

Substituting $U(\mathbf{x},t)$ into Eq. (4) gives the sequence of equations

$$\Delta U_0+U_0(1-|U_0|^2)=0, \tag{A8}$$

$$\Delta U_1+(1-2|U_0|^2)U_1-U_0^2\bar{U}_1=i\dot{\xi}_j(t)U_0. \tag{A9}$$

The solution of the first equation,

$$U_0(R,\theta,t)=f_0(R)e^{in}j^{\theta(t)+i\theta}0, \tag{A10}$$

in which $\theta(t)$ and θ_0 are the *same* as in the exterior solution, must be found subject to the conditions

$$\begin{cases} f_0(0)=0, \\ f_0(\infty)=1 \end{cases}. \tag{A11}$$

The direct substitution of U_0 from Eq. (A10) into Eq. (A8) gives an equation for f_0:

$$f_0''+\frac{1}{R}f_0'-\frac{n_j^2}{R^2}f_0+(1-f_0^2)f_0=0. \tag{A12}$$

It can be shown that there exists a single solution of equation (A12) with boundary conditions (A11) which at *large R* satisfies the relation:

$$1-f_0^2-(n_j^2/R^2)=O(1/R^4), \tag{A13}$$

from which we find

$$f_0\approx1-\frac{n_j^2}{2R_2^2}+O\left(\frac{1}{R^4}\right).$$

We seek U_1 in the form[4]

$$U_1(R,\theta,t)=f_1(R,\theta,t)e^{in}j^{\theta+i\theta}0=[(A_r(R)$$
$$+iA_i(R))\cos\theta+(B_r(R)$$
$$+iB_i(R))\sin\theta]e^{in}j^{\theta+i\theta}0.$$

Substituting U_0 and U_1 into Eq. (A9) gives four equations for A_r, A_i, B_r, and B_i (see Ref. 4), and the solution $U_1(R,\theta,t)$ at *large R* takes the form

$$U_1(R,\theta,t)=e^{in}j^{\theta+i\theta_0}\left[\frac{n_jC_{-1}}{R}\left(\dot{\xi}_j^\perp\cdot\frac{\mathbf{X}}{R}\right)+\frac{iR}{2}\left(\dot{\xi}_j\cdot\frac{\mathbf{X}}{R}\right)\right.$$
$$\left.+\frac{iA_{-1}}{R}\left(\dot{\xi}_j\cdot\frac{\mathbf{X}}{R}\right)+O\left(\frac{1}{R^3}\right)\left(\dot{\xi}_j\cdot\frac{\mathbf{X}}{R}\right)\right],$$

where $\dot{\xi}_j=(\dot{\zeta}_j,\dot{\eta}_j)$, $\dot{\xi}_j^\perp=(-\dot{\eta}_j,\dot{\zeta}_j)$.

We then obtain the *complete solution* $U=U_0+\varepsilon U_1$ for large R:

$$U(\mathbf{X},t)=e^{in}j^{\theta+i\theta_0}\left[1+\frac{i}{2}(\dot{\xi}_j\mathbf{X})+O\left(\frac{1}{R^2}\right)\right.$$
$$\left.\times\left(1+\varepsilon\left(\dot{\xi}_j\cdot\frac{\mathbf{X}}{R}\right)\right)\right],$$

which approximates the solution in the region near the boundary of a vortex, where the quantity $R=|\mathbf{X}|=|(\mathbf{x}-\xi_j(t))/\varepsilon|$ is large.

*E-mail: zueva@ilt.kharkov.ua

[1] V. L. Ginzburg and L. D. Landau, Zh. Éksp. Teor. Fiz. **20**, 1064 (1950).
[2] D. R. Tilley and J. Tilley, *Superfluidity and Superconductivity* [Wiley, New York (1974); Mir, Moscow (1977)].
[3] J. C. Neu, Physica D **43**, 385 (1990).
[4] E. Weinan, Physica D **77**, 384 (1994).
[5] P. de Gennes, *Superconductivty of Metalls and Alloys* [Benjamin, New York (1966); Mir, Moscow (1968)].
[6] A. V. Nikiforov and É. B. Sonin, Zh. Éksp. Teor. Fiz. **85**, 642 (1983) [Sov. Phys. JETP **58**, 373 (1983)].
[7] A. A. Thiele, Phys. Rev. Lett. **30**, 230 (1973).
[8] S. J. Putterman, *Superfluid Hydrodynamics* (Vol. 3 of Low Temperature Physics Ser.) [Elsevier–North-Holland, Amsterdam–New York (1974); Mir, Moscow (1978)].
[9] L. D. Landau and E. M. Lifshitz, *Statistical Physics*, Vol. 2: *Condensed-Matter Theory*, by E. M. Lifshitz and L. P. Pitaevskiĭ [Pergamon Press, Oxford (1980); Nauka, Moscow (1978)].
[10] A. D. Tyuptsov and T. I. Zueva, Mat. Fiz. Anal. Geom. **1**, 529 (1994).
[11] M. Abramowitz and I. A. Stegun, *Handbook of Mathematical Functions* [Dover, New York (1965); Nauka, Moscow (1979)].
[12] M. A. Lavrent'ev and B. V. Shabat, *Methods of the Theory of Functions of a Complex Variable* [in Russian], Nauka, Moscow (1973).
[13] A. D. Tyuptsov and T. I. Zueva, Fiz. Nizk. Temp. **20**, 1116 (1994) [Low Temp. Phys. **20**, 877 (1994)].
[14] L. M. Milne-Thomson, *Theoretical Hydrodynamics*, 4th ed. [Macmillan, London (1960); Mir, Moscow (1964)].

Translated by Steve Torstveit

SUPERCONDUCTIVITY, HIGH-TEMPERATURE

Lower critical fields of textured high-temperature superconductors. III. Experimental study of the anisotropy of the fields H_{c1} of the HTSC YBa$_2$Cu$_3$O$_{7-\delta}$

V. A. Finkel'* and V. V. Derevyanko

National Science Center, Kharkov Institute of Physics and Technology, ul. Akademicheskaya 1, 61108 Kharkov, Ukraine
(Submitted April 21, 1999; revised August 16, 1999)

The dependence of the critical currents I_c of textured samples of the HTSC YBa$_2$Cu$_3$O$_{7-\delta}$ ($T = 77.3$ K) on the value of an external magnetic field $\mathbf{H}_{ext}$ applied beforehand is investigated for various angles between the field direction and the sample. By a technique developed in the present study the measured angular dependence of $I_c(H)$ is used to determine the values of the lower critical fields H_{c1} of the HTSC YBa$_2$Cu$_3$O$_{7-\delta}$ in two directions: the direction of the principal axis of the orthorhombic lattice, $H_{c1}^{ab} = 89$ Oe, and in the perpendicular direction, $H_{c1}^{c} = 383$ Oe; the ratio of the effective masses of the electron in the two directions is $m^c/m^{ab} = 18.5$. © *2000 American Institute of Physics.* [S1063-777X(00)00202-4]

INTRODUCTION

The idea that the anisotropy of the lower critical fields H_{c1} of high-temperature superconductors (HTSCs) in textured samples can be investigated by making a series of measurements of the critical fields for several values of the angle of rotation φ of the sample about an axis perpendicular to the direction of an external magnetic field $\mathbf{H}_{ext}$ was conceptualized in an earlier paper[1] (the angle φ is measured from the Z axis of the laboratory coordinate system, which is the direction of the field $\mathbf{H}_{ext}$). It was assumed that the angular dependence of the lower critical fields of a HTSC can be described theoretically by models of the magnetic properties of uniaxial type-II superconductors; these models, which had been developed in the framework of the anisotropic Ginzburg–Landau theory long before the discovery of high-temperature superconductivity,[2–4] have subsequently been applied successfully to HTSCs.[5,6] For example, according to Ref. 2, under conditions where the external magnetic field $\mathbf{H}_{ext}$ is at an angle γ to the magnetic anisotropy axis $\boldsymbol{\nu}$, which for all known HTSCs is the crystallographic direction $\langle 001 \rangle$ (c) of the the tetragonal or orthorhombic lattices of HTSCs, the angular dependence of the lower critical field H_{c1} is described by the equation

$$H_{c1} = \frac{H_{c1}^{c}}{[\cos^2 \gamma + (m^c/m^{ab})\sin^2 \gamma]^{1/2}}, \qquad (1)$$

where H_{c1}^{c} is the value of H_{c1} in the direction of the magnetic anisotropy axis c, m^c and m^{ab} are components of the "effective mass tensor" of the electron in the anisotropic Ginzburg–Landau theory along the principal axis (m^c) and in the direction perpendicular to it (m^{ab}).

As was shown in Refs. 1 and 7, a real textured HTSC sample can be placed in correspondence with a single crystal which is oriented in the laboratory coordinate system XYZ

(the Z axis is in the direction of the external magnetic field $\mathbf{H}_{ext}$; see above) in such a way that the angular dependence of its lower critical field $H_{c1}(\varphi)$ in the XZ plane is analogous to that for the textured polycrystal. For the simplest case of a conical texture (which is nevertheless quite realistic for HTSC ceramics), where the magnetic anisotropy axis $\boldsymbol{\nu}$ precesses around a certain direction in the laboratory coordinate system (the "limiting" case of such a texture is the planar texture, for which, e.g., the basal plane ab is parallel to the surface of the sample), the value of the lower critical field of Eq. (1) has the following behavior[1] as the sample is rotated around the Y axis, from the Z axis toward the X axis, by an angle φ:

$$H_{c1}(\gamma)$$

$$= \frac{H_{c1}^{c}}{\left[\dfrac{m^c}{m^{ab}} + \left(1 - \dfrac{m^c}{m^{ab}} \right) \left(-\dfrac{\sin \gamma \sin \varphi}{\sqrt{2}} + \cos \gamma \cos \varphi \right)^2 \right]^{1/2}}. \qquad (2)$$

To determine the values of the lower critical fields H_{c1}^{c} and H_{c1}^{ab} (we recall that $H_{c1}^{ab} = H_{c1}^{c}(m^c/m^{ab})^{-1/2}$; Ref. 8), the effective-mass ratio m^c/m^{ab}, and the angle γ between the magnetic field $\mathbf{H}_{ext}$ and the averaged position of the magnetic anisotropy axis $\boldsymbol{\nu}$ in a particular sample, one must solve a system of equations of the type (2) for three different angles of rotation of the sample ($\varphi_i = 0, \varphi_1, \varphi_2$). As was shown in Ref. 1, everything ultimately reduces to the solution of a rather simple equation:

$$A \cos^2 \gamma + B = C \sin \gamma \cos \gamma, \qquad (3)$$

in which the coefficients A, B, and C are explicit functions of only the experimentally measured values of the critical fields determined in the directions corresponding to angles of

rotation φ_i of the sample in the XZ plane of the laboratory coordinate system. Then the values of interest to us are easily found:

$$\frac{m^c}{m^{ab}} = \frac{(-\sin\gamma\sin\varphi_i/\sqrt{2}+\cos\gamma\cos\varphi_i)^2-[H_{c1}(\varphi_i)/H_{c1}(0)]\cos^2\gamma}{[H_{c1}(\varphi_i)/H_{c1}(0)]\sin^2\gamma-1+(-\sin\gamma\sin\varphi_i/\sqrt{2}+\cos\gamma\cos\varphi_i)^2}, \tag{4}$$

$$H_{c1}^c = H_{c1}(0)[m^c/m^{ab}-(1-m^c/m^{ab})\cos^2\gamma]^{1/2}, \tag{5}$$

$$H_{c1}^{ab} = H_{c1}^c(m^c/m^{ab})^{-1/2}. \tag{6}$$

The goal of the present paper is to lay an experimental foundation for the possibility of studying the anisotropy of the lower critical fields in textured polycrystalline objects, taking as an example the HTSC $YBa_2Cu_3O_{7-\delta}$.[1]

The optimum way of implementing this idea experimentally[7] is to measure the critical currents of textured (in particular, ceramic) HTSC samples after imposing a magnetic field directed at various angles to the axes of the sample at temperatures $T<T_c$. As a rule, it is assumed that the value of the lower critical fields H_{c1} in experiments of this kind corresponds to the onset of a dependence of the critical current in zero magnetic field, $j_c(0)$, on the strength of the magnetic field H_{ext} applied beforehand (see, e.g., Refs. 7, 9, and 10).[2] The relatively low current-carrying capacity of ceramic samples ($j_c \sim 10^2 - 10^3$ A/cm² at $T=77.3$ K) does not preclude making measurements of H_{c1}; moreover, because of the low transport currents and, consequently, low magnetic fields H_{tr} generated by these currents, these fields do not lead to appreciable distortions of the picture as to the effect of external magnetic fields of different orientations on the $I_c(H_{ext})$ curves, from which the lower critical fields H_{c1} of the HTSC are determined.

EXPERIMENTAL TECHNIQUE

The object of study was a sample of the HTSC $YBa_2Cu_3O_{\sim 6.95}$ synthesized by the ''standard'' ceramic technology (see, e.g., Ref. 11). The x-ray diffraction patterns reveal that a relatively weak texture, close to the texture of the basal plane (001) of the orthorhombic lattice,[12,13] was formed in the stage of uniaxial pressing of the powders prior to the final operation in the synthesis — baking in an oxidizing atmosphere. The dimensions of the sample were $19.0 \times 3.2 \times 2.0$ mm. The low-resistance current and potential contacts were formed by the vacuum deposition of silver from the vapor phase at a temperature of ~ 200 °C.

The current–voltage (I–V) characteristics were recorded on an IBM PC/AT 386 computer with a special attachment[14] consisting of control units for the current of the magnetic field source (solenoid) and the source of the transport current flowing through the sample. All the measurements were made in an automated mode.

The experiments essentially consisted of precision zero-field measurements of the critical currents in $YBa_2Cu_3O_{\sim 6.95}$ at $T=77.3$ K as functions of the magnitude and direction of

an external magnetic field $\mathbf{H}_{ext}$ ($0 \leqslant H_{ext} \leqslant 500$ Oe) applied beforehand at the same temperature, i.e., in essence, measurements of the value and orientation of the the trapped magnetic flux.[7] To do this, a Dewar containing a rotating device, the sample holder, was placed in a solenoid. The rotating device was used to set the angle φ between the axes of the sample and solenoid to an accuracy of $\delta\varphi \sim 2°$. The measurements were made for angles φ from 0 to 90° with a step of $\Delta\varphi = 10°$.

A current I_{sol}, producing a field H_{ext}, was sent through the solenoid by the the control unit for the magnetic field source with the sample at a temperature $T=77.3$ K. Then the current I_{sol} was turned off, and the control unit for the transport current sent a transport current through the sample. The transport current was increased smoothly until a voltage $U=1$ μV appeared across the sample, which was arbitrarily taken as the criterion for the onset of the transition of the superconductor to a mixed state, and the corresponding value of $I_c(0)$ was stored in the computer. Then the cycle of measurements was repeated at the next (higher) value of I_{sol}.

EXPERIMENTAL RESULTS

Figure 1a shows a typical curve of the critical current in zero field, $I_c(0)$, at $T=77.3$ K ($\varphi=50°$) as a function of the magnitude of the magnetic field H_{ext} applied beforehand at the same temperature. There are three pronounced regions on the curve:

1) $0<H_{ext}\lesssim 60$ Oe, where the critical current does not depend on the field;

2) $60 \lesssim H_{ext} \lesssim 150$ Oe, where the critical current decreases severalfold as the magnetic field strength increases;

3) $H_{ext} \gtrsim 150$ Oe, where the critical current is practically independent of H_{ext}.

The initial (practically horizontal) part of the curve apparently corresponds to Meissner behavior of the $YBa_2Cu_3O_{\sim 6.95}$ sample,[3] i.e., to the situation $H_{ext}<H_{c1}$. The region of the steep drop is where the trapping of magnetic flux by variously oriented granules begins. The final part of the curve corresponds to the onset of penetration of the external magnetic field into the interior of the granules.[7] It must be kept in mind, however, that the positions of the boundaries of the different regions on the field dependence of the critical current cannot be determined very strictly. In a study of the anisotropy of the lower critical fields H_{c1} of a HTSC one must very carefully take into account the demagnetizing factor D, i.e., to correct the value of the magnitude H_{ext} of the external magnetic fields $\mathbf{H}_{ext}$. In other words,
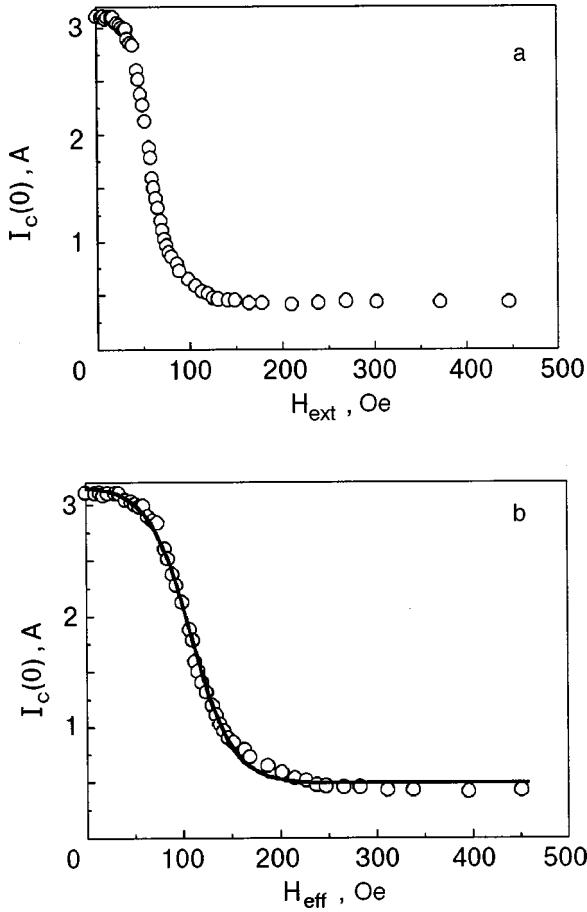
FIG. 1. Field dependence of the critical current in a sample of the HTSC superconductor $YBa_2Cu_3O_{\sim6.95}$ ($\varphi=50°$) at $T=77.3$ K. a: $I_c(0)=f(H_{ext})$; b: $I_c(0)=f(H_{eff})$.

these field values must be converted into the magnitudes of ''effective'' fields H_{eff} applied to the sample. As we know, for a superconductor in the absence of a magnetic-field penetration effect one has

$$H_{eff}=H_{ext}/(1-D_i),\qquad(7)$$

where D_i are the components of the tensor of demagnetizing coefficients of the sample.[16]

For a triaxial ellipsoid with ''long'' axis in the z direction (an object with a shape similar to the sample under study) the values of the tensor components D_i are[17]

$$D_X=\frac{y}{x+y}-\frac{3}{2}\frac{xy}{z^2}\ln\left(\frac{4z}{x+y}\right)+\frac{xy(3x+y)}{4z^2(x+y)},$$

$$D_Y=\frac{x}{x+y}-\frac{3}{2}\frac{xy}{z^2}\ln\left(\frac{4z}{x+y}\right)+\frac{xy(3y+x)}{4z^2(x+y)},\qquad(8)$$

$$D_Z=\frac{xy}{z^2}\left[\ln\left(\frac{4z}{(x+y)}\right)-1\right].$$

For a HTSC sample rotated by an angle φ about the Y axis away from the Z direction (which in our experimental geometry corresponds to the direction of the vector $\mathbf{H}_{ext}$) toward the X axis of the laboratory coordinate system, the value of D_φ, as was shown in Ref. 18, is

$$D_\varphi=D_X\cos^2\varphi+D_Z\sin^2\varphi.\qquad(9)$$

Figure 1b shows the results of the measurements of the current-carrying capacity of a $YBa_2Cu_3O_{\sim6.95}$ sample at $\varphi=50°$, after correction for the demagnetizing factor, and Fig. 2 shows the entire set of data collected in this study.

DISCUSSION OF THE RESULTS

The results of the measurements of $I_c(H_{eff},\varphi)$ shown in Fig. 2 clearly enable one to perform the main task of this study — to establish the orientation dependence of the lower critical field H_{c1} of the HTSC $YBa_2Cu_3O_{\sim6.95}$ at $T=77.3$ K. For this it is necessary to recover the character of the function $H_{c1}(\varphi)$ from the experimental data.

One can assume that for any textured ceramic sample of a HTSC the probability density for the distribution of granules over orientations has a normal (Gaussian) character. The probability density of the lower critical fields should clearly have the same character:

$$\Psi(H_{c1})=\frac{1}{\sqrt{2\pi}\Delta H_{c1}}\exp\left[-\frac{(H_{eff}-H_{c1})^2}{2\Delta H_{c1}^2}\right],\qquad(10)$$

where ΔH_{c1} is the error in the determination of the lower critical field H_{c1}

The same probability distribution for the values of the lower critical fields $F(H_{c1})$ in the interval $H_{c1}^{ab}\leqslant H_{c1}\leqslant H_{c1}^c$ is of the form[19]

$$F(H_{c1})=\frac{1}{\sqrt{2\pi}\Delta H_{c1}}\int_{H_{c1}^{ab}}^{H_{c1}^c}\exp\left[-\frac{(H_{eff}-H_{c1})^2}{2\Delta H_{c1}^2}\right]dH_{eff}.\qquad(11)$$
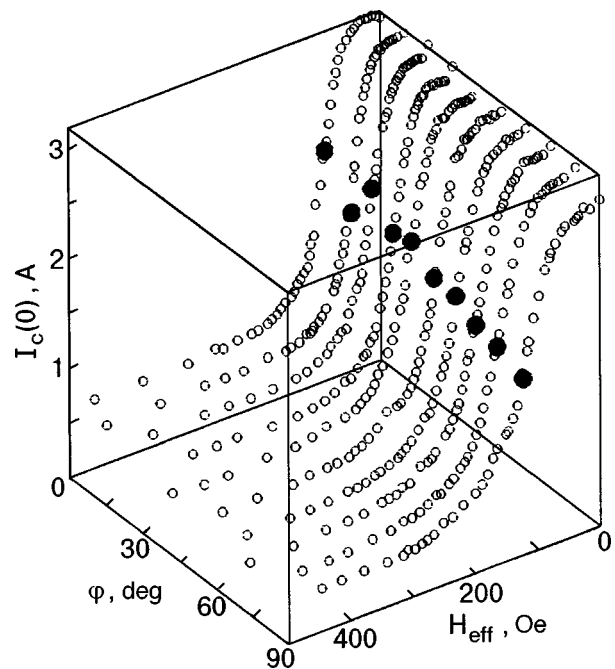

FIG. 2. Field dependence of the zero-field critical current $I_c(0)$ in $YBa_2Cu_3O_{\sim6.95}$ at $0\leqslant\varphi\leqslant90°$: ● — the values of H_{c1} at the different angles φ.
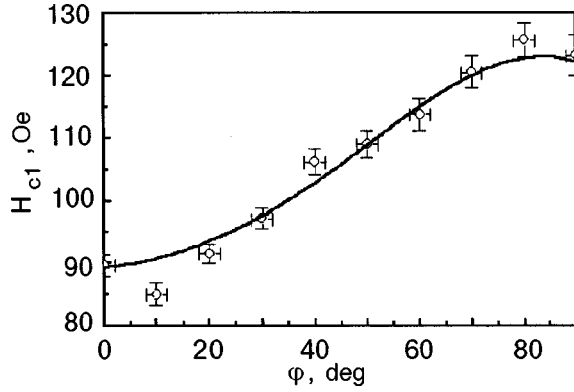
FIG. 3. Dependence of the lower critical field H_{c1} of the HTSC YBa$_2$Cu$_3$O$_{\sim 6.95}$ on the angle of rotation of the sample ($0 \leqslant \varphi \leqslant 90°$).

FIG. 4. Value of the magnetic flux ΔM trapped at the transition of a sample of the HTSC YBa$_2$Cu$_3$O$_{\sim 6.95}$ to a mixed state, as a function of the lower critical field H_{c1}.

It is clear that in experiments measuring the dependence of the critical current on the magnetic field, an analog (measure) of the probability is the value of the critical current in zero magnetic field $[F(H_{c1}) = I_c(0)]$ in the interval $H_{c1}^{ab} \leqslant H_{c1} \leqslant H_{c1}^{c}$, and the $[I_c(0)](H_{eff})$ curve should be described by the same equation (11). It would seem that any $[I_c(0)](H_{eff})$ curve obtained at an arbitrary value of the sample rotation angle φ should carry exhaustive information about the anisotropy of the lower critical fields H_{c1}: the beginning[4] and end of the region of the sharp drop should correspond to the minimum and maximum values of the lower critical field, H_{c1}^{ab} and H_{c1}^{c}, respectively, and the inflection point on the curve should correspond to the most probable value of H_{c1} for the given orientation of the HTSC sample with respect to the external magnetic field. Unfortunately, only a very rough estimate of H_{c1}^{ab} and H_{c1}^{c} can be obtained in this way. In real experiments on textured HTSC samples the beginning and end of the various regions on the $[I_c(0)](H_{eff})$ curves are too indistinct [see Fig. 1b]. However, the $[I_c(0)](H_{eff})$ curves obtained for different values of the angles φ make it possible to determine the most probable value of the fields H_{c1} to rather good accuracy [by processing these curves according to Eq. (11)]. For example, the inflection point of the continuous curve in Fig. 1b corresponds to a value $H_{c1} = 109.0 \pm 0.7$ Oe.

The angular dependence of the lower critical fields H_{c1} obtained in this way for the HTSC YBa$_2$Cu$_3$O$_{\sim 6.95}$ at $T = 77.3$ K is shown in Fig. 3. When the algorithm described above was used to process the experimental data (the values obtained for the fields H_{c1} for angles of rotation φ equal to 0°, 50°, and 90°) were ''summed'' in the computational formulas), we obtained the following parameter values: for the angle between the magnetic anisotropy axis and the external field, $\gamma = 94.5°$, for the lower critical fields, $H_{c1}^{ab} = 89$ Oe and $H_{c1}^{c} = 383$ Oe, and for the effective-mass ratio of the electron, $m^c/m^{ab} = 18.5$. The continuous curve in Fig. 3, which was constructed according to Eq. (2) for these values of γ, m^c/m^{ab}, and H_{c1}^{c}, satisfactorily describes the entire set of experimental data.

One notices that there is a clear correlation between the values of the lower critical field $H_{c1}(\varphi)$ and the trapped magnetic flux $\Delta M(\varphi)$[5] — as H_{c1} increases, ΔM decreases
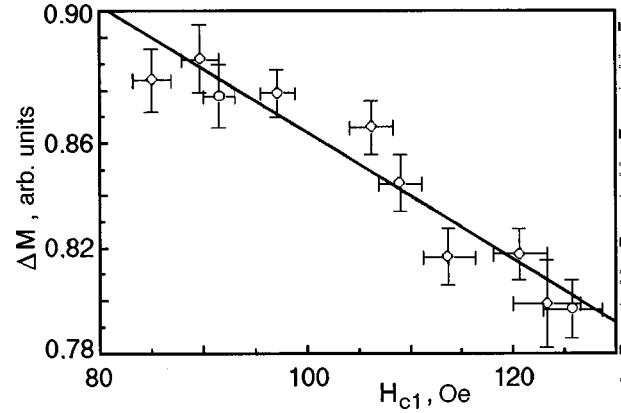
in a practically linear manner (Fig. 4). This effect is apparently somehow related to the anisotropy of the fundamental quantities — the coherence length ξ and the magnetic-field penetration depth λ for the type-II superconductor,[6] but at the present time it is not possible to make any quantitative estimates.

CONCLUSION

The results of our study of the anisotropy of the lower critical fields of the HTSC YBa$_2$Cu$_3$O$_{\sim 6.95}$ at $T = 77.3$ K are internally consistent (the best evidence of this is that all the experimental points conform fairly well to the calculated curve; see Fig. 3), a fact which is a weighty argument in favor of the correctness of the approach developed here (and in our previous papers)[1,7] for measuring the fields H_{c1}^{ab} and H_{c1}^{c} in textured HTSC samples. The values obtained in this paper for the fields H_{c1}^{ab} and H_{c1}^{c} and for the anisotropy parameter m^c/m^{ab} for YBa$_2$Cu$_3$O$_{\sim 6.95}$ at $T = 77.3$ K differ very little, within the scatter of the available data (see, e.g., Refs. 20–24), from the results of direct measurements on single crystals.

The present study is largely of a methodological character, having the goal of confirming the feasibility of a new way of investigating the anisotropy of the lower critical fields of HTSCs without requiring the use of oriented single-crystal samples. The next step in these investigations should be a broad study of the anisotropy of the lower critical fields of a number of high-temperature superconductors, including those for which it is very difficult or altogether impossible to obtain single crystals (we are thinking of HTSCs with a substitution of elements in different positions of their crystal lattices).

[1] A texture analysis, i.e., a study of the texture by diffraction methods, for example, is not part of the program.
[2] It will be shown below that this way of determining H_{c1} is not entirely correct.

[3])Of course, since complete penetration of the magnetic field into the intergranular medium occurs for $H \gg H_{c2J}$, and H_{c2J} is not more than a few oersteds (see, e.g., Refs. 10 and 15), such a state of the HTSC is far from one of ideal diamagnetism.

[4])Recall that the field at which this region begins is the value ordinarily adopted as H_{c1} for a given orientation of a HTSC sample.[7,9,10]

[5])ΔM was determined as the difference of the ordinates of the first and third parts of the $I_c(H_{ext})$ curve (see Fig. 1).

[6])Recall that $H_{c1}^c/H_{c1}^{ab} = H_{c2}^{ab}/H_{c2}^c = \xi^{ab}/\xi^c = \lambda^c/\lambda^{ab} = (m^c/m^{ab})^{1/2}$ (Ref. 8).

[1] V. A. Finkel', Fiz. Nizk. Temp. **25**, 554 (1999) [Low Temp. Phys. **25**, 410 (1999)].

[2] A. V. Balatskiĭ, L. I. Burlachkov, and L. P. Gor'kov, Zh. Éksp. Teor. Fiz. **90**, 1478 (1986) [Sov. Phys. JETP **63**, 866 (1986)].

[3] D. R. Tilley, Proc. Phys. Soc. **85**, 1177 (1965).

[4] E. A. Kats, Zh. Éksp. Teor. Fiz. **56**, 1675 (1969) [Sov. Phys. JETP **29**, 897 (1969)].

[5] R. A. Klemm, Phys. Rev. B **47**, 14630 (1993).

[6] L. Burlachkov, Y. Yeshurun, M. Konezkowski, and F. Holtzberg, Phys. Rev. B **45**, 8193 (1992).

[7] V. A. Finkel' and V. V. Toryanik, Fiz. Nizk. Temp. **23**, 824 (1997) [Low Temp. Phys. **23**, 618 (1997)].

[8] Y. Iye, Int. J. Mod. Phys. B **3**, 367 (1989).

[9] E. Altshuler, S. Garsia, and J. Barroso, Physica C **177**, 61 (1991).

[10] A. A. Zhukov, D. A. Komarkov, and G. T. Karapetov, Physica B **169**, 661 (1991).

[11] V. A. Finkel', V. M. Arzhavitin, A. A. Blinkin, V. V. Derevyanko, and Yu. Yu. Razdovskii, Physica C **235–240**, 303 (1994).

[12] A. S. Kapcherin, I. I. Papirov, P. I. Stoev, V. V. Toryanik, V. A. Finkel', V. A. Shkuropatenko, and T. I. Bukharova, Sverkhprovod. KIAE **5**, 113 (1992) [Superconductivity **5**, 114 (1992)].

[13] V. A. Finkel' and V. V. Toryanik, Functional Mater. **3**, 190 (1996).

[14] V. V. Toryanik, V. A. Finkel', and V. V. Derevyanko, Fiz. Khim. Obrab. Mater. , No. 5, 55 (1995).

[15] N. N. Efimova, Yu. A. Popkov, M. B. Ustimenkova, and V. A. Finkel', Fiz. Nizk. Temp. **20**, 343 (1994) [Low Temp. Phys. **20**, 273 (1994)].

[16] T. Van Duzer and C. W. Turner, *Principles of Superconductive Devices and Circuits* [Elsevier, New York (1981); Radio i Svyaz', Moscow (1984)].

[17] J. A. Osborn, Phys. Rev. **67**, 351 (1945).

[18] U. Yaron, I. Felner, and Y. Yeshurun, Phys. Rev. B **44**, 12531 (1991).

[19] N. A. J. Hastings and J. B. Peacock, *Statistical Distributions; a Handbook for Students and Practitioners* [Wiley, New York (1975); Statistika, Moscow (1980)].

[20] A. F. Hebard, A. T. Fiory, and D. R. Harshman, Phys. Rev. Lett. **62**, 2885 (1989).

[21] S. Sridhar, Dong-Ho Wu, and W. Kennedy, Phys. Rev. Lett. **63**, 1873 (1989).

[22] L. Krusin-Elbaum, A. P. Malozemoff, Y. Yeshurun, D. C. Cronemeyer, and F. Holtzberg, Phys. Rev. B **39**, 2936 (1989).

[23] Ch. Heinzel, Ch. Neumann, and P. Ziemann, Europhys. Lett. **13**, 531 (1990).

[24] V. V. Moshchalkov, C. Marin, J. Y. Henry, J. Rossat-Mignod, and J. F. Jacqout, JETP Lett. **53**, 166 (1991).

Green function of fermions in $2D$ superconducting Fröhlich model with inhomogeneous order parameter

V. M. Loktev*

Bogolyubov Institute of Theoretical Physics, National Academy of Sciences of Ukraine, Metrologichna Str. 14-b, Kiev-143, 03143, Ukraine

V. M. Turkowski

IIASS ''E. R. Caianiello'', 84019 Vietri sul Mare (SA) and Universitá degli Studi di Salerno, 84081 Baronissi (SA), Italy

The fermion Green function and spectral characteristics for the $2D$ Fröhlich model of superconductivity at static fluctuations in the phase of the order parameter are calculated. The results demonstrate strongly non-Fermi-liquid properties of the system at finite temperatures and relate with the pseudogap behavior of high-T_c superconductors at relatively small charge carrier densities. © *2000 American Institute of Physics.*
[S1063-777X(00)00302-9]

1. INTRODUCTION

The theoretical description of cuprates with high critical superconducting temperatures remains one of the most exiting and intriguing questions of modern solid-state physics. Because of the electronic and structural complexity of these metaloxide compounds there is a lack of theoretical tools for describing their normal and superconducting properties, which are evidently different from those of low-temperature superconductors.

One of the most interesting pecularities of cuprates is the presence of a pseudogap in the normal state of samples with lowered carrier densities n_f and temperatures T above the critical value T_c. Many theoretical explanations of this phenomenon have been proposed. Among them are explanations based on the model of the nearly antiferromagnetic Fermi liquid,[1] consideration of spin/charge-density waves,[2] and pre-superconducting fluctuations (see, for example, Refs. 3–17). The last characteristic has been studied by many approaches. For example, a T-matrix approximation was used in Refs. 3–9. But this approach does not permit a description of ordered states in $2D$ models (for example, the Berezinskii-Kosterlitz-Thouless (BKT) transition), which are the most suitable for description of cuprates.

It is possible to investigate such states by separating the order parameter (or, for low-dimensional degenerate systems, the so-called complex ordering field) into its modulus $\rho(x)$ and phase $\theta(x)$: $\Phi(x) = \rho(x)\exp[i\theta(x)]$. Although states with $\langle\Phi(x)\rangle \neq 0$ are forbidden in $2D$ systems at finite temperatures (the Coleman–Mermin–Wagner–Hohenberg (CMWH) theorem,[19]) states with $\rho \equiv \langle\rho(x)\rangle \neq 0$ and $\Phi = \rho\langle\exp[i\theta(x)]\rangle = 0$ can exist.

This approach has been used previously for studying the phase diagram in the $4F$ model[14,15] and in the more realistic Fröhlich model of superconductivity.[16,18] It was shown that in both cases the phase diagram consists of three regions: 1) $T > T_\rho$, where ρ vanishes, i.e., the normal state, 2) $T_\rho > T > T_{BKT}$ (T_{BKT} is the BKT transition temperature), where $\rho \neq 0$ and for $\langle\Phi*\Phi\rangle$ the correlations decay exponentially, and 3) $T_{BKT} > T$, where these fluctuations have a power-law decay.

This method was also used in Ref. 17 for the one-fermion Green function calculation in the two-dimensional $4F$ model in order to study the fermionic spectral function. It characterises the density of states and allows one to check for the presence of quasiparticle excitations in a system. (For a description of recent experiments on the angle-resolved photoemission spectra (ARPES) of high-T_c superconductors, which contain information about these properties, see Ref. 20. It was shown that right above the critical temperature the width of the quasiparticle peaks noticeably broadens, although the gap in quasiparticle spectrum still remains; this can be connected with the pseudogap properties of the underdoped high-T_c superconductors.

However, the $4F$ model does not take into account many of the properties of real systems, in particular, the retarded nature of the attractive interparticle interaction. As was shown in Refs. 16, and 18, including this property changes the behavior of a system drastically in comparison with the $4F$ case. For example, the width of the region with $T_\rho > T > T_{BKT}$ now goes to zero rather quickly at large charge carrier densities (optimal and overdoped regions).

The aim of this paper is to generalize the results obtained in Ref. 17 to the case of the more realistic Fröhlich model with the retarded interaction. For simplicity we consider the dispersionless ''optical'' phonon mode $\omega(k) = \omega_0 = \text{const}$. Nevertheless, the parameter ω_0 should be considered as the effective weighted value of the frequency of bosons with arbitrary dispersion law $\omega(k)$. This allows us to apply the given approach for an efficient study of any fermion–boson system with fluctuating order parameter.

2. THE MODEL

Let us start with the Fröhlich model Hamiltonian density in the standard form:

$$\mathcal{H} = \Psi_\sigma^+(x)\left(-\frac{\nabla^2}{2m} - \mu\right)\Psi_\sigma(x)$$
$$+ g\varphi(x)\Psi_\sigma^+(x)\Psi_\sigma(x) + \mathcal{H}_{ph}, \tag{1}$$

where $x = \mathbf{r}, \tau$ denotes the space and imaginary time variables; $\Psi_\sigma(x)$ is a fermion field with spin $\sigma = \uparrow, \downarrow$; m is the effective fermion mass; μ is the chemical potential; $\varphi(x)$ is the phonon field operator, and g is the fermion–phonon coupling constant; we put $\hbar = k_B = 1$. Below we shall use also the Pauli matrices τ_1, τ_2, τ_3 in the standard form.

In (1) $\mathcal{H}_{ph}$ is the Hamiltonian of free phonons with the simplest propagator (in the Matsubara formalism)

$$D(i\Omega_n) = -\frac{\omega_0^2}{\Omega_n^2 + \omega_0^2}, \quad \Omega_n = 2n\pi T, \tag{2}$$

where ω_0, as was pointed out, is the phonon frequency and n is an integer. It was also mentioned in the Introduction that in general this value is the weighted effective frequency of bosons with a momentum-dependent dispersion law $\omega(\mathbf{k})$.

Let us introduce in the Nambu representation $\Psi^+(x) = (\Psi_\uparrow^+(x)\Psi_\downarrow(x))$ the complex superconducting order parameter $\Phi(x) = \Psi^+(x)\tau\Psi(x) = \Psi_\downarrow\Psi_\uparrow$, where $\tau = (\tau_1 - i\tau_2)/2$.

Then in order to study the order-parameter-fluctuation dependences of the Green function

$$G(x) = \langle\Psi(x)\Psi^+(0)\rangle, \tag{3}$$

it is convenient to use the parametrization

$$\Phi(x) = \rho(x)\exp[i\theta(x)]^{1)} \tag{4}$$

with the simultaneous spinor substitution[1]

$$\Psi(x) = \exp[i\tau_3\theta(x)/2]y(x),$$
$$\Psi^+(x) = Y^+(x)\exp[-i\tau_3\theta(x)/2]. \tag{5}$$

As we have said, we shall consider the situation when ρ is a spatially homogeneous, or constant, quantity and the phase $\theta(x)$ is a random quantity. In fact, the spinors $Y(x)$ and $Y^+(x)$ are none other than the neutral fermion operators. In this case the Green function can be naturally separated into the charge and spin parts (see also, Ref. 17). Namely, in the momentum representation:

$$G(i\omega_n, \mathbf{k}) = T\sum_{m=-\infty}^{\infty}\int\frac{d^2p}{(2\pi)^2}$$

$$\times \sum_{\alpha,\beta=\pm} P_\alpha\mathcal{G}(i\omega_m, \mathbf{p})p_\beta D_{\alpha\beta}$$

$$\times (i\omega_n - i\omega_m, \mathbf{k} - \mathbf{p}). \tag{6}$$

Here $\mathcal{G}(i\omega_m, p)$ is the Green function of neutral fermions (see, for example, Ref. 16),

$$\mathcal{G}(i\omega_n, \mathbf{k}) = -\frac{i\omega_n\hat{I} + \tau_3\xi(\mathbf{k}) - \tau_1\rho}{\omega_n^2 + \xi^2(\mathbf{k}) + \rho^2} \tag{7}$$

with $\xi(\mathbf{k}) = \mathbf{k}^2/2m - \mu$; $D_{\alpha\beta}$ is the correlation function of the phase fluctuations

$$D_{\alpha\beta}(i\Omega_n, \mathbf{q}) = \int_0^{1/T}d\tau\int d^2r\exp[i\Omega_n\tau - i\mathbf{q}\mathbf{r}]$$

$$\times\langle\exp[i\alpha\theta(\tau,\mathbf{r})/2]\exp[-i\beta\theta(0)/2]\rangle \tag{8}$$

and $P_\pm = 1/2(\hat{I} \pm \tau_3)$ are the projectors. The Green function (7) of the neutral fermions coincides identically with that obtained in the $4F$ model, and the electron–phonon (boson) interaction enters this expression through ρ, which goes to zero if the coupling constant g (see (1) vanishes.

It is important to stress once again that in (7) $\rho = $const, i.e., homogeneous. But, of course, the neutral ρ does not play the role of a genuine order parameter in a system, so there is not any contradiction with the CMWH theorem.

3. THE GREEN FUNCTION

According to the previous section, for calculation of the Green function (6) it is necessary to know the phase fluctuation correlator $D_{\alpha\beta}$ (8). This quantity can be calculated using a functional integral[17]

$$D_{\alpha\beta} = \int\mathcal{D}\theta(x)\exp\left\{-\int_0^{1/T}d\tau_1\int d^2r_1\right.$$

$$\left.\times\left[\frac{1}{2}\theta(x_1)D_\theta^{-1}(x_1)\theta(x_1) + I(x_1)\theta(x_1)\right]\right\}$$

$$= \exp\left[\frac{1}{2}\int_0^{1/T}d\tau_1\int_0^{1/T}d\tau_2\int d^2r_1\right.$$

$$\left.\times\int d^2r_2 I(\tau_1,\mathbf{r}_1 D_\theta(\tau_1 - \tau_2, \mathbf{r}_1 - \mathbf{r}_2)I(\tau_2,\mathbf{r}_2)\right], \tag{9}$$

with the corresponding Green function

$$D_\theta(x) = \langle\theta(x)\theta(0)\rangle \tag{10}$$

of the phase fluctuations and the source of the θ field

$$I(x_1) = -i\frac{\alpha}{2}\delta(\tau_1 - \tau)\delta(\mathbf{r}_1 - \mathbf{r}) + i\frac{\beta}{2}\delta(\tau_1)\delta(\mathbf{r}_1).$$

$$\alpha, \beta = \pm. \tag{11}$$

In the second-derivative order the Green function (10) has the form:

$$D_\theta^{-1}(x) = -J(\mu,T,\rho)\nabla_r^2 - K(\mu,T,\rho)(\partial_\tau)^2. \tag{12}$$

The coefficients $J(\mu,T,\rho)$ and $K(\mu,T,\rho)$ have the physical sense of the superfluid stiffness and compressibility, respectively. One can readily obtain the following expressions for them (see, for example, Refs. 16 and 18):

$$J(\mu,T,\rho) = \frac{1}{8\pi}\{\sqrt{\mu^2+\rho^2}+\mu$$

$$+2T\ln[1+\exp(-\sqrt{\mu^2+\rho^2}/T)]\}$$

$$-\frac{T}{4\pi}\left[1-\frac{\rho^2}{4T^2}\frac{\partial}{\partial(\rho^2/4T^2)}\right]$$

$$\times\int_{-\mu/2T}^{\infty}dx\frac{x+(\mu/2T)}{\cosh^2\sqrt{x^2+\rho^2/4T^2}},$$

and

$$K(\mu,T,\rho)=\frac{m}{8\pi}\left(1+\frac{\mu}{\sqrt{\mu^2+\rho^2}}\tanh\frac{\sqrt{\mu^2+\rho^2}}{2T}\right.$$

$$-\frac{1}{8}\frac{\rho^2}{4T^2}\frac{\partial}{\partial(\rho^2/4T^2)}$$

$$\left.\times\int_{-\mu/2T}^{\infty}dx\frac{\tanh\sqrt{x^2+\rho^2/4T^2}}{\sqrt{x^2+\rho^2/4T^2}}\right).$$

Note that in comparison with the $4F$ case the functions J and K contain new terms with the derivative. But formally the general expressions for $D_\theta(x)$ in both cases are the same, so let us use below the formulas obtained for the $4F$ model in.[17]

Thus, in the static case $\tau=0$ at $T<T_{BKT}$ and when the coherence length is larger than the lattice spacing (as is justified for cuprates) the correlator has the usual (i.e., power law) form

$$D(\mathbf{r})=\left(\frac{r}{r_0}\right)^{-T/8\pi J}\tag{13}$$

(this is the expression for the only nonzero components $D_{++}(\mathbf{r},0)$ and $D_{--}(\mathbf{r},0)$). In (13) the quantity r_0 is

$$r_0=\frac{2}{T}\left(\frac{J}{K}\right)^{1/2}.\tag{14}$$

Note that in Ref. 17 it was assumed that $J\sim\varepsilon_F$ (the Fermi energy) and $K\sim$const. Under these assumptions r_0 is equal to $2\sqrt{\varepsilon_F/m}/T$ and has the meaning of the single-particle de Broglie wavelength. Whereas these approximations for K and J are justified for the physical regions in $4F$ model, in the boson-exchange case at large carrier densities the asymptotic behavior of J is different ($J\sim$const, so in this region r_0 does not have such a simple physical interpretation.

At $T>T_{BKT}$ it was proposed to use for $D(r)$ the expression from the theory of the BKT transition.[21,22]

$$D(\mathbf{r})=\left(\frac{r}{r_0}\right)^{-T/8\pi J}\exp\left(-\frac{r}{\xi_+(T)}\right),\tag{15}$$

where

$$\xi_+(T)=C\exp\left(\frac{T_\rho-T}{T-T_{BKT}}\right)^{1/2}.\tag{16}$$

This expression could be considered as a general form of $D(\mathbf{r})$ at any temperature if one puts $\xi_+(T)=\infty$ for

$T<T_{BKT}$. The constant C can be estimated as $r_0/4$, the value obtained from the assumption that ξ_+ cannot be much less than the only natural cutoff r_0 in the theory.

Then substitution of expression (7) for $\mathcal{G}$ and the Fourier transform of expression (15) for $D(\mathbf{r})$ into formula (6) results in the next representation for the Green function:

$$G(i\omega_n,\mathbf{k})=-\frac{Am\xi_+^{2\alpha}}{2\pi\alpha}$$

$$\times\left[\frac{A_1}{(u_1u_2)^\alpha}F_1\left(\alpha,\alpha,\alpha;\alpha+1;\frac{u_1-1}{u_1},\frac{u_2-1}{u_2}\right)\right.$$

$$\left.+(\sqrt{\omega_n^2+\rho^2}\to-\sqrt{\omega_n^2+\rho^2})\right],\tag{17}$$

where

$$A=\frac{4\pi\Gamma(\alpha)}{\Gamma(1-\alpha)}\left(\frac{2}{r_0}\right)^{2(\alpha-1)},\quad\alpha=1-\frac{T}{16\pi J},$$

$$A_1=\frac{1}{2}\left(\tau_3-\frac{\omega_n}{\sqrt{\omega_n^2+\rho^2}}\right),\tag{18}$$

and F_1 is the Appell function.[23] The quantities u_1 and u_2 are defined by

$$u_1=m\xi_+^2\left(\frac{k^2\xi_+^2+1}{2m\xi_+^2}-\mu+i\sqrt{\omega_n^2+\rho^2}+\sqrt{D}\right),$$

$$u_2=m\xi_+^2\left(\frac{k^2\xi_+^2+1}{2m\xi_+^2}-\mu+i\sqrt{\omega_n^2+\rho^2}-\sqrt{D}\right)\tag{19}$$

with

$$D\equiv\left(\frac{k^2\xi_+^2+1}{2m\xi_+^2}-\mu+i\sqrt{\omega_n^2+\rho^2}\right)^2$$

$$+\frac{2}{m\xi_+^2}(\mu-i\sqrt{\omega_n^2+\rho^2}).\tag{20}$$

For studying the spectral properties of the system in the next Section we'll need the retarded Green's function, which can be obtained from (17) after the analytical continuation $i\omega_n\to\omega+i0$.

For now let us just say that for $T<T_{BKT}$ this function has the structure

$$G(\omega,\mathbf{k})\sim\Gamma^2(\alpha)\left(\frac{2}{mr_0^2}\right)^{\alpha-1}A_1[-(\mu+\sqrt{\omega^2-\rho^2})]^{-\alpha}$$

$$\times\left[\frac{\Gamma(1-2\alpha)}{\Gamma^2(1-\alpha)}+\frac{\Gamma(2\alpha-1)}{\Gamma^2(1-\alpha)}\right.$$

$$\left.\times\frac{1}{(1-z_1)^{2\alpha-1}}\right],\quad z_1=1.$$

Thus the Green function is of the non-Fermi-liquid theory type; it has a non-pole character and contains a branch cut. So the Fermi-liquid behavior of the system is broken by strong phase fluctuations of the complex ordering field.

4. THE SPECTRAL DENSITY AND DENSITY OF STATES

The spectral density contains information about many properties of systems, for examples, such features as the density of states and the presence of a gap. For cuprates this quantity was measured in the ARPES experiments (see Ref. 20). Below we obtain the expressions for the spectral density and density of states which follow from the retarded Green function (recall that it is defined by (17) with the analytical continuation $i\omega_n \to \omega + i0$).

Let us first calculate the spectral density[19] using the expression

$$A(\omega, \mathbf{k}) = -\frac{1}{k} \text{Im } G_{11}(\omega + i0, \mathbf{k}). \tag{21}$$

After substitution of the analytically continued expression (17) in (21) one can directly come to:[17]

$$A(\omega, \mathbf{k}) = \frac{\Gamma(\alpha)}{\Gamma(1-\alpha)} \left(\frac{2}{mr_0^2} \right)^{\alpha-1} \text{sgn } \omega \, \theta(\omega^2 - \rho^2)$$

$$\times \left[\frac{(A_1)_{11}}{D_2^{\alpha/2}} F_1 \left(\frac{\alpha}{2}, \frac{1-\alpha}{2}; 1; \right. \right.$$

$$\left. -4 \frac{\frac{k^2}{2m}(\mu + \sqrt{\omega^2 - \rho^2})}{D} \right) \theta(\mu + \sqrt{\omega^2 - \rho^2})$$

$$\left. -(\sqrt{\omega^2 - \rho^2} \to -\sqrt{\omega^2 - \rho^2}) \right]. \tag{22}$$

The chemical potential μ is determined by the equation that fixes the carrier density.[16] However, in the case of large carrier densities the equality $\mu = \varepsilon_F$ is almost exactly fulfilled. Note that the expression (22) for $A(\omega, \mathbf{k})$ is not the BCS sum of two parts with δ-function peaks at $\omega = \pm E(\mathbf{k})$ which correspond to the addition and removal of an electron, but the sum of two ''mixed'' terms.

It is possible to check analytically the sum rule for the spectral density. Namely, as in the $4F$ model, we have

$$\int_{-\infty}^{\infty} d\omega A(\omega, \mathbf{k}) = \frac{\Gamma(\alpha)}{\Gamma(2-\alpha)}. \tag{23}$$

Let us estimate the quantity on the right side in the region $T \sim T_{BKT}$. For the stiffness at $T = T_{BKT}$ we have $J = 2/\pi T_{BKT}$, which gives [see (18)] $\alpha = 1 - 1/32 \approx 1$ at $T \sim T_{BKT}$. Therefore the formula (22) for the spectral density is quite good in the temperature region-near T_{BKT} at large carrier densities. Since we are studying the region of large carrier densities, at temperatures in the pseudogap phase the condition $T \sim T_{BKT}$ is always true, because at large n_f the pseudogap region is narrow and shrinks as $n_f \to \infty$ (again, see

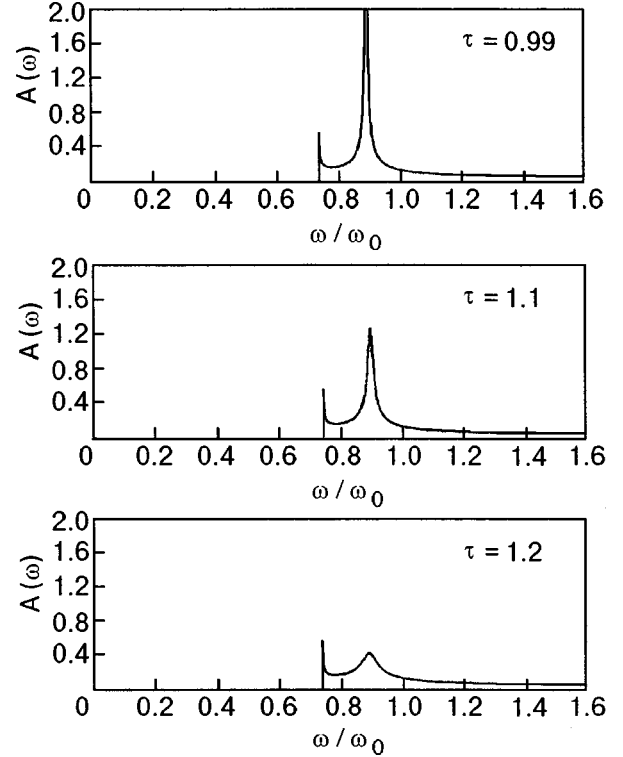
FIG. 1. The spectral density as a function of ω is presented for the case $k > k_F$ at different values of $\tau = T/T_{BKT}$.

Ref. 16). This is evidently different from the $4F$ case, where the corresponding region decreases much more slowly.

The ω dependences of the spectral density for $T < T_{BKT}$ and $T > T_{BKT}$ in the case $k < k_F$ are presented in Fig. 1 (the behavior in the case $k > k_F$ is analogous). There are two quasiparticle peaks at the points $\omega = \pm E(\mathbf{k})$ and another two at $\omega = \pm \rho$. The presence of the last two is caused by the non-pole structure of the Green function. At $k = k_F$ these two kinds of peaks coincide, because at this point one has $E(\mathbf{k}_F) = \rho$. The peaks at the frequencies $\omega = \pm E(\mathbf{k})$ decrease with increasing temperature, and when $T > T_{BKT}$ (where these peaks are finite) quickly go to zero. This is in qualitative agreement with the ARPES experiments,[20] which show that the spectral function broadens on passing to the normal phase.

For $\omega < |\rho|$ we have $A(\omega, \mathbf{k}) = 0$, and therefore the gap exists at any T. The same conclusion is also correct for the $4F$ model. Note again that our results are obtained by using the static approximation. The empty region must disappear (as well as the quasipeaks at $\omega = \pm \rho$) if dynamical fluctuations are taken into account. Evidently, the filling of the empty region should be different for $T < T_{BKT}$ and $T > T_{BKT}$.

As is seen in Fig. 1, a smooth crossover takes place as the temperature changes from $T < T_{BKT}$ to $T > T_{BKT}$. This is in agreement with experiments (for instance, on ρ)[20] and differs from the BCS theory. Let us also note that our results are obtained for not very small ρ. When $\rho \to 0$ (low carrier densities) its (i.e., modulus) fluctuations must be taken into account.

The end of this Section is devoted to a calculation of the density of states. The desired expression can be obtained from the formula

$$N(\omega) = N_0 \int_0^W d\,\frac{k^2}{2m} A(\omega, \mathbf{k}), \tag{24}$$

where $N_0 \equiv m/2\pi$ is the density of states in the normal phase, and W is the bandwidth.

This expression together with (22) results in the representation

$$N(\omega) = N_0 \frac{\Gamma(\alpha)}{\Gamma(2-\alpha)} \left(\frac{2}{mr_0^2}\right)^{\alpha-1} \operatorname{sgn}\omega\,\theta(\omega^2 - \rho^2)$$

$$\times \left\{ (A_1)_{11} \left[\left(\frac{1}{2m\xi_+^2} + W - \mu - \sqrt{\omega^2 - \rho^2}\right)^{1-\alpha} \right.\right.$$

$$\left. - \left(\frac{1}{2m\xi_+^2}\right)^{1-\alpha} \right] \theta(\mu + \sqrt{\omega^2 - \rho^2})$$

$$\left. - (\sqrt{\omega^2 - \rho^2} \to -\sqrt{\omega^2 - \rho^2}) \right\}, \tag{25}$$

which formally also coincides with formulas obtained in Ref. 17, although there is different behavior on account of the different carrier dependences of the neutral order parameter ρ in these ($4F$ and boson-exchange) superconducting models.

At zero temperature and large carrier densities ($\mu \gg \rho$) the formula (25) reproduces the BCS result

$$N(\omega) = N_0 \frac{|\omega|}{\sqrt{\omega^2 - \rho^2}}. \tag{26}$$

The density of states for different cases are presented in Fig. 2. As in the case of the spectral densities, the gap in the density of states exists at temperatures near and above T_{BKT}, which plays the role of the critical temperature in a pure 2D metal. The form of the density of states qualitatively coincides with the BCS one. The crucial difference is in the smooth change of the curves at the phase transition point.

Let us repeat again that dynamical fluctuations can be responsible for the filling of gap and that at small carrier densities the ρ fluctuations must also be taken into account.

5. CONCLUSION

In this paper the analytical calculation of the fermion Green function has been generalized to the case of the Fröhlich model of superconductivity, although some expressions have proved to be similar to those obtained for the case of a 2D metal with a nonretarded inter-fermion attractive interaction. This result could be important for several reasons: First, as a general result for the theory of fluctuations in boson-exchange quantum solid state systems. Second, because there is as yet no generally accepted theory of high-temperature superconductivity, and it now appears possible that some boson-exchange model will be appropriate for the description of this phenomenon. Thus an analytical investigation of the Green function in the boson-exchange case could be very
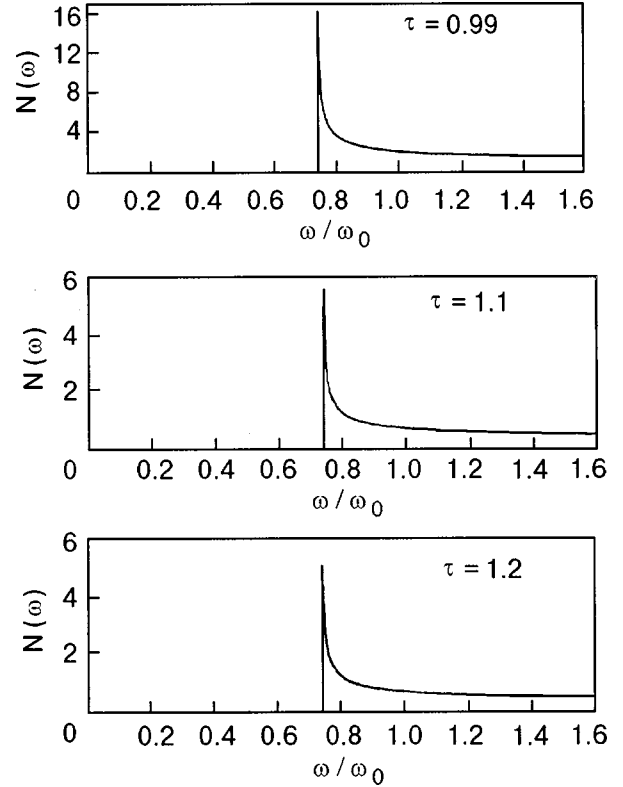

FIG. 2. The density of states (in N_0 units) is plotted versus ω for different values of $\tau = T/T_{BKT}$.

important, because it gives much more information than the numerical studies often employed. For example, it has been shown that the transverse phase fluctuations result in non-Fermi-liquid behavior of the system below (but for $T \neq 0$) and above T_{BKT}.

Along with this there are many open questions about the problem studied above. For example, the role of superconducting fluctuations in the pseudogap phase formation. Also it is very important to take into account the ρ fluctuations and to generalize the approach to the dynamical fluctuation case.

[1]Here and below we consider $\Psi(x)$ and $Y(x)$ as Grassmann operators and $\theta(x)$ as ordinary variables in functional integrals. In the Hamiltonian formalism the former obey Fermi statistics, while $\theta(x)$ preserves ordinary (commutational) algebra.

[1] D. Pines, Turkish J. Phys. **20**, 535 (1996); A. V. Chubukov and A. J. Schmalian, Phys. Rev. B **57**, R11085 (1998).
[2] R. A. Klemm, in *Proceedings of the First International Conference on New Theories, Discoveries, and Applications of Superconductors and Related Materials*, Baton Rouge, 1998, to be published in Int. J. Mod. Phys. B.

[3] G. Baym, Phys. Rev. **127**, 1391 (1962).

[4] R. Haussmann, Z. Phys. B **91**, 291 (1993).

[5] O. Tchernyshyov, Phys. Rev. B **56**, 3372 (1997).

[6] J. Serene, Phys. Rev. B **40**, 10873 (1989); J. J. Deisz, D. W. Hess, and J. W. Serene, Phys. Rev. Lett. **80**, 373 (1998).

[7] R. Mičnas, M. H. Pedersen, S. Schafroth, T. Schneider, J. J. Rodrígues-Nuñez, and H. Beck, Phys. Rev. B **52**, 16223 (1995).

[8] R. Haussmann, Phys. Rev. B **49**, 12975 (1994).

[9] M. Letz and R. J. Gooding, J. Phys.: Condens. Matter **10**, 6931 (1998).

[10] B. Janko, J. Mali, and K. Levin, Phys. Rev. B **56**, R11407 (1997), preprints cond-mat/9710187, cond-mat/9805018; I. Kostin, Q. Chen, B. Janko, and K. Levin, Phys. Rev. B **58**, R5936 (1998), preprint cond-mat/9807414.

[11] J. R. Engelbrecht, A. Nazarenko, M. Randeria, and E. Dagotto, Phys. Rev. B **57**, 13406 (1998).

[12] M. Randeria, in *Proceedings of the International School of Physics ''Enrico Fermir,''* Varenna, 1997 IOS Press, Amsterdam (1998); preprint cond-mat/9710223.

[13] J. M. Singer, M. H. Pedersen, T. Schneider, H. Beck, and H.-G. Mattutis, Phys. Rev. B **54**, 1286 (1996).

[14] V. P. Gusynin, V. M. Loktev, and S. G. Sharapov, JETP Lett. **65**, 182 (1997).

[15] V. P. Gusynin, V. M. Loktev, and S. G. Sharapov, preprint cond-mat/9709034; JETP **115**, 1243 (1999).

[16] V. M. Loktev, S. G. Sharapov, and V. M. Turkowski, Physica C **296**, 84 (1998).

[17] V. P. Gusynin, V. M. Loktev, and S. G. Sharapov, JETP Lett. **69**, 126 (1999); preprint cond-mat/9811207.

[18] V. M. Loktev and V. M. Turkowski, Zh. Éksp. Teor. Phys. **114**, 605 (1998) [JETP **87**, 329 (1998)].

[19] N. D. Mermin and H. Wagner, Phys. Rev. Lett. **17**, 1113 (1966); P. C. Hohenberg, Phys. Rev. **158**, 383 (1967); S. Coleman, Comum. Math. Phys. **31**, 259 (1973).

[20] For a recent review see M. Randeria and J. C. Campuzano, in *Proceedings of the International School of Physics ''Enrico Fermi,''* Varenna, 1997 IOS Press, Amsterdam (1998); cond-mat/9709107.

[21] M. Plischke and B. Bergersen, *Equilibrium Statistical Physics*, Prentice-Hall, Englewood Cliffs, New Jersey (1989), p. 167.

[22] S. W. Pierson, Philos. Mag. **B76**, 715 (1997).

[23] H. Bateman and A. Erdélyi, *Higher Transcendental Functions*, McGraw-Hill, New York (1953).